Participation au développement d'un aimant haut champ 30T en REBaCuO

Mohamad Rajab Alharake

université
PARIS-SACLAY

Participation in the development of a high-field 30 T REBaCuO magnet

Participation aux développements d'un aimant haut-champ 30 T en REBaCuO

Thèse de doctorat de l'Université Paris-Saclay

École doctorale n°579 Science mécaniques et énergetiques, matériaux et géosciencs
Spécialité de doctorat: Solides, structures et matériaux
Graduate School : Sciences de l'ingénierie et des systèmes, Référent : ENS Paris-Saclay

Thèse préparée dans les unités de recherche: unité de recherche : LMPS - Laboratoire de Mécanique Paris-Saclay (Université Paris-Saclay, CentraleSupélec, ENS Paris-Saclay, CNRS) et Département des Accélérateurs, de la Cryogénie et du Magnétisme (Université Paris-Saclay, CEA), sous la direction de Olivier Hubert, Professeur, le co-encadrement de Philippe Fazilleau, Ingénieur- chercheur

Thèse présentée et soutenue à l'ENS Paris-Saclay, le 21 Mars 2022, par

Mohamad Rajab ALHarake

Composition du jury

Jacques Noudem Professeur, CRISMAT - Caen	Président
Michel Coret Professeur, GEM - Nantes	Rapporteur
François Debray Ingénieur recherche HDR, CNRS LNCMI - Grenoble	Rapporteur
Laurence Bodelot Maître de conférence HDR, LMS Ecole Polytechnique	Examinateur
Olivier Hubert Professeur, ENS Paris-Saclay	Directeur de thèse
Xavier Chaud Ingénieur-chercheur, CNRS LNCMI - Grenoble	Invité

THESE DE DOCTORAT

NNT : 2022UPAST042

université PARIS-SACLAY

ÉCOLE DOCTORALE
Sciences mécaniques et énergétiques, matériaux et géosciences (SMEMAG)

Titre: Participation aux développements d'un aimant haut-champ 30 T en REBaCuO

Mots clés: MI REBCO galette, Calcul des contraintes, Déplacement plein champ, Corrélation d'images numériques.

Résumé: Les supraconducteurs sont divisés en deux catégories, les supraconducteurs à basse température critique (LTS) et les supraconducteurs à haute température critique (HTS). Avec les LTS, des limitations strictes sont imposées sur la température de refroidissement (< 14 K) et le champ magnétique réalisable (< 28 T). Lorsqu'il s'agit de HTS, des températures de refroidissement et des champs magnétiques plus élevés sont autorisés. Cela offre une plus grande flexibilité dans les applications, d'autant plus que l'azote liquide peut être utilisé dans le processus de refroidissement.

Divers projets et applications R&D sont devenus envisageables avec la baisse significative du coût des rubans HTS. Plus le champ magnétique est élevé, plus les capacités d'applications telles que la RMN, l'IRM, etc. sont possibles. Différents electro-aimants ont été construits et testés pour obtenir des champs élevés à l'aide de rubans REBCO. Par exemple, l'aimant « Nougat » a atteint 32.5 T, dont 14.5 T provenant de l'insert REBCO et 18 T d'un electro-aimant résistif extérne. L'insert "Nougat" est composé d'un empilement de galettes REBCO métal-isolant (MI). Les bobinages MI offrent une protection contre le quench grâce à leur capacité de dérivation de courant et un renfort mécanique supplémentaire avec un ruban d'isolation métallique rigide.

Lorsque la contrainte est calculée au niveau du plan médian de la galette centrale de l'aimant « Nougat » où les forces radiales de Laplace sont les plus élevées, la contrainte radiale était positive dans une majeure partie de celui-ci. Cela indique que les spires peuvent être séparées là où la contrainte est positive. Cela va à l'encontre de la nécessité d'un contact dans les galette MI HTS pour maintenir l'aspect de protection contre la quench d'une telle configuration d'aimant.

Par conséquent, dans cette thèse, une meilleure compréhension de la mécanique des galettes MI REBCO est recherchée. Ainsi, différentes formulations analytiques mécaniques sont discutées concernant les trois chargements : enroulement (prétension), refroidissement (contraction thermique) et énergisation (effet des forces de Laplace). De plus, le surbandage comme support mécanique et les contributions de précontrainte sont discutés. Ensuite, l'identification des paramètres du matériau se fait à l'aide d'essais de traction et de compression diamétrale avec corrélation d'images numériques (CIN), pour les utiliser dans le recalcul des contraintes de Nougat et d'un prototype de modélisation en galette avant son essai. Ces tests ont mis en évidence l'importance du processus d'enroulement et son effet sur le module radial du test de compression diamétrale, et l'effet de courbure du rapport de Poisson dans les matériaux en feuille comme le REBCO et les rubans métalliques isolants du test de traction. Enfin, une nouvelle configuration adéquate a été développée pour permettre des mesures in-situ du déplacement de plein champ de galette MI à des températures cryogéniques à l'aide de CIN. La configuration est utilisée pour valider les formulations analytiques.

Title: Participation in the development of a high-field 30 T REBCO magnet.

Keywords: MI REBCO pancake, Stress calculation, Full Field Displacement, Digital Image Correlation

Abstract: Superconductors are divided into two categories, low temperature superconductors (LTS) and high temperature superconductors (HTS). With LTS, strict limitations are posed on the cooling temperature ($<$ 14 K) and achievable magnetic field ($<$ 28 T). On the other hand, higher cooling temperatures and magnetic fields are allowed when dealing with HTS. This provides higher flexibility in the applications, especially since liquid nitrogen can be used in the cooling process.

Various R&D projects and applications are becoming more conceivable with the significant decrease in the HTS tapes cost. The higher the magnetic field, the higher the capabilities are of applications like NMR, MRI, etc. Different magnets were built and tested to obtain high fields using REBCO tapes (they are proven to achieve high fields at 4K). For example, "Nougat" magnet achieved 32.5 T, with 14.5 T coming from the REBCO insert and 18 T from a resistive outsert; this magnet is composed of a stack of metal-as-insulation (MI) REBCO pancakes. The MI configuration provides protection against quench with its current bypassing capability, and mechanical support with a stiff metal-as-insulation tape.

When the stress was calculated at the mid-plane of the central pancake of the "Nougat" magnet where radial Laplace forces are the highest within the whole magnet, radial stress was positive in a major part of it. This indicates that the turns may have separated where the stress is positive. This stands against the necessity of contact in MI HTS pancakes to maintain the quench protection aspect of such magnet configuration.

Hence, in this thesis, a better mechanical understanding of MI REBCO pancakes is sought. Thus, different mechanical analytical formulations are discussed regarding the three loadings: winding (with pre-tension), cooling (thermal contraction), and energizing (Laplace forces effect). In addition, the over-banding as mechanical support is also discussed. Then, identification of material parameters is done using tensile and diametric compression testing with digital image correlation (DIC), to use them in recalculating Nougat stresses and a prototype pancake modeling before its testing. These tests highlighted the importance of the pre-tension and its effect on radial modulus from the diametric compression test, and the poisson ratio curving effect in foil materials like REBCO and metal-as-insulation tapes from the tensile test. Finally, a new adequate setup was developed that allow in-situ measurements of full field displacement of MI pancakes at cryogenic temperatures using DIC. The setup is used to validate the analytical formulations.

Acknowledgement

With the ending of a journey, another one begins. The PhD journey has been quite an experience, an into the unknown experience. So much unexpected events occurred during the three years of the PhD, especially the COVID pandemic and its profound effects on work and life starting from my second year. The pandemic left no option but to trust the unknown and the future, whether it is regarding work or personal life especially for the safety of my parents.

However, here I am, at the end of the journey, with new experience in work and life. I would like to thank CEA Saclay for funding my thesis at DACM-LEAS, my supervisor Philippe Fazilleau for this opportunity to work on metal-as-insulation high temperature superconductors pancakes, and my thesis director Olivier Hubert for his guidance and patience during the PhD. I would like to thank Lionel Quettier for his help in everything related to resources whether it is the administrative procedure for the DIC experimental setup manufacturing or reserving the cryogenic technician's aid for the experiments at cryogenic temperature.

The list of people that I would like to thank goes on and on, but there are some people that I must thank as well. I would like to thank Julien Avronsart, Mahmoud Abdel Hafiz and Clément Genot for the pleasant environment they created and their companionship during my PhD. I wish to extend my special thanks to Hugo Reymond for his aid in improving the DIC setup design and drawings required for manufacturing, and Jean-Christophe Guillard for his help in placing the setup manufacturing order and following its progress. I would like to thank Michel De Sousa for manufacturing the pieces I required for my experiments and Thibault Lecrevisse for his aid in the winding process.

I wish to show my appreciation to Bertrand Baudouy and Bertrand Hervieu for their advice regarding the cryogenic aspect of the DIC setup, Guillaume Dilasser for his help with the tips he gave me regarding LabVIEW program, Aurélien Godfrin for his help in DIC setup assembly and the tests as well, and Clement Hilaire and Charles Maillert for their invaluable aid in handling of the cryogenics for the DIC experiments.

I would like to thank Francois Nunio for his help and patience in regards to Cast3m questions and inquiries, and François Hild for his patience in answering the DIC questions I had and help in adjusting the FEMU code of LMT for the diametric compression tests.

Last but not least, I would like to thank all my Lebanese friends that I had the pleasure to know during the PhD who I consider like my second family. Their support was invaluable during this journey. Still, life goes on, it will not wait or stop for anyone, so no matter what the future has, one has to "keep moving forward" as Martin Luther King said.

Contents

List of Figures

List of Tables

Introduction

Superconductivity is a state of matter where conduction current flows while encountering negligible resistance. This phenomenon, discovered in 1911, allowed for the development or improvement of many modern tools such as magnetic resonance imaging (MRI), nuclear magnetic resonance (NMR), particle accelerators, etc. However, no significant application of this discovery was proposed until 1955 and the production of superconducting niobium wire with which a superconducting magnet was made of. In 1962, the ductile niobium-titanium alloys were discovered suitable to applications of up to 15 T. This material ushered the increase of superconducting magnets as it became the backbone of MRI, NMR and particle accelerator applications. However, the superconductors so far were limited with low critical temperature; being called low temperature superconductor "LTS" where critical temperature is few Kelvins (requiring liquid helium cooling) and critical magnetic field can reach around 28 T for niobium-tin.

Later on, in 1986, a new family of superconductors was discovered, the high temperature superconductors "HTS", with the critical temperature above 30 K, achieving 93 K in YBaCuO (Rare earth Barium Copper Oxide) superconductor. The critical temperature of YBaCuO (REBCO) is above boiling point of liquid nitrogen at atmospheric pressure (77 K), opening a new venue of applications for superconductors at liquid nitrogen temperature: the cooling is significantly simplified as nitrogen is cheaper, abundant, and has much higher vaporization enthalpy than liquid helium. The initial discovered HTS superconductor was based on cuprate perovskite materials, but other materials of different families were discovered later like magnesium diboride or iron-based superconductors belonging to the same HTS family.

The critical temperature was not the only advantage of HTS comparing to LTS. It was shown that the critical magnetic field is much higher than 23.5 T in HTS when using them at lower temperature (liquid helium - LHe for instance). Experiments like "Nougat" magnet that is the result of a joint effort of CEA Saclay – LNCMI (Laboratoire National des Champs Magnétiques Intenses) reaching 32.5 T or the hybrid magnet at NHMFL-US (National High Magnetic Field Laboratory) reaching 45.5 T proved the capability of HTS conductors to maintain superconductivity at high fields at liquid helium temperature. However, these accomplishments were not achieved until approximately 35 years after HTS discovery, as the required manufacturing process was being improved significantly to produce both mechanically strong and flexible conductors. Indeed Cuprate based superconducting materials are brittle. With the use of superconducting HTS layer deposition on a high strength Hastealloy substrate, different magnets were produced in laboratories. However, the quench phenomenon that any superconductor is prone to – that is the sudden transition from superconducting state to the resistive state – proved to be an issue in HTS magnets unlike in LTS magnets.

The quench propagation is fast in LTS magnets, being in range of meters per second up to tens of meters per second, allowing for direct quench detection and protection. The fast quench propagation in a superconducting magnet causes a large part of the magnet to become resistive; thus increasing the measured resistive voltage at the terminals significantly permitting quench detection by voltage measurement. In addition, in this case, the stored energy is dissipated over a large part of winding of the magnet and over a dump resistor, if active protection is implemented, limiting the temperature attained in the magnet to safe levels. Unlike LTS

magnets, in HTS magnets the quench propagation is slow with only a few millimeters up to few centimeters per second, complicating the quench detection and protection significantly. Slow quench propagation velocities result in having excessive heat build-up in the quenched zone of the magnet exceeding the cooling rate. Thus, a thermal runaway can occur and degrades irremediably the magnet.

In 2011, the no-insulation HTS magnet was tested [1]. No insulation means that the REBCO tapes are wound without any insulation between the turns; thus turns have a direct electrical contact between each other. No-insulation HTS were compared to that of insulated HTS magnets regarding the quench phenomenon. It was found that the no-insulation configuration protected the magnet which was quenched several times by allowing the current to by-pass the quenched region to the next superconducting turn radially. Unfortunately, the current ramp rate was significantly affected because of the radial currents generated during ramping due to mutual inductance between turns with very high time constants. This point was tackled by introducing the metal-as-insulation (MI) configuration, where the REBCO HTS tapes are co-wound with a thin mechanically stiff metal tape. This metal tape increases the contact resistance significantly thus decreases the radial currents during ramping and lowering their time constants. In addition, it provides additional mechanical support to the magnet allowing for higher fields to be achieved.

On the other hand, REBCO tapes were found to degrade if the mechanical stress exceeds yield stress or an axial strain limit. The rectangular shape of the REBCO tape imposes bending limitations that are to be considered in the mechanical design. Thus, the mechanical study of MI HTS REBCO magnets is quite important to ensure its proper functioning, especially at high field where Laplace forces are quite high. Previous computational mechanical studies have been done regarding superconducting magnets with simplifying assumptions, but still now no experimental measurement are available to be compared to calculations regarding MI HTS REBCO pancake magnets.

This manuscript focuses on different mechanical aspects regarding MI HTS REBCO pancake magnet for high field applications. Specifically, an experimental setup is developed allowing for real time measurement of deformations during cooling and energizing using digital image correlation (DIC). Experimental measurements are compared with outputs of both new analytical formulations and finite element simulations. Objective is to use the analytical formulation for fast evaluation of different magnet forming processes and geometries at the stage of design. These evaluations are relevant for future improvements.

In chapter 1, superconductivity is introduced, and the MI HTS magnet aspects are presented. In chapter 2, different analytical formulations and assumptions are discussed and used to calculate the mechanical state after the main loading stages of a MI REBCO pancake (winding, cooling, energizing). Analytical formulations results are compared to the results of a reference finite element calculation using the Cast3m code. This comparison allows for the most appropriate analytical formulation to be chosen as the most representative of stress and deformation distribution. Later in the chapter, Nougat magnet stresses are evaluated using both analytic formulation and Cast3m for bench marking. Effect of over-banding and pre-tension during winding on the mechanical stress distribution in the pancake are finally studied.

In chapter 3, the mechanical properties identification of both tapes (REBCO and stainless steel (SS)) using digital image correlation (DIC) is presented. Tensile and diametric compression testing have been used for identifications. A dedicated finite Element Method Update (FEMU) has been developed and employed for that purpose. It highlighted the effect of winding process

on the bulk material properties of tapes.

In chapter 4, a new experimental setup is presented that allows for real time image acquisition of the deformation of the MI REBCO pancake during cooling and energizing. First, the setup and image acquisition are validated during liquid nitrogen cooling of stainless steel 304 disc. Then, a co-wound copper beryllium – stainless steel 304 pancake undergoes a cooling test at liquid nitrogen. The deformation results during the tests acquired from DIC are compared to the outputs of analytic formulation. Chapter 5 draws the general conclusions of this manuscript.

1 - Metal-as-Insulation HTS Coil

1.1 . Superconductivity

Normal conductors carry electric current with a resistance generating heat. However, some materials can conduct electricity with negligible to no resistance under specific conditions. These materials are called superconductors, and they conduct large currents in specific temperature and magnetic field ranges. After explaining superconductivity and associated properties, high temperature superconductivity is introduced and the main corresponding materials *BSSCO and REBCO* are described. Since BSCCO is mechanically weaker than REBCO as it will be discussed in this chapter, REBCO is the superconductor used in this PhD. Then, few usage examples of REBCO are presented followed by explanation of quench and metal-as-insulation of REBCO magnets. Finally, the chapter ends with the outline of the thesis manuscript.

1.1.1 . Superconducting Properties

Superconductivity was first discovered in 1911 by H. Kamerlingh Onnes during an attempt at measuring the electrical resistivity of mercury at low temperatures [2]. The discovery that the resistance dropped so much that it measured zero with his equipment at 3 K was astounding. The resistance was so small that his equipment could not measure it. At the same time, it was discovered that above a certain temperature, there was a sudden jump back to the resistive state, this temperature is called *critical temperature* T_c. Above T_c, superconductor changes back to resistive state, which is called *normal state*.

A second property, that makes a superconductor different from a perfect conductor, was discovered later on in 1933 by W.Meissner and R.Ochsenfeld [3]. They found that a superconductor will expel a surrounding magnetic field outside its body by creating currents in thin depth near its surface to shield the remaining volume from the magnetic field. This is the *Meissner state*, and the currents generated are *Meissner currents*.

1.1.2 . Limits of Superconductivity

Thereafter, it was discovered that for a material to remain superconductive, not only its temperature has to be lower than T_c, but also the magnetic field should be lower than a *critical field Bc* [4]. Later on, in 1957, Abrikosov [5] found analytically a difference between two types of superconductors regarding their reaction to the magnitude of the external magnetic field applied.

Type I superconductor has a very low single critical magnetic field B_c (less than 200 mT). Beyond this B_c, it directly reverts back to the *normal state*. B_c is also inversely dependent of temperature (T) (Fig. 1.1a). Type I superconductors are mostly pure elements like mercury, lead and aluminum.

However, *type II* superconductor has two critical magnetic fields : lower field $B_{c,1}$, and upper field B_{c_2}. Type II behaves like type I below $B_{c,1}$ which has nearly same magnitude as *Bc* of type I. However, between $B_{c,1}$ and $B_{c,2}$, type II enters a mixed state where normal and superconducting regions are present. In the mixed state, the magnetic field can penetrate the superconductor at some points while remaining superconducting. Above $B_{c,2}$, it reverts back

to the normal state (Fig. 1.1b).

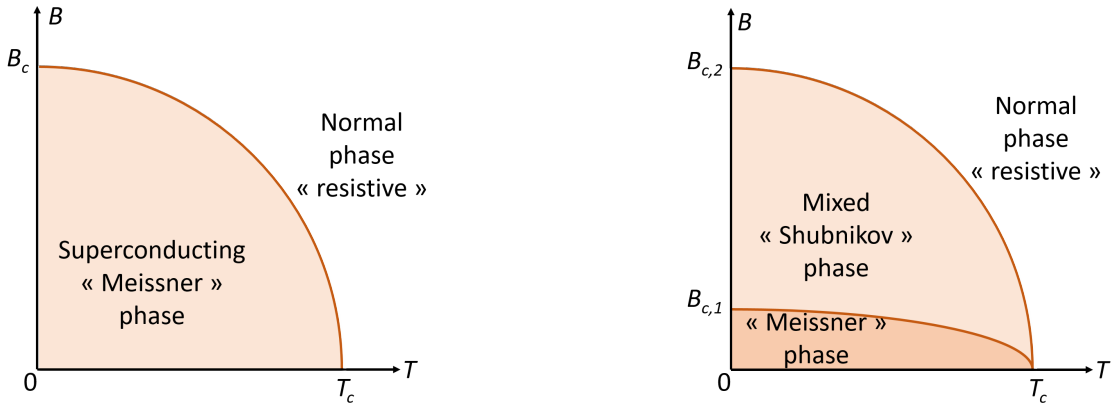

(a) Type I superconductor

(b) Type II superconductor

Figure 1.1 – Magnetic field (*B*) vs temperature (*T*) phase diagrams of a superconductor

Type I has an issue regarding B_c as it is very small leading to a fast transition to normal state. Even the self-field that it generates when supplied with current can be enough to cause its revert back to the normal state [4]. This limits the practical application of type I superconductors.

On the other hand, in type II, $B_{c,2}$ can reach hundred of Teslas (> 150 T for YBCO), which is much greater than B_c of *Type I*. This made it practical for high current density applications and high magnetic field generation. Several compounds belong to this category, but the most used ones are Niobium-Titanium (NbTi) and Niobium-Tin (Nb_3Sn).

Additionally, the superconducting phase is also limited by a maximum current density J_c called *critical current density* (Fig. 1.2). Crossing J_c is different between *Type I* and *Type II*, where in the former it is based on dislocation of Cooper pairs while for the latter it is due to unpinning of vortex. J_c of a type II material is set based on energy dissipation criterion. However, for calculation of magnetic field and mechanical stresses, engineers use *engineering current density* J_e. It is used because superconducting tapes or wires usually are a composite material with a superconducting layer or wire.

Each of the above mentioned parameters (T_c, B_c, and J_c) of a superconductor are dependent upon one another. Hence, the superconducting domain of a material is usually represented in the 3D space (*T,B,J*) bounded by a *critical surface* (Fig. 1.3). Below the surface, the material is superconductor, while above the surface it reverts back to the resistive state.

Depending on its critical temperature (Fig. 1.4), a superconductor can be either classified as low temperature superconductor (LTS, below 14 K) or high temperature superconductor (HTS). Well known LTS *NbTi* has been extensively used for various applications (MRI, accelerator magnets, etc. [8–10]) because of its low cost, long length production, mechanical rigidity, and achievable magnetic field strength of 10 - 15 T. Nb_3Sn can achieve higher fields (up to 28 T) than NbTi and requires heat treatment, but it is mechanically weaker than NbTi leading for the latter to be used whenever possible. However, with its limited critical magnetic field, complex cooling requirement, and desired high field generation in various applications, new superconductors are sought.

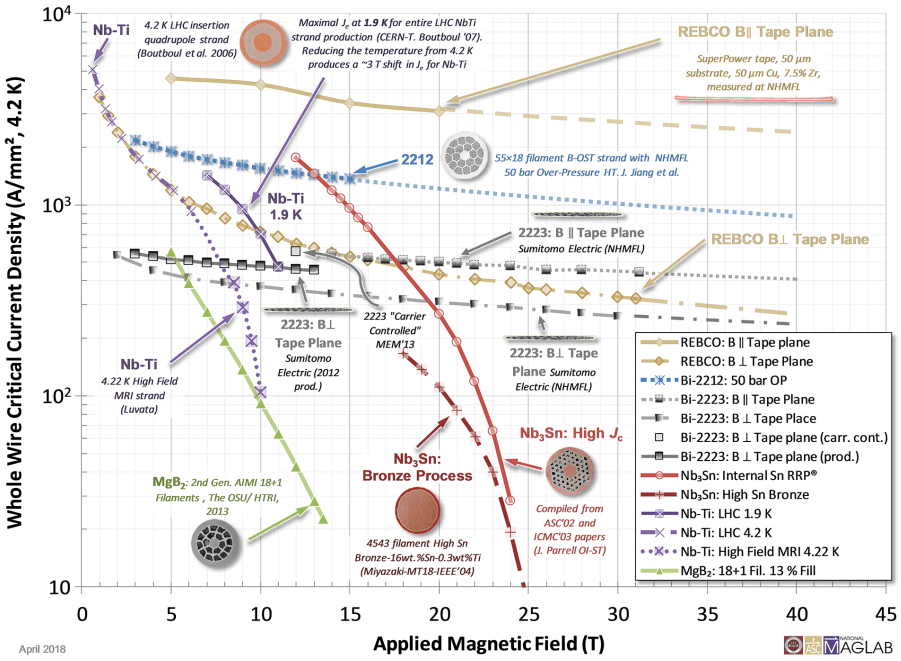

Figure 1.2 – Engineering current density of various superconductors at 4.2K with applied magnetic field [6]

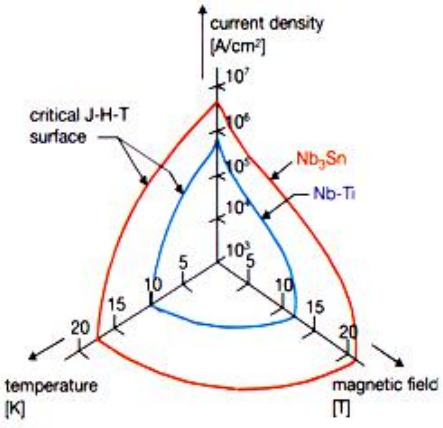

Figure 1.3 – Critical surface of common superconductors [7]

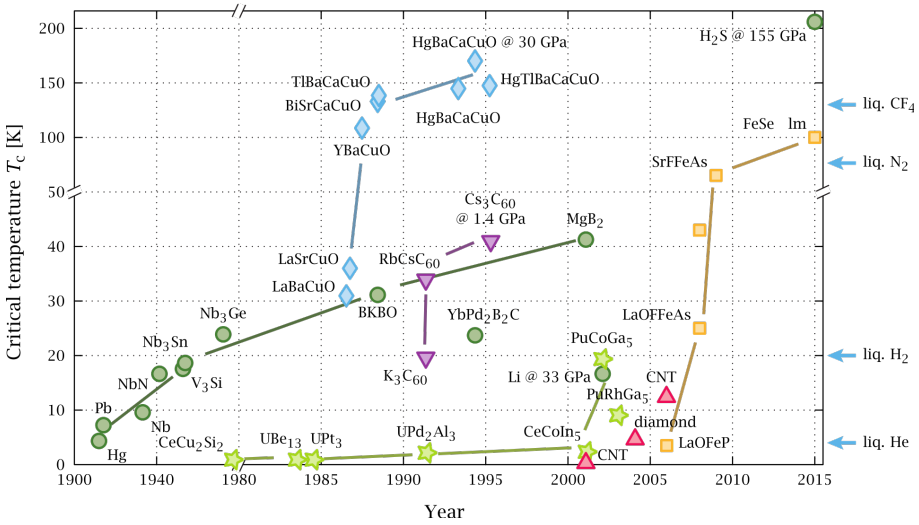

Figure 1.4 – Critical temperature T_c of various superconducting materials and their year of discovery (Classes: BCS (dark green), Heavy-Fermions(Light green), Cuprate(Blue), Buckminsterfullerene(Purple), Carbon-allotrope(Red), Iron-pnictogen(Orange-yellow)) [11]

1.2 . REBCO High Temperature Superconductor

Achieving superconductivity at high temperature (above 20 K) was thought to be impossible after the discovery of the first group of superconductors, i.e. low-temperature superconductor (LTS). However, approximately 40 years after the discovery of Nb_3Sn, other superconductors with *Tc* higher than 30 K were discovered (Fig. 1.4). They are called high temperature superconductors (HTS) [12].

Unlike LTS superconductors, HTS superconductors can operate under high magnetic field while still having high critical current densities as seen in Fig. 1.2 at low temperature. This feature has been validated by characterizing the HTS tapes at high magnetic field [13, 14].

1.2.1 . Discovery of High Temperature Superconductor

In 1986, high temperature superconductivity was discovered in transition metal oxides. The superconductivity was discovered in *Lanthanum-Braium-Copper-Oxide* [12, 15]. This discovery resulted in finding other HTS superconducting materials, especially in cuprates family. It was also noticed that HTS superconductors have higher current densities than LTS superconductors at low temperature under high magnetic field.

Recently, superconductivity has been discovered in various compounds while pushing the critical temperature to unprecedented values. It was discovered, for example, in *Magnesium Diboride* in 2001 [16] and in *Iron Pnictide* in 2008 [17] (Fig. 1.4). However, surprisingly, superconductors with critical temperature close to room temperature were recently discovered: *Hydrogen Sulfide* H_2S (200 K) [18] and *Lanthanum Hydride* LaH_3 (250 K) [19]. Unfortunately, both of them require very high pressures, for example, H_2S requires 155 GPa (Fig. 1.4) and LaH_3 requires 170 GPa making them unusable for practical applications.

1.2.2 . BSCCO and REBCO HTS Superconductors

From the discovered HTS materials, few are commercially available and suitable for magnet manufacturing, such as: *Bismuth Strontium Calcuium Copper Oxide* (*BSCCO*) and *Rare Earth Barium Copper Oxide* (*REBCO*).

BSCCO HTS

BSCCO superconductor, of general formula $Bi_2Sr_2Ca_{n-1}Cu_nO_{2n+4}$, was discovered in 1988 [20]. Various versions of BSCCO exist depending on Copper content n, but the interesting ones are those with $n = 2$ (BSCCO 2212) and $n = 3$. BSCCO 2212 has critical temperature close to 90 K [21] with a large critical field ($>$ 30 T) [22] (Fig. 1.2). BSCCO 2223 has even a higher critical temperature close to 105 K [21].

BSCCO can be manufactured in different ways, one of them is conventional metallurgic powder-in-tube process (PIT). PIT is used to make round wires of BSCCO 2212 (Fig. 1.5), which can be grouped to form cables. Unfortunately, even though the fabrication is a well-known method, it has significant difficulties. The PIT process starts with different precursors that need to be reacted to produce BSSCO 2212. Reaction of the precursors is very exhaustive. It requires heat treatment at a temperature of $900°C$ for a very long time [24], with demanding constraints on pressure and oxygen atmosphere [25].

In addition, silver is chosen as the matrix that supports BSCCO filaments as it meets the conditions required in the manufacturing process [24]. Unfortunately, the wire is weak mechan-

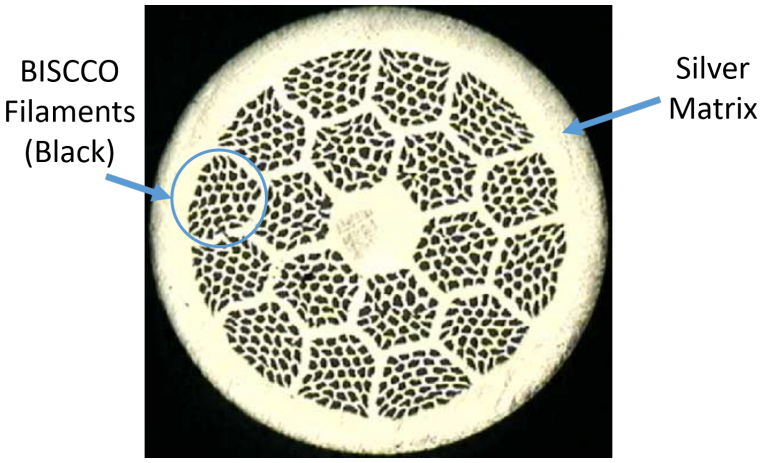

Figure 1.5 – BSCCO 2212 round wire cross section [23]

ically as the silver matrix has low yield stress. With the low yield stress of BSCCO wire, its use at high fields is further limited in comparison to REBCO tape.

REBCO HTS

REBCO was initially discovered in the form of YBCO in 1987 [26]. Unlike BSCCO which can be manufactured with conventional metallurgical methods, manufacturing REBCO requires a special technique called *thin film deposition*. Critical temperature of YBCO is 93 K and the upper critical field is greater than 100 T [27].

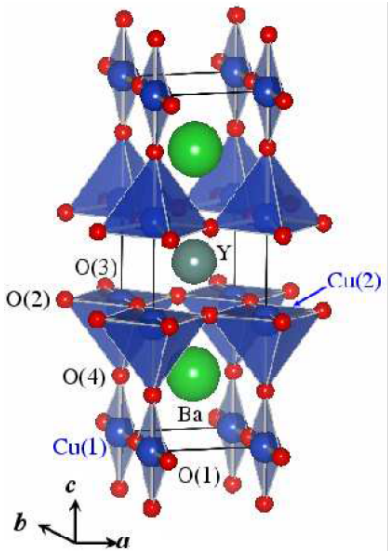

Figure 1.6 – Crystal lattice of YBCO superconductor [28]

REBCO is a family of superconducting materials, based on cuprates, of general chemical composition: $REBa_2Cu_3O_{7-x}$, where RE represents a rare earth element like Yttrium(Y) in the case of YBCO or Gadolinium (Gd) in the case of GdBCO. It is a common feature of all superconductors of REBCO crystallography to be formed of CuO planes (Fig. 1.6, crystal lattice of a member of REBCO family). However, the exact mechanism that results in superconductivity in REBCO materials is unknown until now. We call them the unconventional superconductors, as

opposed to the conventional superconductors explained by BCS theory [29]. It is worth noting that the CuO planes could have a potential role in the superconductivity of HTS material [30].

In high field applications, large Laplace forces are generated. REBCO is preferred to BSCCO because of its high mechanical strength and more supplies of REBCO worldwide [24, 31]. REBCO tape is the material considered in this PhD (Figs. 1.2 and 1.8).

1.2.3 . REBCO Tape Manufacturing Process

REBCO tape manufacturing process is quite different than that of other superconductors like BSCCO or NbTi (**PIT**). The manufacturing starts with a substrate tape that is usually Hastelloy C276 or nickel alloy ($Ni5W$) [32]. The tape width can vary depending on the manufacturer (2 to 12 mm), and the thickness can vary from $30\mu m$ to $150\mu m$ [33]. The substrate is the building block upon which all layers are deposited. It is the thickest layer in the tape and mostly defines the mechanical properties of the tape in the longitudinal direction.

To produce a superconducting layer with a high critical current J_c , it is paramount that the crystallographic lattice of the REBCO layer must be carefully aligned as grain boundaries and misorientations have critical effect on the REBCO layer's current density [34]. Hence, the REBCO layer is grown over a bi-axially textured support to control its orientation and achieve high critical current density. Several techniques have been developed to produce high quality REBCO tapes [35], which can be grouped, depending on the process used, whether physical or chemical [36]. In the chemical group, there are *Ion Beam Assisted Deposition* (*IBAD*) and the *Rolling-Assisted Biaxially Textured Substrate* (*RABITS*) techniques. In the physical, there is *Pulsed Laser Deposition* (*PLD*) technique [37]. IBAD and PLD are subsequently discussed .

IBAD process method starts with a Hastelloy C276 substrate. The substrate is first polished before adding the other materials and cleaned to obtain a good surface structure for depositing other layers. Buffer layers are deposited on the substrate progressively while controlling the lattice orientation for the REBCO deposition step. Previously, a buffer template composed of *Yttria-stabilized-Zirconia* (*YSZ*) is deposited on a substrate by using two ion sources, one directed at the YSZ buffer precursor while the other was directed at the substrate to help in the deposition of YSZ layer [38]. However, the slow deposition rate and film growth were a problem from an industrial point of view, so other methods were studied to tackle this problem. It was found out that buffer layer $Zr_2Gd_2O_7$ can grow faster than YSZ buffer. Also, CeO_2 deposition was discovered to improve in-plane grain alignment [35].

As for the PLD process, a pulsed laser of power approximately 300 W with a frequency of 300 Hz is used [36]. This laser is aimed at the precursor to be deposited in a vacuum chamber. The precursor is vaporized forming a plume, which is layered on the substrate. PLD process yields high grade superconducting layer while having a slow deposition rate. However, this is solved with multi-turn and multi-plume systems for REBCO layers [35].

After the deposition of superconducting layer is achieved, it is covered with a silver layer to act as a protection layer against chemical reactions for REBCO layer. After that, the tape is encased in copper by electroplating or lamination, and this helps protecting the tape from oxidation and enhancement of tape stability (electrically and thermally) [32]. Usually the final REBCO tape measures tens or hundreds of micrometers in thickness (30 to 150 μm) and few millimeters in width. Figure 1.7 shows a scheme of the production process of REBCO tapes (Fig. 1.8) that uses PLD process.

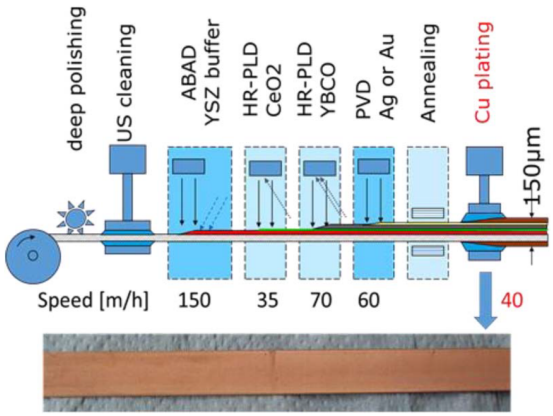

Figure 1.7 – PLD manufacturing process, Burker Manufacturer [32]

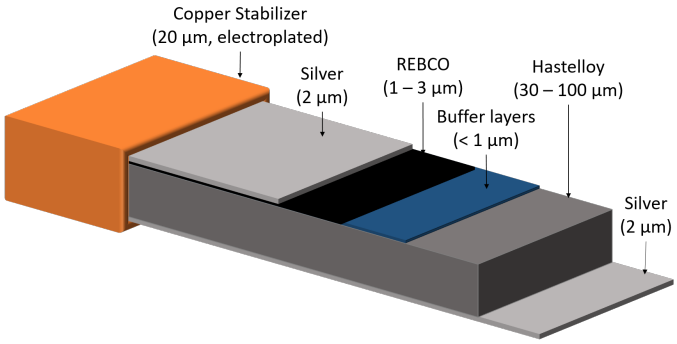

Figure 1.8 – REBCO coated conductor structure

1.3 . REBCO Tape Application

With the decrease in REBCO tape price and the possibility to choose between several suppliers, several R&D and commercial applications (Fig. 1.9) have risen up. The tape is used in projects of high-current cables in electrical networks [40–42], superconducting fault current limiter [43, 44], superconducting magnet energy storage [45–47], dipole magnets [48–50], etc.. In this section, high magnetic field generation, and nuclear magnetic resonance REBCO tape applications are discussed briefly.

1.3.1 . High Magnetic Field

As REBCO tapes can withstand high magnetic fields at low temperatures and still maintain high current densities in comparison to other superconducting materials, this makes them a prime candidate for the design of high field magnets. The magnet design is open to various configurations, from a single REBCO magnet, to REBCO concentric magnets, or a combination of REBCO magnet with another magnet such as LTS or resistive. This combination is called a hybrid magnet. REBCO hybrid magnet uses the conductors effectively based on their properties, and usually is composed of REBCO insert because REBCO sustains high fields and outsert magnet, which can be resistive or LTS used in the low field region. A REBCO pancake is a REBCO magnet that is composed of flat spiral winding of the REBCO tape unlike the layered magnet that utilizes layer winding.

The "*Nougat*" magnet is a solenoidal HTS insert composed of a stack of REBCO coils. It achieved a world record 32.5 T total magnetic field with a 38 mm bore, 18 T from external

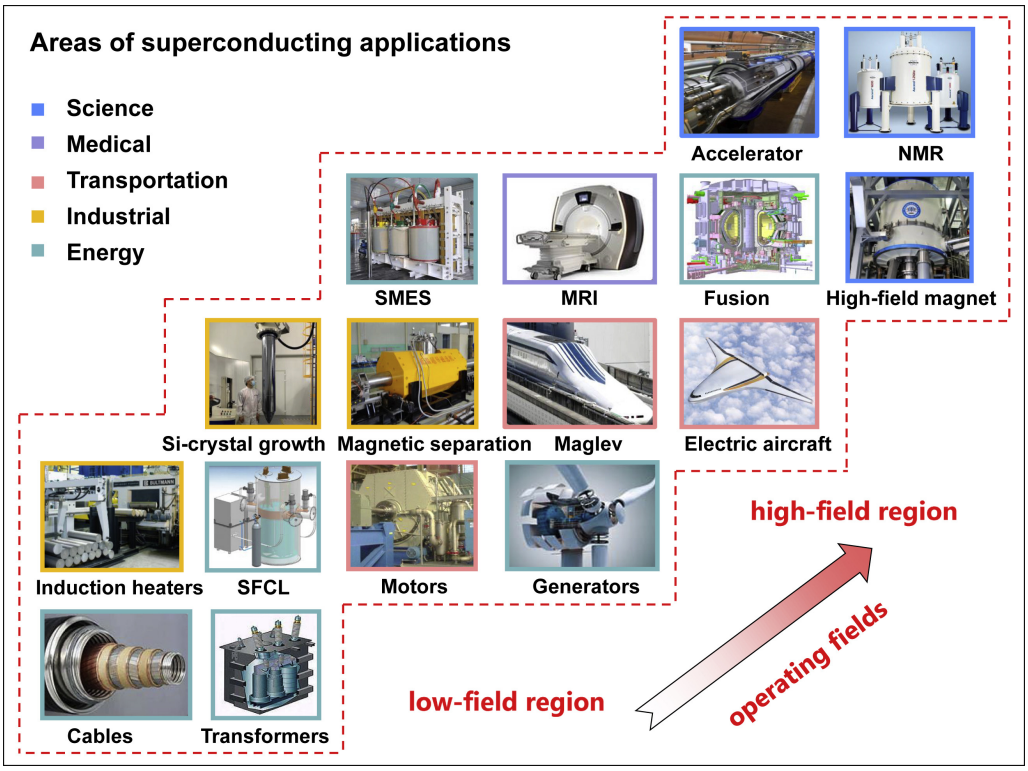

Figure 1.9 – Various applications of superconductors [39]

resistive magnet and 14.5 T by itself [51] (Fig. 1.10a). Another magnet achieved 45.5 T, its resistive outsert generated 31.1 T, and its REBCO insert generated 14.4 T [52]. This magnet is more of a demonstration magnet with an internal bore not useful contrary to Nougat. Additionally, an-all REBCO magnet was done achieving 26 T central magnetic field [53]. Furthermore, a 32 T HTS / LTS high field magnet is open to users at NHMFL for measurement of various physical properties [54] with field homogeneity of 2.5 ppm. The focus of the project this PhD belongs to is to achieve a magnet characterized by a high field and stable operation. The higher the magnetic field is, the higher mechanical stresses are limiting achievable magnetic field and stability.

1.3.2 . Nuclear Magnetic Resonance / Magnetic Resonance Imaging

High field magnets are of great interest in the domains of *Nuclear Magnetic Resonance* (*NMR*) and *Magnetic Resonance Imaging* (*MRI*). These domains impose high demands on the quality of the magnetic field requiring it to be homogeneous and very stable for measurements to be possible [56]. The high field magnitude is of great interest due to the ability of increasing the image resolution. Despite its high constraints, a commercial **NMR** has been produced by Bruker achieving 28.2 T, it uses HTS insert / LTS outsert configuration [55] (Fig. 1.10b). Additionally, other projects regarding MRI are in progress [57–60] where MRI cooling is done by conduction.

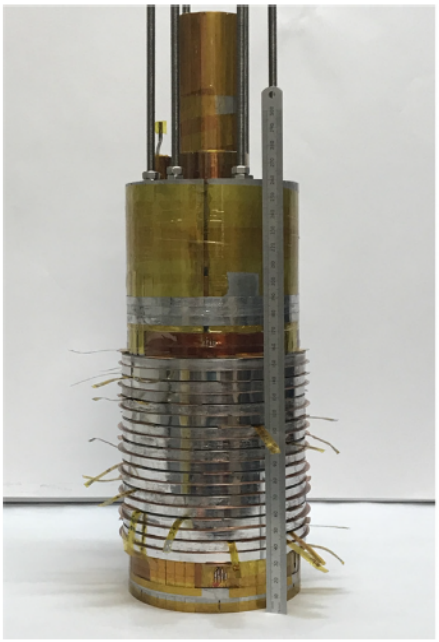

(a) *Nougat* Magnet[51]

(b) Ascend 1.2 GHz HTS / LTS NMR [55]

Figure 1.10 – Applications of REBCO tape

1.4 . Quench in superconductor magnets

As specified in Section 1.1.2, superconductivity defines a critical surface in the (*T,B,J*) space, below which materials are superconducting, and above which they revert to resistive state. This transition can happen due to several reasons, it might be due to an increase of temperature (radiation, Joule effects), magnetic field, or current density. This transition occurs at T_c. However, there is another temperature called *current sharing temperature* (T_{cs}), above which a part of the current flows in the matrix of the superconducting tape/wire resulting in Joule effect while remaining superconducting. Always, T_{cs} is less than T_c, and it depends on the loading conditions of the superconductor (magnetic field and current density).

Heat is generated in the local resistive state of superconductor in superconducting magnet by Joule effect. This heat is transmitted by conduction (longitudinal and transversal) to the adjacent conductors. The magnet in this case has quenched. Resistive zone growth continues until energy dissipation stops. Energy dissipation stops either if the cooling system managed to restore resistive zone to its superconducting state, or if all the energy is dumped in an external resistor or the power supply.

1.4.1 . Minimum Propagation Zone

Knowledge of the outcome of a resistive zone is important for the magnet stability. It can either propagate and quench the magnet or support the heating without growing and quenching the magnet while the heat is being absorbed by the cooling system. The largest zone that can support the heating without propagating is called the ***minimum propagation zone*** (**MPZ**) [61–63]. If the resistive zone is higher than MPZ, the magnet quenches. MPZ differs greatly based on several factors starting with the magnet structure, superconducting material, constituents of the superconducting wire, specific heat, loading conditions, etc.. MPZ is much lower in LTS magnet than in HTS when both are compared at the same low operating

temperature because for LTS magnet it is quite close to its critical temperature while for HTS there is a large margin between the operating and critical temperature (depending on the loading conditions). This means that mechanical disturbances can rarely quench an HTS magnet unlike the LTS magnet that can face a quench more easily because of such a disturbance.

1.4.2 . Minimum Quench Energy

The minimum energy pulse required to initiate the quench in the magnet is called the ***minimum quench energy*** (**MQE**). MQE is equal to energy required to give rise to MPZ. The source of this energy can be anything ranging from radiation, mechanical deformation, wire defect, etc. [64]. The value of MQE is dependent on several factors as well, like specific heat of superconducting material (wire components), operating temperature, magnet's loading condition (current density, magnetic field), etc.. Estimating MQE is important as it can give an idea of how much the magnet can accept energy before it quenches, this allows to better design a quench protection system. MQE estimation is based on MPZ value with the following approximative formula:

$$MQE = V_{MPZ} \int_{T_0}^{T_{cs}} C_{pe}(T) dT \tag{1.1}$$

Such that, MQE is the minimum quench energy, V_{MPZ} is the volume of the minimum propagation zone, T_0 and T_c are the initial operating temperature of magnet and the critical temperature of superconductor under load conditions respectively, and C_{pe} is the volumic specific heat of the conductor. The higher MPZ, the higher MQE, and this makes the magnet more stable.

The critical surface of HTS superconductors is much larger (especially in the temperature direction) than that of LTS superconductors due to the high critical temperature, the critical current and the high critical magnetic field. This leads to have an MQE value in the range of Joules for HTS magnets while it is in a range of milli-Joules for LTS magnets [65, 66] (Table 1.1). This results in LTS magnets being more prone to quench than HTS magnets.

1.4.3 . Propagation Velocity of quench

For the magnet to quench, MPZ has to propagate until the whole magnet transmutes to resistive state. The speed at which it propagates is called *normal zone propagation velocity* (ν_{nzp}). The propagation velocity ν_{nzp} is of extreme importance when considering the stability of the magnet and quench protection system as it is a critical factor in determining the temperature increase. A slower propagation means that the energy stored will be dissipated in a smaller region of the magnet resulting in a higher temperature in the region unlike faster propagation.

Propagation velocity depends on several parameters such as thermal conductivity, heat capacity, Joule effect in the resistive part, etc.. These parameters depend on the temperature, and thus the propagation velocity as well. For example, REBCO tape is mainly composed of Hastelloy and Copper stabilizer, and the specific heat of copper increases by 2 orders from 4 K to 30 K, and 3 orders from 4 K to 80 K [67]. This results in slow propagation velocity as it is inversely proportional to the specific heat. The propagation velocity at adiabatic conditions [63] is:

$$\nu_{nzp} = J \sqrt{\frac{\rho_n(T_t) k_n(T_t)}{\left[C_n(T_t) - \frac{1}{k_n(T_t)} \frac{dk_n}{dT}|_{T_t}\right] \int_{T_{op}}^{T_t} C_s(T) dT}} \tag{1.2}$$

J, $C_n(T)$,$C_s(T)$, $k_n(T)$, $\rho_n(T)$, T_{op}, and T_t are respectively the current density, normal state

Quantity	LTS	HTS
Thermal margin	few K	several decades K
MQE	mJ	J
MPZ (at LHe temperature)	0.1 - 10 mm	0.1 - 0.6 m
Normal-zone propagation velocity	up to hundred m/s	up to few cm/s

Table 1.1 – Comparison of quench characteristics of LTS/HTS magnets [65, 68]

heat capacity, superconducting state heat capacity, thermal conductivity, electrical resistivity and transition temperature.

ν_{nzp} of LTS magnet quench can reach up to 100 m/s, while in HTS magnets ν_{nzp} is just few cm/s [65, 66] (Table 1.1). One of the factors that leads to high ν_{nzp} in LTS magnets is the low thermal margin that is few Kelvins, while in HTS magnets the thermal margin is in tens of Kelvin affecting the specific heat and other parameters that determine ν_{nzp}.

1.4.4 . Thermal Stability

Due to the complex working conditions of a superconducting magnet (cooling, power requirement, and mechanical limitation), ensuring thermal stability is critical so that the magnet remains functional over time without any degradation. It is very important due to their high cost and end application. Whether the magnets are MRI, NMR or particle accelerators, they are made to have a long life cycle. In the case of NMR and MRI, they are normally energized only once.

Additionally, the magnet applications (MRI,NMR...) require homogeneity and field stability in order to achieve their end target. The magnet is operated with a safety margin in place so that slight disturbances can be accommodated whether it is a small temperature increase or a small magnetic field disturbance.

The safety margin can be defined as how much an increase or a change in the different critical parameters (T, B, J) can be tolerated before the conductor transits to the resistive state. The critical surface in Fig. 1.3 shows an interdependence between the three parameters (T, B, J). For example, if J and B are fixed, a temperature margin can be found, where it is the difference between the critical temperature at (B,J) and the operating temperature. Another example is a superconducting magnet acting as insert; the additional external field that can be added to insert field is limited by a magnetic field margin at the insert operating conditions. Field margin is the difference between the critical field at J,T and the field generated by insert.

In real superconducting magnet operation, quench can occur due to several reasons (cooling malfunction, disturbance in power supply, etc.). Thus, a detection and protection system against quench is required to ensure magnet protection from a quench damage.

1.4.5 . Quench Protection

When a magnet quenches, the magnetic energy stored in it will be transformed into heat by Joule effect. The protection goal is to limit the temperature rise in the magnet to an acceptable level between 150 K and 300 K. This is for mechanical reasons in order to avoid high gradients of temperature that can cause high thermal stresses. If the magnet can sustain the quench by itself, the protection is passive.

However, sometimes the energy stored can be rather large; the quench temperature exceeds

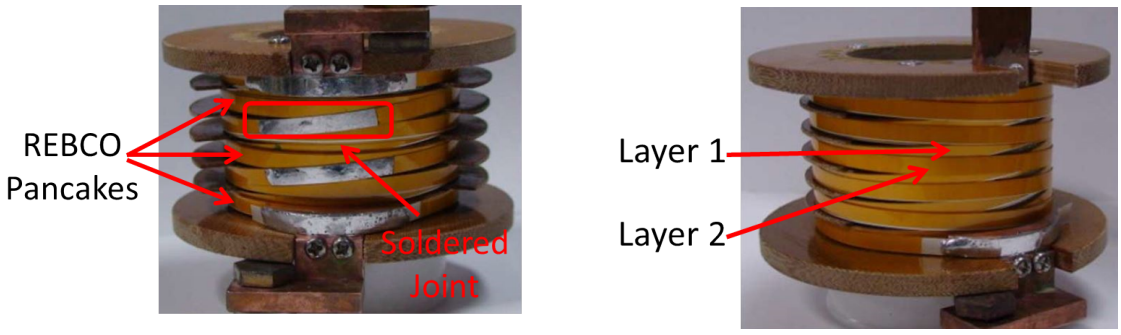

(a) REBCO pancake winding

(b) REBCO layer winding

Figure 1.11 – REBCO winding configurations [72]

the safety limits if all the magnetic energy is dissipated in the magnet. Therefore, a combined protection system can be implemented, where a part is dissipated in the magnet while the other is dumped into an external resistor when a quench is detected. An example of such a case is the CMS LTS magnet [69] where 50 % of the energy (in order of GJ) is dissipated in an external resistor.

In other cases, because of some considerations, whether it is cryogenic (minimizing helium consumption) or quench temperature, the magnetic energy has to be dumped into an external resistor. In order to do so, the quench has to be detected at first. Quench is detected by voltage measurement, which is a delicate process. The voltage at the terminals of a magnet is smaller than the voltage of resistive zone, this complicates the detection. This protection is an active protection.

The fast quench propagation in LTS magnets results in whole magnet quench and high voltage increase at magnet's terminals allowing for easy quench detection by voltage. However, in HTS magnets, quench propagation is slow; this leads to high temperature increase in the quenched zone and complicates detection by voltage since its increase is rather very small in comparison to the case of LTS requiring sensitive instrumentation.

1.5 . Metal-as-Insulation HTS REBCO magnets

In this section, the different coil configurations of HTS REBCO magnet will be discussed. With the rectangular shape and the aspect ratio (1:100) of the REBCO conductor, two different winding techniques are allowed; layer-wound or pancake-wound [70, 71] as seen in Fig. 1.11. However, the pancake-wound technique is preferred for REBCO tapes as it requires smaller length than layer-wound in magnet manufacturing. Also, it grants the ability to change a damaged pancake or part instead of the whole magnet.

1.5.1 . Issues faced in HTS REBCO insulated /impregnated magnets

As stated in Section 1.4, magnet stability and quench protection are of extreme importance for proper functioning of the magnet. In LTS magnets, quench protection is rather straight forward because propagation velocity is high (1 to 100 m/s). This results in very fast propagation of the resistive region, and the energy is dissipated over a large volume of conductor. The hot spot in a superconducting magnet is the small region in the winding that attains the highest temperature after a quench; usually it is at quench initiation point [63].

However, in insulated HTS REBCO magnet, propagation velocity is low as seen before.

This results in having the stored energy being dissipated in a smaller zone. This can achieve dangerous high temperatures for the HTS REBCO. It can either cause conductor degradation or total failure.

Due to the slow propagation velocity, the temperature increase in the zone will be much higher than the cooling capacity, with the temperature being higher than the critical temperature *Tc*. This causes accelerated temperature increase with the resistivity increasing leading to a *thermal runaway* in the HTS REBCO manget [73]. In addition, the slow propagation velocity makes it difficult to build a protection system against thermal runaway. This is because conventional systems used for LTS magnets can not be used in this case. Even after detection is done, due to the slow propagation velocity [74], active protection is the only possible option.

Moreover, insulated-impregnated HTS REBCO magnet has another issue regarding the magnet's cooling. The difference in thermal contraction between the resin and the REBCO tape may cause de-lamination of the tape, which results in magnet failure [75, 76].

1.5.2 . No-Insulation HTS REBCO magnets and Current By-passing during a Quench

In order to overcome the issues faced in HTS REBCO insulated magnet, another coil configuration was implemented: the *No-Insulation (NI) HTS REBCO magnet* [1]. In this configuration, as its name suggests, the coil is wound without any insulation between the turns. This configuration was tested before with NbTi superconductor [77].

During magnet energizing, as turns are in contact with each other, current will pass in hoop and radial directions. The radial current is the result of inductive voltage due to mutual inductance between the two adjacent turns and the contact resistivity. The amount of current that bypasses is strongly dependent on the current ramp rate [78] and contact resistivity. At steady state, the current only flows in the REBCO tape.

The advantage of NI-HTS REBCO magnet is the self passive protection [79–81]. The current by-passing aspect acts as a passive protection system in case of a quench. When a quench occurs, the current will by-pass the resistive zone to the adjacent superconducting turn; thus limiting the temperature increase and decreasing the hot spot temperature. Time constant of radial current redistribution is long; thus time constant of field is long.

Furthermore, the protective aspect of NI-HTS REBCO magnet was proved experimentally in different magnet designs at different loading of current and magnetic field [53, 82–84]. The different magnets in these articles were composed of stacks of NI REBCO double pancakes i.e. two pancakes connected together. When a quench occurred at some position in a pancake in these magnets, the current increases in the other pancakes due to the magnetic coupling among one another in order to conserve the total magnetic flux. This leads to a quench in the other pancakes, and the NI configuration protects each pancake from burnout.

In addition, in this configuration, all mechanical stresses are supported by the REBCO tapes. The mechanical properties of the REBCO tape that is being used lead to an additional limitation on the REBCO magnet design. However, as shown in Fig. 1.8, the substrate constitutes the main part of the tape. Hence, a mechanically stiff substrate like Hastelloy may enhance the tape's stiffness in the tensile direction, permitting higher field applications that result in higher stresses.

1.5.3 . Metal-as-Insulation HTS REBCO magnets

As mentioned in Section 1.5.2, two drawbacks are present in NI HTS REBCO magnet. In order to solve the issue of slow current ramp rate and time constant, the contact resistance between the turns has to be increased significantly as current bypassing is inversely dependent on it. In addition, the achievable magnetic field is rather limited by mechanical properties of the REBCO tape.

One of the possible solutions for current ramping delay problem is to apply non magnetic stainless steel cladding on the REBCO tape [85, 86]. This will result in increasing the contact resistance between turns. Thus, current ramp rate can be increased significantly in comparison to NI REBCO HTS without losing the self-protecting feature.

Another solution that can eliminate the current ramp rate drawback of the NI configuration and provide additional mechanical strength is the *Metal-as-Insulation (MI) HTS REBCO magnet* [87]. In this configuration, the REBCO tape is co-wound with a non-magnetic stainless steel (SS) tape. In this scenario, the adjacent REBCO turns are separated by stainless steel tape which increases the contact resistance significantly by two orders of magnitude. Thus, the bypassing currents are decreased and ramping rate can be increased significantly [88].

Moreover, co-wound stainless steel tape acts as a structural support for REBCO tapes with its high mechanical strength. Furthermore, adding stainless steel at the end of the REBCO winding acts as an additional mechanical reinforcement; this is called over-banding. Over-banding can decrease the mechanical stresses the magnet is subjected to [89], this point will be addressed more clearly in the next chapter. With this configuration, we can get the best of a REBCO tape in high magnetic fields while remaining within its mechanical limits.

A MI REBCO magnet [82] was tested to check its electromagnetic stability and magnetic coupling response inside of a resistive magnet. The results showed that in case of fast discharge of the resistive magnet, the MI REBCO magnet maintained a self-protection feature due to conservation of total magnetic flux and current by-passing inside the pancakes. This magnet was a prototype for the Nougat magnet [51] that was fast discharged on purpose at 29 T central field without the magnet being damaged. Hence, the MI REBCO magnet configuration has been proved its self-protecting feature while eliminating the drawbacks of the NI configuration. The advantage of MI configuration is further proved by the positive results of Nougat magnet insert that reached 32.5 T [51].

1.5.4 . Necessity of Contact

In both NI and MI HTS REBCO magnet configurations, when a zone quenches, current by-passing occurs to the adjacent turns that are *in contact* with the quenched zone. Should the turns be separated, this self-protective trait is lost. Hot spot formation and conductor degradation may occur.

Also, when turns are separated, each turn will support the external forces applied on itself alone which increases significantly the mechanical failure's possibility. Thus, maintaining contact between all the turns is a requirement in the design and for the stability of NI or MI HTS REBCO magnet.

1.5.5 . Stress and Strain Distribution

Due to the significant advantages of MI over NI configuration regarding current loading delay and mechanical strength, MI HTS REBCO magnet has been chosen for this study. Both tapes, REBCO and stainless steel, have their own respective mechanical properties and limits. During the design analysis of the magnet, these limits are to be considered with a safety margin. Maintaining contact is a critical aspect as well in the design study, and it is ensured by having radial stress in compression during nominal operation. However, there is a threshold on tensile radial stress up to 10 MPa before de-lamination occurs [70, 76], and in radial compression (100-150 MPa) before superconductor degradation occurs). The critical current decreases with the increase of hoop strain.

Several studies reported that a relationship exists between critical current and elastic stress (strain) as shown in Fig. 1.12 where critical current degrades in a reversible manner with the stress (strain) until a certain limit [90–98]. Beyond this limit, critical current degrades in an irreversible manner. Thus, these stress limits must be considered during the mechanical design of MI magnets.

Furthermore, additional mechanical limits exist on the tape and hence the magnet because of the tape's rectangular shape. The minimum soft bending radius is high (bending in flat circumferential winding direction), it is defined as the lowest radius for which irreversible critical current degradation, i.e. decrease from nominal critical current, is less than 5%. Also, the hard bending, like the angular winding transition from turn to turn in layer winding, requires a large smooth curvature to be done due to the tape's rectangular shape. Hence, pancake winding configuration is chosen in this thesis due to bending requirements and limited length of REBCO tape, both of which are not suitable for layer winding.

The effect of soft bending on critical current has been studied previously [99–101]. The soft bending strain can be expressed as:

$$\epsilon_{sb} = \pm \frac{d}{2R} \tag{1.3}$$

Where ϵ_{sb} is the soft bending strain, d is the thickness of the substrate, and R is the bending radius. ϵ_{sb} is calculated assuming that the presence of the neutral axis is along center the center of the substrate, the bending strain is substrate shape dependent, REBCO layer thickness is much lower than that of substrate, and the bending radius is much larger than the substrate thickness. Soft bending can facilitate REBCO tape degradation if it is in tensile state which occurs when REBCO layer is above the neutral axis. However, when REBCO layer is below the neutral axis, it is in compressive state which is more favorable for the tape in terms of critical current reversible degradation.

Moreover, MI REBCO pancake is subjected to three mechanical loadings from the following processes: winding, cooling, and energizing. During winding, the coiling is done with a pre-tension to maintain the turns in contact with one another. The pre-tensioning used with turn n results in a pressure P_n being applied on the previous turn $n-1$ expressed as (simplified formula):

$$P_n = \frac{r_{n+1} - r_n}{r_n}\sigma_n \tag{1.4}$$

Where r_{n+1} and r_n are the external and internal radius of turn n, and σ_n is the pre-tensioning stress. The winding load is proportional to the pre-tension and inversely proportional to the radial position. Over-banding is part of the winding load, since over-banding turns are wound with pre-tension.

In cooling from room temperature to cryogenic temperature, for example to 77 K or 4 K, thermal contraction occurs. Since MI REBCO pancake is composed of two tapes, REBCO and SS, thermal stresses occur because of the different thermal contraction of each tape while assuming that the whole pancake is at the same temperature. Since the MI pancake is dry-wound, the de-lamination issue of REBCO tape is avoided.

In energizing, the axial field and the current density in hoop (tangential) direction (J_h) generate radial Laplace forces. These forces are applied only on the REBCO tape as current flows in it only at steady state. Since REBCO tapes are very thin and can carry large currents, the engineering current density, magnetic fields, and Laplace forces (hundreds of MPa) are high. A general stress equilibrium equation with the radial Laplace force is expressed as:

$$r\frac{\partial \sigma_r}{\partial r} + \sigma_r - \sigma_h + rJ_hB_z(r) = 0 \tag{1.5}$$

σ_r, σ_h, J_h, $B_z(r)$, r are respectively the radial stress, hoop stress, current density, axial magnetic field and radius.

At high fields and high current densities, Laplace forces can cause the turns to separate if there are no residual compressive radial stresses. These stresses can be generated during the winding process through pre-tensioning. Thus, to maintain the turns in contact, the total radial stress after energizing should remain compressive, this requires winding with pre-tension to achieve such result. For these three loading calculations, the young modulus, Poisson ratio and thermal contraction properties of REBCO and SS are required.

1.6 . Outline of the Thesis

As stated in Section 1.5, mechanical study of MI HTS REBCO magnet is of critical importance for proper nominal functioning. Previous computational mechanical studies have been done regarding superconducting magnets with simplifying assumptions, but there was no experimental measurement that verified the calculations regarding MI HTS REBCO pancake magnets. In addition, the proposed analytical stress calculation in the thesis is done turn-wise, at the turn extremities, of the MI REBCO pancake instead of a whole body as previously done like in the case of impregnated REBCO pancakes. This turn-wise calculation is necessary since the magnet is not impregnated. At the same time, it is much faster than FE calculation allowing for significant time saving in the initial stress calculation and design phase of a MI REBCO magnet. With it, various crucial points regarding MI REBCO pancake can be studied like constant contact between turns for quench protection, winding process contribution to pancake mechanical robustness, and respecting the stress limits of the materials.

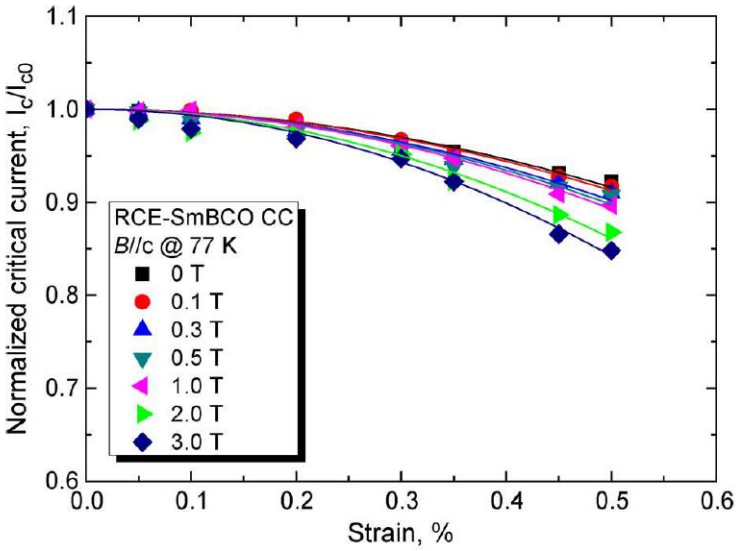

Figure 1.12 – Normalized critical current, as a function of uni-axial strain under various magnetic fields ($B//c$) at 77 K in RCE−SmBCO (fitted curves are shown as solid lines) [93]

The thesis focuses on the mechanical aspect of MI HTS REBCO pancake magnet for high field application. An experimental setup is developed allowing for real time measurement of the deformation during cooling and energizing of MI HTS REBCO pancake using digital image correlation (DIC). The experiment is used to verify the stress analytical formulation and finite element calculation of a test MI REBCO pancake with external field. Using the experiment, stress analytic formulation can be checked if it is representative of what is happening in reality. The stress analytic formulation can also provide a multi-level optimization tool helping at the design of a new generation of MI RBCO pancakes to be used in high field application (cost, mechanical stress, magnetic field, quench).

Hence, the manuscript is organized as follows:

- In chapter 2, different stress analytical formulations regarding MI REBCO pancake magnet for the different loadings (winding, cooling, energizing) have been developed and are discussed while comparing the results with calculations from the Cast3m FE code. Furthermore, de-bonding between turns is considered in the analytical formulation, and winding process parameters (pre-tension, over-banding) contribution to stress distribution and contact between turns is studied.
- Mechanical properties identification of both tapes (REBCO and INOX) using two testing setups with DIC is presented in chapter 3 to have a more precise stress calculation. In addition, a study is done on the mechanical properties of the materials to understand their effect on contact between turns and radial stress.
- In chapter 4, an experimental setup for MI REBCO pancake field displacement measurement during testing is developed. The considered loadings are:
  - Stainless steel 304 disc liquid nitrogen cooling.
  - MI CuBe2/SS304 pancake liquid nitrogen cooling.

  Experimental results are compared with both analytical and numerical modeling.
- Finally, chapter 5 will be the general conclusion of this manuscript.

2 - Analytical Formulations of Displacements and Stresses within a MI HTS Coil

2.1 . Introduction

A superconducting magnet undergoes three processes: winding, cooling, and energizing. Winding is done with a pre-stress to maintain the conductors in their position. Moreover, over-banding, i.e. winding additional turns for mechanical support, is a part of the winding process that leads to an additional mechanical loading by pre-tensioning. Then, the magnet is cooled to cryogenic temperature to reach the superconducting state of the conductors. After cooling, the magnet is energized for operation.

Mechanical stress analysis of superconducting magnets is a critical part of the design process because of the high forces that arise during the three processes, especially during cooling and energizing in high field magnets. There are various analytical formulations proposed for the stress calculation of the three processes (winding [102–108], cooling [102, 105–112], energizing [105, 106, 108, 111–117]).

The aim in this chapter is to find an analytical formulation that best describes the stresses during these three stages of the magnet (winding, cooling, energizing) starting from the general equilibrium equation. The analytical formulations, plane stress and generalized plane strain, are compared against Cast3m finite element calculation on an exemplary MI REBCO pancake magnet then bench-marked on the real MI REBCO magnet *"Nougat"* [51]. Each process is studied separately due to the linear behavior of the materials in the elastic region that allows a superposition of the results. Then, a study is done on pre-tensioning and over-banding using plane stress assumption on Nougat case to understand their contribution to the mechanical stress and state of the pancake. Finally, an analytical formulation that best describes the stress distribution is chosen.

2.2 . General mechanical formulation

The stress-strain relation in matrix form is:

$$\boldsymbol{\epsilon} = \mathbf{S} : \boldsymbol{\sigma} \tag{2.1}$$

where $\boldsymbol{\epsilon}$ is the strain tensor, $\boldsymbol{\sigma}$ is the stress tensor, and $\mathbf{S}$ is the compliance tensor (stress and strain are in voigt notation in Section 2.2). The stress calculations for solenoids is done at the mid-plane of the magnet where the axial field is the highest resulting in the highest Laplace force at the aforementioned position.

Since magnet is cylindrical, axial symmetry condition simplifies the calculation. In reality, the winding is spiral, but to simplify the calculations, the turns are considered as concentric cylinders. In cylindrical coordinates, the general stress balance equations for a body with a distributed force are well known. The magnet materials are assumed orthotropic. Hence, the

stress-strain relation can be expressed as:

$$\begin{bmatrix} \epsilon_r \\ \epsilon_\theta \\ \epsilon_z \\ \epsilon_{\theta z} \\ \epsilon_{zr} \\ \epsilon_{r\theta} \end{bmatrix} = \begin{bmatrix} \frac{1}{E_r} & \frac{-\nu_{r\theta}}{E_r} & \frac{-\nu_{rz}}{E_r} & 0 & 0 & 0 \\ \frac{-\nu_{r\theta}}{E_r} & \frac{1}{E_\theta} & \frac{-\nu_{\theta z}}{E_\theta} & 0 & 0 & 0 \\ \frac{-\nu_{rz}}{E_r} & \frac{-\nu_{\theta z}}{E_\theta} & \frac{1}{E_z} & 0 & 0 & 0 \\ 0 & 0 & 0 & \frac{1}{2G_{\theta z}} & 0 & 0 \\ 0 & 0 & 0 & 0 & \frac{1}{2G_{zr}} & 0 \\ 0 & 0 & 0 & 0 & 0 & \frac{1}{2G_{\theta r}} \end{bmatrix} \begin{bmatrix} \sigma_r \\ \sigma_\theta \\ \sigma_z \\ \tau_{\theta z} \\ \tau_{zr} \\ \tau_{r\theta} \end{bmatrix} \tag{2.2}$$

Also, since it is axially symmetric, shear stresses $\tau_{r\theta}$, $\tau_{\theta z}$, displacement in hoop direction, and the derivative in hoop direction is zero $\frac{\partial}{\partial \theta} = 0$. With axial symmetry (homogeneous tape material) the form of stress balance equations become:

$$\begin{aligned} \frac{\partial \sigma_r}{\partial r} + \frac{\partial \tau_{rz}}{\partial z} + \frac{\sigma_r - \sigma_\theta}{r} + X_r = 0 \\ \frac{\partial \tau_{rz}}{\partial r} + \frac{\partial \sigma_z}{\partial z} + \frac{\tau_{rz}}{r} + X_z = 0 \end{aligned} \tag{2.3}$$

X_r and X_z are the body forces in radial and axial directions respectively. σ_r is the radial stress, and the σ_θ is hoop stress.

Maintaining contact between turns, which is an important aspect, results in the continuity of radial displacement and radial stress at the interface between turns as boundary conditions.

The REBCO and the metal-as-insulation stainless steel (SS) tapes used in MI REBCO pancake winding are ductile elasto-plastic materials, i.e. their behavior in the elastic region below the yield stress is linear. In addition, for a functional magnet, the REBCO tape mechanical limits are to be considered, i.e. the total stress after energizing must remain below the yield stress. Hence, according to the superposition principle, the three processes' resultant stresses and displacement can be summed.

Hence, assumptions considered in the stress calculation are:

- concentric cylinder geometry,
- axisymmetric,
- perfect contact between turns ($u_n(r_n) = u_{n+1}(r_n)$),
- superposition of stresses from the three processes (linear elastic region),
- no shear stress (no friction for saving computational time).

with the following conditions:

- zero radial stress at inner and outer radius of MI REBCO pancake,
- same mechanical properties at room temperature and 4 K (insignificant increase of Young modulus, explained in chapter 3 - uni-axial tensile test section).

2.3 . Winding Process

The first step in making MI REBCO pancake is winding it. The winding process is critical in determining the mechanical integrity of the pancake. Any mistake during the process may

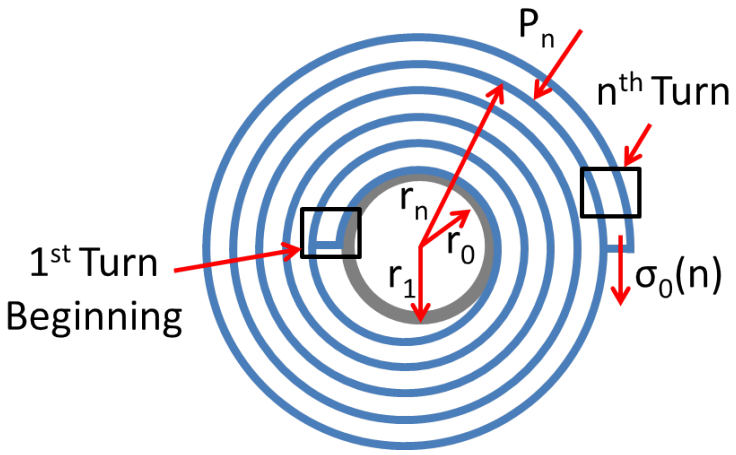

Figure 2.1 – Pressure due to winding: mandrel in gray, winding in blue

result in the magnet's weakness. This may happen due to over-tensioning, choosing a wrong mandrel, or damaging of the REBCO tape.

The winding method exploited in such applications is exactly the same as that used with web materials such as paper, plastic, and steel rolls. Several studies have been conducted on the winding process using these materials. They covered various aspects of the process such as the winding configuration (center winding, center winding with nip roller, etc.), the winding parameters (winding speed, tension), and even the winding material itself [118–122].

The center winding is the method used in this thesis. The winding tension (stress) used in the calculation can be a constant or a function of the turn's number. The turns are assumed to be concentric cylinders in contact with one another and wound on a cylindrical mandrel. In addition, the tape used in winding is assumed to be flat resulting in a perfect cylinder geometry of turns. The tape material is assumed homogeneous but not the whole winding.

2.3.1 . One-turn winding resultant stresses

During the winding (Fig. 2.1), body forces are null. The winding tension results in an external pressure on the already-wound part of the coil [123]. The resulting axial force is negligible, and the axial length of the coil is very small compared to the diameter. Hence, the assumption of *plane stress* is used here, where $[\boldsymbol{\sigma}] = [\mathbf{C}][\epsilon]$ (NB: with $\mathbf{C} = \mathbf{S}^{-}1$) is simplified to 2D terms only (Eq. (2.4)), i.e. terms of plane $r\theta$ such that τ_{rz} and axial stress σ_z are zero.

$$[\boldsymbol{\sigma}] = \begin{bmatrix} \sigma_r & 0 \\ 0 & \sigma_\theta \end{bmatrix} \tag{2.4}$$

r_0 and r_1 are the inner and outer mandrel's radii respectively, and $\sigma_0(n)$ is the winding stress. Using the equilibrium equation of a wound tape in the case of circumferential (spiral) winding from [123], the radial pressure is:

$$P_n = \sigma_0(n)\frac{r_{n+1} - r_n}{r_n} \tag{2.5}$$

For each turn, we calculate the radial and hoop stresses and the displacement; we assume a zero shear stress due to axis symmetry. Eq. (2.3) becomes:

$$\frac{\partial \sigma_r}{\partial r} + \frac{\sigma_r - \sigma_\theta}{r} = 0 \tag{2.6}$$

Assuming an orthotropic material, we obtain a differential equation in terms of the displacement or the radial stress. In this case, the strains are defined as functions of the stresses:

$$\epsilon_r = \frac{\sigma_r}{E_r} - \nu_{\theta r}\frac{\sigma_\theta}{E_\theta} \tag{2.7}$$

$$\epsilon_\theta = \frac{\sigma_\theta}{E_\theta} - \nu_{r\theta}\frac{\sigma_r}{E_r} \tag{2.8}$$

$$\epsilon_r = \frac{\partial u}{\partial r} = \frac{\partial r\epsilon_\theta}{\partial r} \tag{2.9}$$

$$\epsilon_\theta = \frac{u}{r} \tag{2.10}$$

$$\tag{2.11}$$

Where u is the radial displacement, E_r, E_θ are the radial and hoop Young's modulus respectively, and $\nu_{r\theta}$ is the Poisson ratio ($\frac{\nu_{\theta r}}{E_\theta} = \frac{\nu_{r\theta}}{E_r}$). Rearranging the terms, Eq. (2.6) becomes:

$$r\frac{\partial \sigma_r}{\partial r} + \sigma_r = \sigma_\theta \tag{2.12}$$

Hence, by substituting Eq. (2.12) in Eq. (2.7) and Eq. (2.8), then substituting in Eq. (2.9), we get:

$$r^2\frac{\partial^2 \sigma_r}{\partial r^2} + 3r\frac{\partial \sigma_r}{\partial r} + (1-k^2)\sigma_r = 0 \tag{2.13}$$

where

$$k^2 = \frac{E_\theta}{E_r}$$

Using Eq. (2.7) and Eq. (2.8), stresses can be expressed in terms of strains:

$$\sigma_r = \frac{E_r}{1-\nu_{r\theta}\nu_{\theta r}}(\epsilon_r + \nu_{\theta r}\epsilon_\theta) \tag{2.14}$$

$$\sigma_\theta = \frac{E_\theta}{1-\nu_{r\theta}\nu_{\theta r}}(\epsilon_\theta + \nu_{r\theta}\epsilon_r) \tag{2.15}$$

Substituting Eq. (2.14) and Eq. (2.15) in Eq. (2.6), and using Eq. (2.9) and Eq. (2.10) into change the strains to displacement, a displacement differential equation is reached:

$$\frac{\partial^2 u}{\partial r^2} + \frac{1}{r}\frac{\partial u}{\partial r} - k^2\frac{u}{r^2} = 0 \tag{2.16}$$

Both Eq. (2.13) and Eq. (2.16) are similar because both were derived from the same equations. Also, Eq. (2.13) was used by [107] in the calculation of stresses due to winding.

In the plane stress calculation, we have $\sigma_z = 0$. The calculation is done on one turn in the beginning to find the equations that govern the displacement and stresses in each turn alone. General solution of Eq. (2.16) is:

$$u(r) = ar^k + br^{-k} \tag{2.17}$$

Where *a* and *b* are constants to be found using the boundary conditions of the turn, which are $\sigma_r(r_1) = -P_1$ and $\sigma_r(r_2) = -P_2$, where P_1 and P_2 are the internal and external pressures. Hence, by replacing Eq. (2.9) and Eq. (2.10) in Eq. (2.14), then substituting u by Eq. (2.17), and finally applying the boundary conditions, the constants *a* and *b* are:

$$R = \frac{E_r}{1-\nu_{\theta r}\nu_{r\theta}} \tag{2.18}$$

$$a = \frac{1}{R(k+v_{\theta r})}\frac{P_1 r_1^{k+1} - P_2 r_2^{k+1}}{r_2^{2k} - r_1^{2k}} \tag{2.19}$$

$$b = \frac{1}{R(k-v_{\theta r})}\frac{P_1 r_2^{2k} r_1^{k+1} - P_2 r_2^{k+1} r_1^{2k}}{r_2^{2k} - r_1^{2k}} \tag{2.20}$$

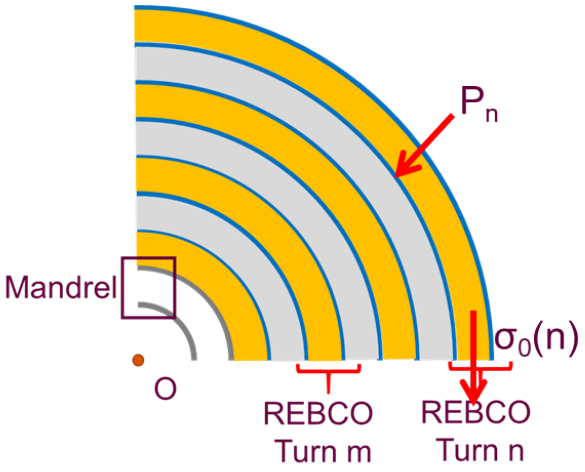

Figure 2.2 – Multi-turn magnet (orange: REBCO, grey: stainless steel)

Finally,

$$u(r) = \frac{1}{R(k+v_{\theta r})}\frac{P_1 r_1^{k+1} - P_2 r_2^{k+1}}{r_2^{2k} - r_1^{2k}} r^k + \frac{1}{R(k-v_{\theta r})}\frac{P_1 r_2^{2k} r_1^{k+1} - P_2 r_2^{k+1} r_1^{2k}}{r_2^{2k} - r_1^{2k}} r^{-k} \tag{2.21}$$

$$\sigma_r(r) = \frac{P_1 r_1^{k+1} - P_2 r_2^{k+1}}{r_2^{2k} - r_1^{2k}} r^{k-1} - \frac{P_1 r_2^{2k} r_1^{k+1} - P_2 r_2^{k+1} r_1^{2k}}{r_2^{2k} - r_1^{2k}} r^{-k-1} \tag{2.22}$$

$$\sigma_\theta(r) = k\frac{P_1 r_1^{k+1} - P_2 r_2^{k+1}}{r_2^{2k} - r_1^{2k}} r^{k-1} + k\frac{P_1 r_2^{2k} r_1^{k+1} - P_2 r_2^{k+1} r_1^{2k}}{r_2^{2k} - r_1^{2k}} r^{-k-1} \tag{2.23}$$

These equations reduce to in the case of an isotropic material as shown by Luganski [105]:

$$u(r) = \frac{1-\nu}{E}\frac{P_1 r_1^2 - P_2 r_2^2}{r_2^2 - r_1^2} r + \frac{1+\nu}{E}\frac{P_1 - P_2}{r_2^2 - r_1^2}\frac{r_1^2 r_2^2}{r} \tag{2.24}$$

$$\sigma_r(r) = \frac{P_1 r_1^2 - P_2 r_2^2}{r_2^2 - r_1^2} - \frac{P_1 - P_2}{r_2^2 - r_1^2}\frac{r_1^2 r_2^2}{r^2} \tag{2.25}$$

$$\sigma_\theta(r) = \frac{P_1 r_1^2 - P_2 r_2^2}{r_2^2 - r_1^2} + \frac{P_1 - P_2}{r_2^2 - r_1^2}\frac{r_1^2 r_2^2}{r^2} \tag{2.26}$$

2.3.2 . Multi-turn winding resultant stresses

In a pancake made of n turns (Fig. 2.2), the boundary conditions using radial displacement and stress continuity are $u_r^{m-1}(r_m) = u_r^m(r_m)$, $\sigma_r^{m-1}(r_m) = \sigma_r^m(r_m)$, and $\sigma_r^1(r_0) = \sigma_r^n(r_{n+1}) = 0$. The mandrel is a part of the mechanical problem in the stress calculation. Hence, there are $2n$ equations and $2n$ unknowns. Using the displacement continuity, a relation between three consecutive pressures can be derived:

$$A_m P_m - B_m P_{m-1} - C_m P_{m+1} = 0 \tag{2.27}$$

$$A_m = \frac{1}{R_m(r_{m+1}^{2k_m} - r_m^{2k_m})}\left(\frac{r_m^{2k_m+1}}{k_m + \nu_{\theta r(m)}} + \frac{r_{m+1}^{2k_m} r_m}{k_m - \nu_{\theta r(m)}}\right) + \frac{1}{R_{m-1}(r_m^{2k_{m-1}} - r_{m-1}^{2k_{m-1}})} \left(\frac{r_m^{2k_{m-1}+1}}{k_{m-1} + \nu_{\theta r(m-1)}} + \frac{r_{m-1}^{2k_{m-1}} r_m}{k_{m-1} - \nu_{\theta r(m-1)}}\right) \tag{2.28}$$

$$B_m = \frac{r_m^{k_{m-1}} r_{m-1}^{k_{m-1}+1}}{R_{m-1}(r_m^{2k_{m-1}} - r_{m-1}^{2k_{m-1}})} \frac{2k_{m-1}}{k_{m-1}^2 - \nu_{\theta r(m-1)}^2} \tag{2.29}$$

$$C_m = \frac{r_m^{k_m} r_{m+1}^{k_m+1}}{R_m(r_{m+1}^{2k_m} - r_m^{2k_m})} \frac{2k_m}{k_m^2 - \nu_{\theta r(m)}^2} \tag{2.30}$$

From Eq. (2.27) and from the pressure relation in Luganski[105], the pressure can be recursively calculated using Eq. (2.31):

$$P_m = \sigma_0(m) \frac{r_{m+1} - r_m}{r_m} + F_m P_{m+1} \tag{2.31}$$

with

$$F_m = \frac{C_m}{A_m - B_m F_{m-1}} \tag{2.32}$$

The first part of Eq. (2.31) is due to the pressure resulting from the winding of turn $m+1$ on turn m; the second term results from solving Eq. (2.27) recursively. After calculating the pressures at each turn while taking into account the stress at the magnet's boundaries, the displacement and stresses at each turn are derived using Eq. (2.24) Eq. (2.25) Eq. (2.26).

2.3.3 . Cast3m Calculations

Cast3m[124] is a finite element modelling tool developed at CEA. It is code-based tool that has vast capabilities and options to model different mechanical cases.

Based on the preceding calculation, Cast3m is done using plane stress, concentric multi-turn, and axisymmetric assumptions for the finite element calculation. The calculation is done at mid-plane of the pancake similarly to the analytical calculation. Results of magnet model is later compared to that of the analytic formulation. The utilized mesh is QUA4 tape-wise. The geometry utilized in the FE calculation is that of cross section of the tapes, i.e. rectangular geometry.

The displacement continuity boundary condition is applied at the interface between the turns with possibility of separation depending on the stress state ($u_r^{m-1}(r_m)$ - $u_r^m(r_m) \leq 0$). Because of assumptions used in Cast3m magnet model, an indirect method of applying the winding pressure is done. The displacement from the winding pressure on the inner windings is calculated. It is added to the initial radial position, which is at edge of last turn, of new turn being wound. Then, applying a tight fitting of the turns and using linear relation of contact interface as specified by the interface boundary condition, the pressure of winding is applied.

For cooling, the thermal deformation is calculated using an inbuilt function in Cast3m, then the stresses resulting from the deformation are calculated. As for energizing, the stress resulting from the Laplace force is calculated and applied to the magnet where only the REBCO turn is subjected to Laplace force. Each turn is subjected to a different force density because the magnetic field depends on its radial position.

2.3.4 . MI REBCO pancake example

The generalized plane strain "GPS" assumption [111] is considered as an intermediate approximation between plane stress and plane strain. In GPS, the calculation is done while assuming axisymmetric magnet, and the calculation is done at magnet's mid-plane. An additional assumption is that the axial strain deformation is assumed to be constant across the magnet; i.e. the magnet conserves its cylindrical shape after deformation (Fig. 2.3). The constant axial

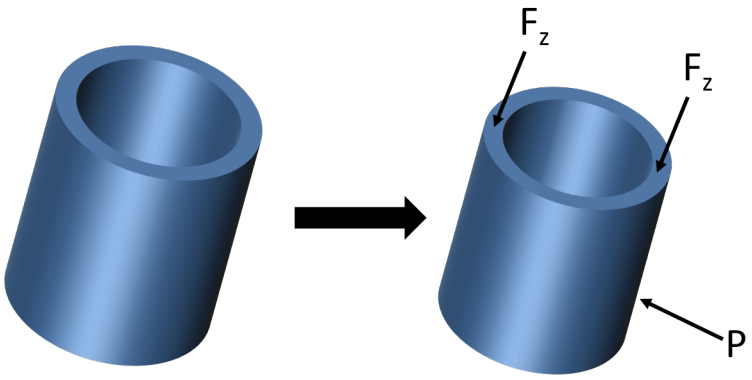

Figure 2.3 – Generalized plane strain deformation scheme

strain results in an additional unknown ϵ_z. Similarly, concentric cylinder assumption of the turns and zero shear stress are assumed in GPS calculation.

Due to the constant axial deformation assumption, an additional boundary condition is needed (Eq. (2.33)). It is related to the static equilibrium of the axial forces at the magnet's mid-plane. This condition allows us to calculate the additional unknown ϵ_z. F_z is the total external axial force being applied at mid-plane of the magnet. It can be a zero external axial pressure or an axial Laplace force.

$$\int_a^b 2\pi r \sigma_z dr = F_z \tag{2.33}$$

A mandrel and a single REBCO turn are considered for the GPS calculation. In this case, the boundary conditions are:

$$\sigma_r^{(1)} = 0 \; at \; r \; = \; r_1, \tag{2.34}$$

$$\sigma_r^{(1)} = \sigma_r^{(2)} \; at \; r \; = \; r_2, \tag{2.35}$$

$$u_r^{(1)} = u_r^{(2)} \; at \; r \; = \; r_2, \tag{2.36}$$

$$\sigma_r^{(2)} = 0 \; at \; r \; = \; r_3, \tag{2.37}$$

$$\int_a^b 2\pi r \sigma_z dr = F_z \tag{2.38}$$

r_1, r_2 represents the inner and outer mandrel radii while r_2 and r_3 are the inner and outer REBCO turn radii. In addition, "$^{(1)}$" and "$^{(2)}$" correspond to the turns number. Unlike cooling and energizing, there is no external force and deformation in the winding case. More precisely, there is no Laplace force and thermal contraction. Consequently, if there is no winding pressure, the equations above give all zero.

The radial stress at the interface between the turn being wound and the previous one is equivalent to the winding pressure. The equations of 2.38 can be solved by replacing $\sigma_r^{(2)}$ with $-P$, where P is the winding pressure. However, the solutions for $\sigma_r^{(2)}$ and $u_r^{(2)}$ are derived from the boundary conditions and not the solution of the equations as a result of replacing $\sigma_r^{(2)}$ by $-P$. This calculation done iteratively each time a new turn is wound to calculate the effect of the new pressure resulting from the winding. The final stresses and displacements are the sum of each turn's winding calculation results.

The Cat3sm results of winding are compared with those of the plane stress and GPS analytical formations using an exemplary MI REBCO pancake whose parameters are in Tables 2.1 to 2.3.

Properties\Materials	Mandrel	Stainless Steel
Young modulus (GPa)	200	190
Poisson ratio	0.29	0.29
Thermal Contraction (RT- 4 K)	-29 $\times 10^{-4}$	-29 $\times 10^{-4}$

Table 2.1 – Material properties [127]

Direction\Properties	Young Modulus (GPa)	Poisson Ratio	Thermal Contraction
Radial	73	0.2 ($\nu_{r\theta}$)	-26.8 $\times 10^{-4}$
Hoop	142	0.35 ($\nu_{\theta z}$)	-26.1 $\times 10^{-4}$
Axial	134	0.18 (ν_{rz})	-26.1 $\times 10^{-4}$

Table 2.2 – Orthotropic REBCO properties [127, 128]

Mandrel material is stainless steel 316L [125]. SS is a non magnetic stainless steel alloy called Durnomag [126]. The MI pancake also includes over-banding turns of SS that act as mechanical reinforcement. The analytical formulations and Cast3m finite element modeling are bench-marked on this MI pancake initially before bench-marking them on a real MI HTS magnet that is 'Nougat' which is made of 9 double pancakes and operated at high fields. All the calculations are done at the boundaries (inner and outer radius) of the mandrel and the turns.

Figure 2.4 shows that the displacement values obtained from the analytic formulations and Cast3m are in accordance. In addition, it shows that the inner turns of the pancake are the most compressed, where the compression decreases as we move towards the last turn. This displacement is the result of the sum of displacement occurring when adding each new turn with pre-tension.

Figure 2.5 shows that the radial stress calculated using the analytical formulations and Cast3m are in accordance. Also, the vertical lines in the plot of Cast3m result is due to the indirect method of applying the pre-tensioning pressure in Cast3m. Moreover, the resultant winding radial stress acts as a residual compressive radial stress in the MI REBCO pancake. This residual stress maintains the turns in contact. It helps to counterbalance the positive radial stress of Laplace force, keeping turns in contact if the total radial stress is compressive. Thus, the resultant winding radial stress is of great importance to ensure mechanical integrity and stability of the MI REBCO pancake magnet.

Parameter	Value
Mandrel, Inner/Outer Radius	24 / 25 mm
REBCO thickness	0.075 mm
SS thickness	0.03 mm
Tape width	6 mm
Pancake configuration	
REBCO + SS (nb of turns)	50
Over-banding SS (nb of turns)	10
Pre-tensioning	100 MPa

Table 2.3 – MI REBCO pancake parameters

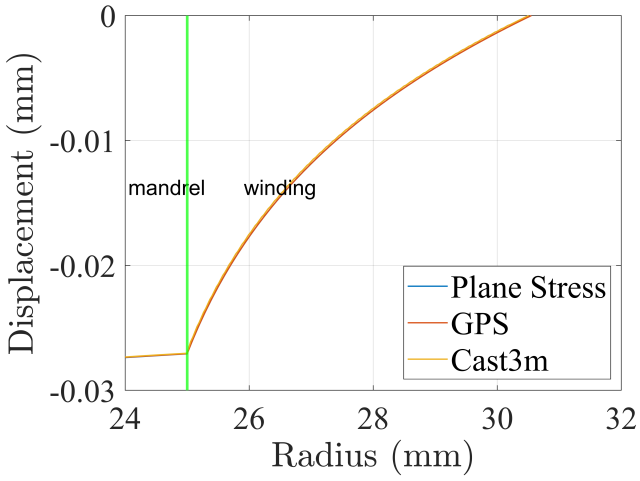

Figure 2.4 – Pre-tension radial displacement

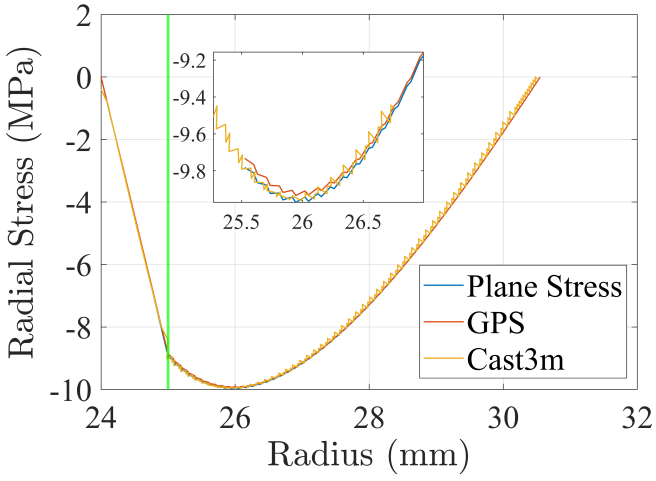

Figure 2.5 – Pre-tension radial stress

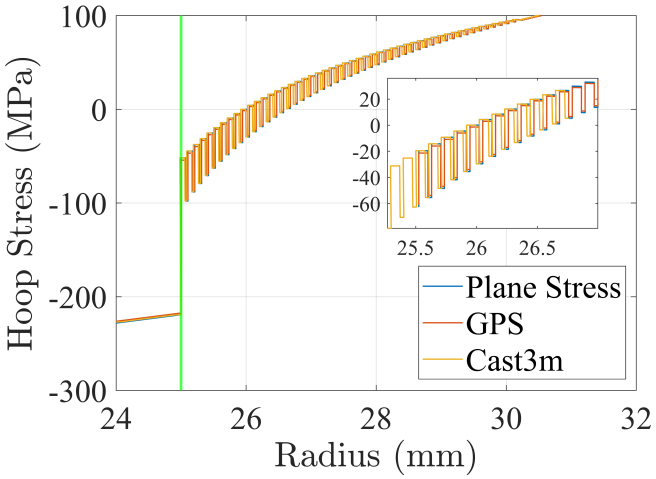

Figure 2.6 – Pre-tension hoop stress

Figure 2.6 shows that the hoop stress computed using the analytical formulations and Cast3m are in accordance. The shape of the graph is due to the calculation being done at the boundaries of mandrel and at each turn, because the REBCO and SS tapes have different mechanical properties.

2.4 . Cooling

During cooling, there are no body forces, and the effect of thermal contraction is included in the displacement. Hence, following the assumptions of plane stress and orthotropic material, the stress differential equation is that given in Eq. (2.6). The cooling is isothermal (room temperature to 4 K), i.e. all turns are supposed to be at the same temperature.

In cooling, thermal strain is included in total strain.

$$\epsilon_r^{tot} = \epsilon_r + \alpha_r \Delta T \tag{2.39}$$
$$\epsilon_\theta^{tot} = \epsilon_\theta + \alpha_\theta \Delta T \tag{2.40}$$
$$\epsilon_z^{tot} = \epsilon_z + \alpha_z \Delta T \tag{2.41}$$

Hence, using Eq. (2.6) ,Eq. (2.7),Eq. (2.8), Eq. (2.39), and Eq. (2.40), the following displacement differential equation is reached:

$$u^{''} + \frac{u^{'}}{r} - k^2 \frac{u}{r} = \frac{1}{r}(\alpha_r \Delta T(1 - k^2 \nu_{r\theta}) + \alpha_\theta \Delta T(k^2 \nu_{r\theta} - k^2)) \tag{2.42}$$

For radial and hoop stress, Eq. (2.14) and Eq. (2.15) still apply, except that ϵ_r and ϵ_θ have to be replaced by $\epsilon_r - \alpha_r \Delta T$ and $\epsilon_\theta - \alpha_\theta \Delta T$.

The solution of Eq. (2.42) (the general plus particular solutions) is:

$$\begin{aligned} u_t &= cr^k + dr^{-k} + r\frac{G}{1-k^2} \\ with \quad G &= (\alpha_r \Delta T(1 - k^2 \nu_{r\theta}) + \alpha_\theta \Delta T(k^2 \nu_{r\theta} - k^2)) \end{aligned} \tag{2.43}$$

The stress equations are:

$$\begin{aligned} \sigma_r &= \frac{E_r}{1 - \nu_{r\theta}\nu_{\theta r}}(\epsilon_r - \alpha_r \Delta T + \nu_{\theta r}(\epsilon_\theta - \alpha_\theta \Delta T)) \\ \sigma_\theta &= \frac{E_\theta}{1 - \nu_{r\theta}\nu_{\theta r}}(\nu_{r\theta}(\epsilon_r - \alpha_r \Delta T) + (\epsilon_\theta - \alpha_\theta \Delta T)) \end{aligned} \tag{2.44}$$

Analogous to the winding case, we are going to develop the solution for a single turn and then generalize to the multi-turn case (2.3.2). Using Eq. (2.7), Eq. (2.8), u_t from Eq. (2.43), σ_r from Eq. (2.44) with external pressure P_1 and P_2 due to strain having elastic and thermal parts, and using boundary conditions for σ_r (P_1 and P_2), the unknown terms of u_t are derived:

$$D = \frac{\Delta T(\alpha_r - \alpha_\theta)(k^2 - \nu_{\theta r})}{1 - k^2} \tag{2.45}$$
$$c = \frac{1}{R(k + \nu_{\theta r})} \frac{P_1 r_1^{k+1} - P_2 r_2^{k+1}}{r_2^{2k} - r_1^{2k}} + \frac{D}{k + \nu_{\theta r}} \frac{r_1^{k+1} - r_2^{k+1}}{r_2^{2k} - r_1^{2k}} \tag{2.46}$$
$$d = \frac{1}{R(k - \nu_{\theta r})} \frac{P_1 r_2^{2k} r_1^{k+1} - P_2 r_1^{2k} r_2^{k+1}}{r_2^{2k} - r_1^{2k}} + \frac{D}{k - \nu_{\theta r}} \frac{r_2^{2k} r_1^{k+1} - r_1^{2k} r_2^{k+1}}{r_2^{2k} - r_1^{2k}} \tag{2.47}$$

The solution here is very similar to that of Section 2.3.1. For an isotropic material, the solution meets the one proposed by Luganski [105].

$$u_k(r) = \frac{1 - \nu_k}{E_k} \frac{P_k r_k^2 - P_{k+1} r_{k+1}^2}{r_{k+1}^2 - r_k^2} r + \frac{1 + \nu_k}{E_k} \frac{P_k - P_{k+1}}{r_{k+1}^2 - r_k^2} \frac{r_{k+1}^2 r_k^2}{r} + \alpha_k r \tag{2.48}$$

Using the same example of MI REBCO pancake as in section 2.3.4, a comparison is done between analytical formulations and Cast3m for the cooling stage.

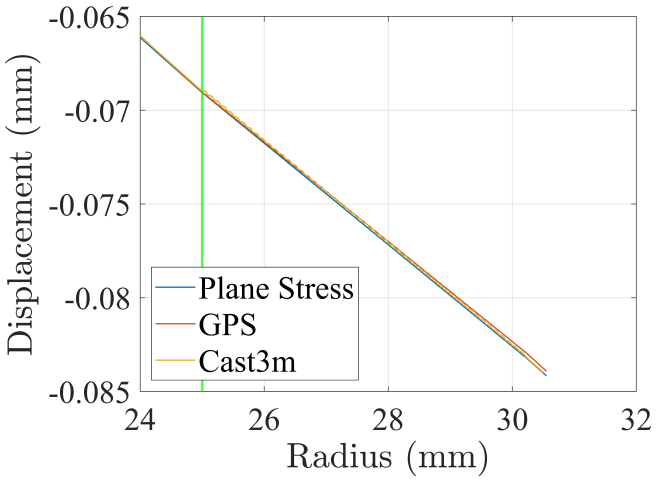

Figure 2.7 – Cooling radial displacement

Figure 2.7 shows that the displacement values obtained from the analytical formulation and Cast3m are in accordance. The contraction increases proportionally to the radius, moving from the first to the last turn. A small change of slope is observed passing from the mandrel to the winding since their dilatation coefficients are slightly different.

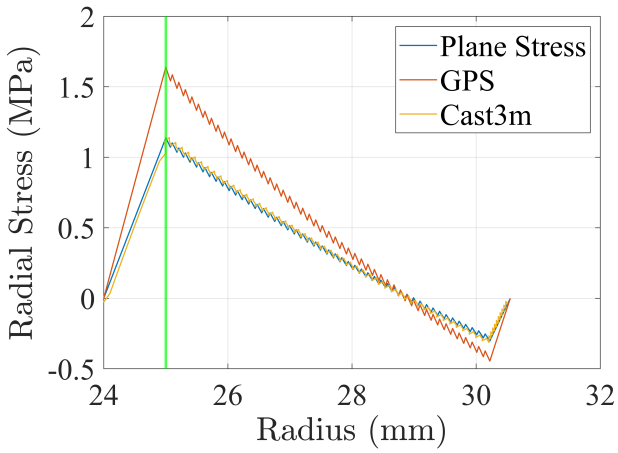

Figure 2.8 – Cooling radial stress

Figure 2.8 shows that the radial stress values obtained from plane stress assumption and Cast3m are in accordance, but generalized plane strain exhibits a discrepancy. This discrepancy is due to the fact that generalized plane strain assumes constant axial strain unlike plane stress. Moreover, the graph shows that a region of the pancake undergoes compressive radial stress while the other region has a positive stress due to cooling. This is due to the two tapes REBCO / SS having different thermal contractions. This indicates that the thermal contraction is rather important to be studied to check the resultant radial stress due to cooling. In addition, in the over-banding region (i.e. the last 10 turns), the radial stress is linearly increasing till it reaches zero since the turns are SS only and the thermal contraction is constant.

The mandrel and the turns contract in all directions in reality (radial, hoop, and axial). The axial contraction varies for each turn in the plane stress assumption. This means, in this case, that axial shearing occurs which is assumed to be zero. In GPS - because of constant axial strain for all the turns - axial shearing is zero; thus respecting the assumptions utilized. Hence, GPS is more representative of real case because MI pancakes are always slightly axially pressed, that explains why axial strain is approximately the same across the pancake.

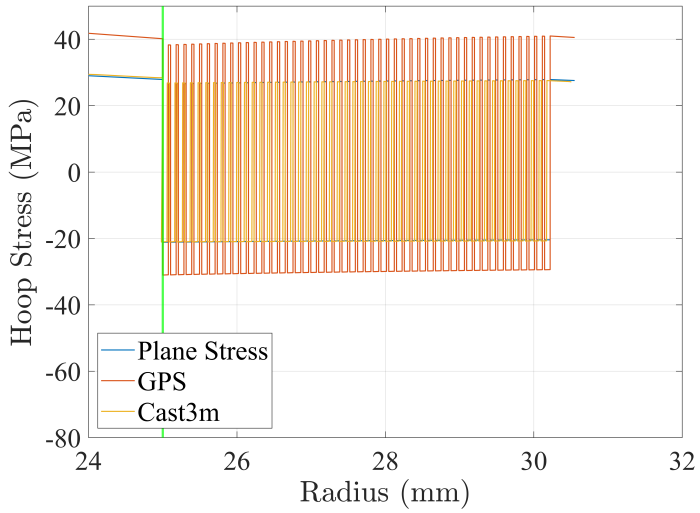

Figure 2.9 – Cooling hoop stress

Figure 2.9 shows that the hoop stress values obtained from plane stress and Cast3m are in accordance. The solution obtained from GPS assumption differs from the other two as expected. Whatever the estimation, it is shown that REBCO turns exhibit hoop compression while SS turns exhibit a hoop tension due to thermal contraction of REBCO being lower than that of SS.

2.5 . Operating the magnet (energizing)

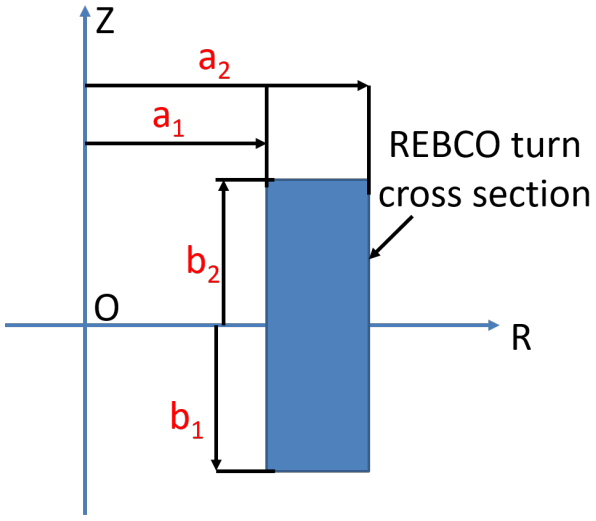

Figure 2.10 – Cross section of circular loop of REBCO tape

2.5.1 . Axial field linearization

The magnetic field has radial and axial components. The axial field results in Laplace force's radial component while the radial results in Laplace force's axial component. The calculation of the magnetic field's components is done using relation between magnetic field (B) and the vector potential (A).

$$B = \nabla \times A \tag{2.49}$$

The MI REBCO pancake is axisymmetric, and the REBCO tapes are of rectangle cross section (Fig. 2.10), this allows us to write the axial magnetic field generated by a single REBCO tape (a_1, a_2, b_1, b_2) at the point (r, z) in cylindrical coordinates as follows [129]:

$$\begin{aligned} B_z &= \frac{\mu_0 j_0}{2\pi}\left[\left[(b-z)F_2 - \frac{\pi}{2}(a-r)[1-sgn(a-r)]sgn(b-z)\right]_{a_1}^{a_2}\right]_{b_1}^{b_2} + B_z' \\ B_z' &= -\frac{\mu_0 j_0}{2\pi}\left\{(b-z)\left\{\frac{1}{r_1}\left[4aK(k) + \frac{(a-r_0)^2}{\rho+r_0}\Pi(\nu_+,k) + \frac{(a+r_0)^2}{\rho-r_0}\Pi(\nu_-,k)\right]\right\}_{a_1}^{a_2}\right\}_{b_1}^{b_2} \end{aligned} \tag{2.50}$$

where:

$$\begin{aligned} R &= a^2 + r^2 - 2ar\cos\varphi + (b-z)^2 \\ r_0 &= \sqrt{r^2 + (b-z)^2} \\ r_1 &= \sqrt{(a+r)^2 + (b-z)^2} \\ k &= \frac{2\sqrt{ar}}{r_1} \\ \nu_\pm &= \frac{2r}{r \pm r_0} \\ F_2 &= \int_0^\pi \operatorname{arctanh}\frac{a - r\cos\varphi}{\sqrt{R}} d\varphi \end{aligned} \tag{2.51}$$

μ_0 is the vacuum magnetic permeability, j_0 is constant hoop current density across the cross section, and sgn is the sign mathematical function. K and Π are the first and third complete elliptic integrals, and z and r are the axial and radial positions at which the axial magnetic field is calculated.

As the calculation of axial field is done at the mid-plane of the pancake; i.e. $z = 0$, the axial field equation is further simplified. Gray [115] checked the effect of assumption of linearized axial field in a thick axisymmetric superconductor solenoid at its mid-plane based on the aspect ratios of its design α and β, where:

$$\begin{aligned} \alpha &= \frac{r_{out}}{r_{in}} \\ \beta &= \frac{h}{2r_{in}} \end{aligned} \tag{2.52}$$

r_{out} and r_{in} are the external and internal radius of the whole magnet, and h is its height. In our case on MI REBCO pancake, with the limit on the bending radius of the tape, the current available tape length, and the tape thickness, this results in:

$$\begin{aligned} 1 \leq \alpha \leq 2 \\ 0.1 \leq \beta \leq 0.5 \end{aligned} \tag{2.53}$$

With the present limits on α and β, the error on the calculated radial force is between -1 % and -0.1 % [115]. The error is calculated as:

$$E = \frac{F_i - F_m}{F_m} \times 100 \tag{2.54}$$

F_i is the Laplace force calculated from linearized field; i.e. linear axial field calculated using the axial field at the inner and outer radius at mid-plane; and F_m is the Laplace force calculated from the actual field.

Hence, this allows us to assume that the axial magnetic field inside the MI pancake is linear at the mid-plane.

2.5.2 . Energizing solution

For energizing, we assume a constant current density, an orthotropic material, and a zero shear stress. Moreover, the plane stress assumption holds. Hence, Eq. (2.3) becomes:

$$\frac{\partial \sigma_r}{\partial r} + \frac{\sigma_r - \sigma_\theta}{r} + X_r = 0 \tag{2.55}$$

where $X_r = B_z J$, with B_z being the axial magnetic field function.

Using Eq. (2.9), Eq. (2.10), Eq. (2.14), Eq. (2.15), with Eq. (2.55) gives:

$$r u^{''} + u^{'} - k^2 \frac{u}{r} = -J B_z r \frac{(1 - \nu_{r\theta}\nu_{\theta r})}{E_r} \tag{2.56}$$

The axial magnetic field function inside the turns can be linearized as proved in the previous section:

$$B_z(r) = Bc - Cr \tag{2.57}$$

where Bc and C are constants determined by the values of B_z at the inner and outer radii of the first and last layers respectively. The current is circulating only in REBCO turns.

The solution of Eq. (2.56) is:

$$u(r) = a r^k + b r^{-k} - \frac{JBc}{4 - k^2} r^2 + \frac{JC}{9 - k^2} r^3 \tag{2.58}$$

The first two terms in in the solution represent the general solution while the last two terms represent the particular solution.

To reach the exact solution, we substitute Eq. (2.58) in Eq. (2.9) and Eq. (2.10) to be able to get the equation of radial stress. Assuming a single turn with compressive stresses on both sides and solving radial stress for these stresses, the unknowns (*a*, *b*) of the displacement equation are found.

By imposing the displacement continuity condition, we obtain a recursive solution relating the three consecutive pressures as done in the previous cases. Note that the continuity displacement condition is not valid if the layers are not in contact.

Using the same example of MI REBCO pancake from section 2.3.4, a comparison is done between the analytical formulations and Cast3m for the energizing phase. The pancake is energized with a current of 270 A (i.e. the current density is $600 A/mm^2$) to simulate a realistic energizing experiment while respecting the magnetic and current limits of the REBCO tape at 4 K. The current density value is within the superconducting limit of the REBCO tape [6, 37]. The pancake generates an inner / outer axial field of 1.038 T / -0.6454 T. In this calculation, the axial force in GPS is neglected to compare results between analytical calculations and Cast3m using the same loads.

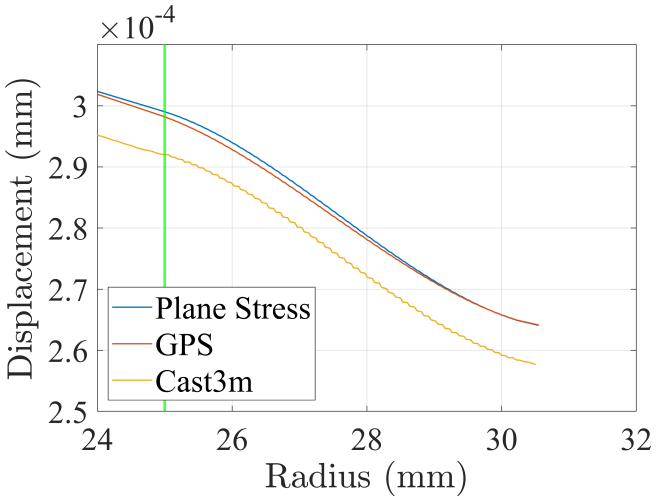

Figure 2.11 – Energizing radial displacement

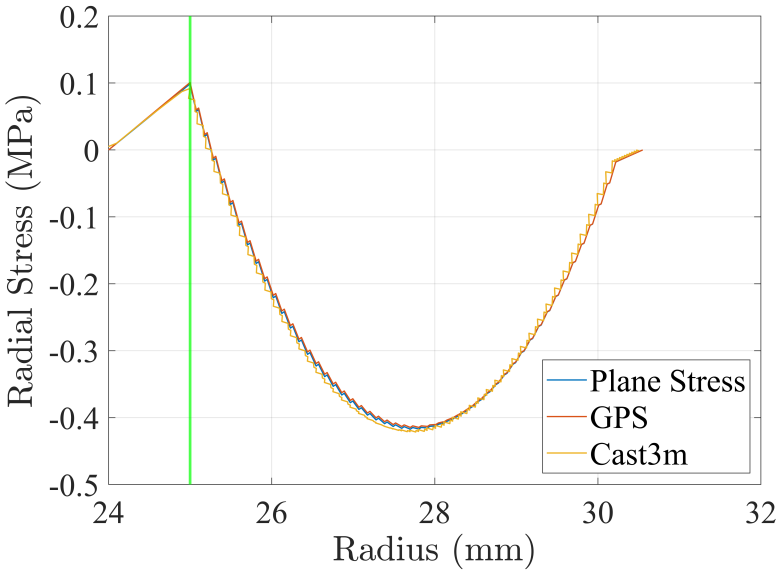

Figure 2.12 – Energizing radial stress

Figure 2.11 shows that the analytical formulations are in accordance with one another with a negligible difference, and Cast3m solution exhibits a small shift with respect to that of the analytical formulations. The offset of Cast3m displacement is due to the indirect method of pre-tensioning which is applied during the winding phase. The negligible difference between the two formulations is due to the axial strain being constant in GPS while in plane stress the axial stress is zero and the axial strain is variable along the pancake's turns. In addition, the displacement shows that the magnet is expanding due to the Laplace force.

The radial stress in Fig. 2.12 has a saw shape because the laplace force is applied only on the REBCO tape, whereas SS is not subjected to any force density. In addition, both the analytical formulations and Cast3m are in accordance with one another. Also, at the initial turns of the pancake, radial stress is positive. This shows that depending on the current density and the axial field, the energizing can de-bond the turns if the loading results in having majority of pancakes winding part submitted to a positive radial stress.

Figure 2.13 shows that the predicted hoop stresses from analytical formulations and Cast3m

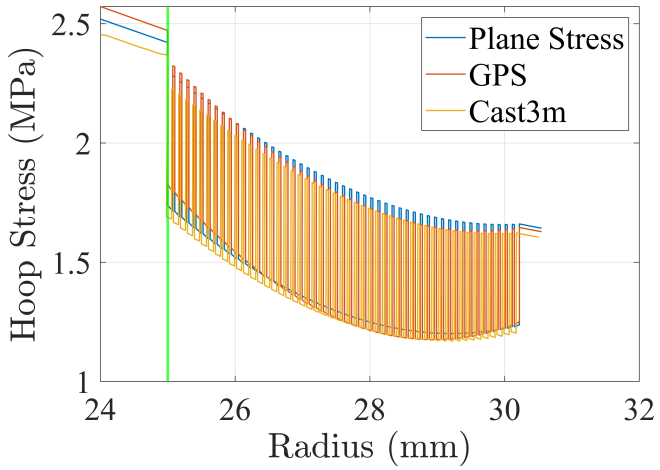

Figure 2.13 – Energizing hoop stress

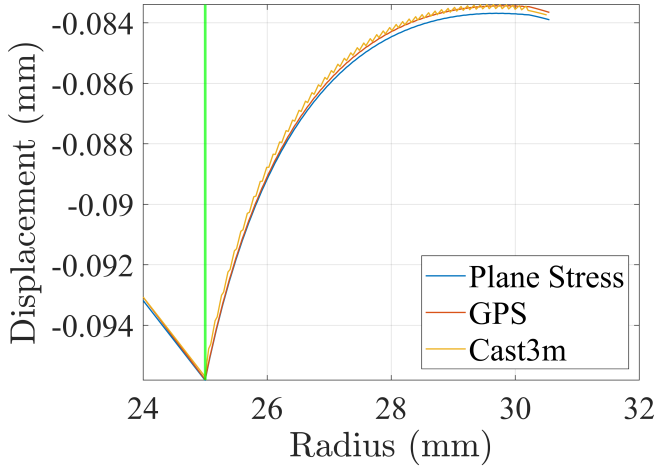

Figure 2.14 – Total radial displacement

are in accordance with one another. In addition, the hoop stress is positive on all turns. This confirms that the Laplace force is expanding the magnet.

2.6 . Total resultant stresses and displacements

As stated in section 2.2, the stresses and displacements can be summed using superposition principle because the REBCO and SS tapes are assumed to remain in the mechanical linear elastic region after energizing and boundary conditions are consistent for the three loadings. The **final radial stress** should be negative, indicating all turns remained in contact with one another, to consider the superposed results as valid. Figure 2.14 shows that the displacement due to cooling contributes the most in the total displacement. The maximum hoop strain achieved is $\epsilon_\theta = -0.38\%$. The strain limits of REBCO tape are respected indicating no degradation of the tape.

Figure 2.15 shows that the total radial stress is kept compressive all over the pancake maintaining all turns in contact. This emphasizes the importance of pre-tensioning and the winding process regarding the magnet's mechanical integrity. There is a slight discrepancy between

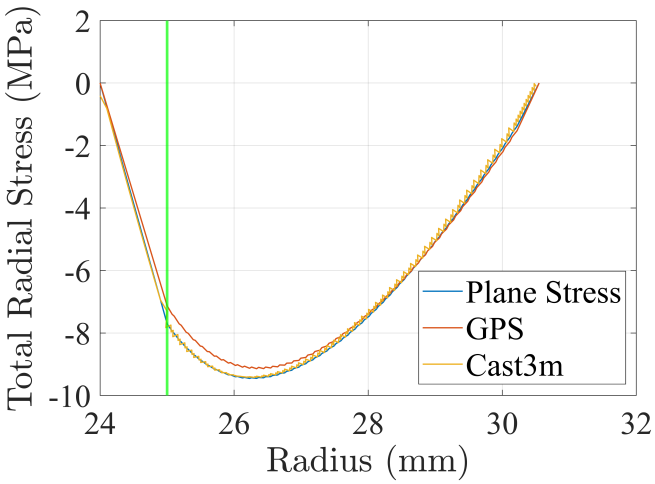

Figure 2.15 – Radial stress after winding, cooling, and energizing

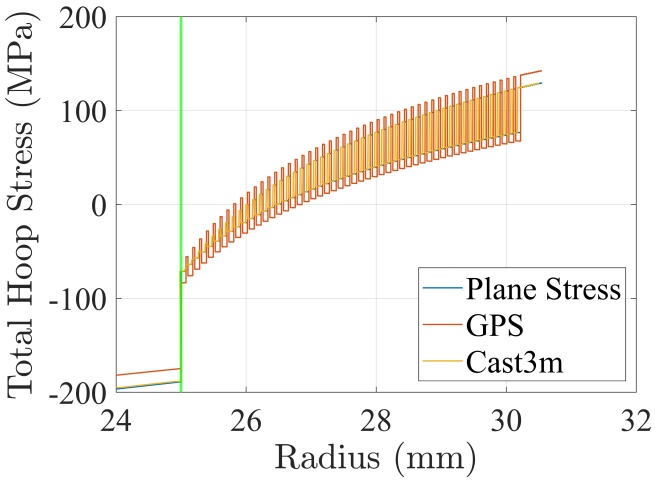

Figure 2.16 – Hoop stress after winding, cooling, and energizing

GPS, and plane stress and Cast3M which is caused by the constant axial strain assumption. This discrepancy can be noticed clearly from the cooling loading.

Figure 2.16 shows that plane stress formulation and Cast3m are in accordance with one another, but generalized plane strain shows a discrepancy. This discrepancy is induced by the assumption of constant axial strain; its effect being clear in the cooling calculation. The calculation on this exemplary MI REBCO pancake emphasized the importance of the stress and displacement calculation for each loading that the pancake undergoes. It is further better to compare the formulations and Cast3m on a real MI REBCO magnet. This point is addressed in following section.

2.7 . Nougat Example

In the previous sections, we have compared the analytical formulation results with those of Cast3m on an exemplary MI REBCO pancake. In this section, the analytical formulations are bench-marked against Cast3m using the MI REBCO magnet "Nougat" [51] according to the specifications mentioned in Table 2.4. Nougat magnet was developed to tackle the issue of

Parameter	Value
Mandrel, Inner/Outer Radius	24/25 mm
REBCO thickness	0.075 mm
SS thickness	0.03 mm
Tape width	6 mm
Nougat configuration	
Nb of turns per pancake (REBCO + SS)	290
Over-banding (nb of turns, SS)	43
Number of Double-Pancakes	9
Operating Current	270 A
External Field	18 T
Total Central Field @ 270 A	30 T
Axial Field at first / last REBCO turn (central pancake)	30.73 T / 16.77 T
Pre-tension during winding	100 MPa

Table 2.4 – Nougat parameters for 30 T center field [51]

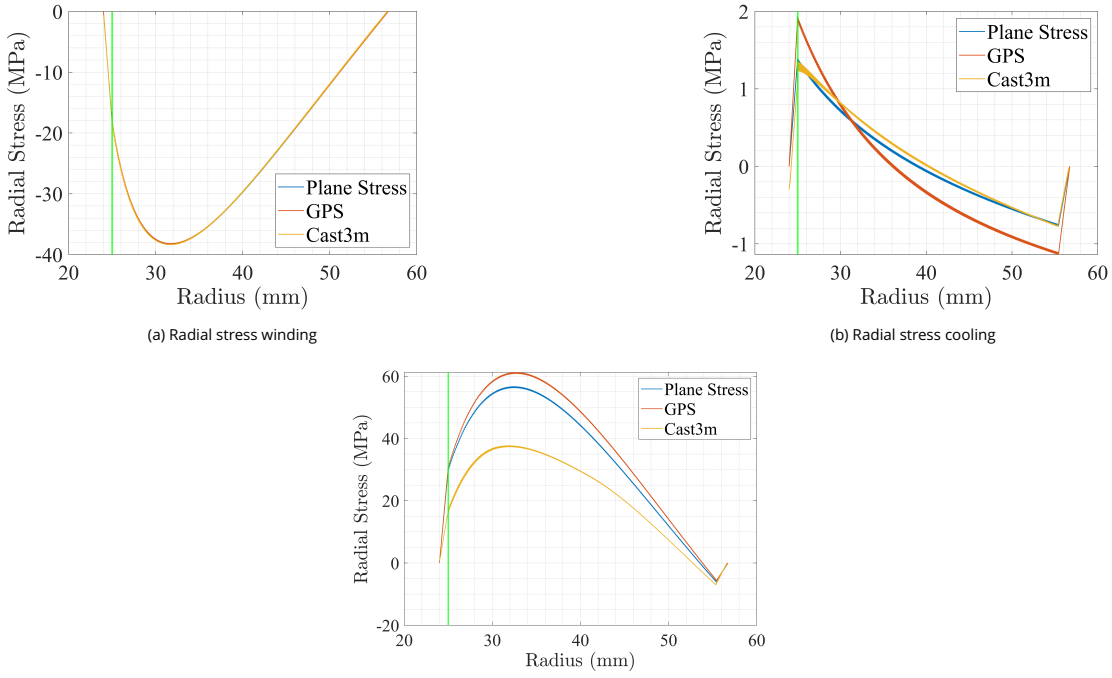

(a) Radial stress winding

(b) Radial stress cooling

(c) Radial stress energizing

Figure 2.17 – Radial stress at mid-plane of central pancake of Nougat magnet at 30 T

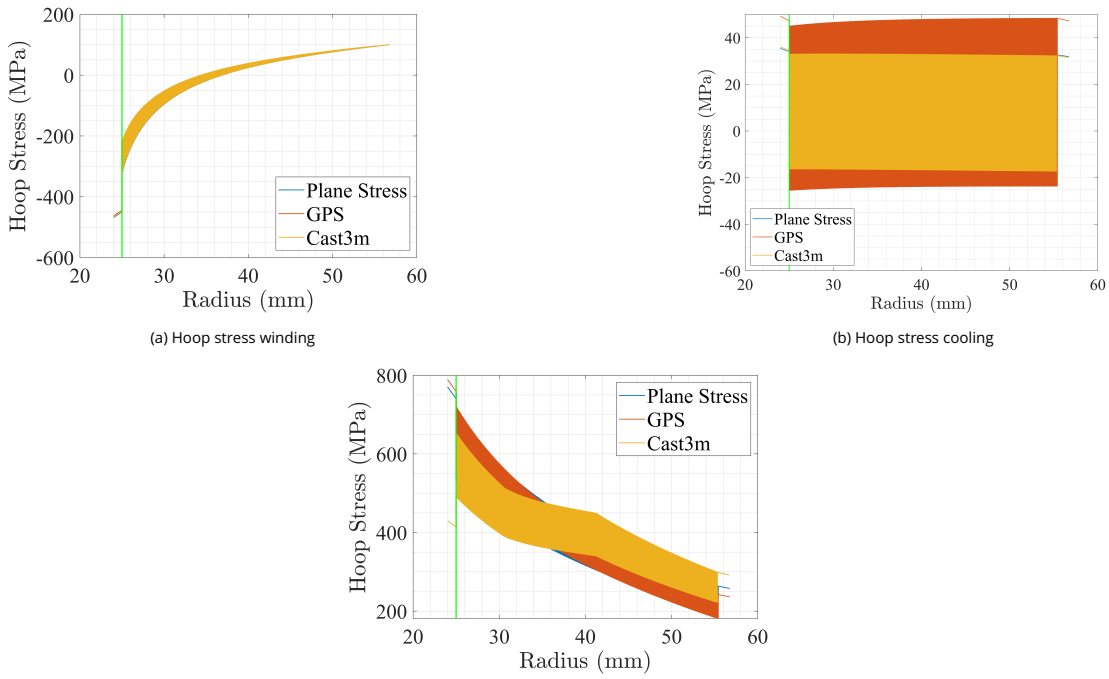

(a) Hoop stress winding

(b) Hoop stress cooling

(c) Hoop stress energizing

Figure 2.18 – Hoop stress at mid-plane of central pancake of Nougat magnet at 30 T

high power and cooling consumption at LNCMI - Grenoble. It is an HTS insert, composed of a stack of 9 MI REBCO double-pancakes, with the goal of producing 10 T inside a 20 T resistive background field. The double-pancake metal-as-insulation winding mode was chosen to benefit from the passive quench protection of MI configuration and to keep REBCO tape length within the available commercial tape length. Fortunately, Nougat exceeded the initial goal and a world record was achieved with 32.5 T, with 14.5 T from Nougat insert which is 45 % higher than the initial goal.

The calculations are done at the mid-plane of central pancake without considering the axial forces for GPS. The results are given for the three loadings: winding, cooling, and energizing. Their effect are summed in a final step. Figures 2.17 and 2.18 show tendencies observed for the exemplary MI REBCO pancake for the three loadings. However, it is quite clear that at high fields and current density, Laplace forces result in significant stresses in radial and hoop direction.

Figure 2.19 shows that the total radial stress calculated using the plane stress and GPS formulations is positive in major part of the magnet; whereas it is zero according to Cast3m. Cast3m indeed predicts that the turns have separated from the mandrel and probably from one another in the positive radial stress region since tensile radial stress indicates that the turn needs to expand radially to maintain contact with the adjacent turn. In Cast3m, the turns had a non-perfect contact between one another allowing them to separate. However, for the plane stress and GPS analytical formulations, the contact is perfect between the turns without separation; this results in the large area of positive radial stress. The assumptions used in the analytical formulations are consequently invalid.

Figure 2.20 shows that there is a discrepancy in the total hoop stress between the plane stress and GPS formulations and Cast3m. This is due to the fact that the contact is considered to be perfect in the formulations while it is not the case in Cast3m (i.e. full contact between

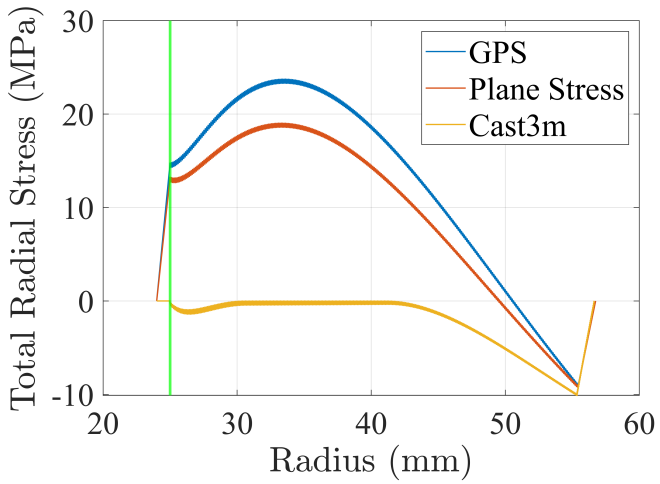

Figure 2.19 – Radial stress after winding, cooling, and energizing at mid-plane central pancake of Nougat

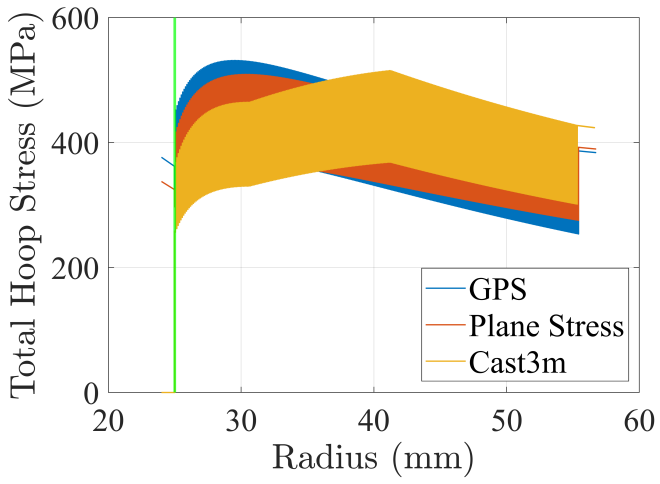

Figure 2.20 – Hoop stress after winding, cooling, and energizing at mid-plane central pancake of Nougat

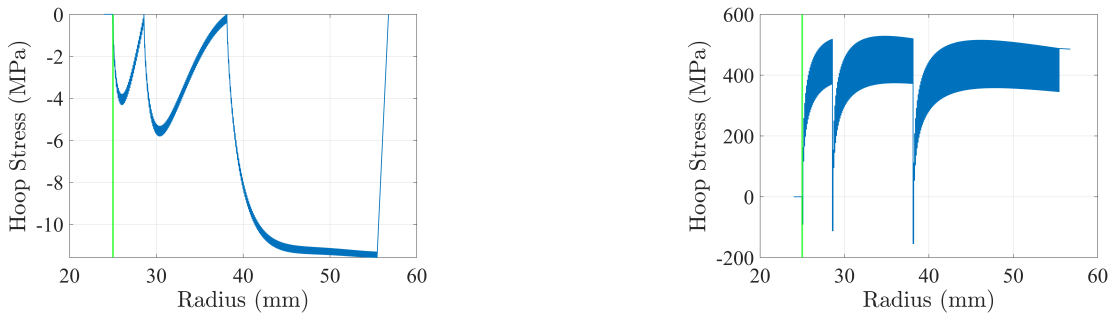

(a) Radial stress after the three loadings

(b) Hoop stress after the three loadings

Figure 2.21 – Plane stress formulation calculation while considering de-bonding effect as complete separation of turns and materials properties remaining constant in Nougat 30 T calculation

consecutive turns or separation are possible). A difference can be noticed between the plane stress and GPS hoop stress because of the constant axial strain assumption in GPS while it is not constant in plane stress.

A new calculation is proposed using plane stress assumption to evaluate the mechanical state in case of separation between turns, since the final aim is to always maintain contact between the turns to preserve the current by-passing quench protection aspect of MI pancakes. In this case, the calculation is done iteratively, where each time a de-bonding occurs because of tensile radial stress, the part before de-bonding point is considered as submitted to the three loadings with updated boundary conditions, that are zero radial stress at de-bonded point and displacement continuity inside the two separated parts. The same calculation is done for the part after de-bonding point. Figure 2.21 shows that the central pancake of Nougat magnet is separated from the mandrel and divided into three regions.

A different plane stress calculation can be proposed, where the de-bonding effect is represented by considering a very low radial young modulus while still perfect contact is assumed in the calculation all over the pancake. The calculation is done iteratively, decreasing the radial young modulus of the turns consecutively starting at the initial point i.e. the mandrel. We observe in Fig. 2.22 that after reaching turn 271 of the winding, the radial stress of the winding remains negative and close to that of Cast3m calculation. All the turns with a changed (decreased) radial modulus have lost contact with the adjacent turns. Furthermore, the displacement between the new analytical calculation and Cast3m in accordance; the hoop stress calculations are in accordance too. In these calculations, radial young modulus of the mandrel, REBCO, and SS were decreased to 10 MPa, 10 GPa, and 10 GPa respectively. This is equivalent to a decrease by 20000, 7, and 19 times for the mandrel, REBCO, and SS respectively.

However, a good dimensioning should lead to a solution where all turns and mandrel remain in contact to preserve current by-passing and protect the electrical junction at the first turn from damage.These results further emphasize the importance of the mechanical study of an MI REBCO magnet to retain its quench protection aspect. A negative radial stress in all the pancake is relevant to maintain the current by-passing and respecting the assumptions used in calculation and superposition while also an accurate formulation that can indicate when loss of contact occurs. The effect of pre-tensioning and over-banding on the results of Nougat calculation are studied in the next section.

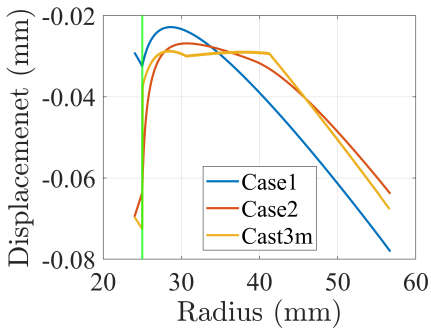

(a) Displacement after the three loadings

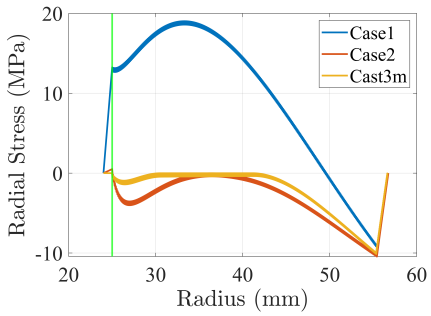

(b) Radial stress after the three loadings

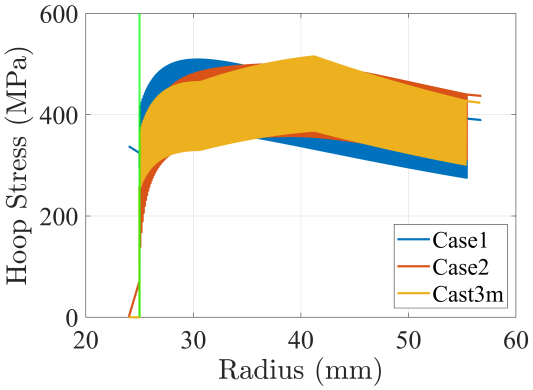

(c) Hoop stress after the three loadings

Figure 2.22 – Plane stress formulation calculation while considering de-bonding effect as a decrease of radial young modulus to negligible value in Nougat 30 T calculation (Case1: reference material properties, Case2: radial modulus becomes negligible as a de-bonding effect)

2.8 . Pre-tensioning and over-banding effect on Nougat results

As seen in the previous section, major part of central pancake of Nougat magnet has lost contact between turns. Using only plane stress assumption calculations can be redone to try various pre-tensioning and over-banding conditions to study their effect on the number of turns separated, on the maximum total hoop stress, and on the maximum compressive radial stress. The study is proposed considering a pre-tensioning range of 0 - 200 MPa with a 10 MPa step, and a number of over-banding SS turns range of 0 - 200 with a 5 turns step.

Figure 2.23 shows that the turns remain separated if pre-tension of 100 MPa is used (as in Nougat design) disregarding the number of over-banding turns. The turns are not separated starting from pre-tension of 160 MPa with 140 over-banding turns (4.2 mm over-banding), and if pre-tension of 170 MPa is used, at least 60 turns of over-banding are required to keep all turns in contact. Increasing the pretension further maintains all turns in contact even if 40 turns of over-banding are used.

Figure 2.24 shows that all over the range of pre-tension and over-banding turns, the maximum total hoop stress is in the range of 420 - 800 MPa. This verifies the importance of pre-tensioning, since without pre-tensioning maximum hoop stress remains above irreversible stress limit of REBCO tape even at 200 over-banding turns. If we consider starting from the same level of pre-tension used in magnet design, i.e. 100 MPa, maximum hoop stress remains in the range of 420 - 500 MPa which is below the irreversible limit.

However, as stated initially, during each loading phase and when adding the stresses from all loads, the values should remain lower than the irreversible stress limit of REBCO tape

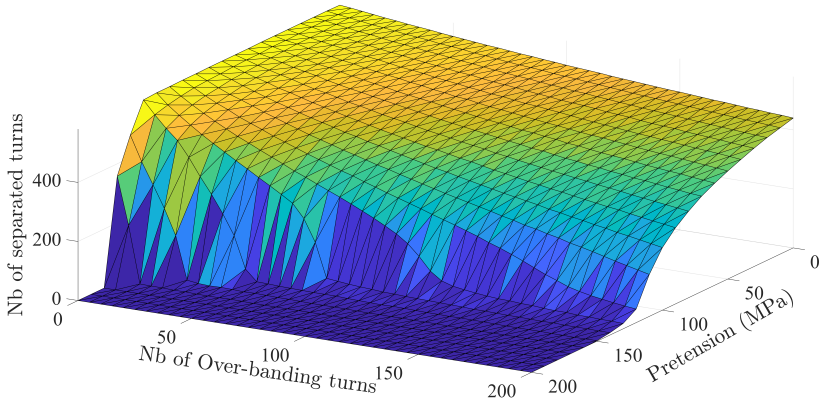

Figure 2.23 – Number of turns separated as a function of pre-tension and number of over-banding turns

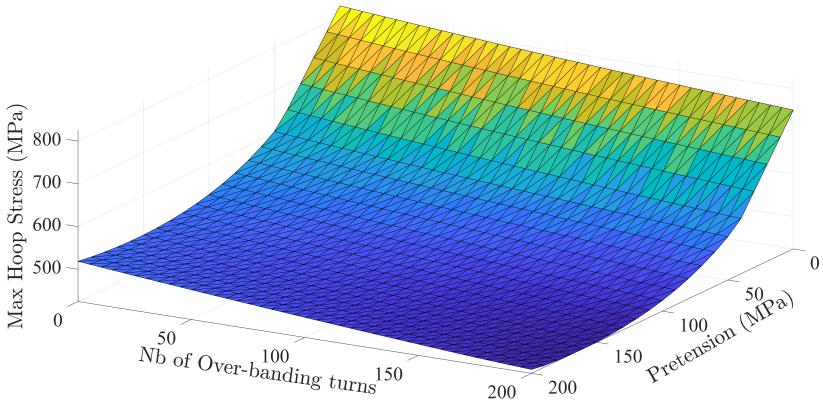

Figure 2.24 – Maximum total hoop stress in the pancake as a function of pre-tension and number of over-banding turns

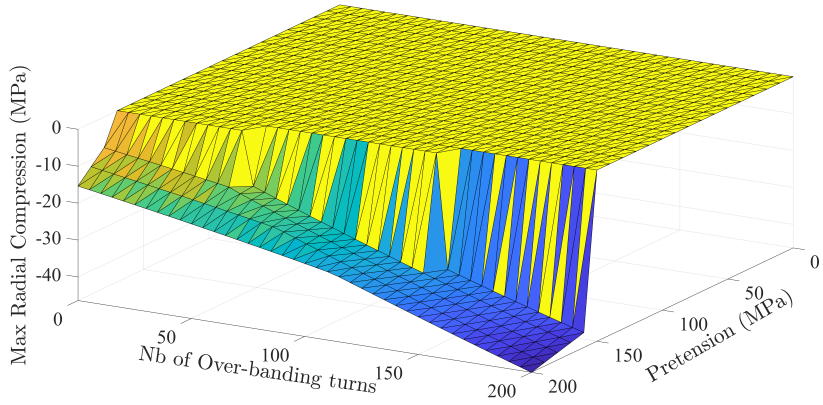

Figure 2.25 – Maximum total compressive radial stress in the pancake as a function of pre-tension and number of over-banding turns (zero indicates that there are separated turns)

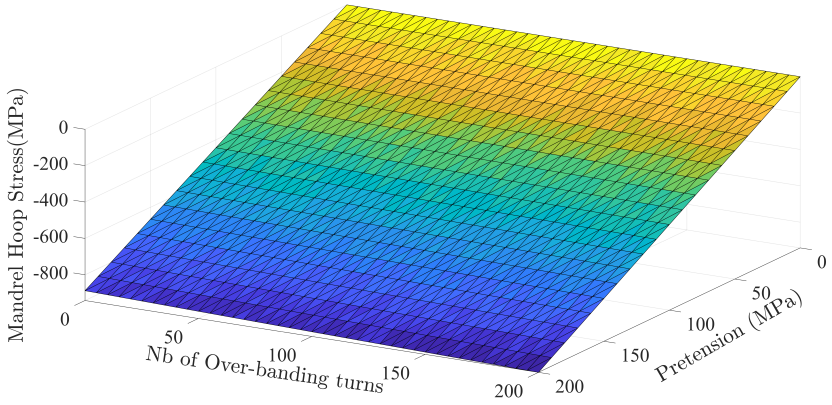

Figure 2.26 – Mandrel hoop stress due to winding as a function of pre-tensioning and over-banding

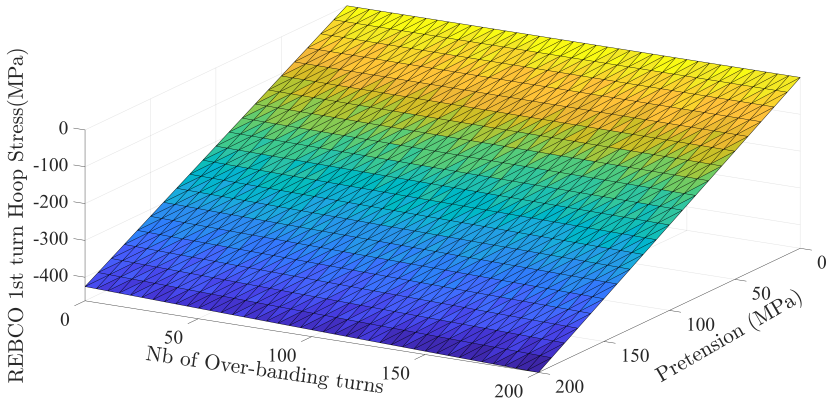

Figure 2.27 – REBCO first inner turn hoop stress due to winding as a function of pre-tensioning and over-banding

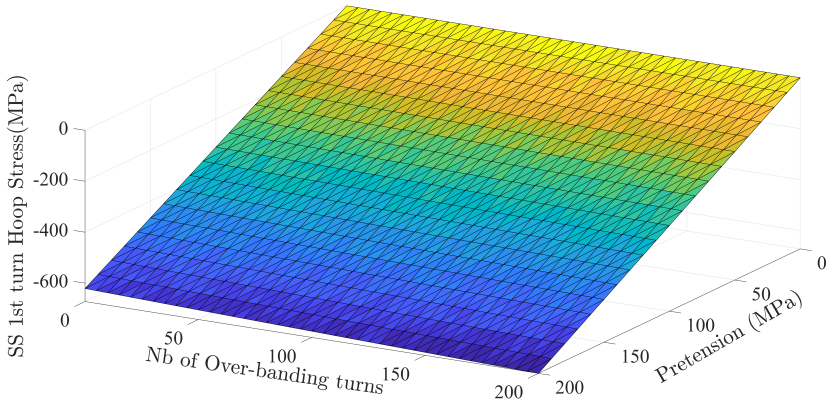

Figure 2.28 – SS first inner turn hoop stress due to winding as a function of pre-tensioning and over-banding

and within the linear elastic region of the mandrel / REBCO / SS. Hence, it is important to consider not only the hoop stress from loading, but also the hoop stress from pre-tensioning. For example, if 200 MPa pre-tension/200 turns over-banding case is considered, the hoop stress for the mandrel and the initial turns is -980 MPa for the mandrel and -450/-650 MPa for the REBCO / SS inital turns in pre-tension. Figures 2.26 to 2.28 show the value of hoop stress that can be achieved with pre-tensioning and over-banding in the mandrel, REBCO and SS tapes first turns; these values emphasize the importance and critical aspect of the winding loading, i.e. exceeding the elastic limit of the materials. Thus, it is important to choose the minimum pre-tension and over-banding that can maintain the turns in contact to meet the mechanical limits of the materials.

Furthermore, Figure 2.25 shows that when the turns remain in contact, the maximum compressive total radial stress is in the range of -15 - -45 MPa. This concludes that for the turns of central pancake of Nougat magnet to remain in contact, *160 MPa of pre-tension and 140 turns of over-banding are a good choice* while the hoop stress reaches -750 MPa for the mandrel, -350 MPa / -520 MPa for REBCO / SS tapes. The stress is increased by 100 MPa comparing to the case of 200 MPa pre-tension/200 turns of over-banding, but the thickness of mandrel needs to be increased to decrease the hoop stress to safe (elastic) stress range. Thus, pre-tensioning and over-banding are critical to ensure mechanical integrity and quench protective aspect of an MI REBCO pancake at high fields.

2.9 . Conclusion

Mechanical stress analysis is very important for the mechanical integrity and stability of MI REBCO pancake magnet. Calculation of stresses in each of the three phases (i.e.: winding, cooling, energizing) is required as each one contributes to the total stress/displacement.

Pre-tensioning and over-banding study is critical as it results in residual compressive radial stress in the pancake. This is important to maintain all turns of the pancake in contact with one another during the remaining two phases (i.e.: cooling, and energizing). It also contributes significantly to the hoop stress which should be monitored at the mandrel - initial turns level to remain within the elastic limit of the materials. Furthermore, from the study done on Nougat magnet pre-tensioning and over-banding, these are the parameters that can be adjusted to achieve total compressive radial stress and respect the stress limits of the materials. Also, during winding, REBCO layer of the REBCO tape should be facing inwards to benefit from the compressive strain resulting from the REBCO layer not being on the neutral axis during bending.

As for cooling, it contributes to largest displacement due to thermal contraction. The resultant radial stress can be compressive in one region of the pancake while tensile in the other, depending on the thermal expansion coefficient of the materials. The resultant stresses are limited and small, unlike pre-tensioning and energizing.

On the other hand, energizing phase can produce huge stresses at high fields and current densities like in "Nougat" magnet's case (Sections 2.7 and 2.8). This shows the importance of the winding phase and the residual compressive radial stress it induces in the pancake to maintain contact between the turns. Without pre-tensioning and over-banding, the hoop stress exceeds the irreversible stress limit. Section 2.8 showed the importance of combining pre-tension and over-banding to reach good values of stresses and maintaining compressive radial stress for all turns.

Furthermore, plane stress and GPS formulations were benchmarked with Cast3m on Nougat magnet showing similar results among them, especially regarding the area where total radial stress is positive. Using the plane stress formulation, a compromise between pre-tensioning and over-banding can be achieved quickly ensuring compressive radial stress in the whole pancake. However, the mechanical properties that have an effect on the stress distribution are to be checked by mechanical testing to verify the stress calculations. The mechanical characterization of the materials is done in chapter 3.

In Nougat magnet, MI REBCO pancakes are stacked upon one another with a small axial pressure similar to other MI or NI REBCO magnets made of a stack of pancakes. This means that utilizing GPS is more representative for MI REBCO pancake as it considers constant axial strain along the whole pancake. This means that no axial shearing is assumed in the calculations. For plane stress assumption, each turn can experience a different axial strain due to axial thermal contraction or Poisson ratio. However, plane stress calculations will be chosen to be compared to the experimental results in chapter 4 since they correspond to planar deformation measurements at the pancake upper surface.

3 - Mechanical Characterization of REBCO/ Durnomag Tape

3.1 . Introduction

The analytical and numerical calculations developed and presented in the previous chapter have shown that depending on the loading situations (winding, cooling and energizing), a large portion of the superconducting magnet is subjected to a zero (or positive if the boundary conditions are not reassessed) radial stress. This situation is for example observed for the "Nougat" benchmark [51].

Separation of the turns, however, probably did not take place in the corresponding experiment since when Nougat quenched at 32.5 T, it was not damaged. The lack of knowledge concerning the mechanical behavior of the materials constitutive of the superconducting magnet (REBCO and SS tapes) is one of the reasons which could explain the difference between the experiment and modeling.

The objective of this chapter is twofold. This involves, on the one hand, measuring the accessible mechanical properties of the materials concerned (in particular those which are not well known) and, on the other hand, setting up the identification experiments necessary for these measurements, experiments which will be repeated for the in-situ measurements presented in chapter 4.

We begin this chapter by a literature review results about the mechanical properties of both tapes and the experimental tests performed to identify them. Then, we introduce the digital image correlation concept for displacement measurement. This tool will help us to identify a part of the mechanical behavior constants from a uni-axial tensile test. Next, the Finite Element Method Update (FEMU) technique is explained. The latter will be exploited to identify the other mechanical constants from a diametric compression test. Finally, we will discuss the winding's effect on the mechanical properties and use the results of the tests to recalculate stresses and displacements on Nougat case.

3.2 . Experimental Setup and Reference Values

Stainless steel (SS), which is being used as a metal-as-insulation, is a homogeneous alloy of commercial name Durnomag [126] that is delivered in form of tapes whose thicknesses are comprised between 30 to 150 μm. The 30 μm thick tape is used in the MI pancake. According to the data sheet, SS exhibits a Young modulus of about 190 GPa and Poisson ratio of about 0.29. REBCO tape is a multilayered composite (Fig. 3.1) with the following composition and mechanical properties [128] (Tables 3.1 and 3.2):

	Hastealloy C276	Copper	Silver	REBCO+Buffer
Thickness (μm)	50	20	4	1

Table 3.1 – REBCO tape composition

Mechanical Property		Value	
Young Modulus (GPa) $E_r \backslash E_\theta \backslash E_z$	73	142	134
Poisson ratio $\nu_{r\theta} \backslash \nu_{\theta z} \backslash \nu_{rz}$	0.4	0.35	0.18

Table 3.2 – REBCO tape properties [128]

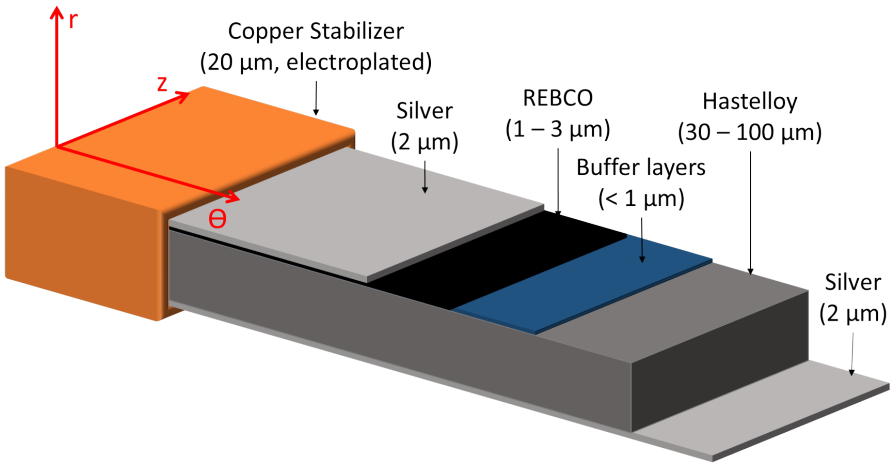

Figure 3.1 – REBCO tape

The mechanical properties that we are looking for define which test has to be carried out. As REBCO is a layered composite of isotropic materials, its average behaviour is transversely isotropic; this means that it has only five parameters to be identified. Hence, compliance matrix for REBCO tape in cylindrical coordinates, where radial / hoop / axial directions are along thickness / length / width directions of the tape, is of the form:

$$\begin{bmatrix} \epsilon_{rr} \\ \epsilon_{\theta\theta} \\ \epsilon_{zz} \\ \epsilon_{\theta z} \\ \epsilon_{zr} \\ \epsilon_{r\theta} \end{bmatrix} = \begin{bmatrix} \frac{1}{E_r} & -\frac{\nu_{\theta r}}{E_\theta} & -\frac{\nu_{\theta r}}{E_\theta} & 0 & 0 & 0 \\ -\frac{\nu_{r\theta}}{E_r} & \frac{1}{E_\theta} & -\frac{\nu_{\theta z}}{E_\theta} & 0 & 0 & 0 \\ -\frac{\nu_{r\theta}}{E_r} & -\frac{\nu_{\theta z}}{E_\theta} & \frac{1}{E_\theta} & 0 & 0 & 0 \\ 0 & 0 & 0 & \frac{1+\nu_{\theta z}}{E_\theta} & 0 & 0 \\ 0 & 0 & 0 & 0 & \frac{1}{2G_{r\theta}} & 0 \\ 0 & 0 & 0 & 0 & 0 & \frac{1}{2G_{r\theta}} \end{bmatrix} \begin{bmatrix} \sigma_{rr} \\ \sigma_{\theta\theta} \\ \sigma_{zz} \\ \sigma_{\theta z} \\ \sigma_{zr} \\ \sigma_{r\theta} \end{bmatrix} \tag{3.1}$$

The five parameters are: radial Young modulus E_r, hoop Young modulus E_θ, Poisson ratios $\nu_{r\theta}, \nu_{\theta z}$, and shear modulus $G_{r\theta}$. For plane stress calculation, only three parameters are required : E_r, E_θ, and $\nu_{r\theta}$. In axisymmetic condition (no shear stress), this simplifies the matrix form to:

$$\begin{bmatrix} \epsilon_{rr} \\ \epsilon_{\theta\theta} \end{bmatrix} = \begin{bmatrix} \frac{1}{E_r} & -\frac{\nu_{\theta r}}{E_\theta} \\ -\frac{\nu_{r\theta}}{E_r} & \frac{1}{E_\theta} \end{bmatrix} \begin{bmatrix} \sigma_{rr} \\ \sigma_{\theta\theta} \end{bmatrix} \tag{3.2}$$

SS is assumed isotropic for simplicity reasons, in accordance with available data sheets. As a result, SS elastic behavior is defined by two parameters, namely, Young modulus and Poisson ratio.

Both tapes are very small in thickness (few μms) and in width (few mms). This gives rise to an additional consideration in the parameter-identification experimental test. Using digital image correlation (DIC), three properties can be identified; they are: hoop Young modulus,

yield stress, and Poisson ratio ($\nu_{\theta z}$). The samples to be tested are rectangular in shape, to extract the aforementioned properties, so that Saint Venant Principle [130] has to be applied. This means that the length of the sample should be ten times or more than its width to remain in uni-axial stress condition.

Hence, from the force acquired from load cell and strain from DIC, an engineering stress / strain curve can be plotted. From the measurement, Young modulus and yield stress are found. In addition, DIC gives lateral strain which allows for the calculation of Poisson ratio.

Radial Young modulus and planar Poisson ratio ($\nu_{r\theta}$) are the two remaining parameters. These parameters are identified using Finite Element Method Update (*FEMU*) diametric compression test [131] (Fig. 3.2). The disk is compressed between the grips of the testing machine at the contact surfaces (S_1, S_2) with a force of value T_1, and the remaining surfaces (S_3, S_4, S_5) of the disk are free. Parameter identification using FEMU is considered as an inverse problem. This is due to the fact that the resultant force and the disk field displacement are used as inputs to determine the constitutive parameters. Let R be the resultant force, U the field displacement, and K(p) the stiffness matrix, then K(p).U=R is the balance equation of the problem, with p being the parameters to identify [131]. FEMU identification approach is based on minimizing the discrepancy between the experimental and predicted data. This concept is explained and illustrated in Section 3.5. The sought properties from FEMU are the elastic parameters.

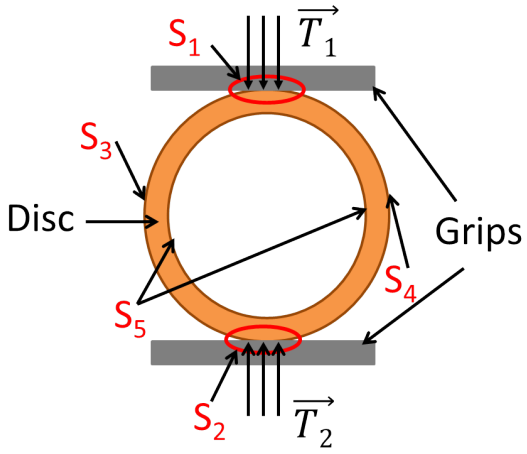

Figure 3.2 – Scheme of disk being compressed between grips ($T_1 = T_2$ compression forces ,(S_1, S_2) surface contacts, (S_3, S_4, S_5) free surface) - none body forces are considered

Both tapes (REBCO and SS) have to be made into a disk shape for mechanical characterization. The winding of the tape cannot however be made "on its own" due to insufficient stiffness. Consequently, a mandrel has been used upon which each tape is wound several times to reach a significant width (few mm). The mandrel must be stiff enough to allow the winding of several millimeters of REBCO or SS tape, and not too stiff (like stainless steel) to allow a significant deformation during the diametric compression while remaining below its yield stress. A Brass (CuZn23Al4) mandrel has been chosen.

It must be noticed that some previous tensile tests have been carried out on brass strips cut from the ingot from which the mandrel was machined. The main idea of this previous test is to get the yield stress and Young modulus of this material.

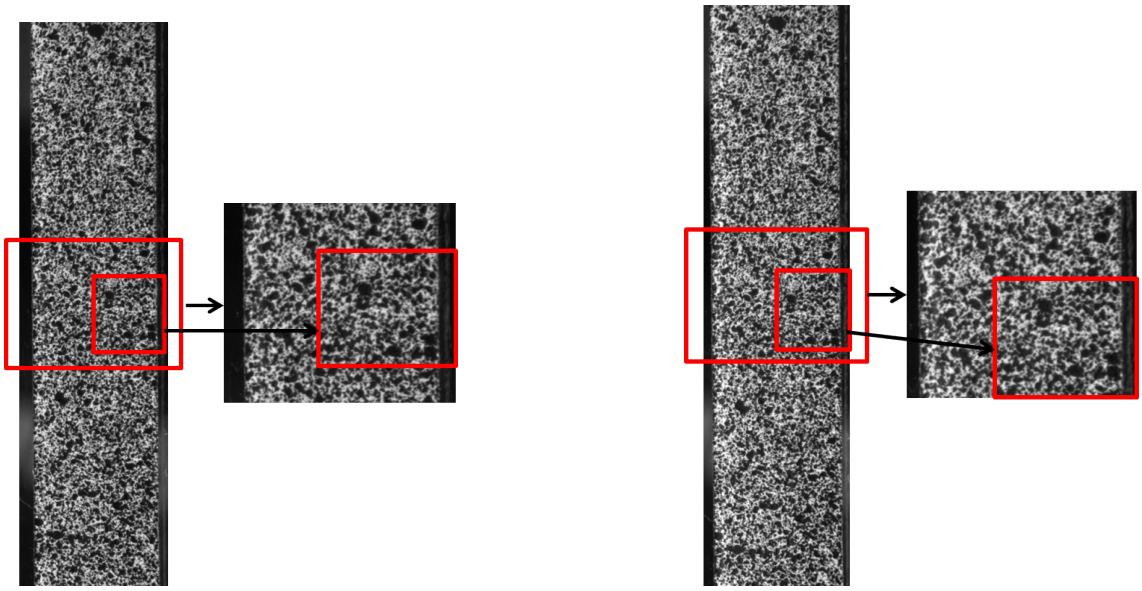

(a) Image of REBCO at reference state

(b) Image of REBCO at deformed state

Figure 3.3 – Images of REBCO for DIC analysis, red rectangle showing a zoomed view at center of sample at both states to highlight speckle movement downward

3.3 . Digital Image Correlation

Digital image correlation is a full-field measurement technique that measures the kinematic fields over large area. It gives quantitative measurement of the 2D displacement (/deformation) fields in the specimen's Region of Interest **ROI**. It is a non-intrusive and non-contact technique as it is based on optical imaging. This allows it to be used on delicate specimens and in harsh environments.

DIC is based on the principle of **Gray-Level Conservation** [132]. It assumes that the gray level is conserved between a reference image (i.e. initial configuration, Fig. 3.3a) $f(\mathbf{x})$ and a deformed image $g(\mathbf{x})$ (Fig. 3.3b) at a deformed state. The only variation between f and g in the gray level is due to the displacement $\mathbf{u}(\mathbf{x})$:

$$f(\mathbf{x}) \approxeq g(\mathbf{x} + \mathbf{u}(\mathbf{x})) \tag{3.3}$$

$\mathbf{u}(\mathbf{x})$ is the displacement field in the deformed configuration. The sought field minimizes the sum of squared differences Φ_c^2 in the chosen region of interest:

$$\mathbf{u}(\mathbf{x}) = argmin(\Phi_c^2) \tag{3.4}$$

with

$$\Phi_c^2 = \int_{ROI} \phi_c^2(\mathbf{x}) dx \tag{3.5}$$

where $\phi_c(\mathbf{x})$ defines the following field of correlation residual

$$\phi_c(\mathbf{x}) = |g(\mathbf{x} + \mathbf{u}(\mathbf{x})) - f(\mathbf{x})| \tag{3.6}$$

The minimization of Φ_c^2 is a nonlinear and ill-posed problem. If no additional information is available, it is impossible to determine the displacement for each pixel independently since there are two unknowns for a given (scalar) gray level difference. Hence, weak formulation is chosen, in which displacement field is discretized as:

$$\mathbf{u}(\mathbf{x}) = \Sigma_n a_n \psi_n(\mathbf{x}) \tag{3.7}$$

where ψ_n is an n-th polynomial spatial function, and a_n corresponds to the associated degrees of freedom.
The resolution of the kinematic field $\mathbf{u}(\mathbf{x})$ is made by solving the linear system at each iteration:

$$[M]\{\partial \mathbf{u}\} = \{\mathbf{b}\} \tag{3.8}$$

where $[M]$ is the DIC matrix formed from the dyadic product of fields $\nabla f.\psi_n$, $\{\mathbf{b}\}$ is a vector that vanishes when a perfect fit is obtained for each pixel, and $\{\partial \mathbf{u}\}$ collects the corrections to the displacement field.

However, DIC is limited due to its ill-posed problem because of the non-linear minimization of Φ_c^2. Hence, a mechanical regularization is introduced [132]. This regularization reduces the problem's ill-posedness significantly. It acts as a low pass filter. It is based on the mechanical admissibility in the Finite Element sense. If linear elasticity is applied, the equilibrium equation is as follows:

$$[K]\{\mathbf{u}\} = \{\mathbf{f}\} \tag{3.9}$$

where $[K]$ is the stiffness matrix, and $\{\mathbf{f}\}$ is the vector of nodal forces. If the displacement field does not satisfy the equilibrium conditions, it will induce an equilibrium gap. In the absence of body forces, interior nodes are free from external loading. Thus, the mechanical regularization, that is equilibrium gap method, is based on minimizing the mechanical residual:

$$\Phi_m^2 = \{\mathbf{u}\}^t[K]^t[K]\{\mathbf{u}\} \tag{3.10}$$

where ^{t} is the transpose operator, and Φ_m^2 is the sum of squared norm of all equilibrium gaps at the interior nodes only. Any displacement field prescribed on the boundary gives rise to a displacement field verifying $\Phi_m = 0$.

3.4 . Uni-axial Tensile Test - Room Temperature

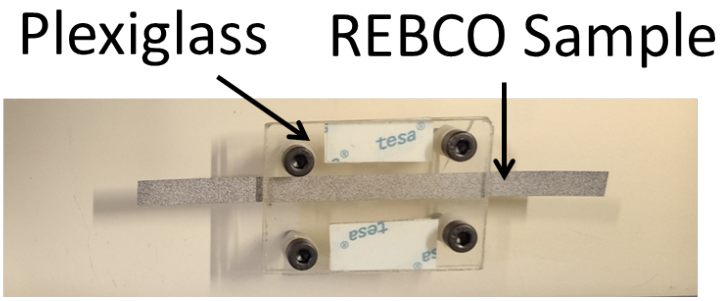

Figure 3.4 – REBCO sample

To do the uni-axial tensile test properly, the width and thickness of a sample should be known before the test. Regarding the two materials REBCO and SS, both are quite small and thin; dimensions cannot be measured using a caliper. Hence, optical microscopy was used to measure the width. The width measurement gives $5.8\ mm$ ($\pm 0.05\ mm$) for REBCO and SS. Scanning electron microscopy was used to measure the thickness yielding a thickness of $29\ \mu m$ ($\pm 1\ \mu m$) for SS and $70\ \mu m$ ($\pm 2\ \mu m$) for REBCO. The length of REBCO and SS was $100\ mm$ ($\pm 1\ mm$).

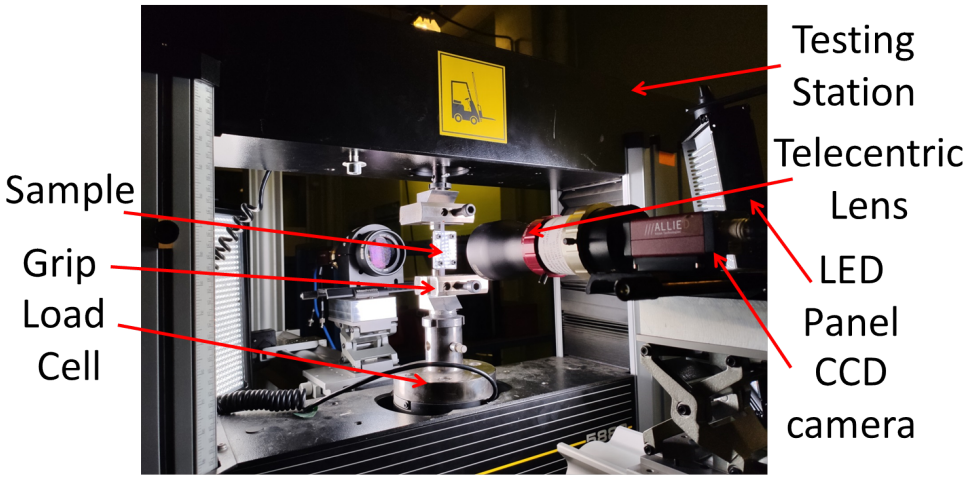

Figure 3.5 – Tensile test setup

Due to their thickness, both materials are considered as foil materials. Following the *ASTM Standard E345-16*, the uni-axial tensile testing is done in displacement load control with tensile machine speed of $0.5\ mm/min$. Parallelepipedic samples have been cut from the brass piece used to machine the mandrel. Samples length, width and thickness are 800 mm, 6 mm ($\pm$ 0.01 mm) and 3 mm, respectively. According to *ASTM Standard E8/E8M-16a*, tensile testing is done in displacement load control with tensile machine speed of $0.5mm/min$. All the specimens should satisfy the *Saint Venant* [130] specification, length being ten times or higher than the width, to get a true uni-axial stress in the middle of the samples.

However, REBCO and SS are so thin (few μm) that a curving of the specimen may occur during tensile testing due to a Poisson effect [133]. The sample curvature prevents proper use of the DIC during the test due to out-of-plane effects. This leads us to exploit a mechanism based on sandwiching the sample between two transparent plexiglass, without pressing tightly on the sample as not to affect the test (Fig. 3.4), to limit the curving.

An additional step to improve the DIC results is the use of telecentric lens for image acquisition. The lens eliminates out of plane motion resulting in acquiring images of plane deformation only. A CCD manta camera and Stream Pix 5 image acquisition program were used with a 1 Hz acquisition frequency. In addition, white light LED panel was used to constantly illuminate the sample, and a black and white speckle pattern was applied on the sample to provide the gray level required for the DIC (Fig. 3.5). The testing station used was the electro-mechanical *Instron 5882* with a load cell of range $\pm$ 400 N, having $\pm$ 2 N error, for the REBCO and SS samples, and a load cell of range $\pm$ 100 KN for the brass samples.

The REBCO, SS, and Brass tensile-test experimental data are presented in Appendix A. The DIC software used is the *Correli* Matlab code developed at LMT [134]. At first, a region of interest (ROI) is specified as illustrated in Fig. 3.6. Then with *GMSH* free meshing program, the ROI is meshed using a TRI3 mesh. GMSH is called in Matlab to do the meshing after specifying the mesh size (Fig. 3.7).

As mentioned in Section 3.3, the DIC can estimate the displacement uncertainty, which can be decreased by using a large mesh. On the other hand, a good spatial resolution requires a small mesh; this means that a compromise has to be found. Using a 30 pixel mesh characteristic size has been estimated to be a suitable compromise avoiding localization phenomenon or sharp heterogeneous deformation.

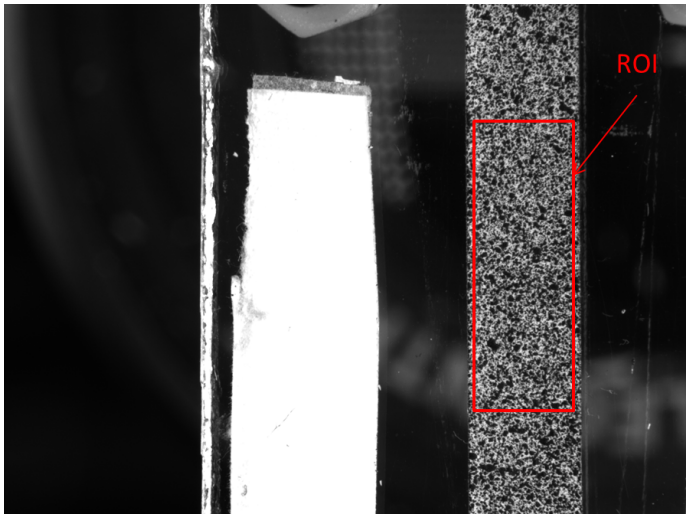

Figure 3.6 – Black / White Speckle on the sample, ROI is red plotted

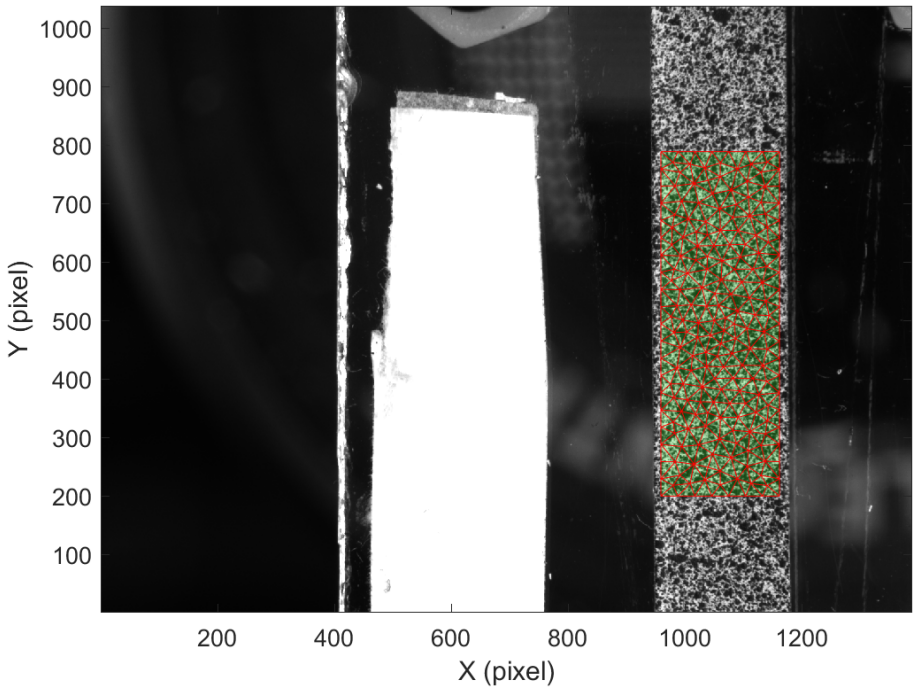

Figure 3.7 – Mesh of ROI with 30 pixel mesh size

By taking a static image sequence of 20 images in total without external load, an uncertainty study is done. The expected displacement should be strictly zero when no load is applied and when no fluctuation of lightning conditions is present. Thus, the calculated displacement field from the static images is giving the uncertainty measurement. It is associated with the texture of black and white speckle, mesh element size and the effect of plexiglass sandwich. With an element size of 30 pixels, the longitudinal displacement uncertainty is about 0.035 pixels. This is acceptable taking into account the presence of plexiglass. Also, the longitudinal and transversal strain uncertainties measurement are estimated to -6.3 $\times$ 10^{-4} $\%$ and 3.4 $\times$ 10^{-3} $\%$ respectively; i.e. they are negligible in comparison to the measured strains that should be at least two orders higher during the tensile test.

All images of tensile test are treated using *Correli*, with a mesh element TRI3 of size 30 pixels. Figures 3.8 and 3.9 give an example of DIC results during the tensile testing of REBCO tape. Figure 3.8 shows slight error at certain points because of the speckle at these points, this slight error is detected at same position in Figure 3.9. Figure 3.8 shows homogeneous results since ROI is taken at the middle of the sample. The same comment can be made for Figure 3.9 results, but the edges show higher deformation which can be interpreted as an effect of Poisson curving. The longitudinal strain is not affected since the curving moves the edges of the tape inward (transversal strain is affected on the contrary).

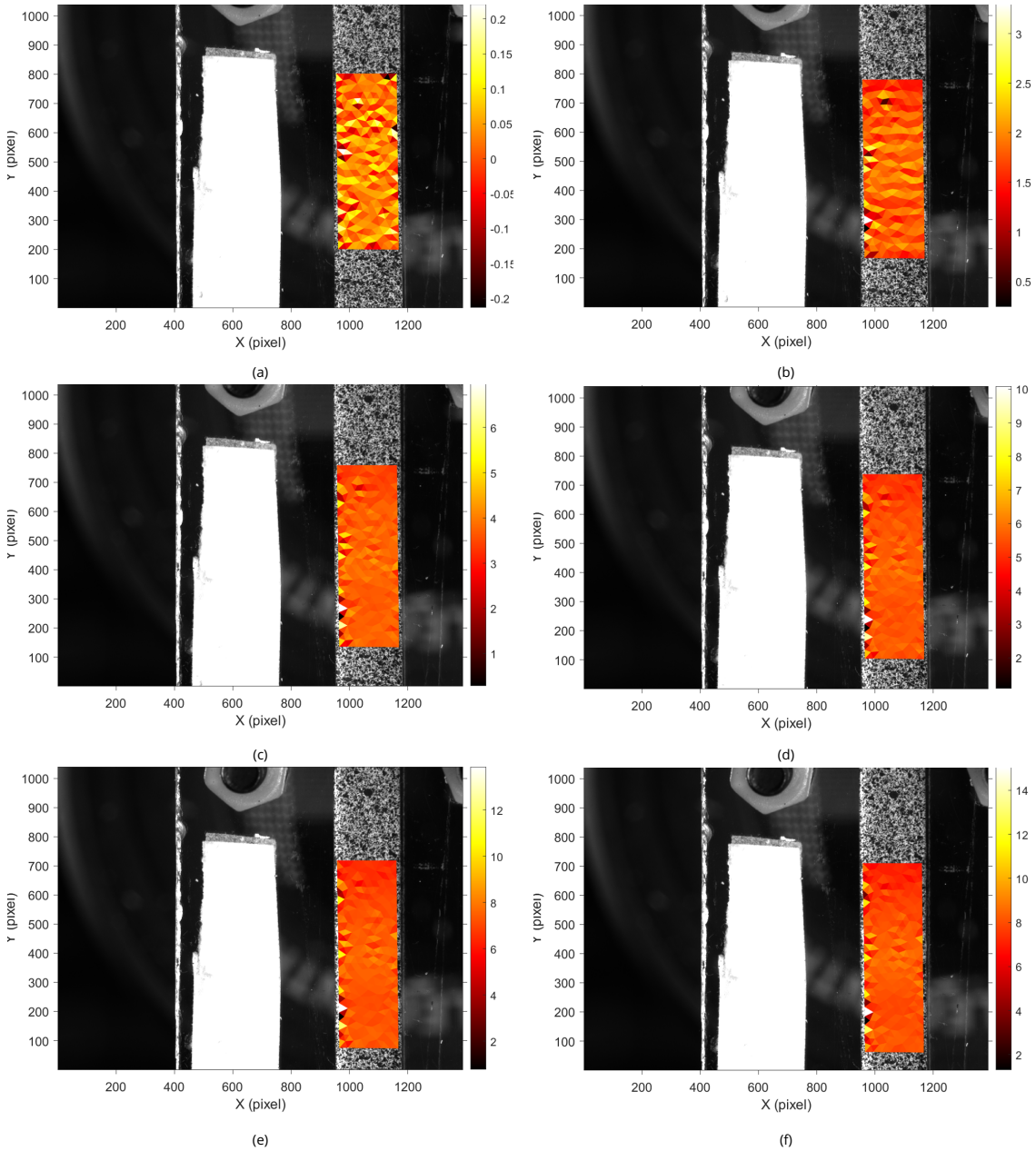

Figure 3.8 – Longitudinal strain field (%) during the tensile testing of REBCO tape at 6 different steps. Steps (a-f) are reported in the stress-strain curve reported in figure 3.10.

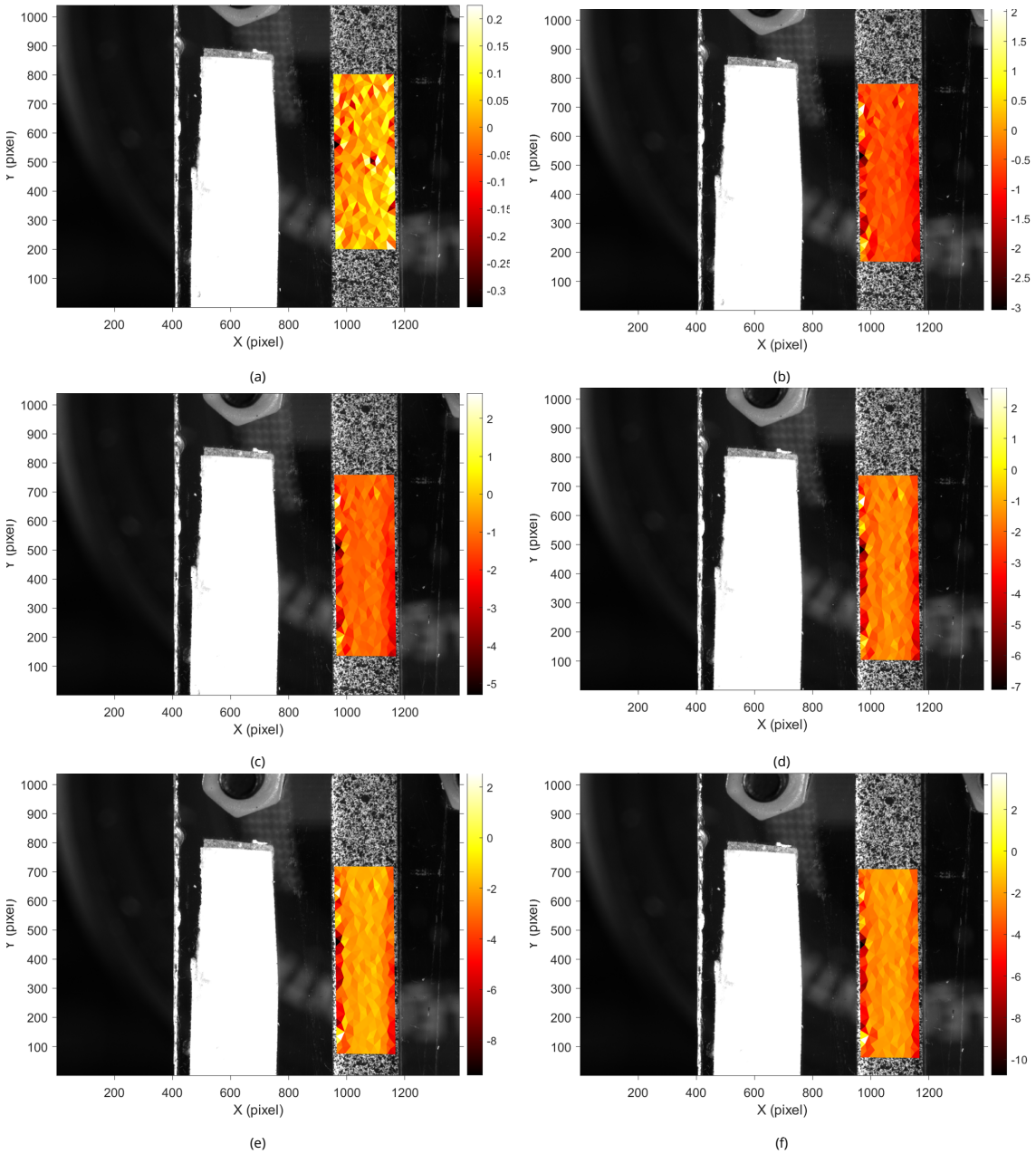

Figure 3.9 – Transversal strain field (%) during the tensile testing of REBCO tape at 6 different steps.

The axial strain that is obtained from Correli is used for plotting the engineering stress strain curve of the samples. The tensile test has been repeated three times to evaluate a reproducibility error. a, b, c, d, e and f points correspond to pictures reported in Figs. 3.8 and 3.9.

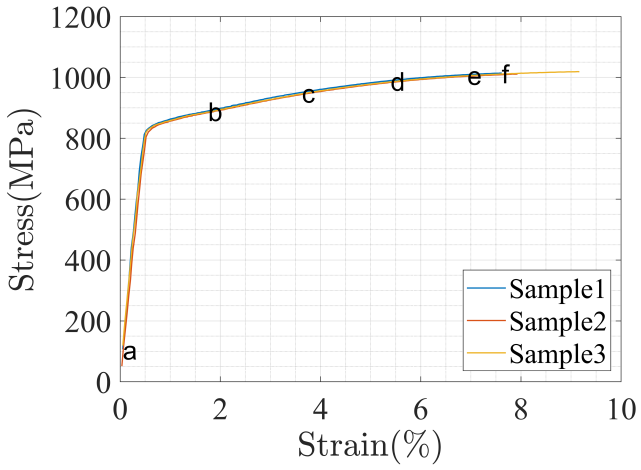

Figure 3.10 – REBCO stress-strain curve (at 293 K)

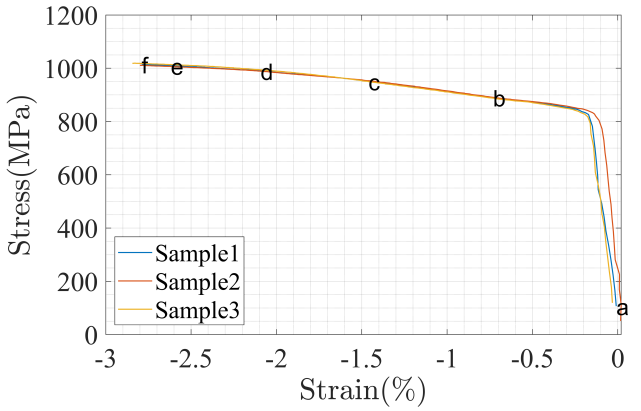

Figure 3.11 – REBCO stress-transverse strain curve (at 293 K)

	Young modulus	Yield stress	Poisson ratio
REBCO	153 (± 5) GPa	820 (± 4) MPa	0.32 (± 0.02)

Table 3.3 – REBCO tape tensile test results

The REBCO tensile tests results (Fig. 3.10 and Table 3.3) are in accordance with values reported in [128]. The results were reproducible as seen from Figs. 3.10 and 3.11 with a maximal stress of 1012 (± 1.2) MPa and a maximal strain of 7.9% (± 0.6).

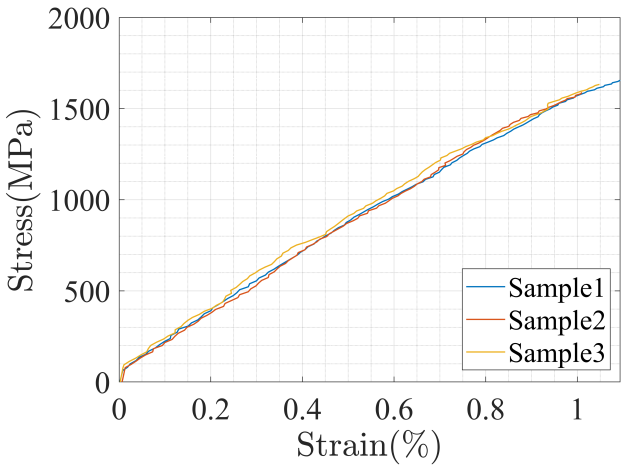

Figure 3.12 – Stainless Steel (SS) stress-strain curve (at 293 K)

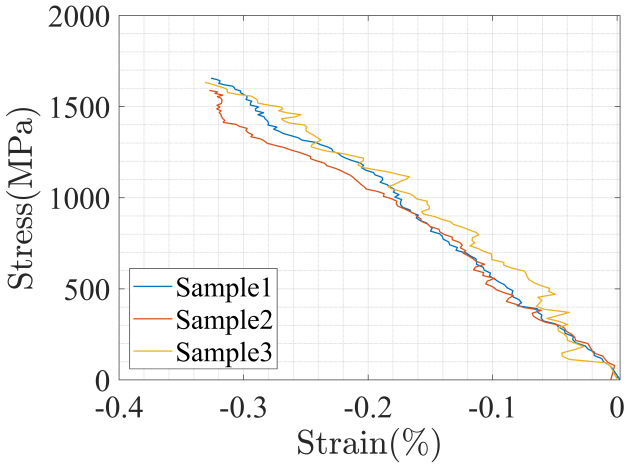

Figure 3.13 – Stainless Steel (SS) stress-transverse strain curve (at 293 K)

	Young modulus	Yield stress	Poisson ratio
SS	162 (± 1.5) GPa	1250 (± 5) MPa	0.29 (± 0.01)

Table 3.4 – Stainless Steel (SS) tape tensile test results

Figs. 3.12 and 3.13 report the stress vs. longitudinal strain and the stess vs. transversal strain behaviour of SS material respectively. A global elastic / brittle behaviour is obtained. A plastic strain of about less than 0.2 % is obtained. The SS yield stress and Poisson ratio (Table 3.4) are in accordance with the material's data sheet [126]. The Young modulus is on the contrary lower than expected. The results in Fig. 3.12 show a good reproducibility among the samples, but Fig. 3.13 shows that Poisson curving has higher effect in SS than in REBCO because of the much lower thickness of SS.

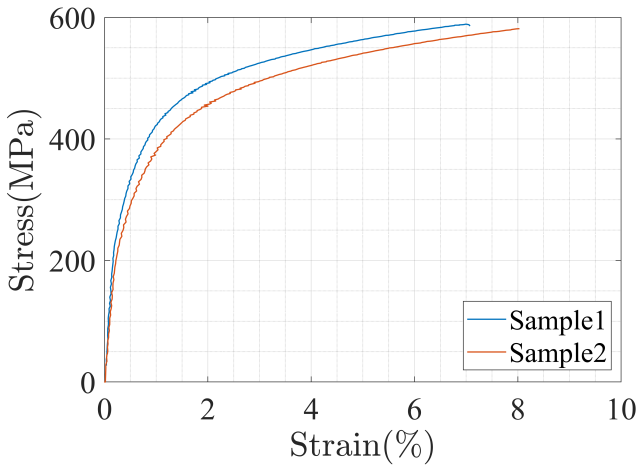

Figure 3.14 – Brass stress-strain curve (at 293 K)

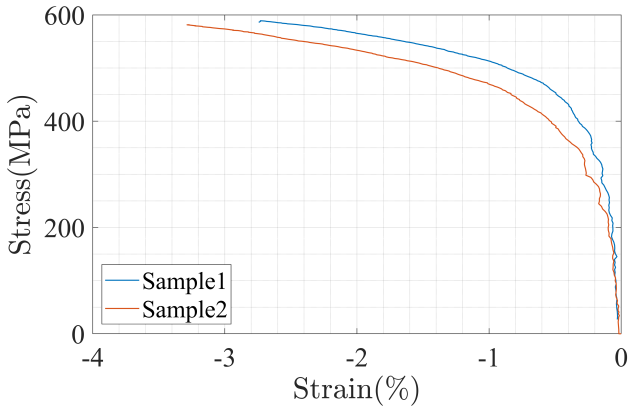

Figure 3.15 – Brass stress-strain curve (at 293 K)

	Young modulus	Yield stress	Poisson ratio
Brass	101.8 ($\pm$6.5) GPa	220 ($\pm$2) MPa	0.39 ($\pm$0.01)

Table 3.5 – Brass tensile test results

Concerning brass, two tests were done because the number of test pieces are limited being machined with the specified dimensions from a 100 mm circular disk. Fig. 3.14 (Fig. 3.15) and Table 3.5 show that the brass yield stress and Young modulus results are close to values reported in reference [135]. These values allow the anticipation of how much force can be applied during the diametric compression test while remaining in the elastic domain of all the materials Brass + REBCO / Brass + SS.

Hence, for more accurate stress distribution calculation in the MI pancake test, we expect to use data obtained from experimental results. The results achieved for the hoop Young modulus and Poisson ratio of REBCO tape are in accordance with the results achieved by analytic and FE homogenization (Appendix G). The tests were done at room temperature because austenitic stainless steel and Hastealloy-C276 exhibit only a small increase in young modulus of approximately 10 GPa at cryogenic temperature (77 or 4 K) [136–138]. The yield stress increases as well at cryogenic temperature for both materials, but considering the lower yield

stress at room temperature is acceptable. It is on the other hand better to consider a low yield stress for calculations to prevent plastic strain and maintain a high critical current as mentioned in chapter 1. Moreover, REBCO tape is mostly composed of Hastealloy-C276 substrate in the tape considered in the thesis preventing too high mechanical properties variations at cryogenic temperature..

3.5 . Finite Element Method Update

Finite Element Method Update "FEMU" is a technique that extracts various mechanical properties at the same time. There are different FEMU versions, either based on the displacement input only (FEMU-U), or on the force input only (FEMU-F), or on both of them (FEMU-UF). FEMU-U is based on the principle of comparing the displacement field acquired from the experiment with that of test-specimen model obtained from the FE until convergence is reached. Parameters are iteratively adjusted until the calculation converges on the parameters that give the closest numerical displacements to that of the experiments. In FE, the boundary displacement is imposed based on the experimental results. The relation between the sought parameters and the resultant displacement is used in FEMU to extract those parameters.

However, finding accurate value of Young modulus is not possible using only displacement in FEMU. Hence, the use of the experimental load will allow us to find the absolute values of Young and shear modulus. Moreover, it is not possible to achieve same exact displacement in FE as the results of the DIC measurement. Thus, equilibrium gap function is introduced as for mechanical regularization in DIC.

In FEMU-U, the parameters are identified by minimizing the weighted-square norm of the difference between the measured and calculated displacements.

$$\chi_u^2(\{\mathbf{p}\}) = \frac{1}{N_u}(\{u_m\} - \{u_c\})^t [C_u]^{-1} (\{u_m\} - \{u_c\}) \tag{3.11}$$

Where $\{\mathbf{p}\}$ is column vector of unknown parameters, N_u is the total number of kinematic degrees of freedom, $\frac{1}{N_u}$ is a normalization factor, u_m is the measured displacement field, and u_c is the calculated displacement field. $[C_u]$ is a block diagonal matrix gathering all covariance matrices $[C_u(t)]$ which is equal to $2\gamma_f^2[M]^{-1}$. γ_f is the standard deviation of noise expressed in gray levels, and $[M]$ is the DIC matrix.

As the calculation starts with an initial guess of parameters $\mathbf{p}$, FEMU has to optimize them at each iteration, that is to correct them iteratively, to reach convergence. The parameter correction increment is calculated as such:

$$\{\partial p\} = [H^{i-1}]^{-1} [S_u^{i-1}]^t [M]' (\{u_m\} - \{u_c^{i-1}\}) \tag{3.12}$$

Where $[S_u^{i-1}]$ is the matrix gathering all sensitivity fields (i.e., $\{\partial u_c\} = [S_u]\{\partial p\}$), $[M]'$ is the block diagonal matrix with the same matrix $[M]$ for each considered time instant t, and $[H^{i-1}] = [S_u^{i-1}]^t [M]' [S_u^{i-1}]$ is the approximated Hessian. Hence, the new parameters are $\{p^i\} = \{p^{i-1}\} + \{\partial p\}\{p^{i-1}\}$.

To determine whether convergence is achieved or not, it is checked by calculating the root-mean-square of parameter correction increment $\{\partial p\}$, and comparing the value to a specified value for the convergence. For example, if $rms(\{\partial p\}) < conv$, with $conv$ being convergence criteria value, then the convergence is achieved.

FEMU-F, differs from FEMU-U by its equilibrium gap function:

$$\chi_F^2(\{p\}) = \frac{1}{\gamma_F^2 N_F}(F_c - F_m)^2 \tag{3.13}$$

Where γ_F is the standard resolution of load measurement, and N_F is the total number of load data.

Identification using both FEMU-U and FEMU-F (FEMU-UF) yields better results, and a new minimization problem appears:

$$\chi_{tot}^2 = (1-w)\chi_u^2 + w\chi_F^2 \tag{3.14}$$

Where w is a dimensionless weight ($0 < w < 1$) that is assumed to balance data from different sources.

In all FEMU calculations (U,F, and UF), a part of the information used for the FE calculation is experimental: displacement and force imposed at the contact boundaries.

3.6 . Diametric Compression Test

As REBCO and SS are tapes, they require to be wound on cylindrical mandrel to perform the diametric compression test (test data in Appendix B) : two " simplified" pancakes are obtained. The chosen mandrel material is Brass (CuZn23Al4) because it has low Young modulus (to reduce the global stiffness and increase sensitivity of diametric compression test to REBCO or SS elastic constants) to a sufficiently high yield stress (Table 3.6). Before implementing the diametric compression test using REBCO or SS simplified pancakes, the brass mandrel (see Table 3.6 for specifications) was tested alone. The idea behind this preliminary test is to verify the elastic parameters identification of brass by FEMU (Fig. 3.16).

	Inner radius	Thickness	Width
Brass	22 ($\pm$0.1) mm	3 ($\pm$0.1) mm	6 ($\pm$0.1) mm

Table 3.6 – Brass mandrel specifications

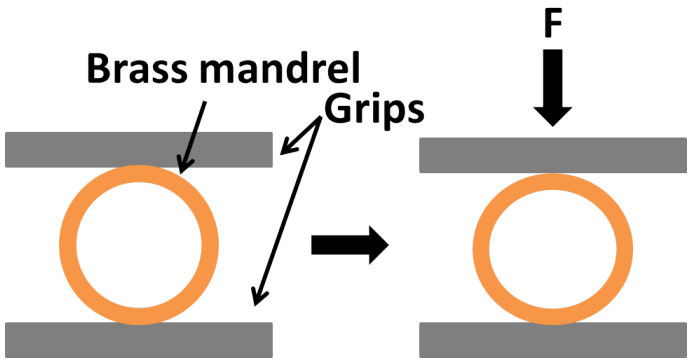

Figure 3.16 – Brass diametric compression test scheme

A Cast3m simulation of the diametric compression test of brass mandrel has been first carried out. It allows us to verify that the overall displacements are detectable by DIC while remaining

below yield stress. This simulation allows evaluating the compression force before testing and adjust the force sensor range. The resultant displacement is in order of hundred of microns (Fig. 3.17), which is detectable by DIC and applied force reaches 200 N.

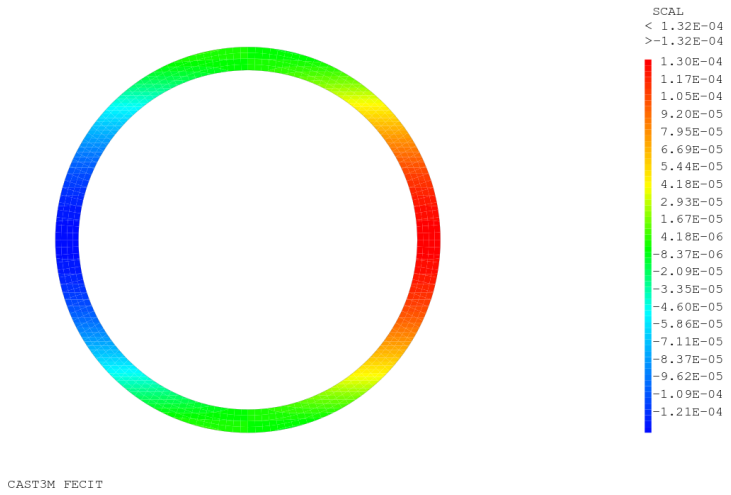

Figure 3.17 – Horizontal displacement (in meters)

After the simulation results regarding the DIC usage, a diametric compression test has been carried out. Fig. 3.18 illustrates the set-up..

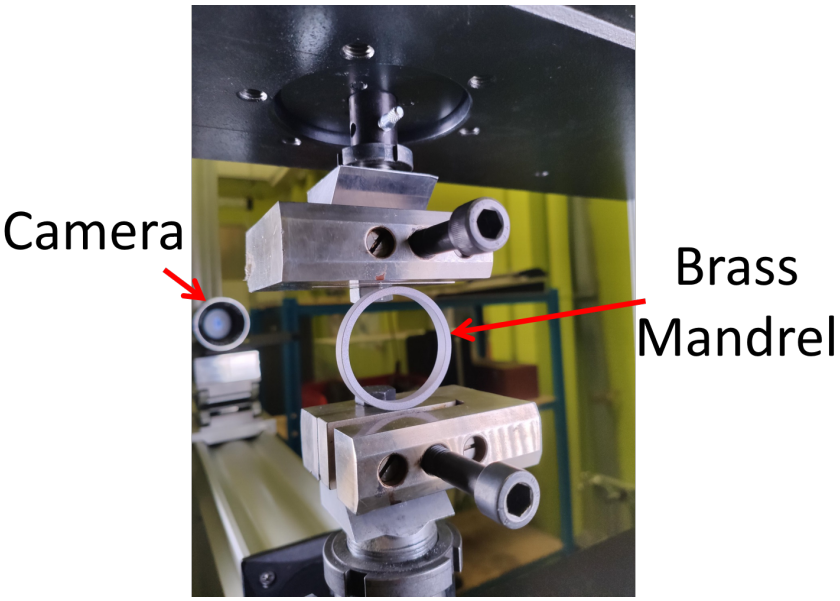

Figure 3.18 – Diametric compression of the brass mandrel

After doing the test, DIC was done on the whole mandrel. The mesh is composed of TRI3 elements with an element size of 9 pixels, so that we are able to perform the FEMU analysis (Fig. 3.19).

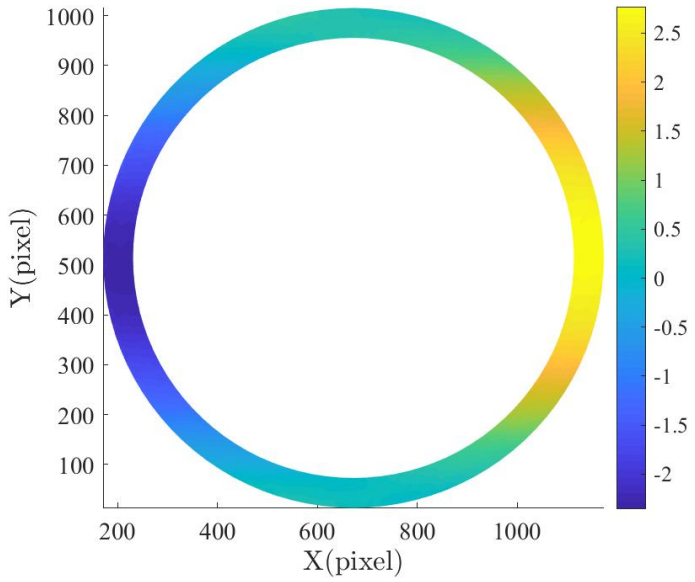

Figure 3.19 – Horizontal DIC displacement results (in pixel) at 200 N compression load

Regarding the FEMU calculation, it is done using a Matlab code developed at LMT. The Matlab code is coupled with Abaqus 6.14 for FE calculation both codes sharing the same mesh. The code was initially developed for plastic parameter identification during a tensile testing [139]. It was adjusted to fit for the diametric compression test with elastic parameter identification. On the other hand, material properties were adjusted to cylindrical coordinates. In addition, the same mesh used for the DIC analysis is used for the Abaqus calculation.

Concerning Abaqus, three contact points between the brass mandrel and the grips are considered where the compression force is being exerted (Fig. 3.20). The other surfaces are stress-free. The elastic problem is solved using plane stress condition. Using FEMU-UF and assuming brass to be Isotropic, Young modulus and Poisson ratio can be estimated.

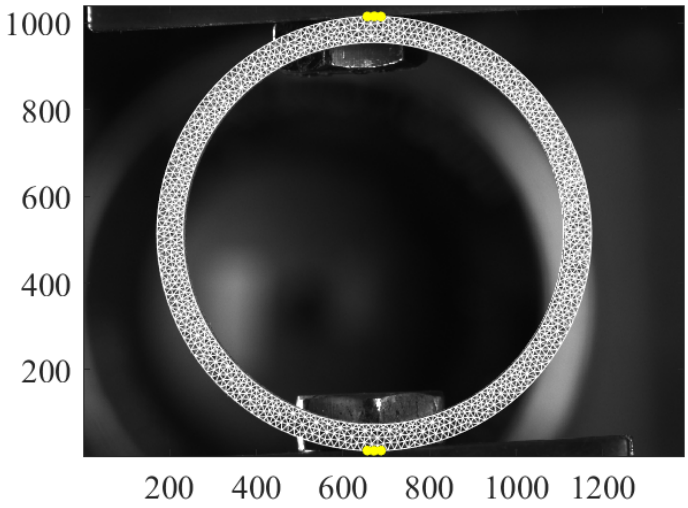

Figure 3.20 – FEMU-UF mesh, contact points (Yellow)

FEMU-UF is used on brass mandrel considering two different initial sets of parameters. The initial values of Poisson ratio and Young modulus used were respectively 0.4 and 50 GPa for the first calculation, and 0.4 and 150 GPa for the second calculation. Both calculations converge

yielding a Young modulus of 93.9 GPa independent of the initial guess, and a Poisson ratio of 0.136.

As seen in Figure 3.21, the force calculated by FEMU-UF evolves with iterations towards the force measured in the experiment. However, a very small discrepancy remains between the FEMU-UF force and the experimental force; it is due to the chosen boundary conditions and the DIC calculation uncertainty error. The difference between the FEMU-UF force and the experimental force is the residual force. Its evolution can be seen in Figure 3.22. This residual force is acceptable as it is of the same range order than the error range of the load cell.

In addition, to check whether the calculation converged or not, the root mean square (RMS) of *dp* (parameter increment) (Fig. 3.23) is compared to a convergence criterion value (10^{-3}). When RMS (*dp*) is lower than the specified value, the calculation converges. In the first calculation, it converged at iteration 33. In fact, the parameters were almost constant after the 25^{th} iteration due to the negligible variations; this makes all the iterations after the 25^{th} one unnecessary and time consuming. The second FEMU-UF calculation is similar to the previous calculation (Appendix C). The Young modulus value is close to that of the brass (100 GPa), but the Poisson ratio is quite low and far from the expected value that is 0.33. The reasons of this discrepancy can be found in the very low deformation range associated with the test, and possibly in the crystallographic texture of the brass. Note that the converged Poisson ratio value is affected by the initial guess. The measurement error can be therefore considered as significantly high.

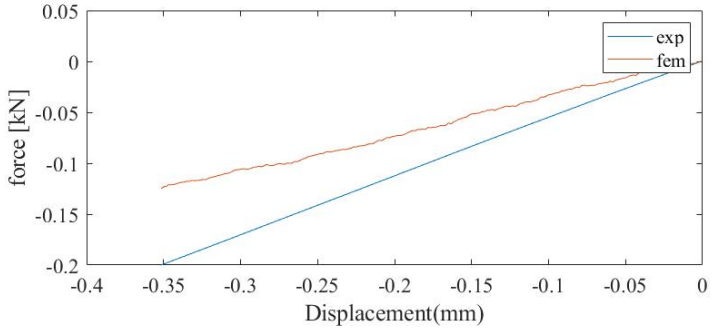

(a) FEMU-UF / Experimental forces at the 3^{rd} iteration of the FEMU-UF calculation

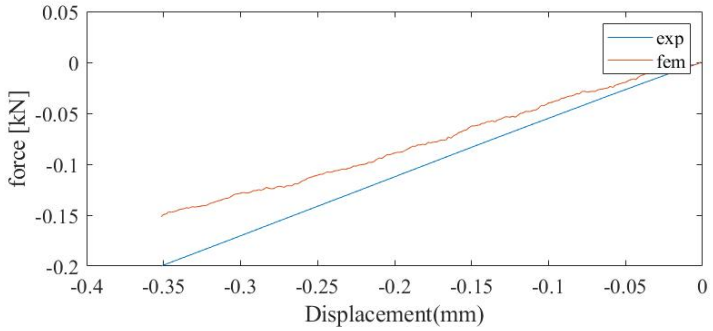

(b) FEMU-UF / Experimental forces at the 5^{th} iteration of the FEMU-UF calculation

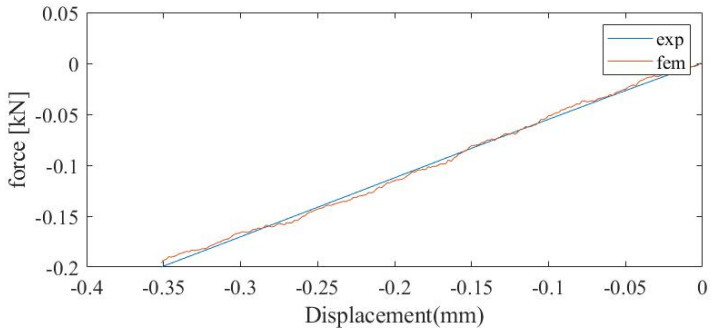

(c) FEMU-UF / Experimental forces at the 20^{th} iteration of the FEMU-UF calculation

Figure 3.21 – Evolution of the FEMU-UF force at contact points at different iterations (initial guess: Poisson ratio 0.4, Young modulus 50 GPa)

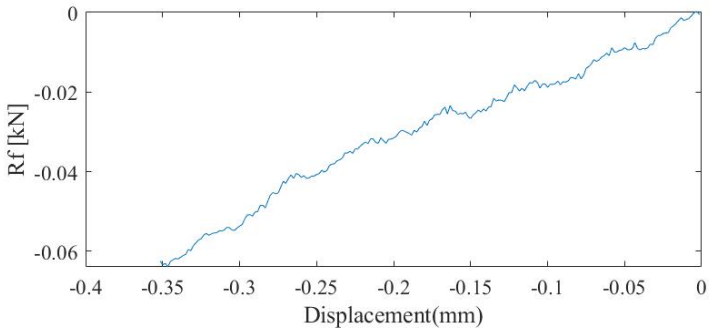

(a) Residual force at the 3^{rd} iteration of the FEMU-UF calculation

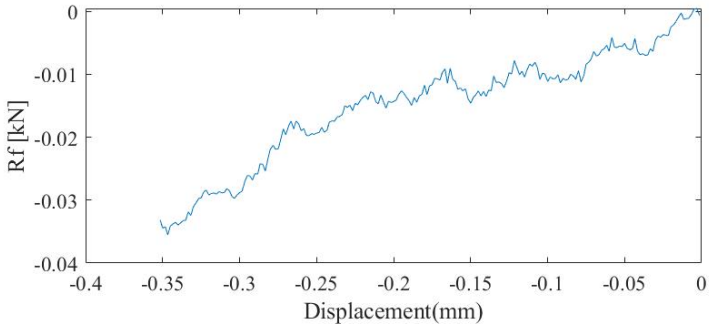

(b) Residual force at the 5^{th} iteration of the FEMU-UF calculation

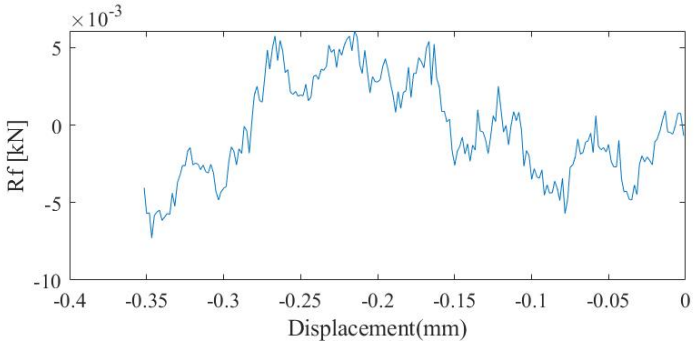

(c) Residual force at 20^{th} iteration of the FEMU-UF calculation

Figure 3.22 – Evolution of residual force with different iterations (initial guess: Poisson ratio 0.4, Young modulus 50 GPa)

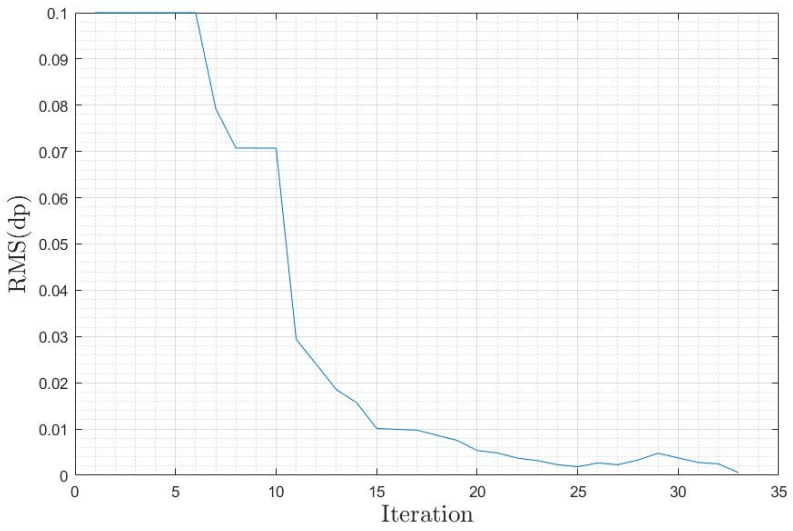

Figure 3.23 – Evolution of RMS (dp) as a function of the iteration number (initial guess: Poisson ratio 0.4, Young modulus 50 GPa)

Brass - REBCO diametric compression

Figure 3.24 – Brass+REBCO sample

Inner Radius	Brass/Brass-REBCO Thikcness	Width	Nb of REBCO turns	REBCO tape thickness
22 mm	3 mm / 6.54 mm	6 mm	40	70 μm

Table 3.7 – Brass-REBCO specifications

After acquiring the mechanical properties of Brass, FEMU-UF can now be used to evaluate the mechanical properties of REBCO (Fig. 3.24) and SS from the diametric compression test (Fig. 3.25). However, additional adjustment to the FEMU code is required to accept the new specimen (Fig. 3.24). Hence, the FEMU calculation must be adjusted to accept two material definitions, where Brass is isotropic and REBCO (respectively SS) is orthotropic.

Since there are two materials, an important aspect rises in the contact between Brass and REBCO. This affects for example the mesh choice. Using a a single mesh covering all Brass-REBCO while considering it as one single material is not valid. Therefore, two mesh options remain, the first option is having perfect contact between Brass and RECBO/SS. That means having one mesh with two element groups, one for each material, and groups have the same nodes at the interface. The second option is to consider a non perfect contact. That means having a different mesh per element groups, one for each material. The two groups have consequently different nodes at the interface.

The chosen contact type here is non-penetration non-perfect contact. This contact takes into account of the possibility of de-bonding at the interface. This contact interface is added to the FEMU code as well. Before FEMU calculation, occurrence of de-bonding at interface has to be verified (Fig. 3.26).

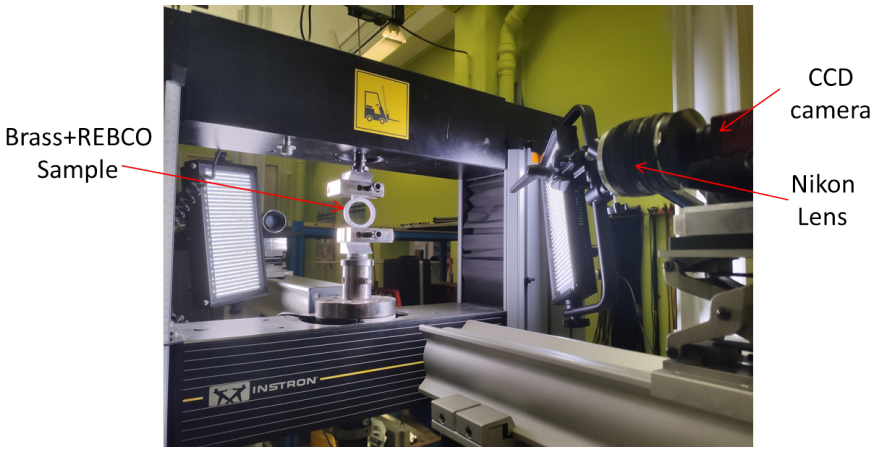

Figure 3.25 – Diametric compression setup of Brass+REBCO

Uncertainty measurement due to image acquisition is done using 27 images taken at initial state. Figs. 3.27a and 3.27b plot the displacement uncertainty map along x and y axes respectively. The mean uncertainty is 0.014 pixel (0.89 μm) along X-direction and 0.018 pixel (1.116 μm) (pixel size: 0.062 mm) along Y-direction. The nodal displacement difference at interface can be considered as significant and representative of de-bonding if the displacement gap is higher than these uncertainties.

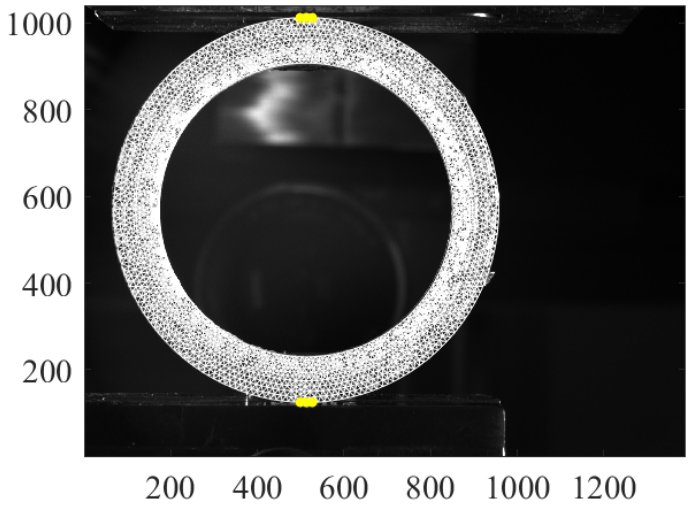

Figure 3.26 – FEMU-UF mesh, contact points (Yellow), element size (8pixel)

Fig. 3.28a plots the values of the de-bonding at the reference state. Values are close to the mean uncertainty measurement indicating that there is no de-bonding. The de-bonding values at the final state are plotted in Fig. 3.28b. They are an order of magnitude higher than values at the reference state. They are also higher than the mean uncertainty measurement. This indicates that indeed de-bonding is occurring at some points at the interface between the two materials. This validates the consideration of non-perfect contact at the interface in the FEMU-UF calculation.

For the material parameter calculation, FEMU-UF with contact interface between brass and REBCO is done. The sample is composed of 40 turns of REBCO wound on the brass mandrel with negligible pre-tension. REBCO is assumed as one-piece material in the FEMU calculation. However, in this calculation, there are two possible cases. The first is having constant brass

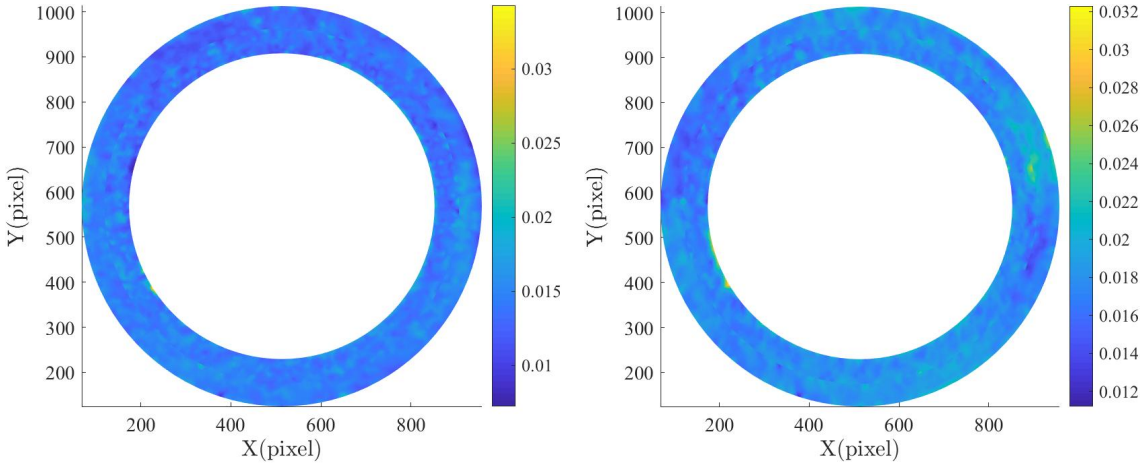

(a) X-Uncertainty (pixels)

(b) Y-Uncertainty (pixels)

Figure 3.27 – Uncertainty measurement

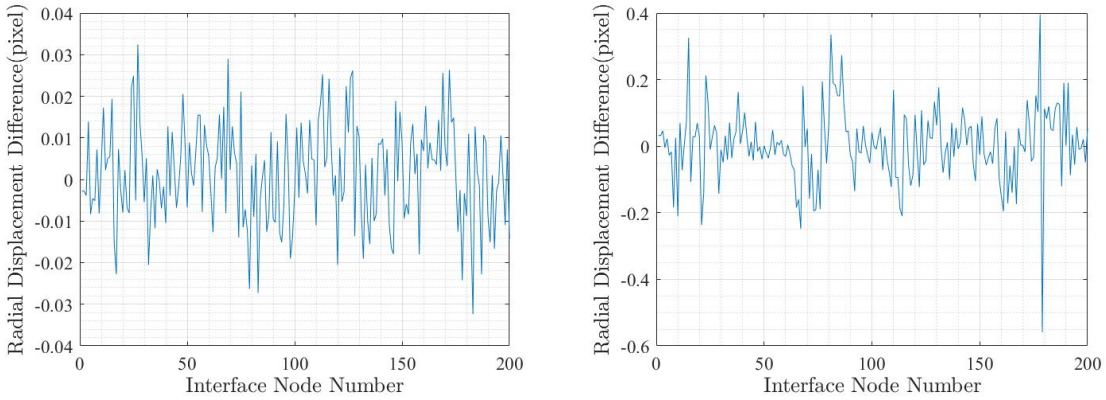

(a) De-bonding value at reference state

(b) De-bonding value at final state/load

Figure 3.28 – De-bonding values at the contact nodes (Nodes 1-200 are clockwise positioned from mid top of circle position, node positions (Appendix D))

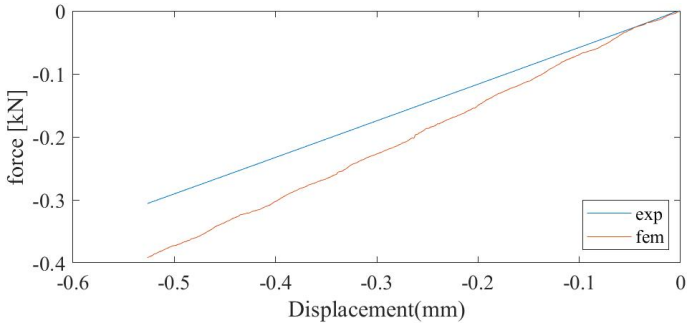

(a) FEMU-UF / Experimental forces at 1^{st} iteration of the FEMU-UF calculation

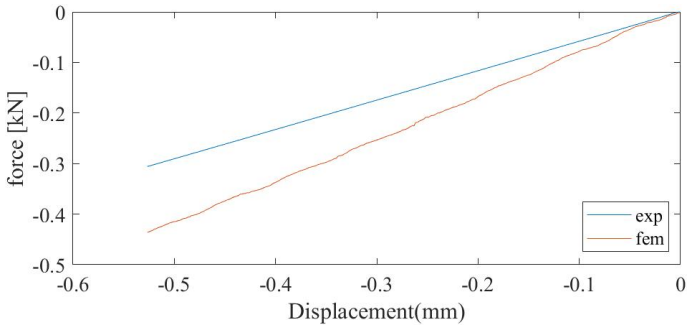

(b) FEMU-UF / Experimental forces at 10^{th} iteration of the FEMU-UF calculation

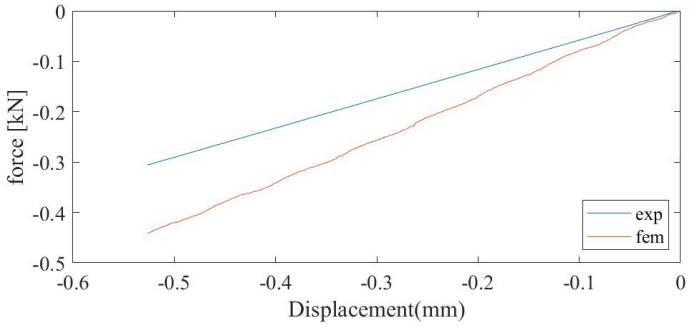

(c) FEMU-UF / Experimental forces at the 20^{th} iteration of the FEMU-UF calculation

Figure 3.29 – Evolution of FEMU-UF force with calculation iteration

properties as that of previous FEMU-UF test. The second case is to consider some possible variation of the brass properties. The case of FEMU-UF with constant brass properties is discussed followed by the other case. FEMU-F for Brass-REBCO and Brass-SS is discussed in Appendix E. The material parameters are:

- for the brass: Young modulus 93.9 GPa and Poisson ratio 0.136
- for the REBCO: radial Young modulus E_r 0.75 GPa, hoop Young modulus E_θ 1.5 GPa, Poisson ratio $\nu_{r\theta}$ 0.3 and shear modulus $G_{r\theta}$ 0.5 GPa.

In a first set of calculations, brass Young modulus an Poisson ratio come from the previous identification (mandrel alone).

Figure 3.29 allows for the comparison of the force calculated by FEMU-UF to the experimental force vs displacement at three different iterations. Unlike the test on a mandrel alone, a clear difference between the experimental and FE forces indicates that convergence was not achieved in the FEMU-UF calculation. The evolution of the parameter increment's RMS (dp) (Fig. 3.30) confirms this tendency, RMS(dp) saturates at 0.04. RMS is a unit-less value that gives an insight on the average change occurring to the parameters, since (dp) is an increment factor of the

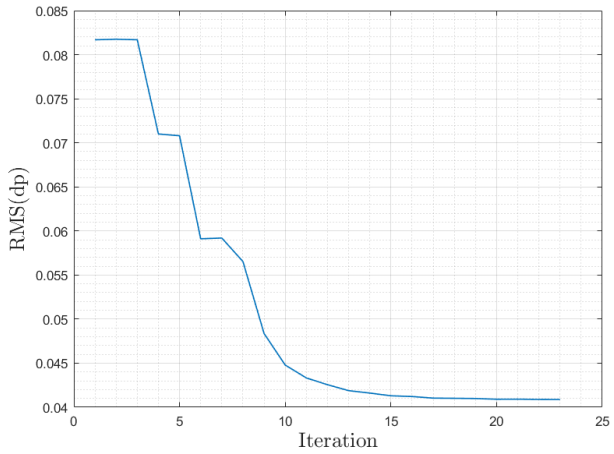

Figure 3.30 – Evolution of RMS(dp) as function of iteration

parameters. Thus, RMS maintaining a value of 0.04 indicates that the increments applied to the properties are not negligible.

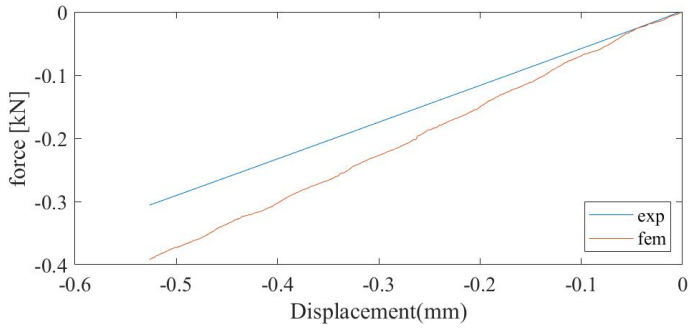

(a) FEMU-UF / Experimental forces at the 1^{st} iteration of the FEMU-UF calculation

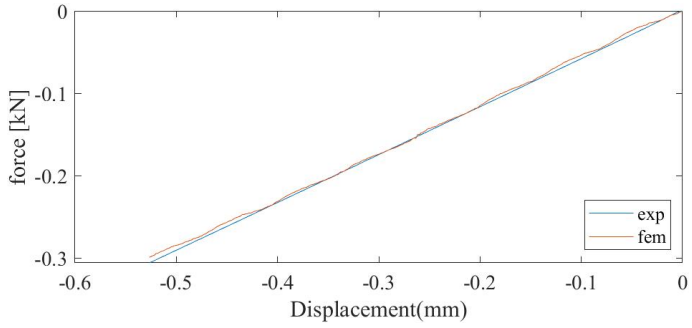

(b) FEMU-UF / Experimental forces at the 10^{th} iteration of the FEMU-UF calculation

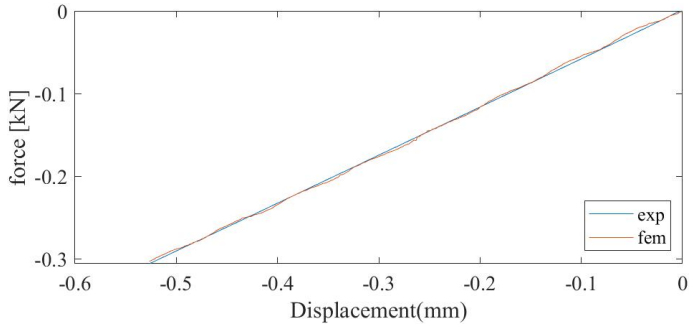

(c) FEMU-UF / Experimental forces at the 23^{rd} iteration of the FEMU-UF calculation

Figure 3.31 – Evolution of FEMU-UF force with calculation iteration - diametric compression of mandrel + REBCO - considering free brass elastic constants

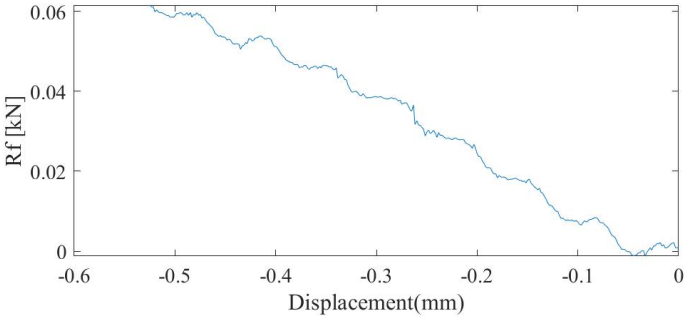

(a) FEMU-UF / Experimental forces at the 1^{st} iteration of the FEMU-UF calculation

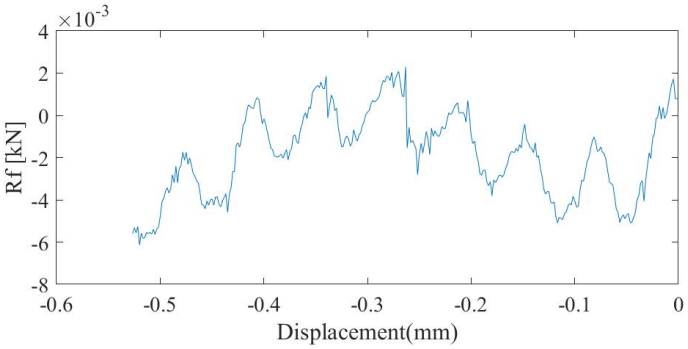

(b) FEMU-UF / Experimental forces at the 10^{th} iteration of the FEMU-UF calculation

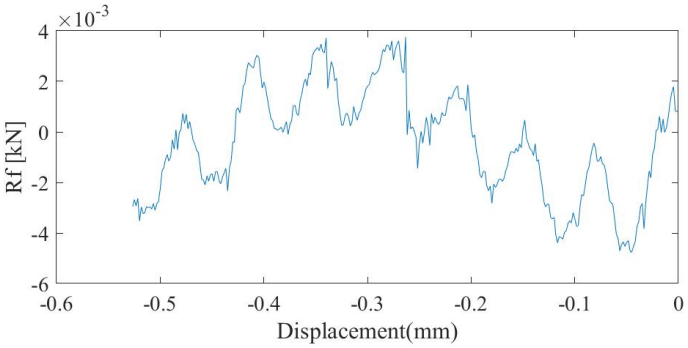

(c) Residual Force at the 23^{rd} iteration of the FEMU-UF calculation

Figure 3.32 – Evolution of the residual force at different iterations - diametric compression of mandrel + REBCO - considering free brass elastic constants

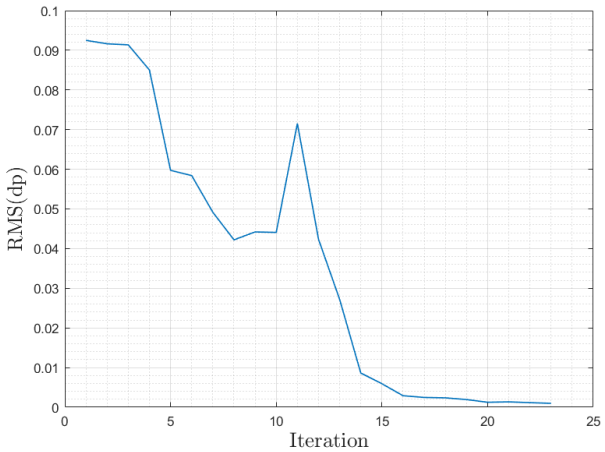

Figure 3.33 – Evolution of RMS(dp) as a function of the iteration number

A second FEMU-UF calculation case has been considered. The results in Fig. 3.31 show

that convergence was reached at the 23^{rd} iteration. In addition, the residual force (Fig. 3.32) achieved is very good as it is within the load cell error's limit. The evolution of RMS (dp) further shows that the convergence criterion is met (RMS (dp) $< 10^{-3}$) (Fig. 3.33). The final set of elastic parameters are the following:

For brass mandrel, the Young modulus decreases from 100 GPa to 60 GPa, and the Poisson ratio stays at 0.15. The too high Young modulus employed for the previous FEMU-UF test probably explains the non-convergence. 60 GPa is however too low to correspond to an intrinsic Young modulus of brass. It is probable that the diametric compression test was accompanied by micro-plasticity. We could indeed see during tensile tests that the yield stress of this material is poorly defined. Crossing the plastic threshold could explain a weaker apparent Young's modulus than expected.

For REBCO winding, the following stiffness constants have been obtained:

- radial Young modulus: 1680 MPa,
- hoop Young modulus 2070 MPa,
- Poisson ratio 0.27,
- shear modulus 2200 MPa.

In order to analyze the significance of these values, it is possible to compare the hoop Young modulus with the Young modulus measured during the tensile tests. Both should match.

We found in previous sections a Young modulus of 150 GPa, approximately 70 times higher than the Young modulus evaluated from the diametric compression test. The Poisson's ratio difference is insignificant. The radial Young modulus and the shear modulus are of the same order of magnitude as the hoop modulus which is consistent. The fact that the radial modulus is lower than that of the hoop modulus is correct. The observed values are however much lower than expected.

The reason for these low values can be found in the imperfect contact between the turns. This leads to a much lower structural stiffness than expected. This point will be addressed more precisely in Section 3.7.

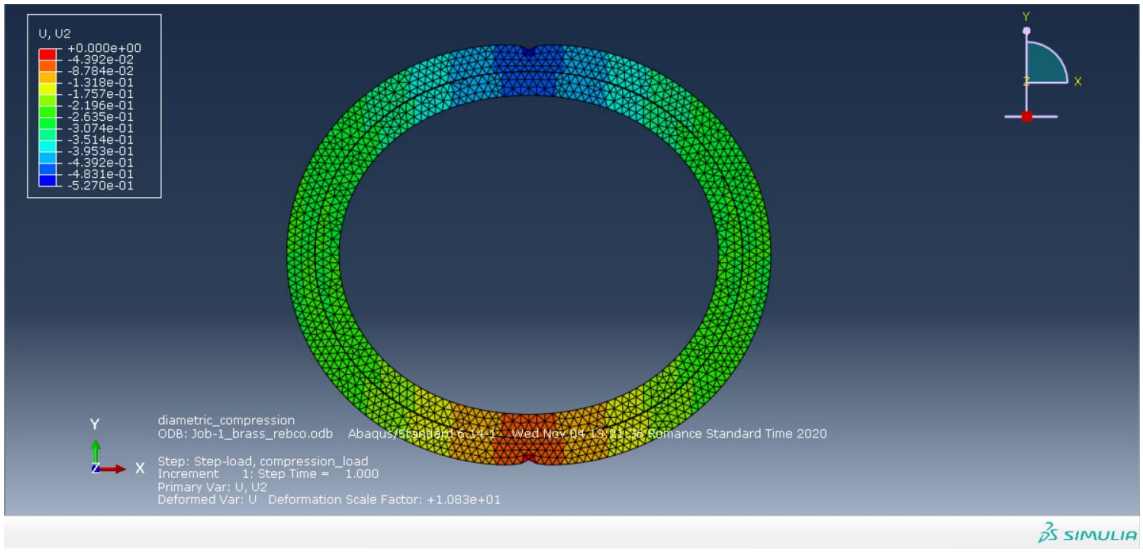

Figure 3.34 – Abaqus model of Brass+REBCO sample in diametric compression (vertical displacement, meters)

A second strategy was employed to obtain a new evaluation of the REBCO elastic constants. A simple model of the sample was done in Abaqus 6.14, and the mechanical properties of REBCO tape were changed iteratively to reach a close vertical displacement to the displacement measured during the experiment. In this model, the contact interface was implemented between Brass and REBCO, keeping the REBCO considered as a one-piece body and not composed of several turns (Fig. 3.34).

This strategy did not make it possible to obtain higher stiffness values. We obtain: radial modulus 1 GPa, hoop modulus 1.5 GPa, Poisson ratio 0.3, and shear modulus 0.55 GPa. Again, these values are much lower than the reference values. This simulation shows however that the values optimized by the FEMU-UF are consistent with the measurements.

Brass-SS Diametric Compression

Inner Radius	Brass/Brass-SS Thikcness	Width	Nb of SS turns	SS tape thickness
22 mm	3 mm / 6.25 mm	6 mm	100	29 μm

Table 3.8 – Brass-SS specifications

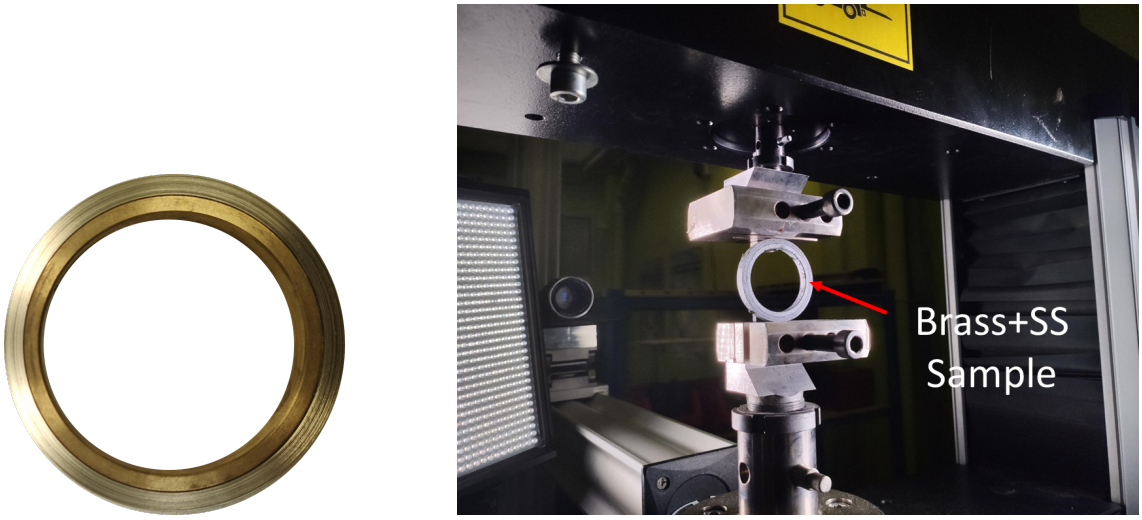

(a) Brass + SS sample

(b) Diametric compression setup of Brass + SS

Figure 3.35 – Brass+SS diametric compression

The same "pancake" was prepared for the identification of SS elastic properties (Fig. 3.35a) by using a diametric compression test (Fig. 3.35b). The procedure used for FEMU-UF calculation is the same as in Brass-REBCO situation. SS is assumed to be orthotropic like REBCO. Sample is composed of 100 turns of SS wound with negligible pretension on the brass mandrel. SS is assumed as one piece material in the FEMU calculation. As for Brass-REBCO pancake, a first set of identification has been made using standard brass elastic properties. The results in Figs. 3.36 and 3.37 show that the calculation didn't converge as for the Brass-REBCO case. The constant RMS value of 0.04 indicates constant non-negligible changes of the mechanical properties.

Brass constants were not considered as fixed for the second set of identification. The results in Fig. 3.38 show that the FEM forces are in accordance with the experimental one and converged at iteration 64. Also, the residual forces (Fig. 3.39) and the evolution of RMS (dp) (Fig. 3.40)

indicate a convergence of results at iteration 64. Like for REBCO, the stiffness constants of SS at convergence are much lower than expected. They are as follow:

- radial Young modulus: 1.2 GPa,
- hoop Young modulus: 0.85 GPa
- Poisson ratio: 0.35
- shear modulus 0.5 GPa

Similarly, as in Brass-REBCO, a simple model of Brass-SS sample was built in Abaqus 6.14. SS mechanical properties were changed iteratively to reach a vertical displacement close to the vertical displacement measured during the experiment. The contact interface was implemented as well in the model, and SS was assumed as a one-piece body (Fig. 3.41).

This simulation gives results very close to those obtained thanks to the FEMU-UF. This demonstrates the relevance of the tool but does not explain the low estimated values. Here again, we can assume a non-negligible influence of an imperfect winding on the estimation of the quantities. This point is discussed in Section 3.7.

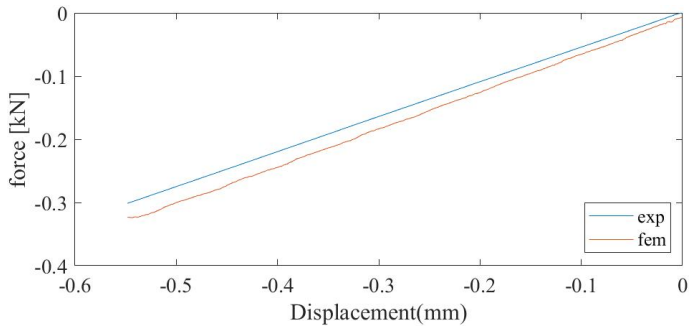

(a) FEMU-UF / Experimental forces at the 1^{st} iteration of FEMU-UF calculation

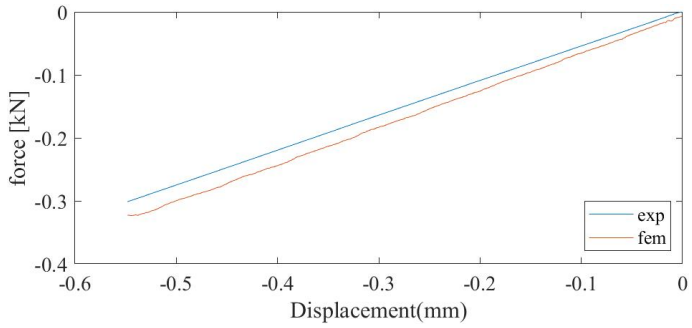

(b) FEMU-UF / Experimental forces at the 10^{th} iteration of the FEMU-UF calculation

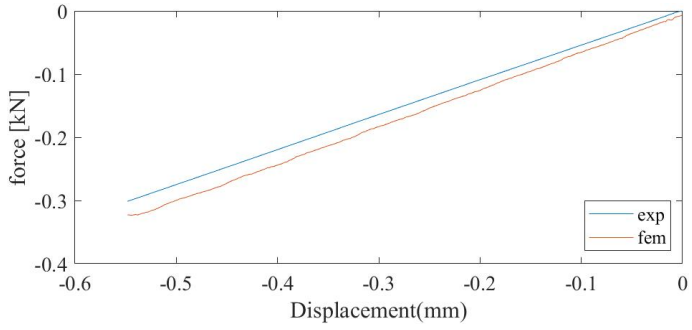

(c) FEMU-UF / Experimental forces at the 21^{st} iteration of the FEMU-UF calculation

Figure 3.36 – Evolution of the FEMU-UF force at different iterations - diametric compression of mandrel + SS - considering previously identified brass elastic constants

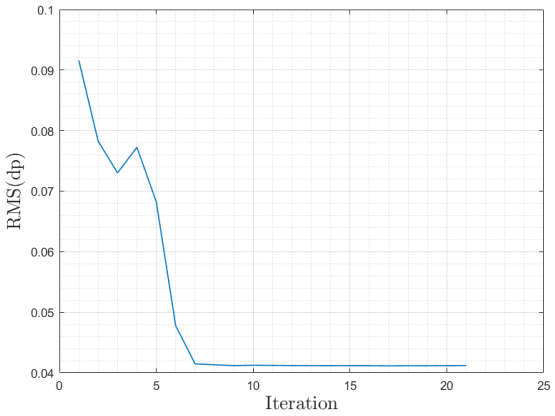

Figure 3.37 – Evolution of RMS(dp) as a function of the iteration number - diametric compression of mandrel + SS - considering previously identified brass elastic constants

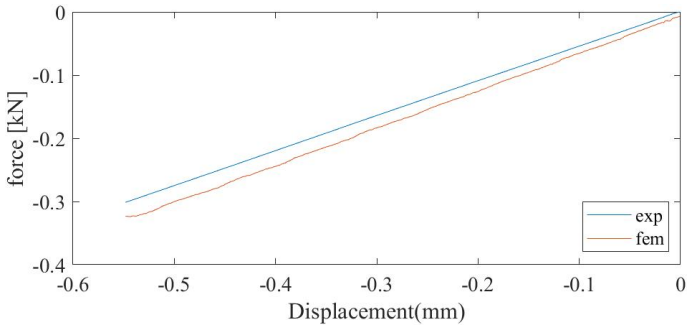

(a) FEMU-UF / Experimental forces at the 1^{st} iteration of the FEMU-UF calculation

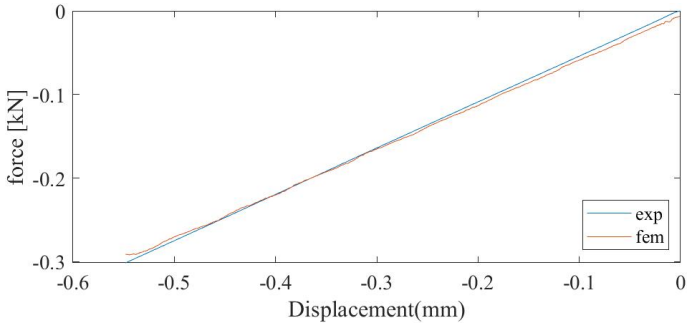

(b) FEMU-UF / Experimental forces at the 30^{th} iteration of the FEMU-UF calculation

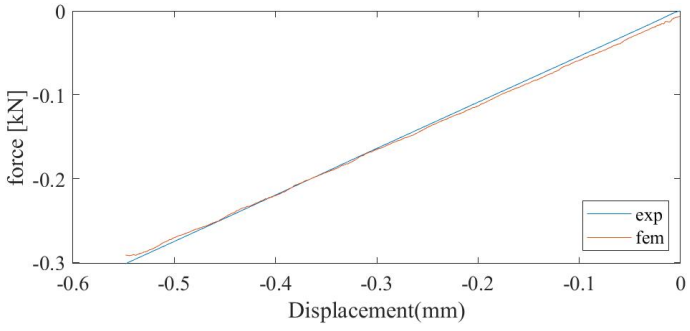

(c) FEMU-UF / Experimental forces at the 64^{th} iteration of the FEMU-UF calculation

Figure 3.38 – Evolution of the FEMU-UF force at different iterations - diametric compression of mandrel + SS - considering free brass elastic constants

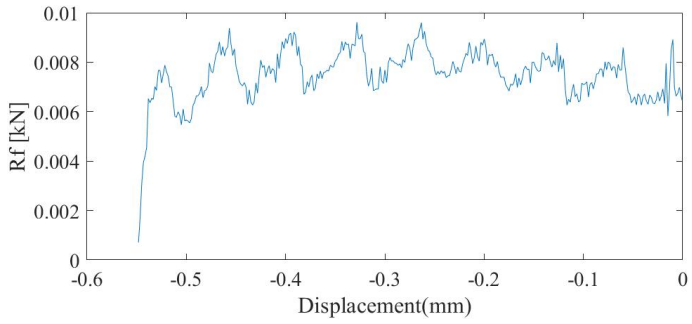

(a) Residual force at the 1^{st} iteration of the FEMU-UF calculation

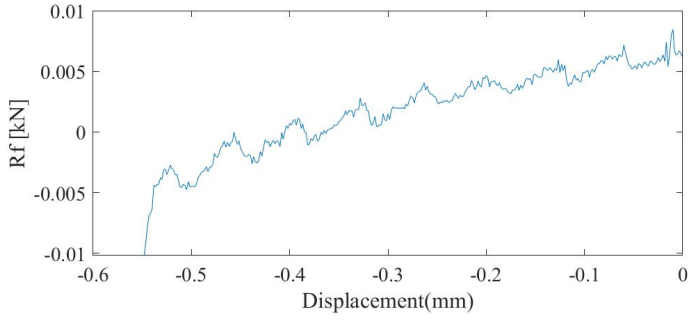

(b) Residual force at the 30^{th} iteration of the FEMU-UF calculation

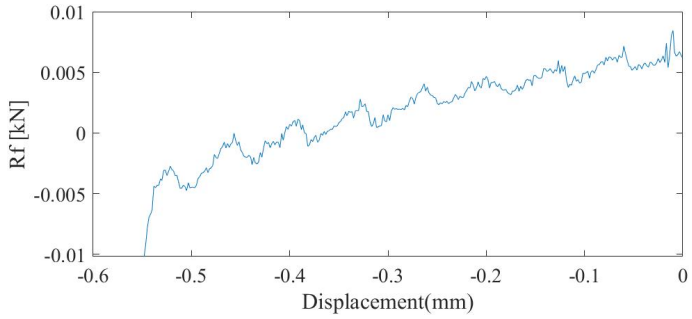

(c) Residual force at the 64^{th} iteration of the FEMU-UF calculation

Figure 3.39 – Evolution of the Residual Force at different iterations - diametric compression of mandrel + SS - considering free brass elastic constants

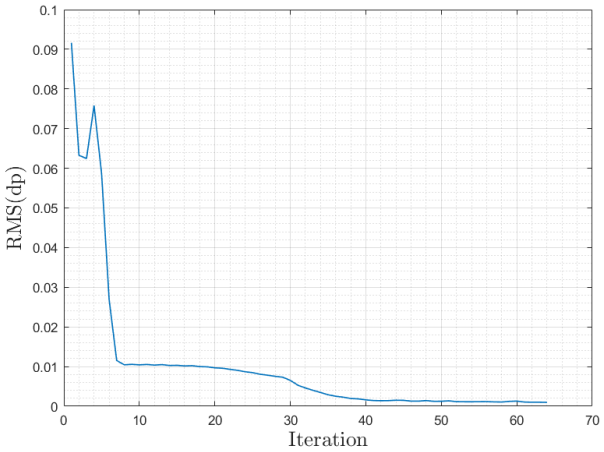

Figure 3.40 – Evolution of RMS(dp) as function of iteration - diametric compression of mandrel + SS - considering free brass elastic constants

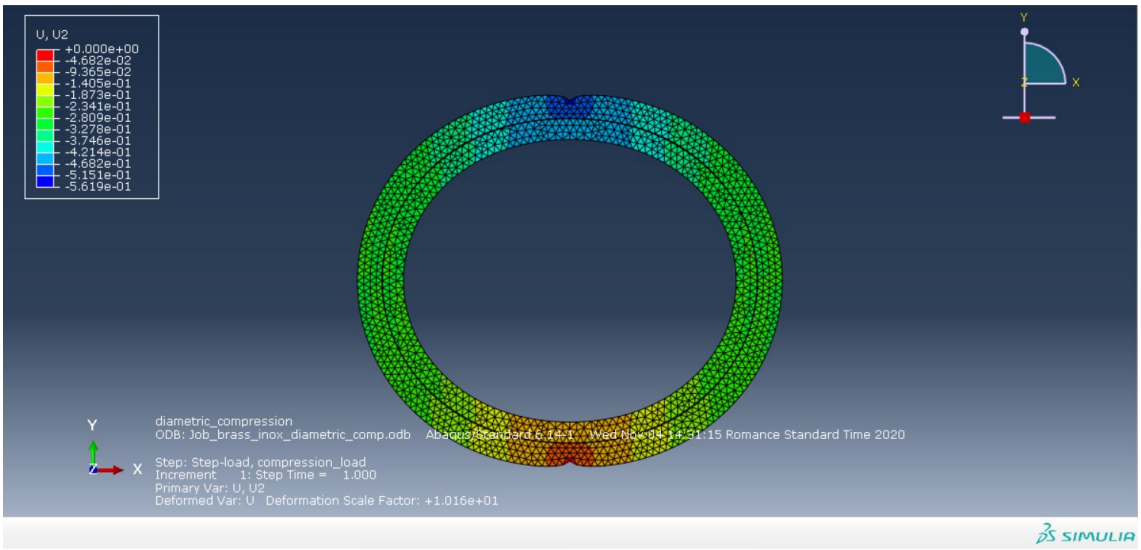

Figure 3.41 – Abaqus model of Brass+SS sample in diametric compression (vertical displacement, meters)

Both diametric compression tests showed much lower results than expected. This indicates the importance of winding on the mechanical integrity of the pancake. Also, both tested pancakes were wound with negligible pre-tension to avoid any effect of a pre-tension. Thus, different pancakes with different pre-tensions can be tested to observe the effect of pre-tension on the measured mechanical properties.

3.7 . Winding effect

The fact that both FEMU calculations gave very low values of the material properties compared to reference and tensile test values in Brass-REBCO and Brass-SS indicate that there are several aspects affecting the results. For the FEMU calculation, REBCO and SS were assumed to be one-piece materials, whereas in reality they are composed of many turns wound above each other. The contact between each two consecutive turns, is probably not perfect affecting the deformation and macro (bulk) mechanical properties.

The turns have a surface roughness, and the contact occurring between them is at the peaks of these roughness resulting in gaps. Hence, during the winding of the samples, gap formation between turns can occur as negligible pretension was used to avoid its effects on the mechanical properties [119]. Moreover, dust can be deposited on the tapes from the surrounding environment during winding. Dust may act as a gap altering the mechanical properties. Consequently, winding process and pretension have probably a great impact on the mechanical properties of the structure, and consequently on apparent mechanical properties of tapes.

The study of the mechanical behavior of a winding has been the subject of several works [118, 122, 140]. It is observed that the bulk radial modulus of wound material is variable. It depends on several parameters like radial stress, surface roughness, friction between turns, surface flatness, surface interpenetration, number of turns, etc.. Being dependent on the radial stress, the radial modulus is variable within the complete wound piece itself. Figure 3.42 shows that the radial modulus is in fact dependent on the number of layers and the applied pressure (radial stress).

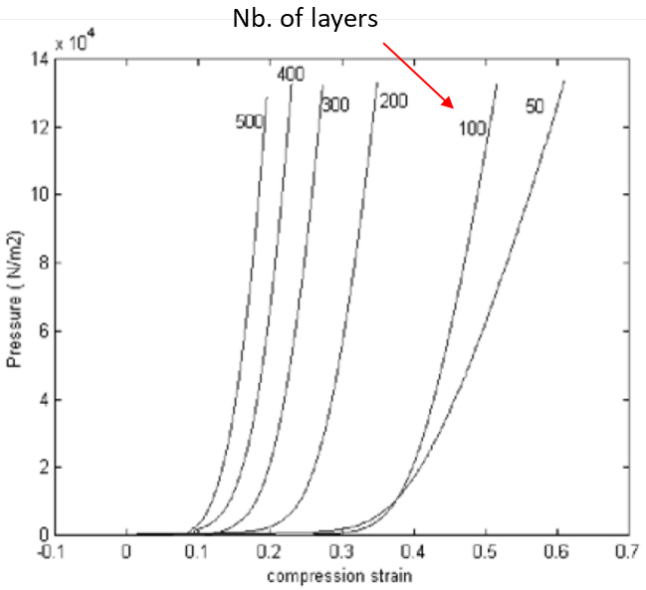

Figure 3.42 – Newsprint Stacks (70 μm thickness of layer) being compressed [140]

Several formulas allow an estimation of radial Young modulus depending on the radial deformation or stress. One of them is the Pfeiffer equation (Eq. (3.15)) and the other is the Hakiel equation (Eq. (3.16)).

$$E_R = K_1 K_2 e^{K_2 \epsilon_R} \tag{3.15}$$

$$E_R = k_1 + k_2 \sigma_R + k_3 \sigma_R^2 \tag{3.16}$$

A more detailed approach was proposed by Weisz-Patrault [118] regarding winding. He considered in his article the surface roughness, contact, and non flatness of tape during the winding process while using bulk moduli of the material. Using a semi-analytical modeling, each infinitesimal tape was added to the roll allowing an estimation of radial stress and displacement. Such approach is implemented in software like Abaqus to model the winding process. It cannot be used to evaluate the stiffness constants.

REBCO and SS tapes are quite thin, being several micrometers in thickness, causing the Poisson ratio's effect of edge curving [133]. Wang [133] showed that depending on several parameters, like bending radius, pre-tension, and tape thickness, there are three type of contacts at interface: the single line contact, the double line contact, and the surface contact. The single and double line contacts significantly limit the contact in comparison to the surface contact affecting the bulk radial modulus. In addition, the edge curving still occurs during the surface contact. Edge curving higher than 1.5mm width was sometimes observed for REBCO and SS windings. This irregular contact may affect the bulk mechanical properties identification from diametric compression tests.

Furthermore, it is possible to propose an analytical calculation to observe the effect of gap inside the winding of REBCO on the mechanical properties of the winding as a whole body. In "Brass + REBCO" case, it is clear that there are gaps present in the winding from the values present in Table 3.7; where thickness of REBCO winding (40 turns $\times$ 70 μm) and brass mandrel (3 mm) is less than thickness of the whole sample (6.54 mm). The total gap thickness in the winding can be estimated to : $6.54 - 5.8 = 0.74mm$. The REBCO winding infinitesimal section is modeled as in Fig. 3.43 for the analytic homogenization calculation, using same procedure as in Appendix F. REBCO and gap are assumed as two layers with isotropic

Figure 3.43 – REBCO winding with gap scheme (blue lines indicate the gap between turns)

properties for calculation simplicity (Table 3.9), since the aim is to check the effect of the gap on the properties of the winding. The gap in the calculation is assumed to have a Poisson ratio of 0.29 and a variable young modulus ranging from 0.1 GPa to 5 GPa with a step of 0.05 GPa, to check the gap's Young modulus effect on the homogenized modulus.

From the Figures 3.44a and 3.44b, it is clear that the gap affects the radial modulus significantly, while effect on hoop modulus is negligible. The lower value of homogenized hoop modulus than that of REBCO tape is due to the gap thickness. From Fig. 3.44a, the required equivalent gap modulus of air to obtain a similar value to that of FEMU-UF results of "Brass+REBCO" is estimated to be 0.15 GPa. This value is quite low as expected but not null, confirming the relevancy of the hypothesis of a significant role of air-gap during the experiment. The same effect of the gap is present in "Brass + SS" case as seen in the Figures 3.45a and 3.45b where gap size is 0.35 mm. From Fig. 3.45a, the required equivalent gap modulus of air to obtain a similar value to that of FEMU-UF results of "Brass+SS" is estimated to be 0.1 GPa. It is interesting to observe a consistency between this modulus and modulus identified in "Brass+REBCO" situation.

These results show that the hoop modulus is slightly affected by the gap thickness, while the effect of gap on the radial modulus on the winding is quite clear. This emphasizes the effect of winding and pre-tensioning, and the variability of radial modulus of the winding. In addition, the assumption of the gap being a layer as REBCO or SS at an infinitesimal section, i.e. concentric layers, does not yield the same results of hoop modulus as that reached by FEMU-UF for both samples. This point remains questionable.

	REBCO	SS
Young Modulus (GPa)	153	163
Poisson ratio	0.3	0.29

Table 3.9 – REBCO/ SS properties for the analytic homogenization calculation

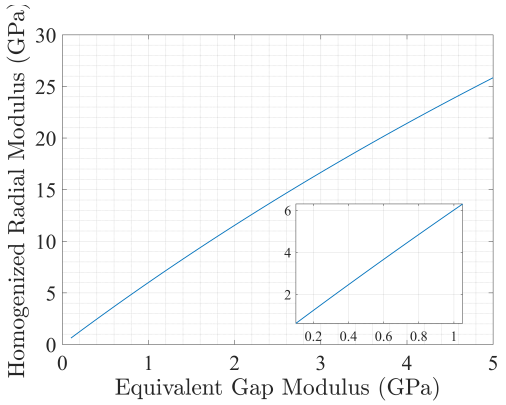

(a) REBCO winding radial modulus variation as function of the gap's Young modulus

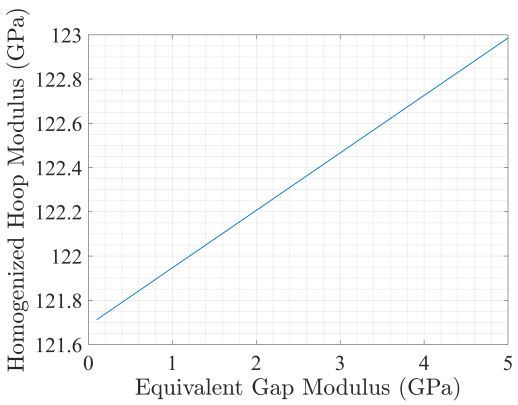

(b) REBCO winding hoop modulus variation as function of the gap's Young modulus

Figure 3.44 – The gap's effect on the homogenized properties of the winding in Brass+REBCO sample

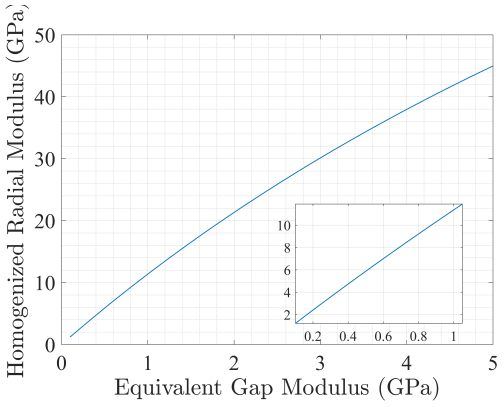

(a) SS winding radial modulus variation as function of the gap's Young modulus

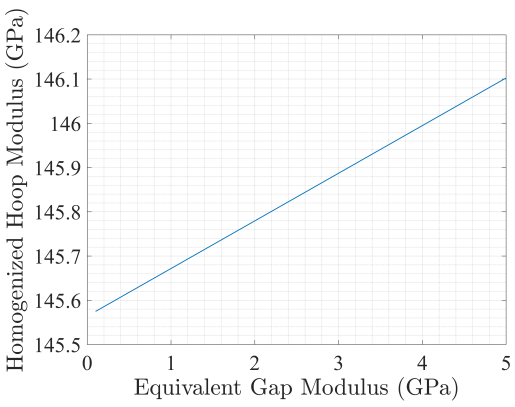

(b) SS winding hoop modulus variation as function of the gap's Young modulus

Figure 3.45 – The gap's effect on the homogenized properties of the winding in Brass+SS sample

3.8 . Radial Stress calculation of Nougat across various Young modulus

Analytical calculation is applied for "Nougat" benchmark at 30 T as in chapter 2 to observe the effect of the variation of Young modulus on the total radial stress. Two scenarios are considered in the calculation: the first is that the mandrel remains in contact with the rest of the pancake; the second is that the mandrel separates from the pancake by giving the mandrel a very small radial Young modulus of about 50 MPa. In each scenario, three cases were considered: 1/ variable Young modulus of SS that is considered isotropic, 2/ variable hoop Young modulus of REBCO with radial modulus being half of the hoop's one, 3/ is the previous two cases combined but with having hoop modulus of REBCO same as that of SS.

The Young modulus is varied from 100 to 300 GPa with a 1 GPa step in this study. For the fixed material, its properties are from Nougat calculation in chapter 2.

Fig. 3.46 shows that disregarding the Young modulus, even at 300 GPa for both REBCO and SS as in Fig. 3.46c, the total radial stress remains positive (tensile) in major part of the central pancake of Nougat. Considering mandrel separation, Fig. 3.47 shows that disregarding the Young modulus, the total radial stress is positive inside the pancake. Thus, this study shows that stiffer metal-as-insulation or REBCO tape does not result in obtaining a compressive radial stress over all the pancake. This further emphasizes the importance of pre-tension and over-banding that was observed in chapter 2 regarding the creation of compressive radial stress in the whole pancake. However, this does not mean that stiffer metal-as-insulation is not a good mechanical support, since it can lower the hoop stress supported by REBCO tape to the range of acceptable stress by REBCO tape.

3.9 . Conclusion

In conclusion, the tensile tests showed that the experimental results of the hoop Young modulus and Poisson ratio of the REBCO tape are in accordance with the theoretical results and the reference [128]. However,a value of 162GPa was obtained for the hoop Young modulus of Durnomag stainless steel. It is 15 $\%$ lower than that of the reference [126]. The experimental Poisson ratio is on the contrary in accordance with a value of 0.29. The DIC use for deformation measurement in tensile testing was relevant to get rid of the Poisson curving effect in foil materials like REBCO and SS tapes. The plexiglass sandwiching technique proved its

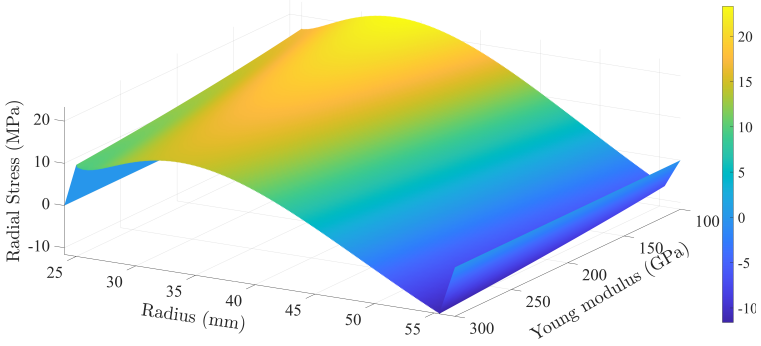

(a) Study of total radial stress as a function of SS Young modulus

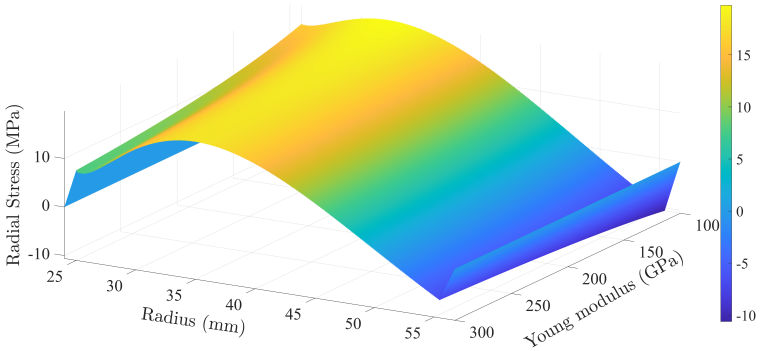

(b) Study of total radial stress as a function of REBCO hoop Young modulus

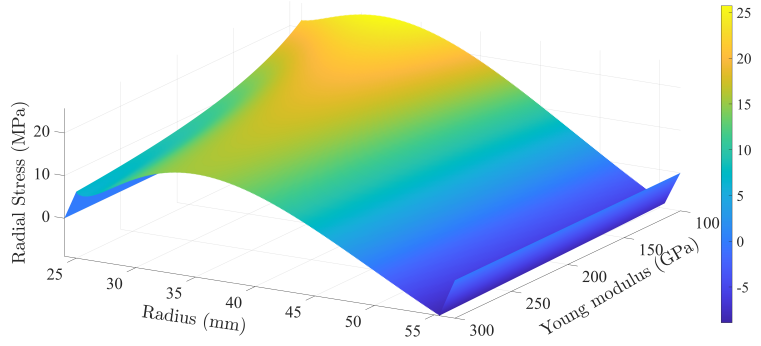

(c) Study of total radial stress as a function of REBCO hoop Young modulus and SS Young modulus

Figure 3.46 – Study of total radial stress as a function of Young modulus while maintaining mandrel contact with the adjacent turns

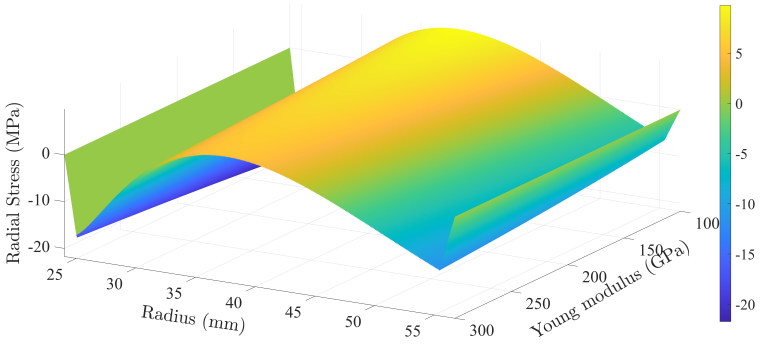

(a) Study of total radial stress as a function of SS Young modulus

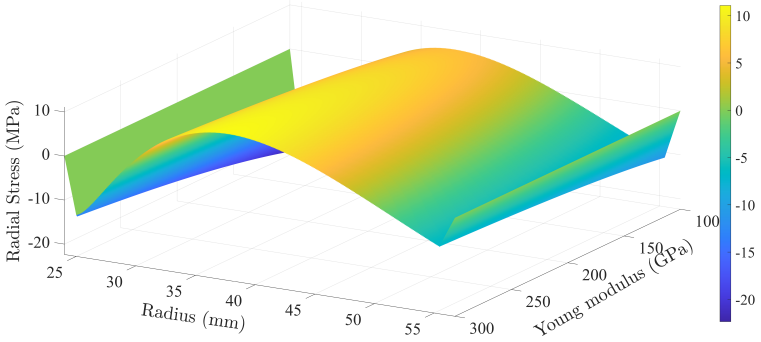

(b) Study of total radial stress as a function of REBCO hoop Young modulus

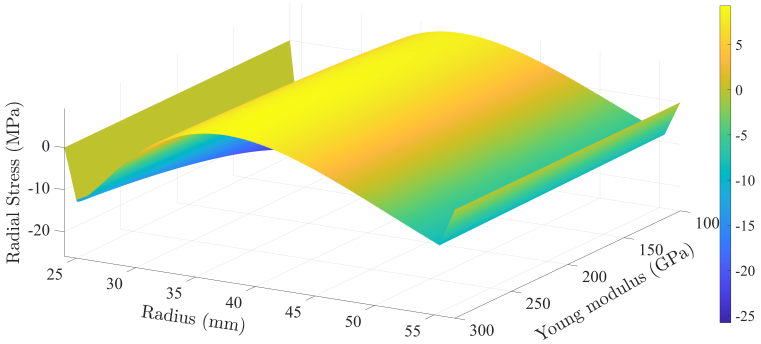

(c) Study of total radial stress as a function of REBCO hoop Young modulus and SS Young modulus

Figure 3.47 – Study of total radial stress as a function of Young modulus while mandrel is separated from the adjacent turns

functionality.

Furthermore, the diametric compression test and FEMU calculation did not yield the expected properties of REBCO or SS. The test highlighted the importance of winding and its effect, but at the same time it showed that it is not suitable for evaluation of the material properties. The brass mandrel was tested initially to implement its parameters in the FEMU calculation for REBCO and SS. The diametric compression test of the brass mandrel, assumed isotropic, showed results in accordance with the reference values regarding the Young modulus [135]. However, the radial moduli results of REBCO and SS from both diametric compression tests of "Brass+REBCO" and "Brass+SS" were much lower than that of the reference values. Similar values were achieved when an Abaqus 6.14 model of the samples was tested using the boundary conditions of the experiments. This showed that the winding process had an effect on the apparent radial modulus.

Several studies showed that the winding process affects the bulk radial modulus, and that the modulus is variable depending on several parameters. Moreover, as REBCO and SS are foil materials, i.e. being several micrometer thick, the Poisson curving effect also affects the bulk radial modulus, since it affects the contact between the wound turns.

Following these material parameter evaluation tests, a study was proposed to observe the effect of Young modulus of REBCO and SS on the total radial stress. As explained in Section 3.8, their contribution to the total compressive radial stress in the MI pancake is insignificant in comparison to the pre-tension and over-banding. Pre-tension and over-banding are essential to maintain contact through-out the MI pancake is important to preserve the quench "current by-passing".

Finally, the objective of this chapter that was to get more relevant stiffness values of materials, was only partially achieved. We have decided to choose the following set ov values for the rest of the dimensioning calculations. The radial Young modulus will be considered as to be half of the bulk radial Young modulus for REBCO and SS. This choice is motivated by our willing to take into account the effect of winding and Poisson curving that reduced (by a factor 2) the contact surface.

4 - Displacement Measurements by Digital Image Correlation on HTS Coil Prototype

4.1 . Introduction

From the mechanical testing campaign in chapter 3, it was observed that winding affects the pancake's mechanical behavior. In addition, the analytical formulations used for stress calculation rely on several assumptions as discussed in chapter 2. These include plane stress calculation, concentric cylinder, zero shear stress, etc..

With the results of the Nougat magnet [51] stress calculation that showed positive radial stress in chapter 2, it is important to monitor the MI pancake mechanical state through displacement or deformation measurements. Hence, an experimental setup has been developed to allow for a real time measurement of what happens to an MI pancake during the cooling and energizing phases. If strain gauges are used, measurements are local, limited, and unable to cover the intermediary turns. Similarly, optical fibers for strain measurement require adhering them to surface of the pancake which will compromise the results. However, in this experiment, the aim is to measure the whole field displacement occurring in the MI pancake. Hence, using digital image correlation (DIC, defined in chapter 3), full field displacement measurement is possible for the whole MI pancake by applying a speckle.

Thus, the experimental setup design is covered at first. Then, the cooling experiment procedure, and temperature and image acquisitions are described. Finally, results of the cooling with liquid nitrogen tests of stainless steel 304 disc and a pancake made of copper beryllium co-wound with stainless steel 304 (SS304) and SS304 over-banding are analyzed. SS304 disc test has been implemented to check the different operation steps.

4.2 . Experimental setup design and assembly

Cooling and energizing tests are done using liquid nitrogen and helium respectively. While liquid nitrogen cooling can be done in any cryostat because of its high latent heat, liquid helium cooling requires minimization of heat load to decrease its consumption due to its low latent heat. Hence, a cryostat (Table 4.1 and Fig. 4.1) with vacuum shield and nitrogen bath shield is used for the tests. Both shields decrease radiation heat load on the cryostat.

Using DIC for displacement measurement in cooling and energizing conditions requires pancake image acquisition during the test. Image acquisition along with the energizing test lead to several requirements in the setup design. They include image view path, pancake position, pancake support, cooling method, and thermal shielding.

Regarding the image view path, a camera and a white LED pointer are positioned outside the cryostat to respect their operating temperature ranges. Therefore, a clear path between the pancake and the camera and LED pointer is necessary while the pancake and the camera are placed parallel to achieve proper DIC results (Fig. 4.2b). Hence, two optical windows are mounted on the cryostat flange for the camera and the LED pointer respectively (Fig. 4.2a).

Conduction cooling is chosen since clear view of pancake is required for DIC. Therefore, the

Design Parameters	Value
Cryostat	
Bore Diameter (mm)	300
Length (mm)	1300
Current Lead (maximum current in A)	400
Aluminum Heat Shields (Quantity)	5
Sample Support - Brass Disc 70/30 (Quantity)	1
Tinned Copper Thermal Braids (Quantity)	24
Optical Windows (fused silica, single walled) (Quantity)	2

Table 4.1 – Main information concerning the experimental set-up designed for in-situ DIC measurement during cooling and energizing

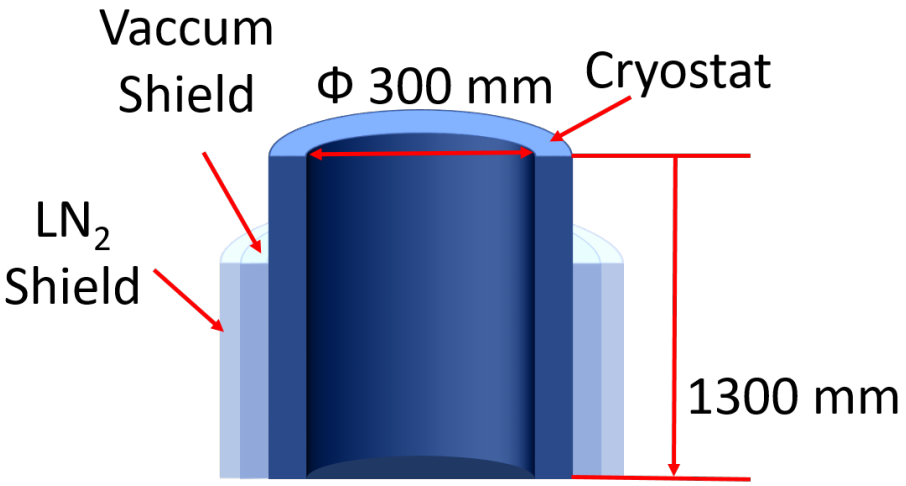

Figure 4.1 – Cryostat cross-section sketch

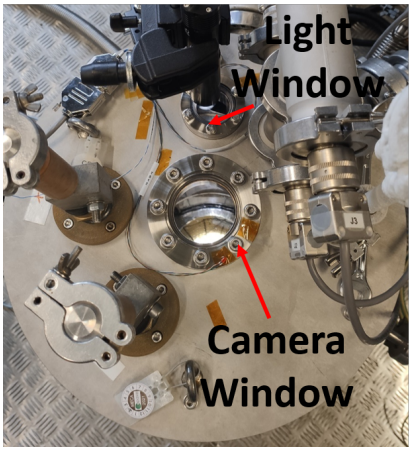

(a) Optical Windows on Cryostat flange

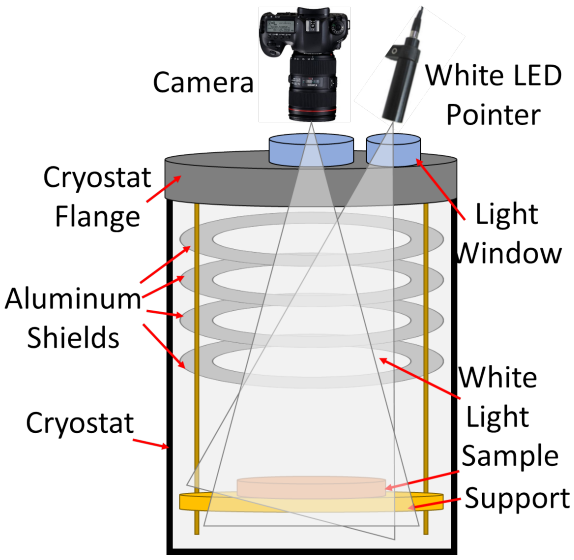

(b) Camera and Light path

Figure 4.2 – Optical windows configuration for pancake viewing

Set-up card-board Prototype Test	
Optical Windows	
Camera Window View / Outer Diameter (mm)	70.4/114
Light Window View / Outer Diameter (mm)	40/70
Image Acquisition	
Camera	Canon EOS 70D
LED Pointer	Effilux LED pointer
Telescopic Lens	Sigma Telephoto 105mm
Tele-converter lens	Sigma 2x
Mock Pancake	
Inner / Outer Diameter (mm)	107/162

Table 4.2 – Set-up card-board prototype test specification

pancake support is chosen to be thermally conductive to cool the pancake. Also, the support should have good electrical resistance to limit eddy currents generated in it during energizing. Thus, limiting its Joule effect and its generated heat. Eddy currents are generated during magnetic flux variation according to Faraday's law. Hence, Brass 70/30 support is chosen with grooves being applied to it to further limit eddy currents.

For conduction cooling, tinned copper thermal braids are used (Table 4.1). The braids are immersed in the cooling bath, which is positioned at the bottom of the cryostat, while being connected to the brass support. To maintain their positions, they are clamped to the brass support by copper clamps. In the bath, they are clamped to a G10 cooling support plate by copper clamps to avoid any shifting during cooling.

Moreover, during the tests, different parameters were measured, such as temperature, voltage, and magnetic field. The sensors' wires will act as an additional heat load conducting heat from the outside pin connectors into cryostat. This default is limited by thermalizing the sensors' wires on the aluminum heat shields (Table 4.1, Fig. 4.5b), that also limit the heat radiation from the cryostat flange, thus decreasing the heat load on cooling. These shields also allow a clear view for image acquisition.

Before manufacturing and assembling the setup (Fig. 4.4, Fig. 4.5a), a mock setup was built using cardboard and styrodur (Fig. 4.3a). This setup is used to verify if the design is suitable for image acquisition. We checked the window dimensions and the camera specification requirements (Table 4.2). Fig. 4.3c presents the image acquired after mounting the camera as shown in Fig. 4.3b. It was found that we need a lens of 200 mm focal length to zoom in on the pancake, and a full-frame camera to capture the whole pancake's image. Fig. 4.3c shows that pancake view is quite clear validating the chosen optical windows viewing diameter (Table 4.2).

After checking validity of setup design with the mock setup, defining the parameters of the MI REBCO pancake prototype is necessary. There are some constraints to be taken into account while choosing the parameters such as: minimum bending radius of REBCO tape, maximum diameter of pancake fitting the setup of 250 mm, and maximum current supply of 400 A that is a limitation of the the Ametek Sorensen power supply and current leads (Table 4.1). In both cooling and energizing, the larger the radius is, a larger displacement is measured by DIC. However, with the chosen optical window and lens, the pancake size is limited to a maximum of 160 mm diameter.

During cooling, the displacement depends mainly on the thermal contraction of the materials

(a) Mock Setup

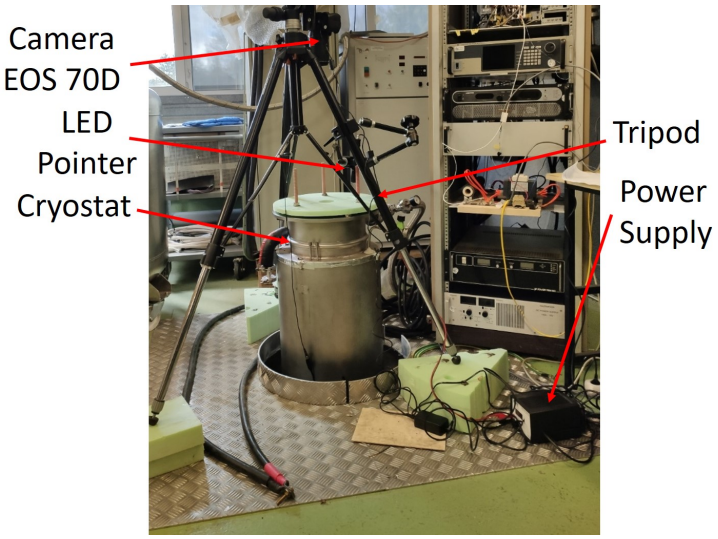

(b) Window size testing

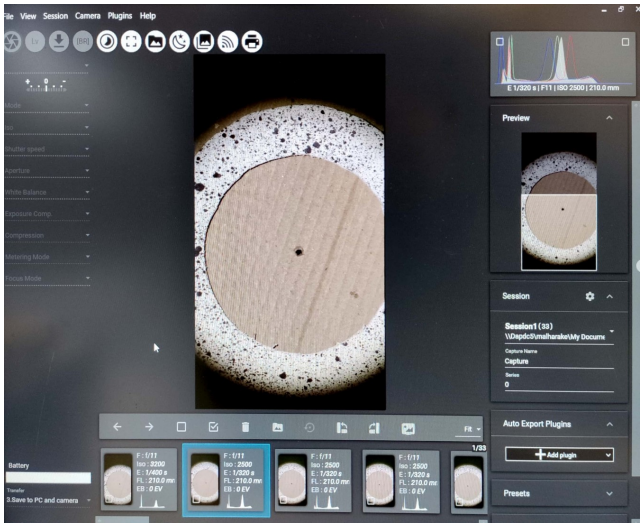

(c) Image acquired by Canon EOS 70D with DigiCam Control

Figure 4.3 – Window dimensioning set-up card-board prototype test

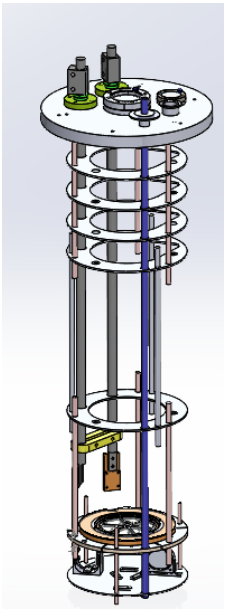

(a) Setup

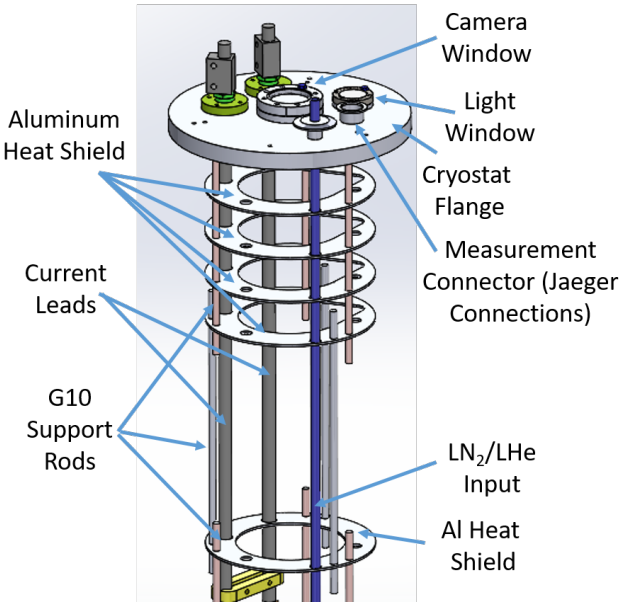

(b) Setup's upper part

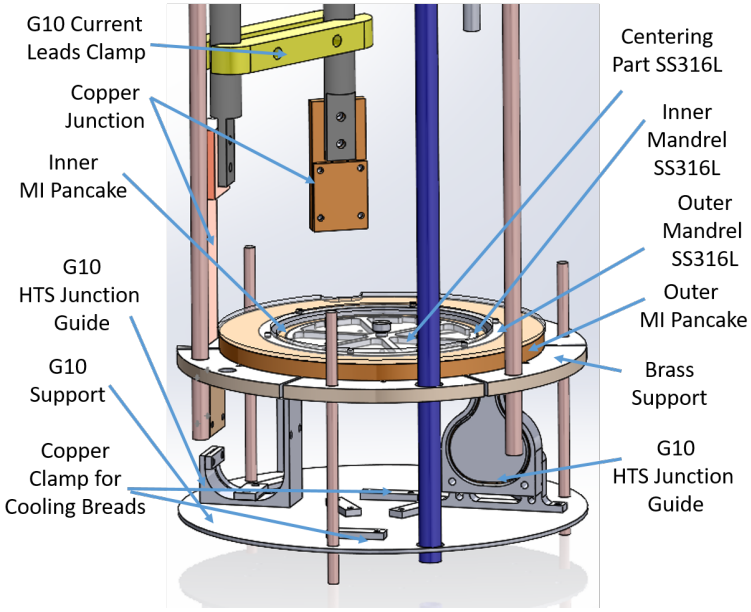

(c) Setup's lower part

Figure 4.4 – Setup design

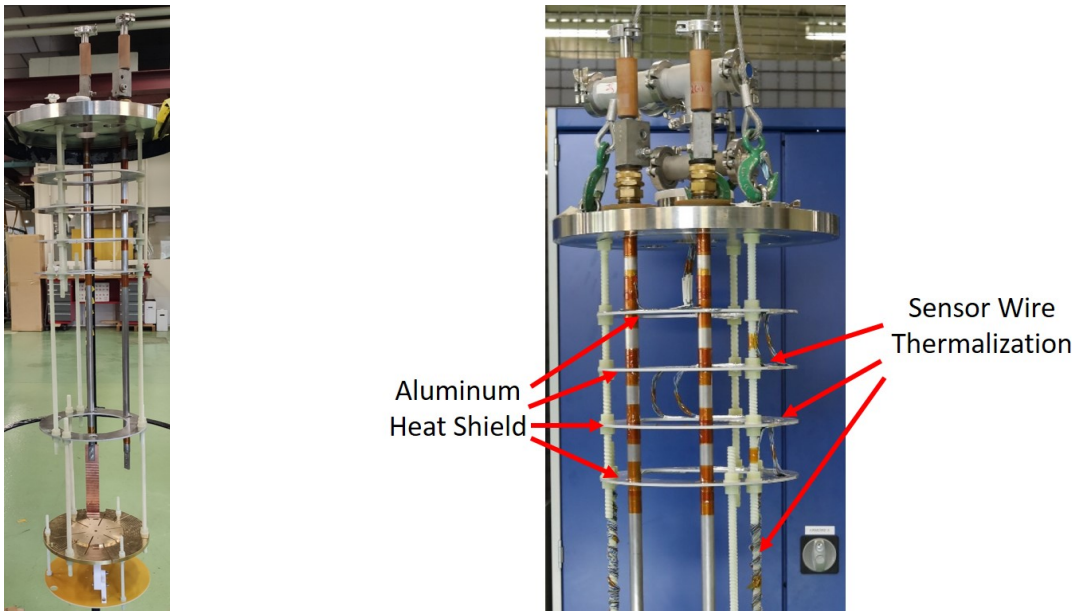

(a) Experimental setup

(b) Sensor's wires thermal shielding

Figure 4.5 – Experimental setup

Parameter	Value
Inner Pancake	
Nb of turns (REBCO + Durnomag)	50
Overbanding turns	10
REBCO thickness / width	65 μm / 4 mm
Durnomag thickness / width	30 μm / 4 mm
Inner radius	69.6 mm
Outer Pancake	
Nb of turns (REBCO + Durnomag)	259
Overbanding turns	10
REBCO thickness / width	70 μm / 12 mm
Durnomag thickness / width	30 μm / 12 mm
Inner radius	88.5 mm

Table 4.3 – Parameters of Inner / Outer MI REBCO pancake

and the radius. However, during energizing, the displacement is dependent on the magnetic field, current density and the radius. Hence, a REBCO tape of 4 mm from Shanghai Superconductors is chosen as it can sustain 350 A at a field of 3 T at liquid helium temperature. However, to increase the energizing displacement even further, we foresee to use an outer MI REBCO pancake that will create an additive magnetic field. It has same mid-plane as the inner MI REBCO pancake which uses the 4 mm tape. A 12 mm REBCO tape from Theva is chosen for the outer pancake as to eliminate the possibility of having a quench in it since its critical current at 3 T / 30 K is higher than 800 A [141]. The pancakes are connected together in series to a single power supply. Using the plane stress analytical formulation from chapter 2 at mid-plane of the inner pancake, the parameters of both pancakes were chosen (Table 4.3) as to achieve high displacement in cooling (Fig. 4.6a) and energizing (Fig. 4.6b). The calculation was done using the material parameters grouped in Table 4.4.

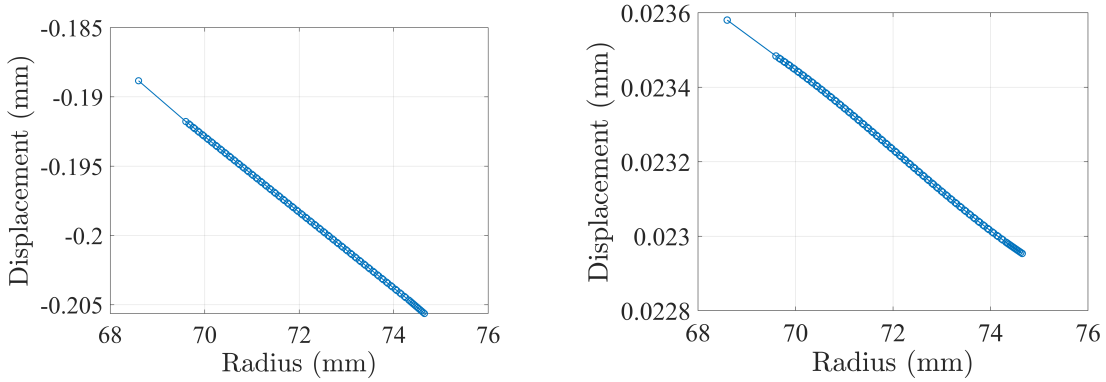

(a) Cooling displacement at 4 K

(b) Energizing displacement at 350 A/4 K

Figure 4.6 – MI REBCO inner pancake displacement

	REBCO	SS
Radial modulus (GPa)	76.5	81
Hoop modulus (GPa)	153	162
Poisson ratio $r\theta$	0.15	0.145
Poisson ratio θz	0.3	0.29

Table 4.4 – REBCO / SS properties

4.3 . Liquid Nitrogen Cooling Test

As the DIC is based on image analysis ([132]), anything that can affect the quality of the sample's acquired image will alter the displacement's measured value. Therefore, a careful handling of the image acquisition process is required (Table 4.5, Fig. 4.7).

As the DIC measurement has to be performed in cooling and energizing conditions, the used speckle should be inert with respect to the testing environment to avoid affecting the tests. Hence, it should be electrically insulating, chemically inert to avoid reacting with MI pancake, and thermally shock resistant. Thus, Boron Nitride ([142]) white spray is used to deposit a white layer on the sample. Then, Rust-Oleum Hard Hat Matt Black spray is used to do a fine black speckle to achieve the contrast required by the DIC. A relevant pattern should lead to a wide contrast between black and white while being non-repetitive and isotropic to enhance gray-scale detection for DIC measurement.

In addition, a clear plexiglass plate is mounted slightly few hundred microns above the sample,

Image Acquisition	
Camera	Canon EOS 5D MARK IV
Lens	Canon EF 70-200 mm f/4 IS USM
Acquisition program	EOS Utility V.3.12
White LED light pointer	Effilux-Sharp-FL-FF
Camera Configuration	
ISO	800
Aperture	F8.0
Shutter speed	1/400 s
Lens : focal length	200 mm

Table 4.5 – Image acquisition setup

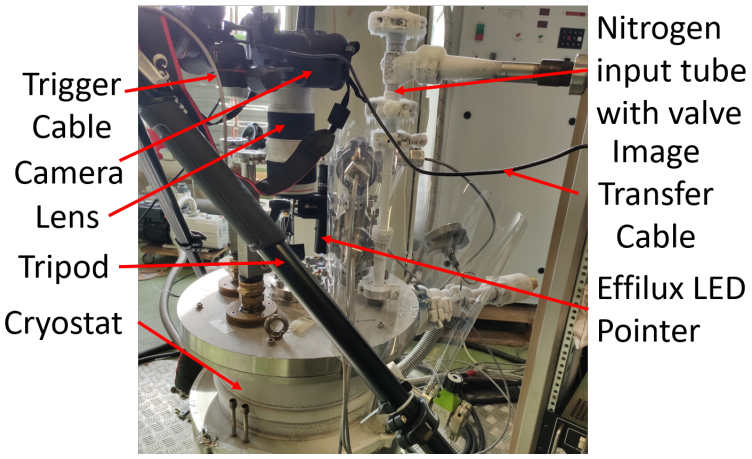

Figure 4.7 – DIC-setup mounted

upon which the centering screw of sample is supported. The plexiglass plate should be clean and clear of scratches for better results.

The light reflection and concentration on certain areas of sample from reflection from the cryostat or heat shields can result in blurred areas. Thus, a careful mounting of the light is required to avoid such an issue. Furthermore, any tripod's vibration will degrade the results, especially because of the applied zoom.

Regarding the DIC cooling test with liquid nitrogen, it is realized with the following experimental protocol:

- The speckle is applied on the sample, and the sample is mounted on the brass support while putting above it a plexiglass plate.
- The setup is inserted inside the cryostat, and the flange is attached tightly to the cryostat by screws.
- Flushing of cryostat environment with nitrogen gas is done three times (vacuuming then filling with nitrogen gas) to avoid ice formation.
- The nitrogen gas pressure inside the cryostat is kept slightly higher than atmospheric pressure at the end of the last flush. This is to ensure that no air enters when changing from the gas to the liquid nitrogen filling tube.
- The image acquisition setup is mounted and calibrated.
- All temperature measurements and image acquisitions are verified before the start of the test by a test run of the LABView data acquisition program.
- The LABView data acquisition program is launched before filling the cryostat with liquid nitrogen.

To synchronize DIC result and temperature measurement, a proper data handling with LABView is required. Fig. 4.8 presents the cooling setup temperature instrumentation. In LABView, twelve temperature measurements are stored along date-time and the camera is triggered simultaneously (Fig. 4.9). To allow the camera triggering with LABView, a Canon trigger cable, that is activated by a relay which is controlled by an NI 10 V 9269 DAQ output module, was

required. The data acquisition program allows for different time intervals between image acquisition based on the user input. The NI DAQ modules used for the instrumentation were NI 9217 and NI 9219 (for PT100 sensor reading), NI 9238 (0.5 V, voltage measurement), and NI 9265 (20mA, current output). The last two modules are dedicated for Cernox sensor readings.

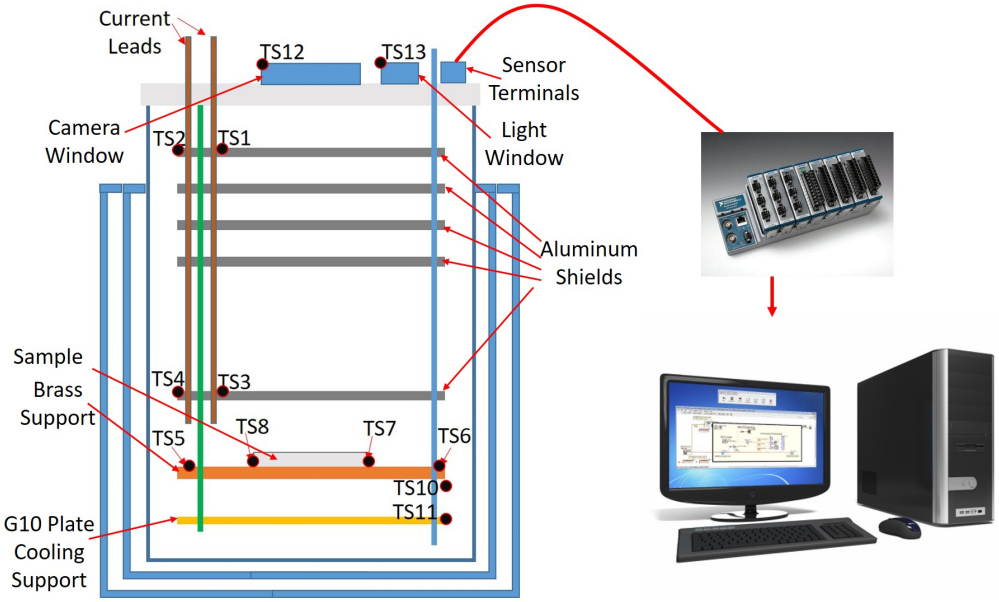

Figure 4.8 – Cooling Setup Instrumentation (TS: Temperature Sensor)

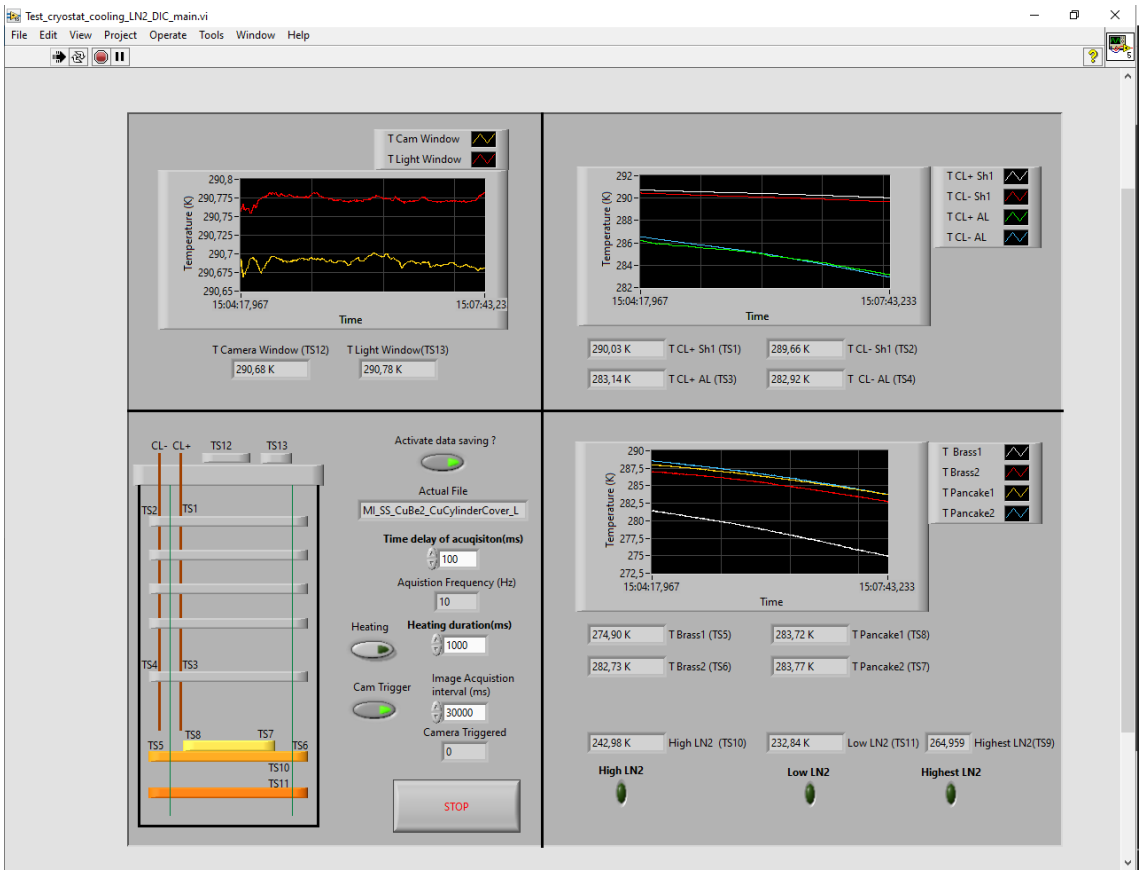

Figure 4.9 – Liquid Nitrogen Cooling LABView program

Stainless Steel 304 Disc	Value
Inner / Outer diameter	8 / 100 mm
Thickness	4 mm

Table 4.6 – SS304 Disc geometrical data

Figure 4.8 illustrates the positioning of all thermal sensors (TS) in the set up. PT100 temperature sensors were used except for TS5 to TS8 that were calibrated Cernox sensors. The sensors placed on the sample and the brass support are placed at diametrically opposite positions to get an idea about the temperature homogeneity. Indeed, temperature homogeneity may be an issue since cooling is done by conduction. The brass support is 14 mm thick. It is thick enough to get a high cooling capacity (cooling capacity is related indeed to specific heat and dimensions). The high number of cooling braids attached to brass support ensure its fast conduction cooling. With the current leads of 900 mm length, PT100 temperature sensors are placed at the first and fifth aluminum shield level to measure the temperature in the setup (Fig. 4.8).

Liquid nitrogen (LN_2) flow is controlled by the valve as to ensure that the liquid level does not reach the brass support. It is achieved by positioning the temperature sensor measurement slightly below the brass support. This way, controlling LN_2 flow can be done based on accurate data. Flow control is done to maintain level below the brass support to get clear images of the sample. Moreover, it was noticed from experiment that convection of nitrogen gas in cryostat during test has a blurring effect of the disc during the test (Fig. 4.10). Hence, the control of the LN_2 flow is an important aspect in the test; a slower flow is preferred to allow for smooth cooling of the whole cryostat.

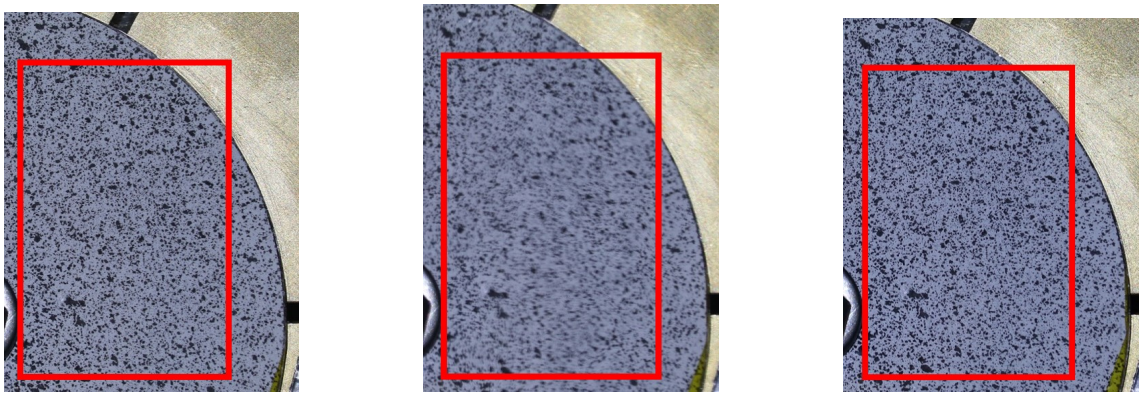

(a) Reference image of Stainless Steel 304 disc before start of test

(b) Blurred image during test due to nitrogen gas convection

(c) Clear image at end of test after nitrogen gas convection settled

Figure 4.10 – Effect of gas convection on image quality of SS304 disc

As applying the DIC to such a setup at cryogenic temperature is new [143], the setup is first tested using a stainless steel 304 "SS304" disc. Indeed, the thermal properties of SS304 are known [138], allowing us to validate the whole setup (Fig. 4.11). SS304 disc (Table 4.6) is cooling tested using LN_2 following the experimental protocol.

Figure 4.11 – SS304 disc mounted

The reference image at room temperature and the last deformed images at 80 K of the cooling test are used to find the thermal contraction displacement. Even though the measured windows' temperature was above the freezing point (i.e. 288 K - 286 K) during the test, water vapor sometimes formed on the windows as shown in Fig. 4.12. This was affecting the acquired images. Thus, a heat gun was used to remove the vapor.

(a) Water vapor on windows

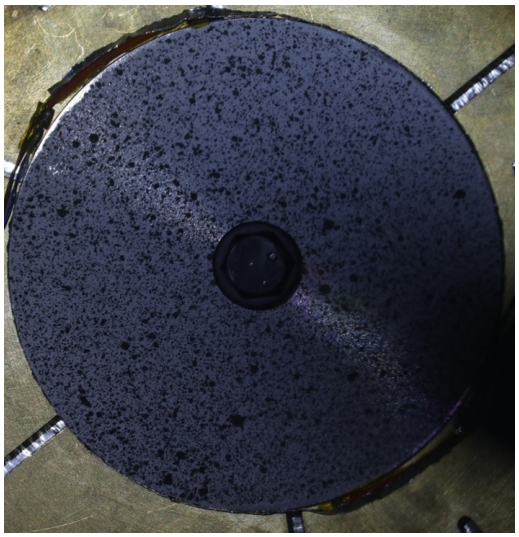

(b) Light dimmed significantly because of water vapor on light window

Figure 4.12 – Effect of water vapor on image quality

4.4 . Data Analysis

At first, SS304 disc is cooled down from 296 K to 80 K. It took slightly more than 2 hours to reach 80 K stable temperature. This test is done to verify the operation of the set-up and image acquisition since SS304 material properties are well established at cryogenic temperatures. Displacement measurement during thermal contraction is done using DIC in the specified region of interest between room temperature and 80 K. After that, the MI CuBe2/SS304 pancake is tested to evaluate the thermal contraction behavior of an MI pancake. CuBe2 and SS304 were chosen to have different thermal contractions and mimic the MI HTS pancake where SS304 plays the role of the stainless steel alloy, and CuBe2 is the substitute of REBCO since it has good thermal contraction and mechanical properties as well.

During all cooling tests, temperature measurement rate was 10 Hz, while image acquisition was 1 image per 30 seconds. The temperature profile of SS304 cooling test is presented in Appendix H. Two cernox sensors were placed on SS304 disc and brass support, to verify the temperature homogeneity. A PT100 was placed on each window to monitor the temperature and prevent ice formation below $0°$C (273 K). Two PT100 were used to get the temperature of the first and fifth aluminum heat shield to monitor the temperature inside the cryostat.

4.4.1 . SS304 disc

DIC mesh choice

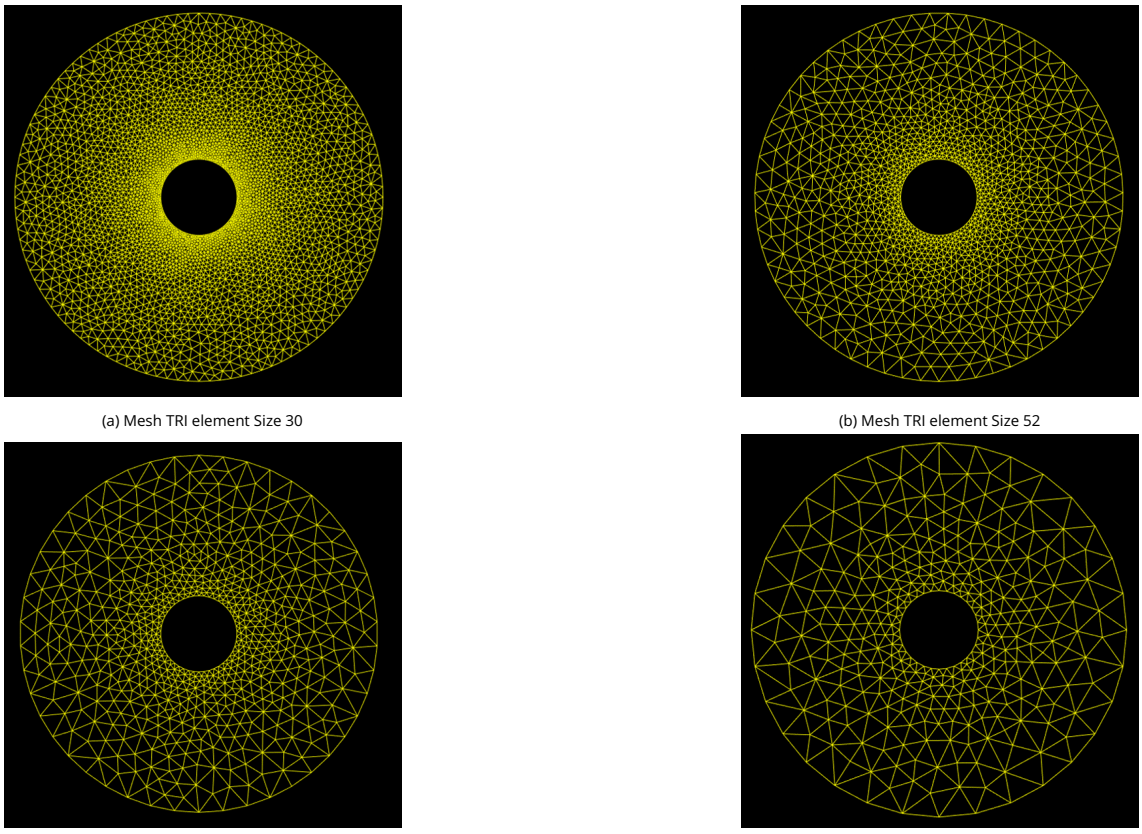

(a) Mesh TRI element Size 30

(b) Mesh TRI element Size 52

(c) Mesh TRI element Size 71

(d) Mesh TRI element Size 101

Figure 4.13 – Mesh TRI of different sizes of SS304 disc

A mesh is required to do the DIC analysis of the images. Uncertainty displacement measurement by DIC is calculated at first to find a suitable mesh in order to know the uncertainty of the

DIC results. It is affected by the parameters chosen for DIC calculation of mesh size, boundaries and region of interest. The choice of mesh size is the result of a compromise concerning the uncertainty displacement results. The higher the element size of the mesh the lower the uncertainty displacement. The price to pay is a lower displacement measurement resolution.

The uncertainty displacement measurement of DIC is done using several images taken at room temperature. As temperature is constant and as the light does not fluctuate, DIC measurement should be zero. The measured displacement is not zero in reality and corresponds to the uncertainty measurement. Uncertainty is calculated as the mean of standard deviation of the displacement measurement results at the nodes [144].

During SS304 cooling test, DIC uncertainty measurement is done using 11 images taken before the start of the test and uses different mesh element sizes (Fig. 4.13). The conversion factor from "pixel" to "mm", is calculated using a picture of outer diameter of SS304 disc.

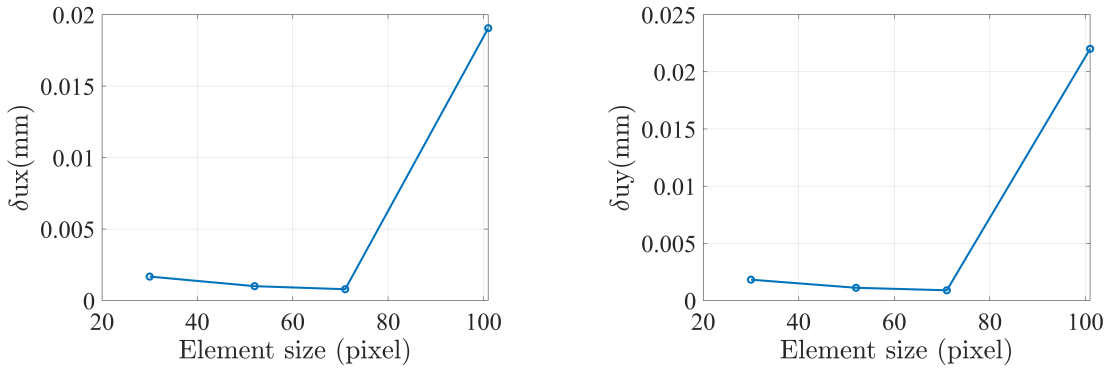

(a) DIC uncertainty in Ux direction

(b) DIC uncertainty in Uy direction

Figure 4.14 – DIC uncertainty of SS304 disc test

From Fig. 4.14, the lowest value of the DIC uncertainty was achieved in a mesh of an element size (Elsize) equals to 71 pixels. Hence, this mesh is chosen to perform the DIC analysis on the deformed image of the SS304 disc. A basic DIC without any mechanical regularization is used to find the displacement field. Results were obtained thanks to the Correli 3.0 code [134].

DIC results

Figure 4.15 shows that the theoretical thermal contraction of SS304 disc calculated using Cast3m is symmetric. However, Figure 4.16 shows that the DIC displacement of SS304 disc does not fit with thermal contraction towards the center from all directions as expected. Also, the DIC displacement values are not symmetric whether in "x" or "y" direction. We deduce that rigid body motion is occurring [145] from the displacement vectoring result (Fig. 4.16). It is occurring because the brass support is rather supported by G10 rods in mid-air which can cause rigid movement of "brass + disc".

To get the actual displacement, we apply a post-processing procedure that eliminates the effect of the rigid body motion. Equations (4.1) and (4.2) describe this procedure:

$$x^{'} = t + R(\theta)x = x + u^{RBM} \tag{4.1}$$

$$u^{RBM} = t + (R(\theta) - I)x \tag{4.2}$$

The displacement field "$x^{'}$", obtained from DIC analysis, can be divided into a rigid translation "t" and a rigid rotation "R". Furthermore, "$x^{'}$" can be seen as the sum of the total rigid body

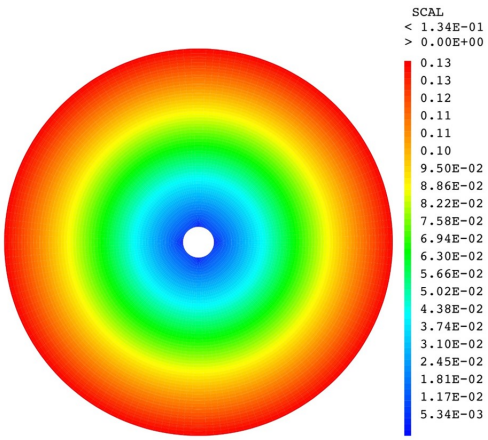

Figure 4.15 – Total thermal contraction (mm) in absolute value of SS304 disc from 300 K to 80 K by Cast3m FEM code

motion "u^{RBM}" and the actual field displacement "x". We assume that the rotation (θ) and the translation (t_x and t_y) of the rigid body motion (RBM) are small in the experiment. Under this assumption, Eq. (4.2) can be simplified to Eq. (4.3), such that x_i and y_i are the mesh-node coordinates. t_x, t_y, and θ are approximated using a linear least square fitting method as in Eq. (4.4).

$$u^{RBM} = (t_x e_x + t_y e_y + \theta(-y_i e_x + x_i e_y)) \tag{4.3}$$

$$min\Sigma_i ||u(x_i) - (t_x e_x + t_y e_y + \theta(-y_i e_x + x_i e_y))||^2 \tag{4.4}$$

After subtracting the approximated rigid body motion u^{RBM} value from the DIC result $x^{'}$, we obtain the results shown in Fig. 4.17. It is noticed that the new displacement vector is now pointing towards the center, where its magnitude is increasing proportionally with the radius. This is what we expect for a disc contraction. In addition, "ux" and "uy" displacements are symmetric in value, in proper direction and position corresponding to what can be expected during a thermal contraction of a disc. Moreover, when checking the displacement magnitude, it is displayed as concentric circles as expected too.

A representative radial displacement (Eq. (4.5)) is calculated from averaging over several radial measurements for different angles from 0 to 2 π (Fig. 4.19).

$$u_{rDIC}(r_k) = \frac{1}{n}\sum_{1}^{n} u_{FT}(r_k)(\theta_i) \tag{4.5}$$

where u_{rDIC} and u_{FT} are respectively the mean total radial displacement at a given radius and the total radial displacement at a mesh point from field displacement. The total displacement magnitude in Fig. 4.19 graph is evaluated using 50 equidistant radial positions with negligible error. The error bar in the graph is the standard deviation of u_{FT}.

The total displacement magnitude and direction are proved to be independent of the mesh size as demonstrated in Figs. 4.18 and 4.19. It is also clearly visible that the total displacement is smaller than the theoretical one. Indeed, when the temperature decreases, the setup contracts due to G10 support rods contraction, leading to a decreasing distance between the disc and the camera. Thus, the disc will enlarge slightly resulting in apparent radial expansion. This effect is corrected by subtracting the enlarging effect from the DIC displacement.

With sample being circular and the magnification being uniform, magnification effect is an artificial positive constant radial deformation upon the sample (Fig. 4.20). In order to get

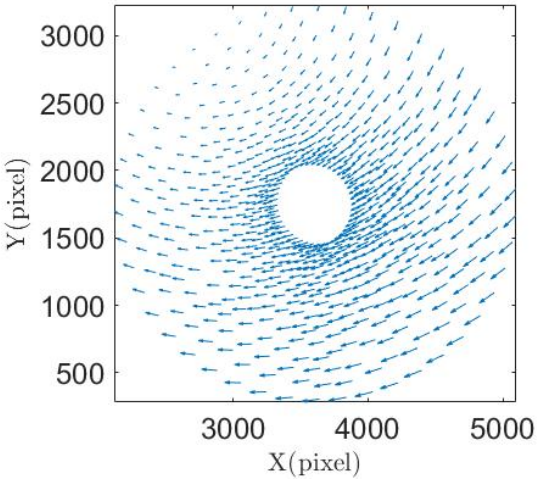

(a) Displacement vectors

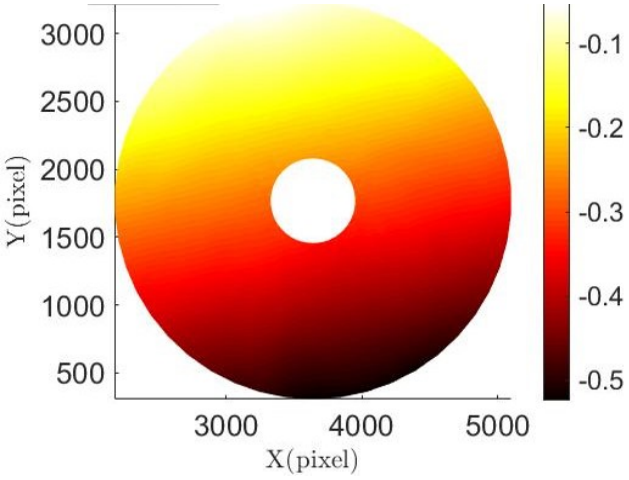

(b) Ux displacement (mm)

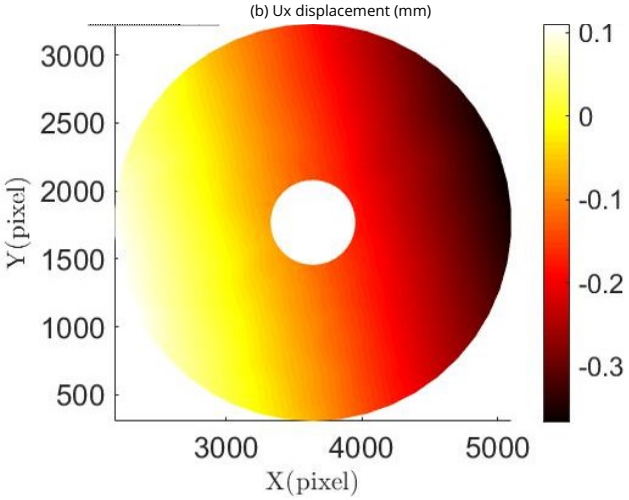

(c) Uy displacement (mm)

Figure 4.16 – Displacement measured by DIC without rigid body motion elimination of SS304 disc

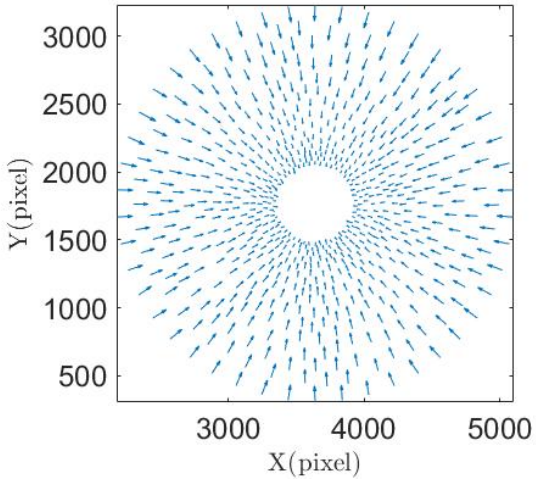

(a) Displacement vectors

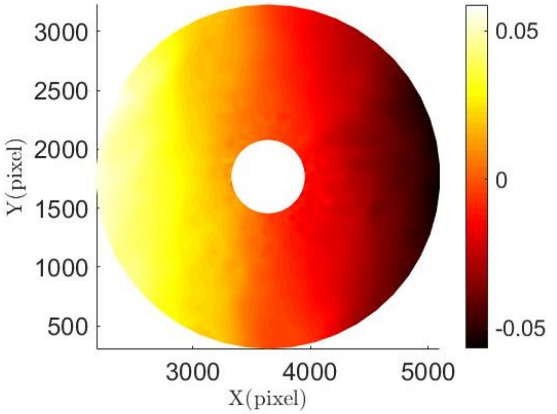

(b) Ux displacement (mm)

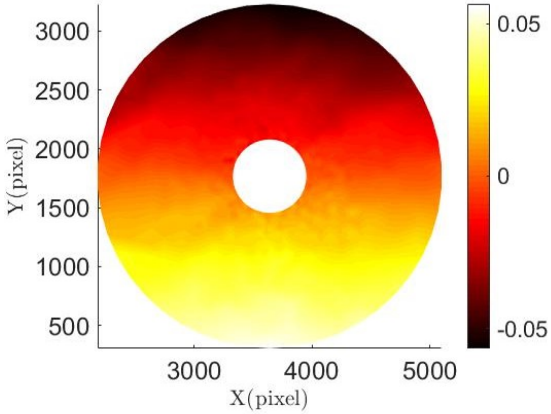

(c) Uy displacement (mm)

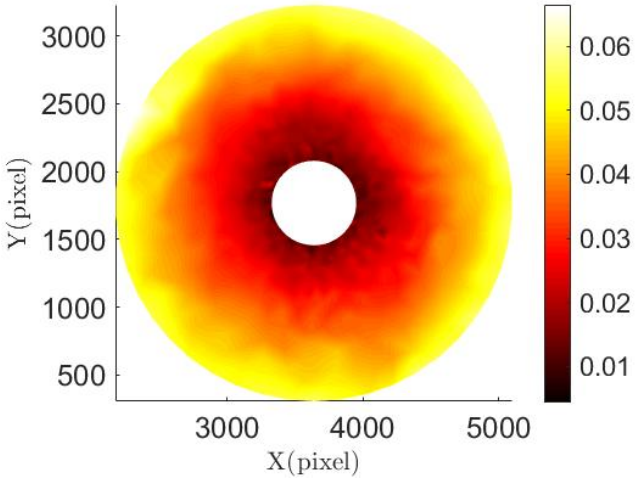

(d) Total displacement magnitude (mm)

Figure 4.17 – Displacement measured by DIC with rigid body motion elimination of SS304 disc

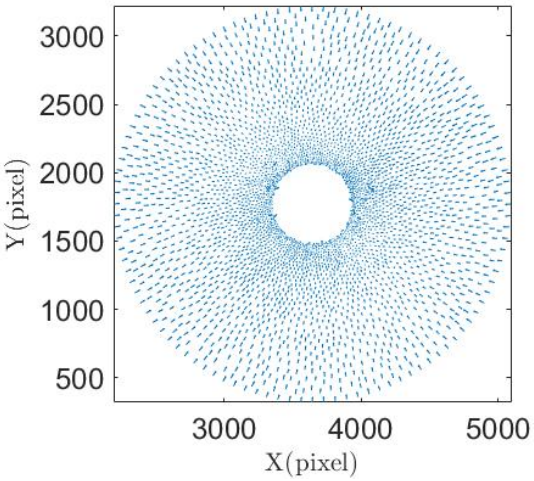

(a) Displacement vectors of mesh Elsize 30 pixels

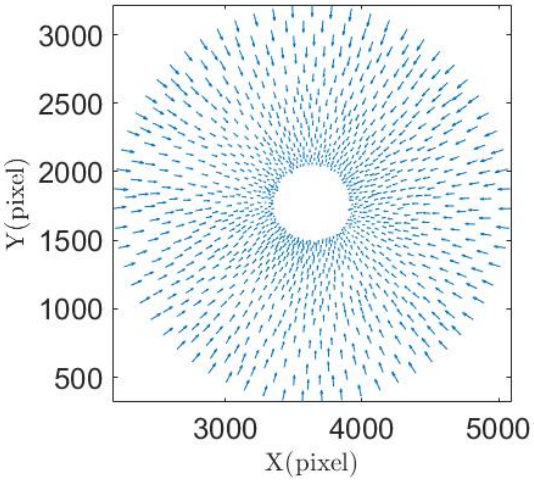

(b) Displacement vectors of mesh Elsize 52 pixels

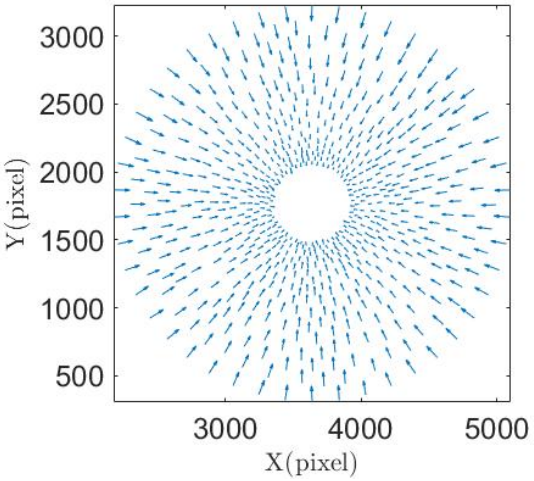

(c) Displacement vectors of mesh Elsize 71 pixels

Figure 4.18 – Displacement vectoring of DIC results with rigid body motion elimination of different mesh sizes of SS304 disc

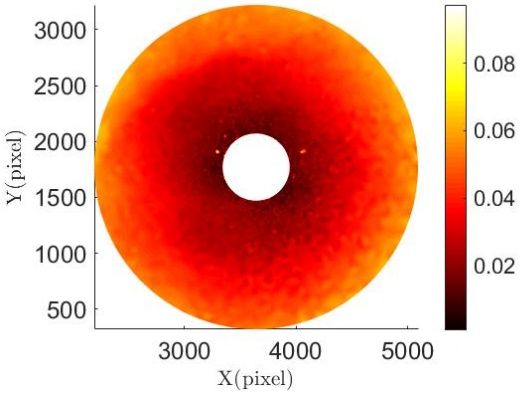

(a) Total displacement magnitude (mm) of mesh Elsize 30 pixels

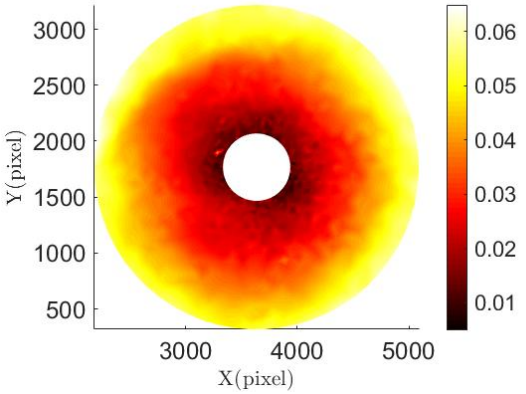

(b) Total displacement magnitude (mm) of mesh Elsize 52 pixels

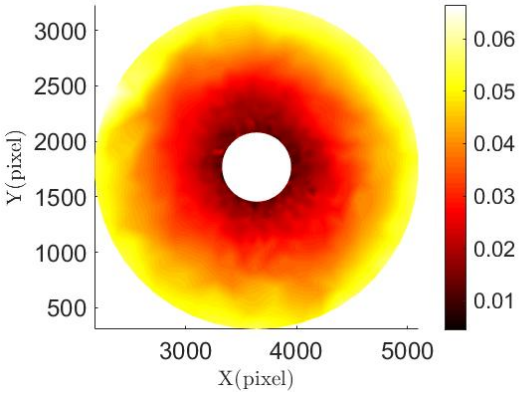

(c) Total displacement magnitude (mm) of mesh Elsize 71 pixels

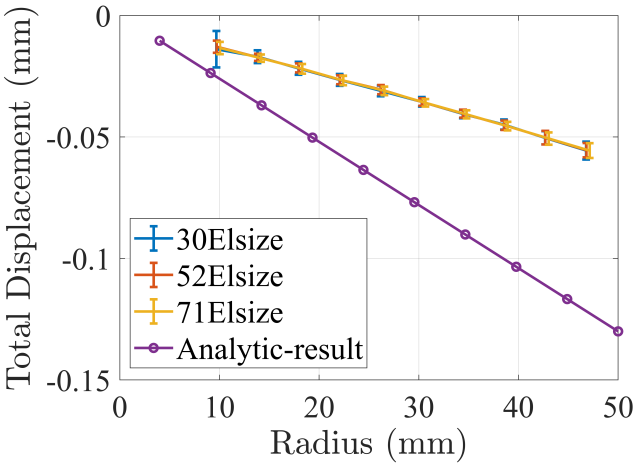

(d) Total displacement (mm) of mesh Elsize 30-52-71 pixels benchmarked with analytic result

Figure 4.19 – Displacement measured by DIC with rigid body motion elimination of different mesh sizes of SS304 disc

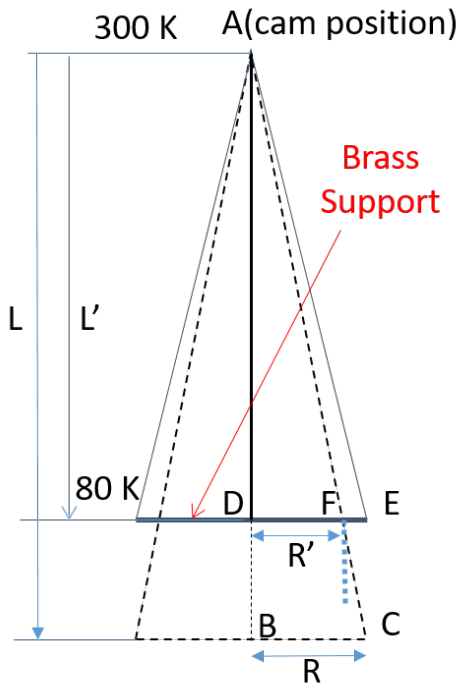

Figure 4.20 – Setup contraction sketch: position of brass support is dotted at reference (room temperature) state and solid at low temperature (at 80 K).

the virtual deformation "ϵ_{rr}" due to setup contraction, the disc shape is assumed to remain constant while finding the enlarging effect of contraction (Eq. (4.6)). Let us assume that the total contraction of the support rods is α_T ($\frac{R'}{R} = \frac{L'}{L}$ from Fig. 4.20):

$$\epsilon_{rr} = \frac{R - R'}{R} = \frac{L - L'}{L} = -\alpha_T \tag{4.6}$$

The total contraction of the support rods is calculated using the temperature measurements via a series of thermocouples and the knowledge of thermal contraction of G10 support rods. It is expressed as follows:

$$\alpha_T = \int_{T1}^{T2} \alpha(T) dT \tag{4.7}$$

where temperatures T1 is greater than T2 and $\alpha(T)$ is the thermal contraction coefficient of G10 rod [138].

Hence, the real displacement of SS304 disc is expressed as follows (Eq. (4.8)):

$$u_r = u_{rDIC} - u_{rimage} = u_{rDIC} - r\epsilon_{rr} \tag{4.8}$$

where r, u_{rDIC} and u_{rimage} are respectively a radial position, the DIC displacement without RBM and the displacement caused by image magnification due to the setup contraction.

Fig. 4.21 shows that the difference between analytic and actual displacement is small. It is only due to total contraction calculated using temperature measurement from sensors placed on current leads and not G10 rods. Since experimental and analytic results of SS304 disc do correspond during the cooling test, since the images are clear enough for DIC calculation and since conduction cooling is proved to be efficient, the set-up has been validated.

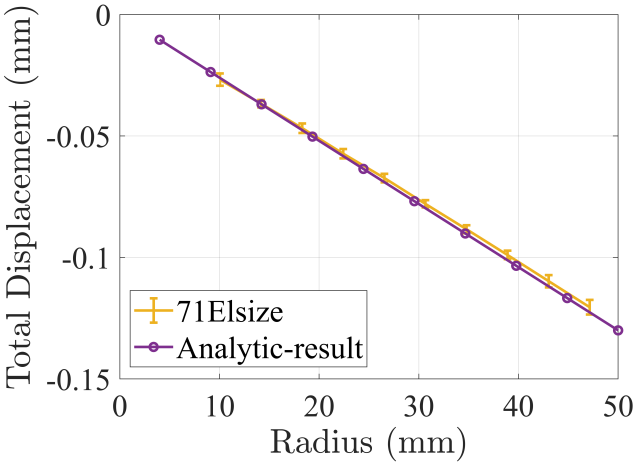

Figure 4.21 – Total displacement magnitude with setup contraction of SS304 disc, α_T = -13.86 $\times 10^{-4}$ mm/mm

Another cooling test of SS304 disc to 80 K has been done using liquid nitrogen, but the difference now is that the holes from the second to the fourth aluminium heat shields are covered with plexiglass for enhanced heat radiation protection in case of liquid helium cooling as seen in Fig. 4.22.

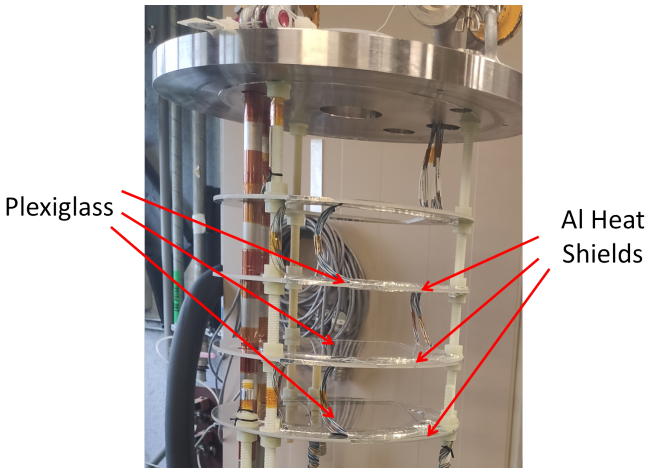

Figure 4.22 – Aluminium heat shields covered with plexiglass

Figure 4.23 shows that covering the heat shields with plexiglass did not affect the DIC results since irrespective of mesh size, same DIC result was achieved. Furthermore, as expected, without the set-up contraction correction, the results were lower than that of the analytical one. However, after applying the set-up contraction correction of α_T = -12.9 10^{-4} mm/mm, the achieved experimental result is much higher than that of analytical one which is inaccurate. This indicates that the set-up contraction that was calculated using the temperature measurement is not accurate since G10 rods are insulating materials. Thus, the temperature measured close to the G10 rods does not represent the temperature of G10 rods themselves.

However, since SS304 is a well evaluated material, the set-up contraction can be deduced by adjusting its value to achieve experimental results in accordance with the analytical one. A contraction value of α_T = -7 10^{-4} mm/mm leads to have experimental result in accordance with the analytical one. This test highlights that evaluating the set-up contraction based on temperature measurement is prone to errors. This means that in order to handle the set-up

contraction magnification point, either a telecentric lens can be used or to employ an accurate method for set-up contraction evaluation. Unfortunately, telecentric lens does not have a large working distance like 1.3 m, so evaluating the contraction is the remaining option. A simple method would be to use a centering part for the tested sample that has well established properties at cryogenic temperature like SS304. Fitting the experimental contraction of the centering part with its theoretical calculation will give the set-up contraction value. Another method of set-up contraction measurement is to use a laser distance sensor position at cryostat flange while measuring the distance to the brass support from room to operating temperature.

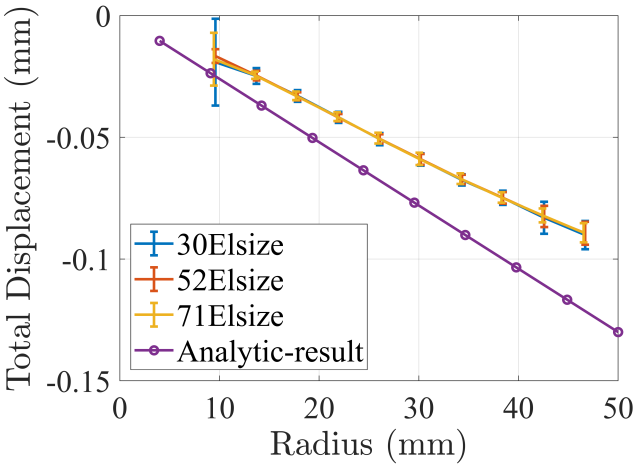

(a) Total displacement magnitude of SS304 disc without setup contraction with plexiglass covered heat shields

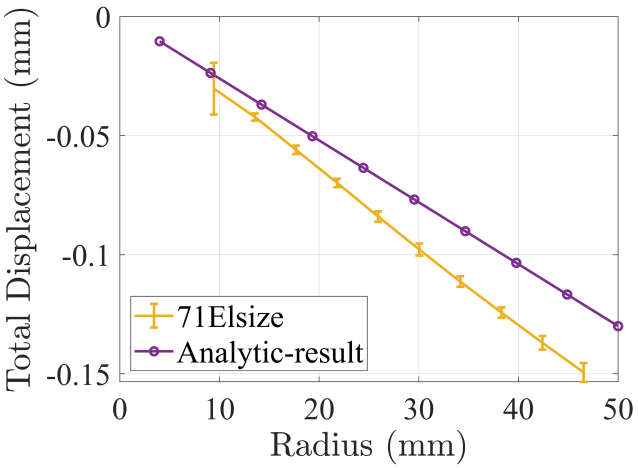

(b) Total displacement magnitude of SS304 disc with setup contraction of α_T = -12.9 $\times 10^{-4}$ mm/mm, with plexiglass covered heat shields

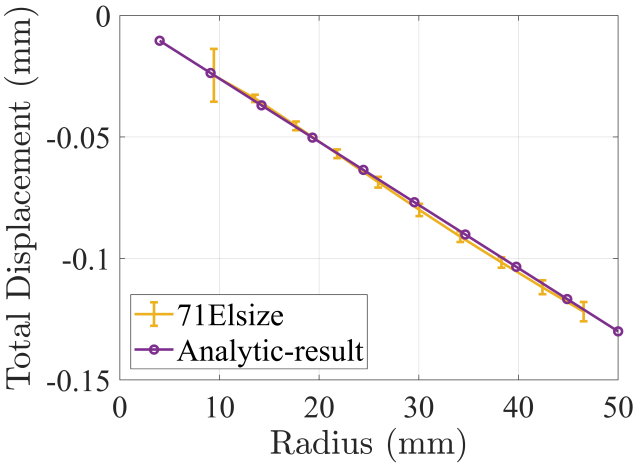

(c) Total displacement magnitude of SS304 disc with setup contraction of α_T = -7 $\times 10^{-4}$ mm/mm, with plexiglass covered heat shields

Figure 4.23 – Thermal contraction of SS304 from room temperature to 80 K with plexiglass covered heat shields

4.4.2 . MI CuBe2 / SS304 pancake

After SS304 disc cooling test validating the DIC and experimental setup, a MI Copper Beryllium / Stainless Steel 304 ("CuBe2 / SS304") pancake is cooled using the same procedure (Table 4.7 and Fig. 4.24).

Brass Mandrel Inner/Outer Radius	Nb of CuBe2 / SS304 turns	Width	Thickness	Overbanding	Pre-tension
22/25 mm	50	6 mm	50 μm	0.35 mm	15N

Table 4.7 – MI CuBe2/SS304 Pancake geometrical parameters

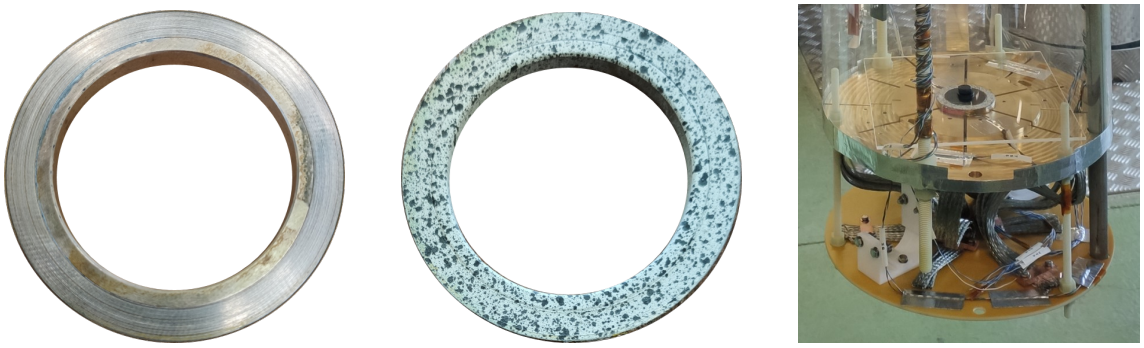

(a) MI CuBe2/SS304 (b) MI Speckle (c) MI Pancake Setup

Figure 4.24 – MI CuBe2/SS304 Pancake

Before the analysis of the deformed image, DIC uncertainty calculation for the MI CuBe2/SS304 pancake test has been carried out using 10 images at room temperature with different meshes (Fig. 4.25).

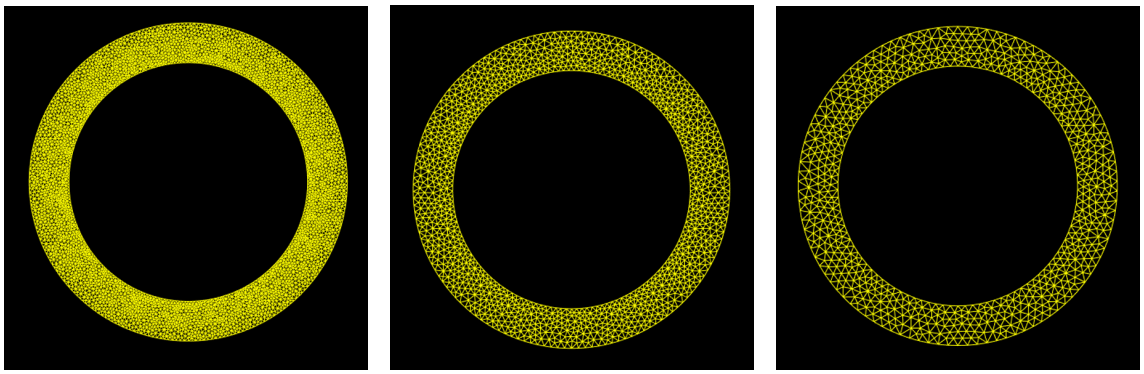

(a) Mesh TRI element size 12 pixels (b) Mesh TRI element size 22 pixels (c) Mesh TRI element size 30 pixels

Figure 4.25 – Mesh of different sizes for the MI CuBe2/SS304 pancake

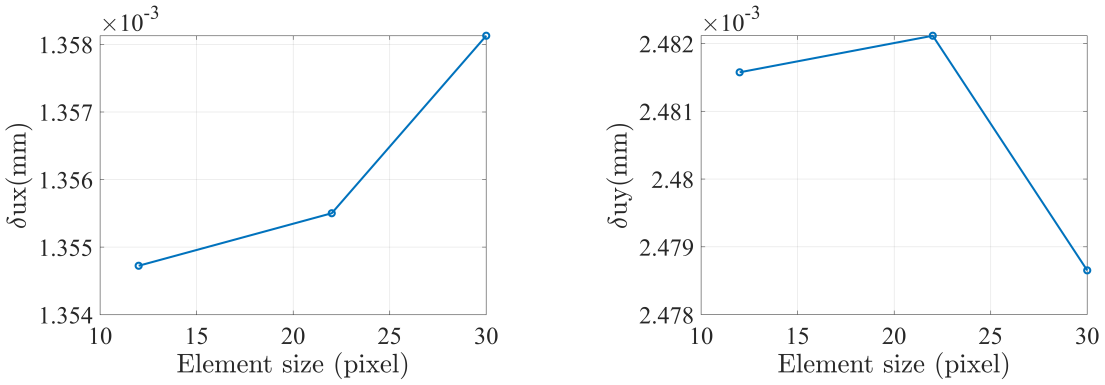

(a) DIC uncertainty in Ux direction

(b) DIC uncertainty in Uy direction

Figure 4.26 – Correlation error

Figure 4.26 shows that DIC uncertainty is insignificant in comparison to expected displacement using analytic formulation of chapter 2 and plotted in Fig. 4.27. MI CuBe2/SS304 is made of the brass mandrel and the winding, the radial position from 22 to 25 mm is occupied by the mandrel while the remaining part is the winding. DIC is done with a regularization length of 24 pixels. This regularization allows for a noise reduction, noise partly due to the small mesh size (Fig. 4.29).

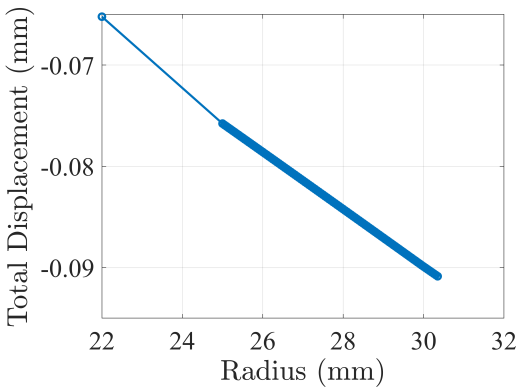

Figure 4.27 – MI CuBe2/SS304 total analytic displacement (290 K - 80 K)

Figures 4.28 and 4.29 show direction and and a good proportionality is obtained between magnitude and radial position.

Total displacement amplitude of MI pancake is lower than the theoretical displacement estimated from the analytic calculation without considering setup contraction (Fig. 4.30a) with negligible mesh size sensitivity (Fig. 4.30a). When the set-up contraction correction is applied(α_T = -12.9 10^{-4} mm/mm) [1] (Fig. 4.30b), the corrected amplitudes become higher than analytic ones. The overestimation reaches 0.02 mm. This can be attributed to the fact that the set-up contraction estimation is not correct as already observed during the second test of SS304 disc. Considering the same set-up contraction as that of second cooling test of SS304 disc (α_T = -7 $\times 10^{-4}$ mm/mm), Fig. 4.30c shows that a slight discrepancy remains between experimental and analytical results. This lower discrepancy could be due to friction between pancake and brass support or an unexpected winding configuration effect.

[1] this value differs from the previous one since temperatures measured along the rod are slightly different from temperatures observed during SS304 cooling

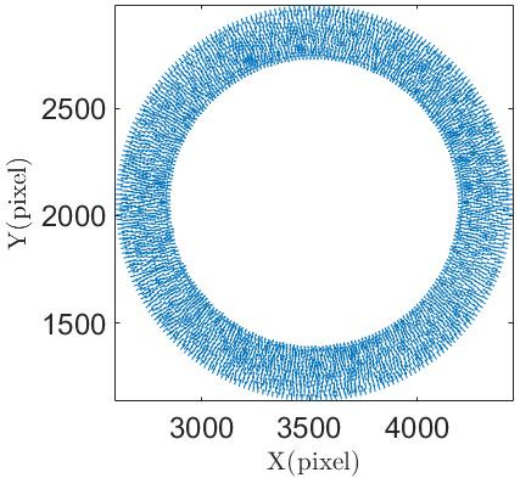

(a) Displacement vectors of mesh Elsize 12 pixels

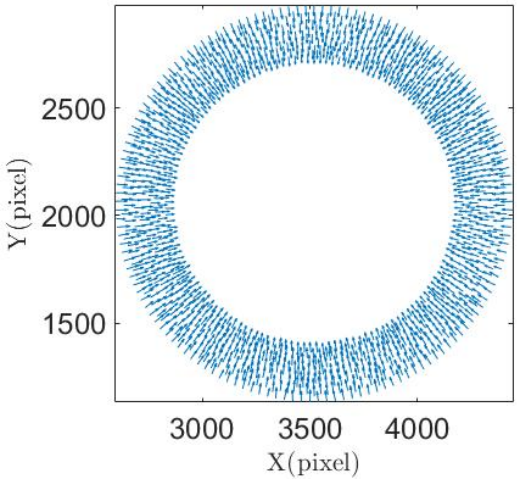

(b) Displacement vectors of mesh Elsize 22 pixels

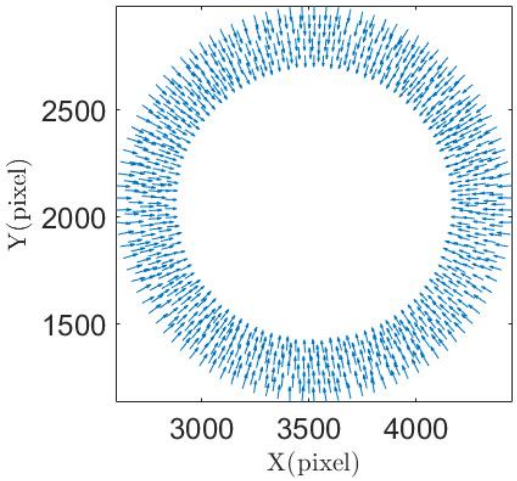

(c) Displacement vectors of mesh Elsize 30 pixels

Figure 4.28 – Displacement vectoring measured DIC results of MI CuBe2/SS304 pancake with rigid body motion elimination on different mesh size

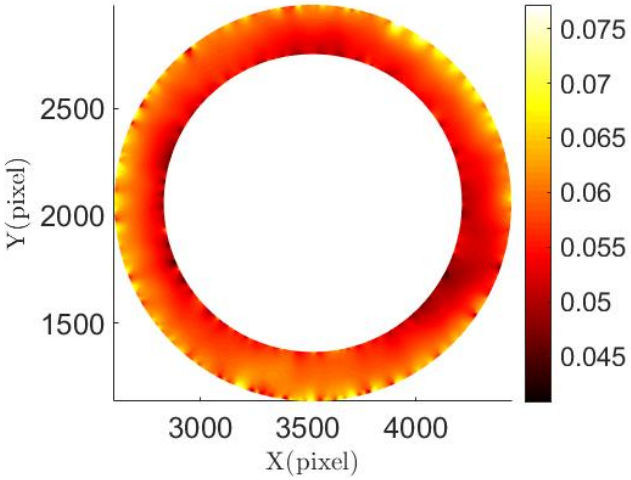

(a) Total displacement magnitude (mm) of mesh Elsize 12 pixels

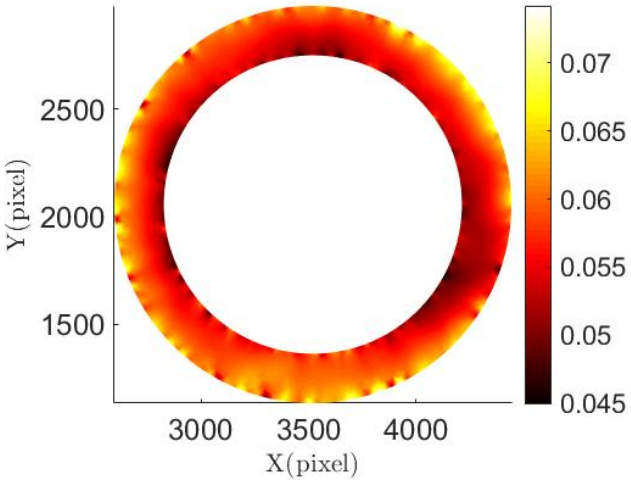

(b) Total displacement magnitude (mm) of mesh Elsize 22 pixels

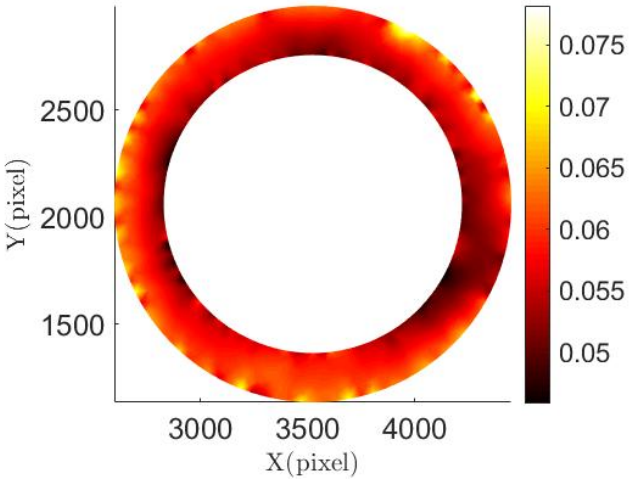

(c) Norm total displacement (mm) of mesh Elsize 30 pixels

Figure 4.29 – Displacement measured by DIC of MI CuBe2/SS304 pancake with rigid body motion elimination on different mesh size

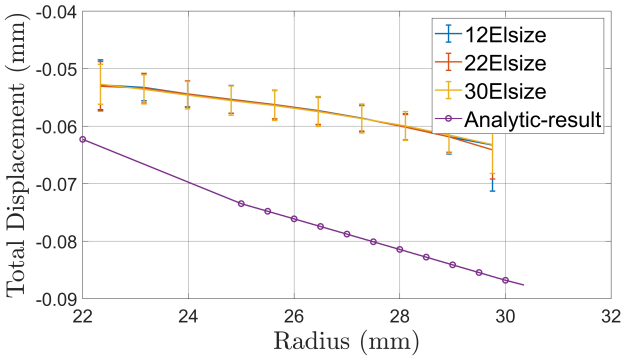

(a) Total displacement (mm) of mesh Elsize 12-22-30 pixels

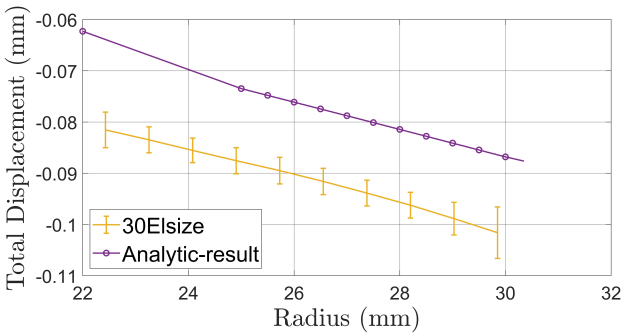

(b) DIC displacement after adding setup contraction effect (α_T = -12.9 $\times 10^{-4}$ mm/mm), 30 Elsize chosen because the higher mesh size the lower DIC noise

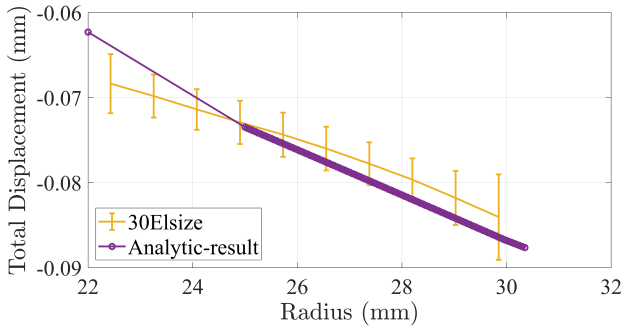

(c) DIC displacement after adding setup contraction effect (α_T = -7 $\times 10^{-4}$ mm/mm)

Figure 4.30 – Total displacement magnitude of MI CuBe2 / SS304 pancake

Hence, with the results of the cooling test of SS304 disc, the image acquisition and experimental setup were validated. The test carried out with SS304 disc and MI CuBe2/SS304 pancake showed the viability and capability of using DIC for in-situ displacement measurement at cryogenic temperatures. The tests highlighted some issues that require post-processing to reach an appropriate evaluation of the displacement. Finally, the cooling test carried out with MI CuBe2/SS304 showed that the winding configuration might have an effect on the thermal contraction too.

4.5 . Conclusion

In conclusion, a setup was developed that allows for full field displacement measurement of MI pancakes at cryogenic temperatures. Rigid body motion elimination and setup contraction correction had to be implemented to acquire the actual displacement. Moreover, proper speckle preparation and DIC setup calibration are important to get relevant results as image and speckle

quality affect DIC results.

A liquid nitrogen cooling test of a SS304 disc allowed for the validation of the set-up. It showed that the speckle used does work at cryogenic temperature, and that DIC yields proper results. A second cooling test of SS304 disc showed that evaluating the set-up contraction from the temperature measurements may be sometimes not accurate depending on the way the axial temperature is estimated. G10 rods for example are insulating materials and measuring temperature at this level seems not accurate. To solve this issue, the use of a well-known material positioned in the central part of the support may be a relevant way to address the true set-up contraction. Another method of set-up contraction measurement is to use a laser distance sensor. In addition, a set-up contraction issue has been observed during MI CuBe2/SS304 cooling as well. When set-up contraction was adjusted, better results were obtained, but a slight discrepancy remained that might be caused by the winding configuration or friction between pancake and brass support. After validating this deformation measurement technique with liquid nitrogen cooling, it can be used at high fields because it is a no-contact at a distance technique based on image acquisition at a safe distance from the testing environment (cryogenic and magnetic). Furthermore, the next step that was planned for the set-up was liquid helium cooling and energizing of a MI REBCO pancake inside an external field generated by another MI REBCO pancake as stated in the set-up design process but was postponed due to COVID situation.

5 - Conclusion and Perspectives

In this thesis, some mechanical aspects of MI HTS pancake have been studied. At first, analytical formulations plane stress and generalized plane strain formulations have been bench-marked against Cast3m for the three main processes involved in the forming (winding) and using (cooling and energizing) of a single representative MI REBCO pancake. The same procedure was applied for the so-called "Nougat" inner magnet central pancake subjected to a 30 T magnetic field.

From the bench-marking on Nougat, the total radial stress was found to be positive from analytical calculation and close to a stress free situation from Cast3m over major part of the pancake indicating separation of turns. This separation is critical because it may disrupt the quench protective aspect of MI pancakes, i.e. current by-passing at quenched zone to adjacent turns. This led to a study of the effect of the pre-tensioning and over-banding on the total radial stress and on the turn separation in the central "Nougat" pancake at 30 T using plane stress formulation. It showed the importance to limit the stresses the REBCO tape is subjected to so that stress remains below the irreversible limit, and to maintain the contact all over the pancake by compressive radial stress. It also highlighted the importance of choosing a compromise between pre-tensioning and over-banding to maintain the stresses from winding process within the permitted range for all materials.

REBCO and SS mechanical properties evaluation was carried out using DIC applied to tensile and diametric compression testing. FEMU-UF was employed to get a better estimation of the stresses in winding+mandrel case. The material properties evaluated from tensile testing were in accordance with the reference values except for the Young modulus of SS. Furthermore, tests showed a Poisson curving effect for both REBCO and SS since they are foil materials requiring sandwiching between clear transparent plexiglass to mitigate this effect.

Furthermore, utilizing the diametric compression testing with FEMU-UF showed that the winding process has a very strong effect on the identified radial Young modulus of REBCO or SS. The reasons of this strong influence can be found in the surface roughness and imperfect flatness of the tape, leading to an irreducible gap between the turns (as proved by the thickness measurement of the total winding higher than the total thickness of each layer). Finally, it has to be concluded that the test was unfortunately not suitable for material parameter evaluation. Some additional tests like increasing the pre-tensioning could be carried out. An appropriate pre-tensioning may lead to a better material parameter estimation. Some other analytical calculations has been implemented considering the Nougat configuration (SS+REBCO+mandrel, magnetic field of about 30 T, given pre-tensioning and over-banding). Young modulus of REBCO and SS was varied until the radial stress becomes compressive for all layers: this situation was proved to be not reachable. This indicates that the pre-tensioning and over-banding are the most important factors to get a compressive radial stress for all layers and maintaining the quench protection aspect of MI winding.

Finally, a large part of the PhD work concerned the development of a new setup that allows a full-field displacement measurement of MI pancakes energized at cryogenic temperature (including inner at outer pancake configuration, and liquid helium temperature). The image acquisition and speckle were shown to work properly. However, post-processing of DIC results is required to remove rigid body motion and set-up contraction magnification effect. SS304

disc cooling test yielded good results and allowed for a verification of the proper functioning of the set-up. The same cooling test was carried out using MI CuBe2/SS304 pancake. A slight discrepancy between analytical and experimental results was observed despite a (a priori) proper correction of set-up contraction magnification effect. Further experiments are necessary including the positioning of a reference material close to the pancake to infer an appropriate set-up contraction correction. Another method of set-up contraction measurement is to use a laser distance sensor. An improvement of the analytical solution by implementing appropriate equivalent stiffness of the multilayered part may be finally necessary.

Furthermore, the cooling of the set-up using liquid helium (reaching 4 K) is a next important step. We have to verify that the same procedure as used for liquid nitrogen can apply (by observing first the thermal contraction). Once this step is validated, an energizing test of a MI REBCO pancake can be implemented to observe the displacements due to the Laplace forces. It is another important step for the validation of the analytical formulation, before to be able to use it as a fast dimensioning tool. Pre-tension and over-banding will be able to be estimated for any MI REBCO magnet design while respecting the stress limits of REBCO tape.

A - Tensile Test Experimental Data

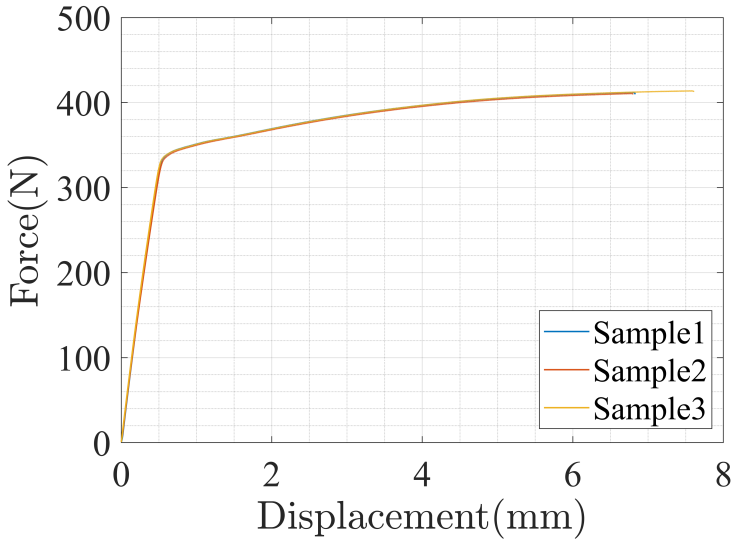

Figure A.1 – REBCO force-displacement

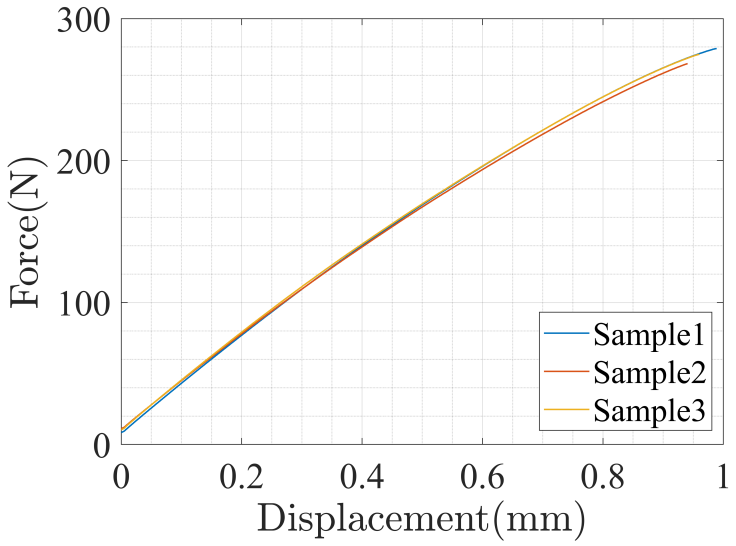

Figure A.2 – SS force-displacement

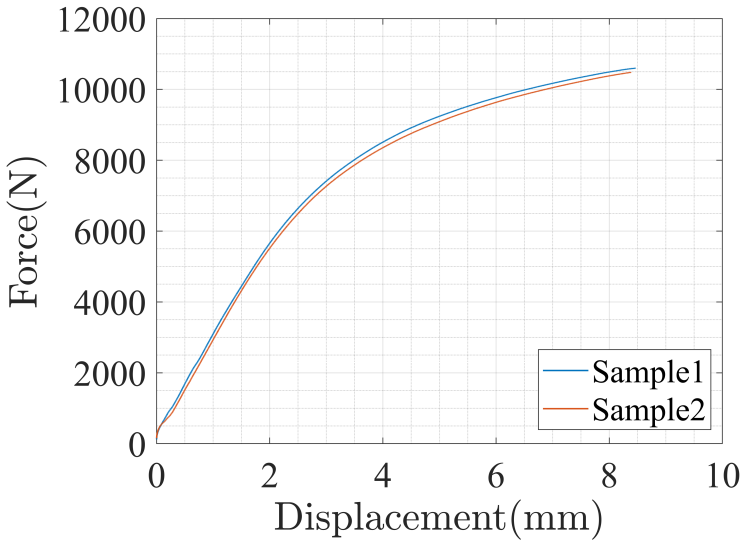

Figure A.3 – Brass force-displacement

B - Diametric Compression Test Experimental Data

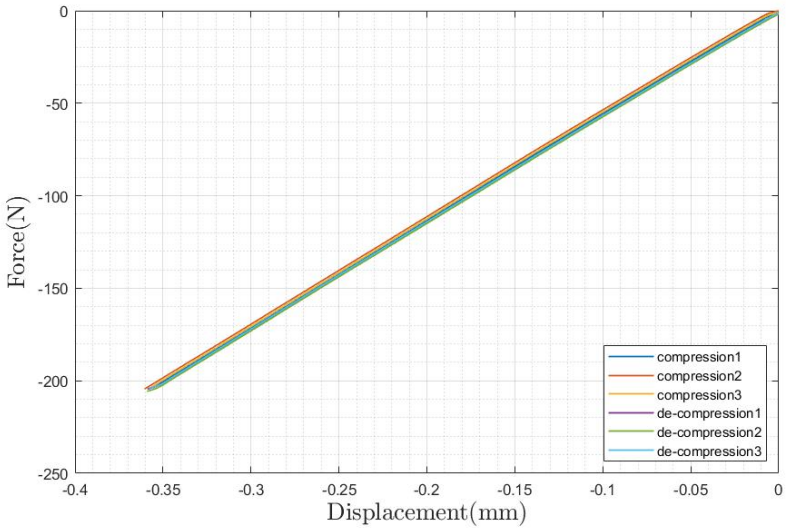

Figure B.1 – Diametric compression of the brass mandrel (compression/de-compression)

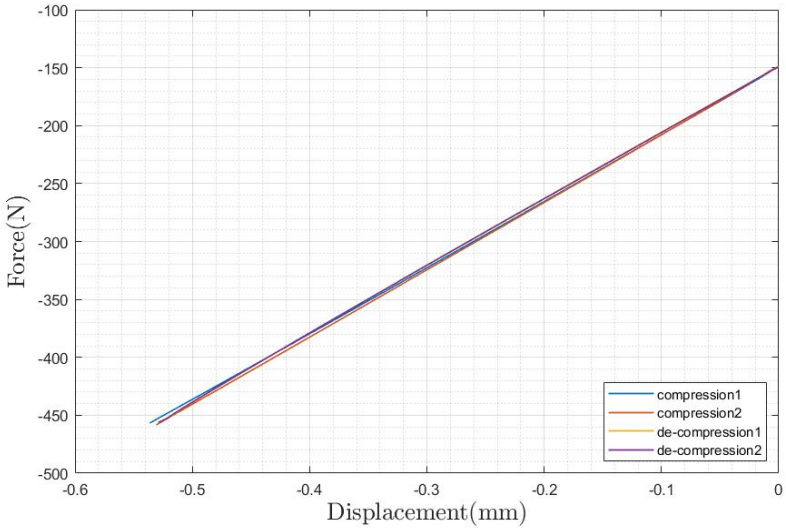

Figure B.2 – Diametric compression of Brass-REBCO with preload 150N (compression/de-compression)

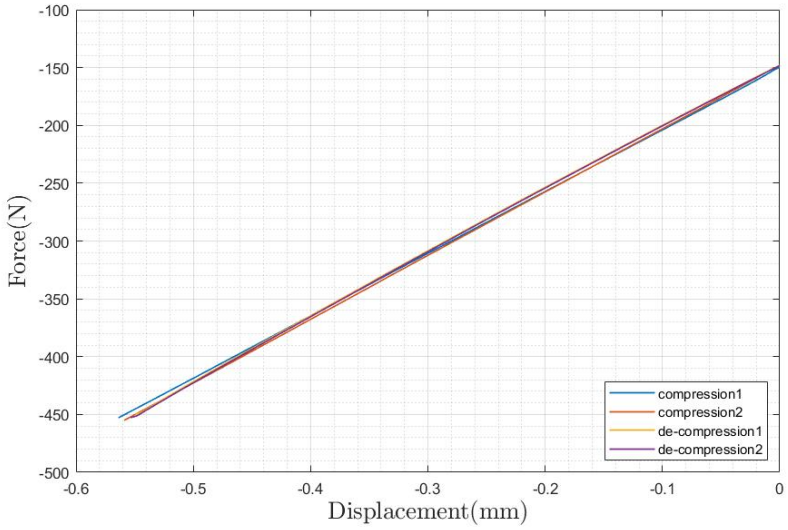

Figure B.3 – Diametric compression of Brass-SS with preload 150N (compression/de-compression)

C - FEMU-UF Brass Mandrel(Case2)

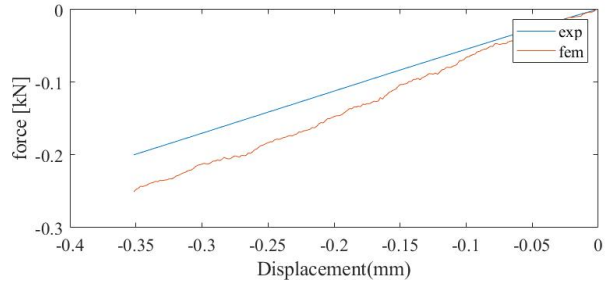

(a) FEMU-UF / Experimental forces at the 3^{rd} iteration of the FEMU-UF calculation

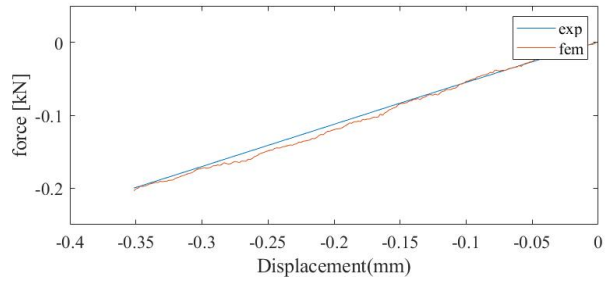

(b) FEMU-UF / Experimental forces at the 5^{th} iteration of the FEMU-UF calculation

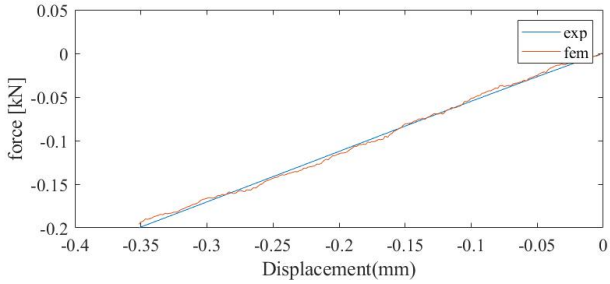

(c) FEMU-UF / Experimental forces the 20^{th} iteration of the FEMU-UF calculation

Figure C.1 – Evolution of FEMU-UF force at different iterations (initial guess: poisson ratio 0.4, Young modulus 150 GPa)

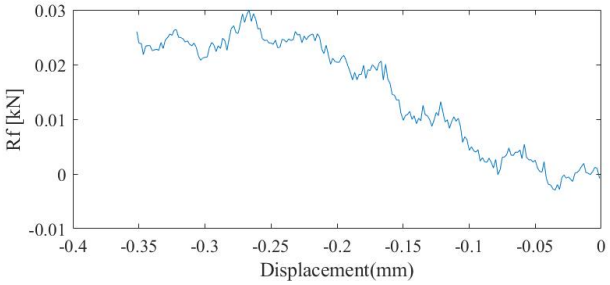

(a) Residual force at the 3^{rd} iteration of the FEMU-UF calculation

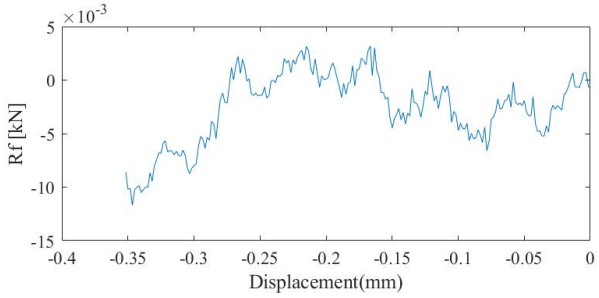

(b) Residual force at the 5^{th} iteration of the FEMU-UF calculation

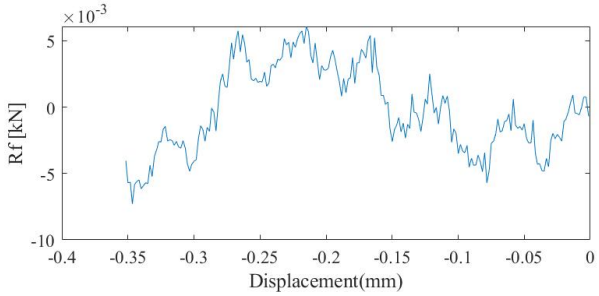

(c) Residual force at the 20^{th} iteration of the FEMU-UF calculation

Figure C.2 – Evolution of residual force at different iterations (initial guess: poisson ratio 0.4, Young modulus 150 GPa)

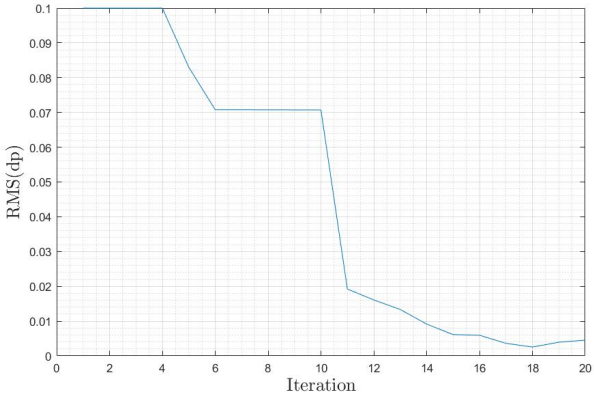

Figure C.3 – Evolution of RMS(dp) as function of the iteration number (initial guess: poisson ratio 0.4, Young modulus 150 GPa)

D - Debonding at the Interface of Brass/REBCO

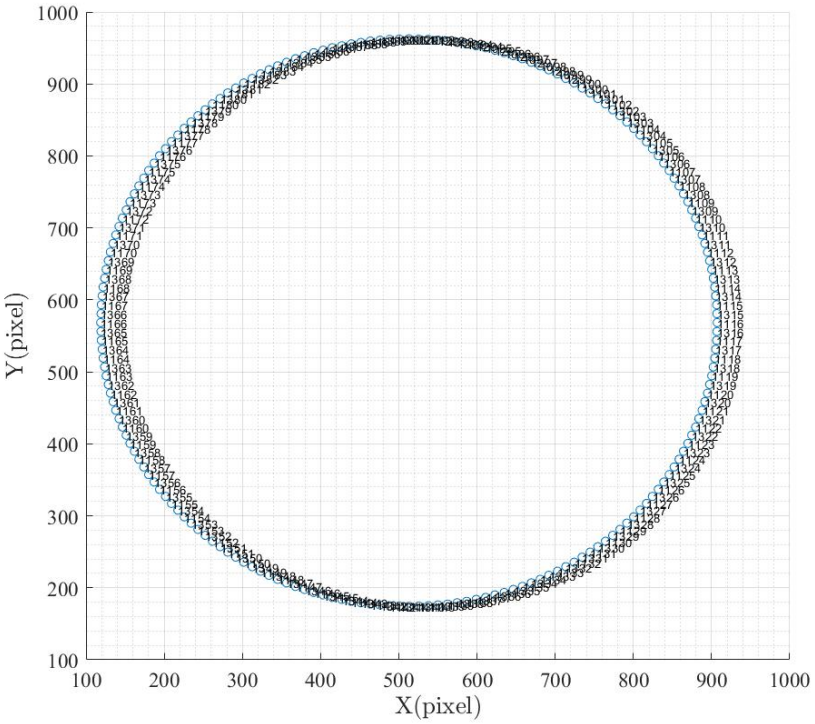

Figure D.1 – Nodes of the Brass mandrel at the interface between Brass/REBCO (200 Nodes, numbered(1091 - 1190) - (1291 - 1390), clockwise numbered from mid-top of circle, numbered as (1091 ,1291 ...))

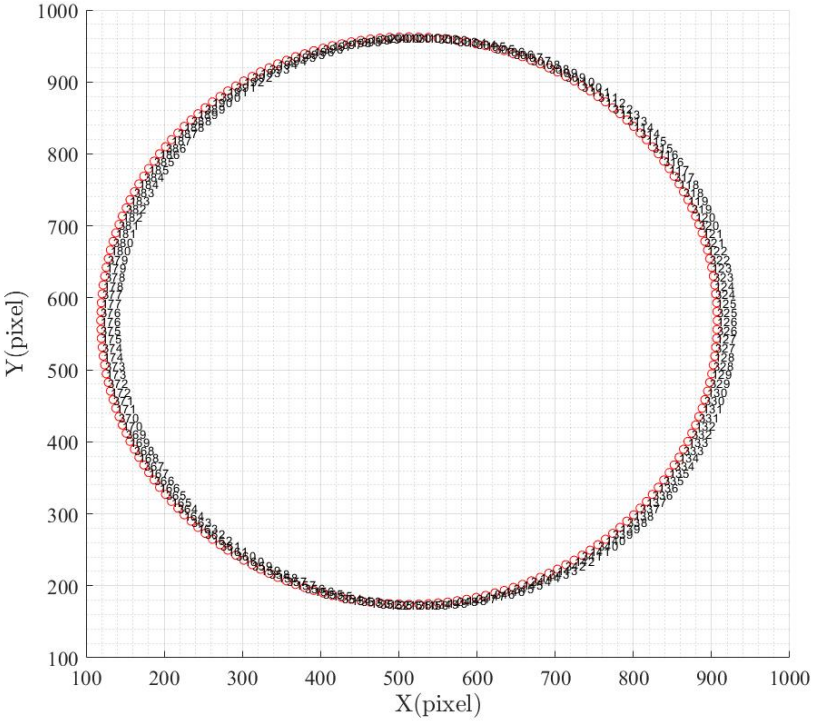

Figure D.2 – Nodes of the REBCO part at the interface between Brass/REBCO (200 Nodes, numbered(101 - 200) - (301 - 400), clockwise numbered from mid-top of circle, numbered as (101 , 301 ...))

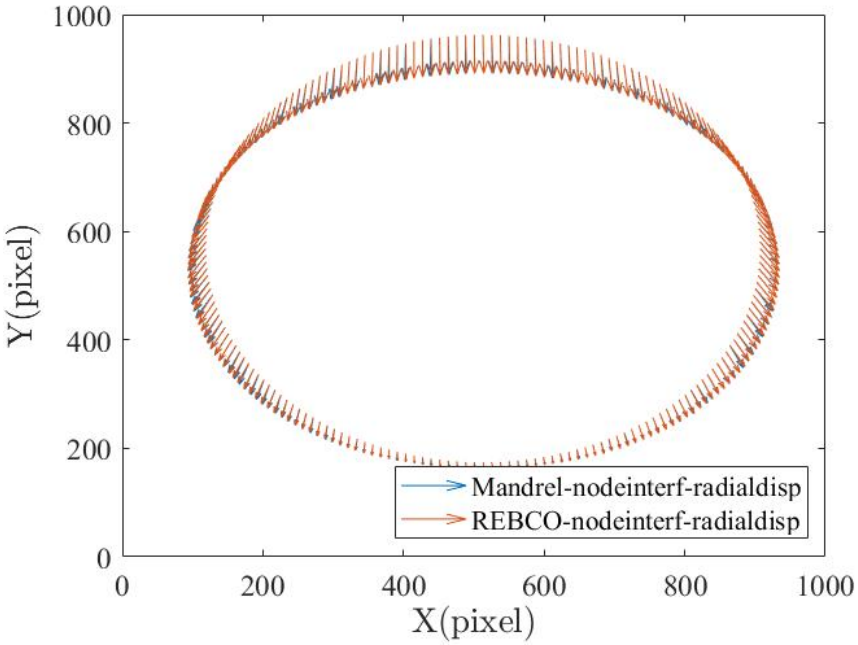

Figure D.3 – Radial displacement of the nodes at the interface of Brass/REBCO at the end of the test (vector representation)

E - FEMU-F Brass-REBCO / Brass-SS

Brass-REBCO

The brass properties are fixed, they are the results of the brass mandrel test

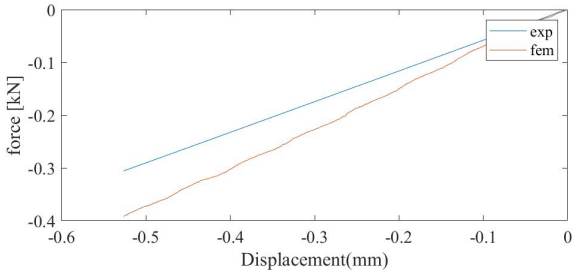

(a) FEMU-F / Experimental forces at the 1^{st} iteration of the FEMU-F calculation

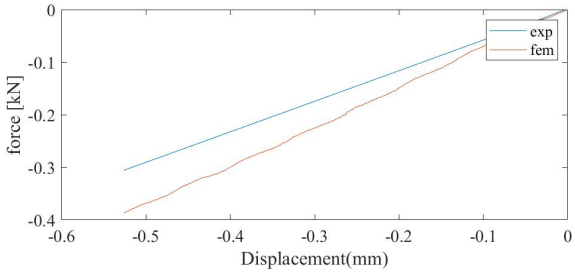

(b) FEMU-F / Experimental forces at the 20^{th} iteration of the FEMU-F calculation

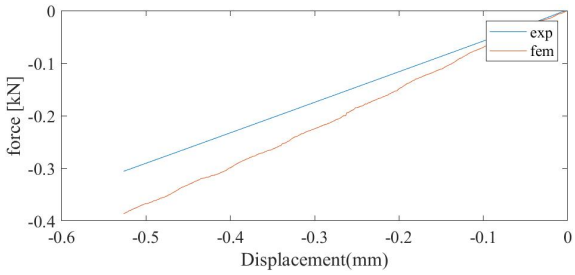

(c) FEMU-F / Experimental forces at the 38^{th} iteration of the FEMU-F calculation

Figure E.1 – Evolution of FEMU-F force at different iterations

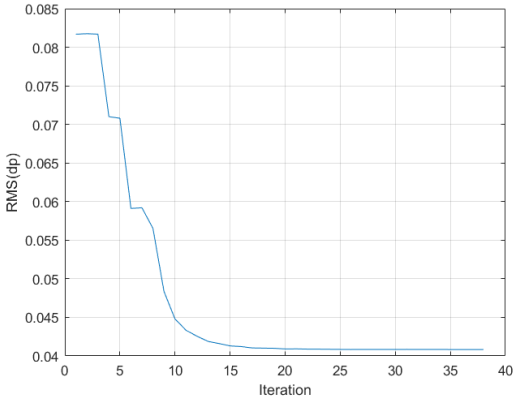

Figure E.2 – Evolution of RMS(dp) as function of the iteration number

Brass-REBCO

The brass properties are variable, but initial guess is the results of the brass mandrel test

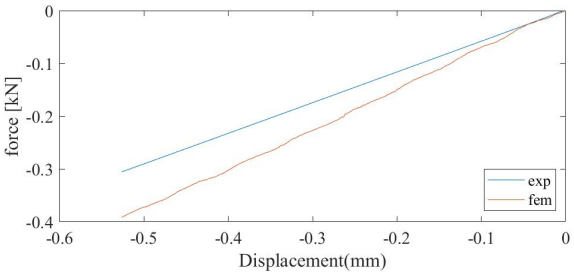

(a) FEMU-F / Experimental forces at the 1^{st} iteration of the FEMU-F calculation

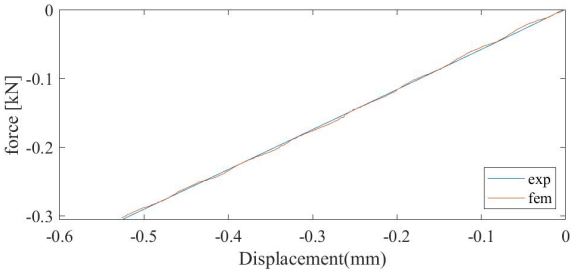

(b) FEMU-F / Experimental forces at the 10^{th} iteration of the FEMU-F calculation

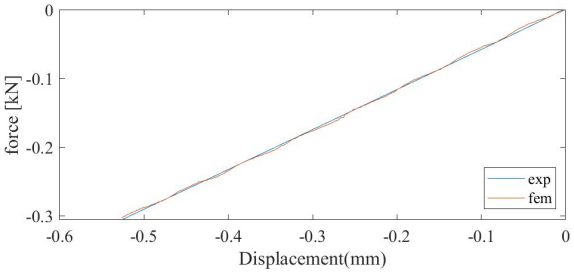

(c) FEMU-F / Experimental forces at the 29^{th} iteration of the FEMU-F calculation

Figure E.3 – Evolution of FEMU-F force at different iterations

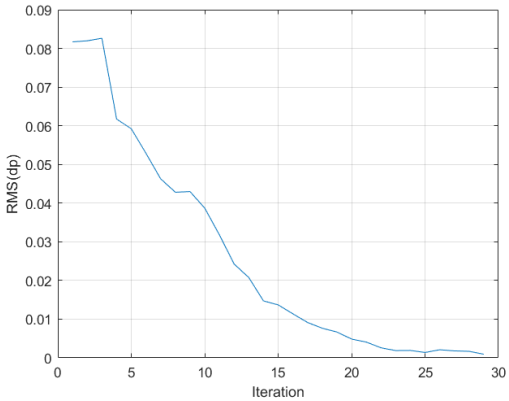

Figure E.4 – Evolution of RMS(dp) as function of the iteration number

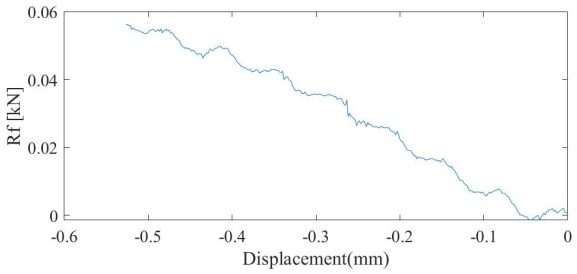

(a) Residual force at the 1^{st} iteration of FEMU-F calculation

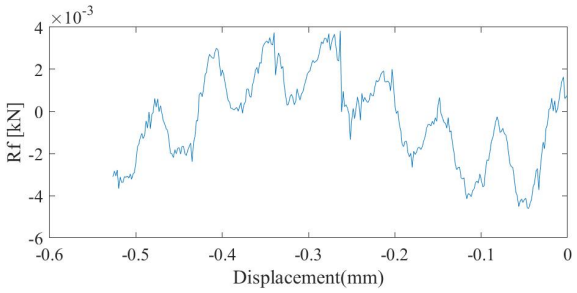

(b) Residual force at the 10^{th} iteration of FEMU-F calculation

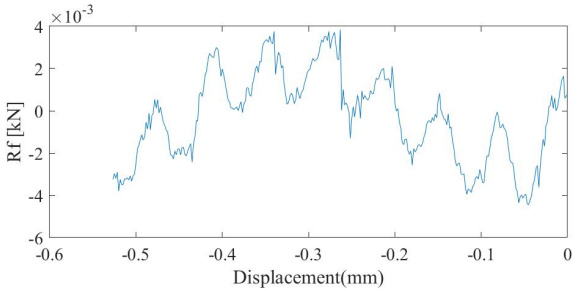

(c) Residual force at 29^{th} iteration of FEMU-F calculation

Figure E.5 – Evolution of residual force at different iterations

Figures E.1 and E.2 show that FEMU-F calculation didn't converge when brass properties are kept constant. However, Figures E.3 to E.5 show that FEMU-F calculation did converge when Brass isotropic properties were variable. However, REBCO properties achieved are still low like in FEMU-UF. The following properties were achieved: radial modulus 1.3 GPa, hoop modulus 364 MPa, Poisson ratio 0.25, and shear modulus 1 GPa. Same as in FEMU-UF, this is due to winding affecting the mechanical properties achieved for REBCO when considered as one piece material.

Brass-SS

The brass properties are fixed, they are the results of the brass mandrel test

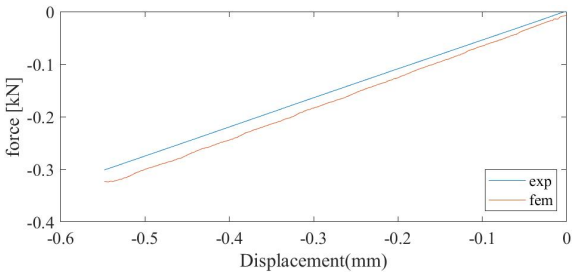

(a) FEMU-F / Experimental forces at the 1^{st} iteration of the FEMU-F calculation

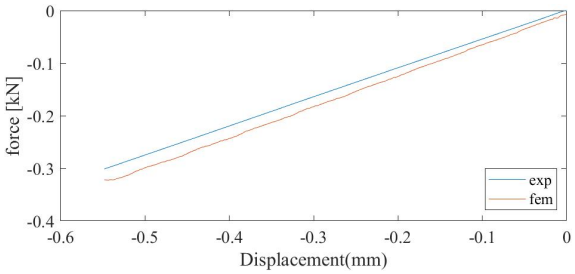

(b) FEMU-F / Experimental forces at the 3^{rd} iteration of the FEMU-F calculation

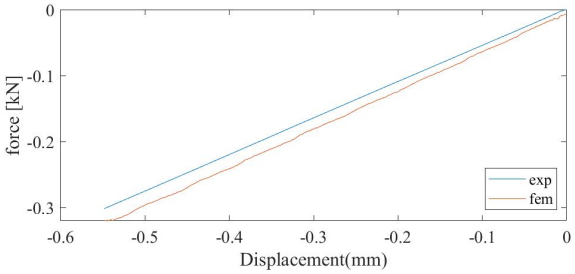

(c) FEMU-F / Experimental forces at the 6^{th} iteration of the FEMU-F calculation

Figure E.6 – Evolution of FEMU-F force at different iterations

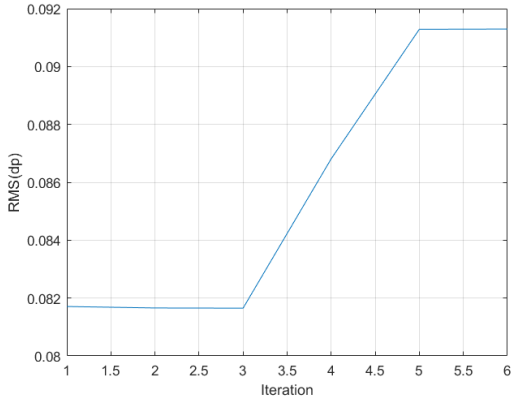

Figure E.7 – Evolution of RMS(dp) as function of the iteration number

Brass-SS

The brass properties are variable, but initial guess is the results of the brass mandrel test

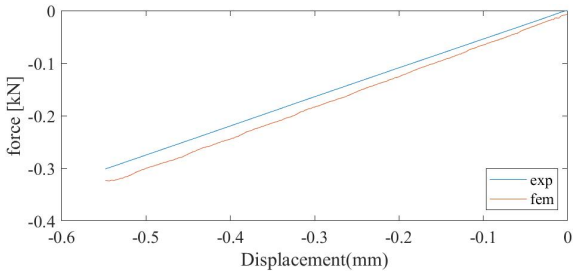

(a) FEMU-F / Experimental forces at the 1^{st} iteration of the FEMU-F calculation

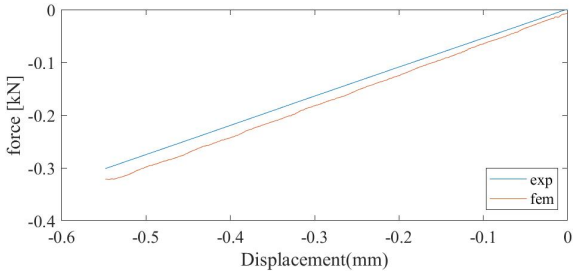

(b) FEMU-F / Experimental forces at 3^{rd} iteration of the FEMU-F calculation

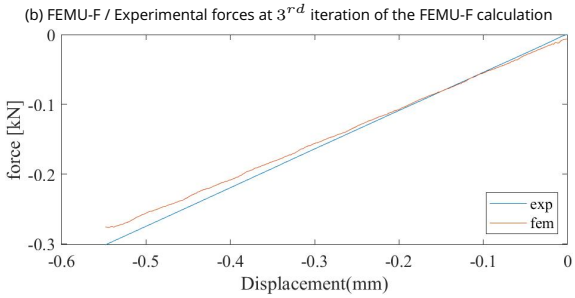

(c) FEMU-F / Experimental forces at 6^{th} iteration of the FEMU-F calculation

Figure E.8 – Evolution of FEMU-F force at different iterations

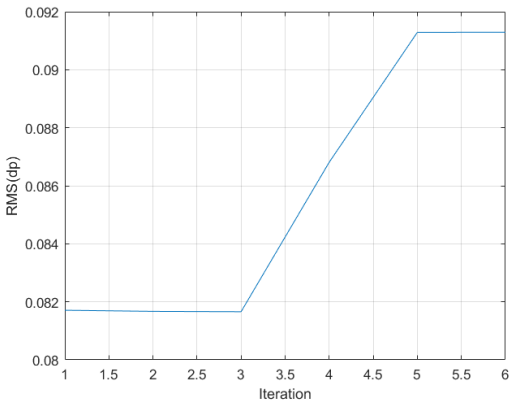

Figure E.9 – Evolution of RMS(dp) as function of the iteration number

As seen from Figures E.6 and E.7, FEMU-F calculation didn't converge when brass properties are kept constant. Moreover, as seen from Figures E.8 and E.9 FEMU-F calculation didn't converge as well when brass properties were variable. During calculation, after iteration 6 is done, Possion ratio of SS becomes above 0.5, which is not possible when SS is considered to be an orthotropic material in the calculation. This is because measured displacement field is not taken into account in the calculation.

F - Analytical Homogenization Calculation

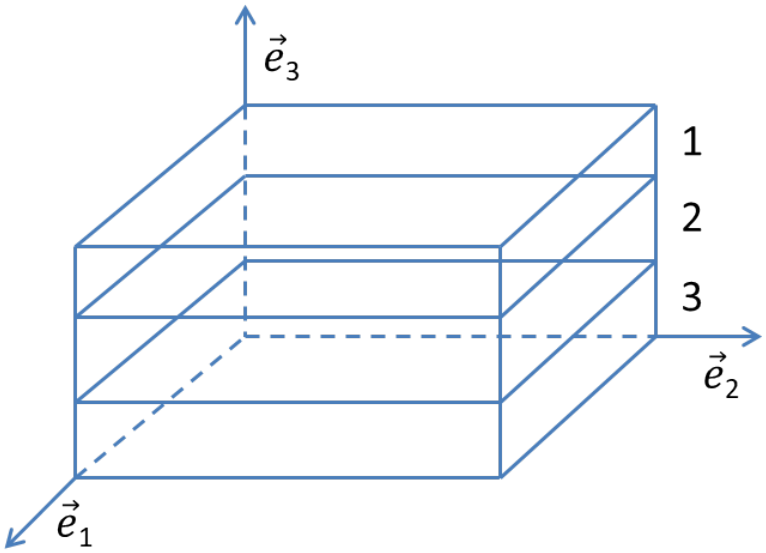

Figure F.1 – Composite material with different layered materials

The analytical homogenization calculation done for the layered composite is based on classical laminate theory. The composite follows the theory's assumptions that are:

- The composite is composed of perfectly bonded layers, i.e. no slipping between adjacent layers.
- Each layer is homogeneous with known properties.
- Each layer is in the plane stress state.
- The individual layers can be isotropic, orthotropic or transversely isotropic.

In the case of REBCO tape, all layers are assumed isotropic. The general relation between strain and stress using the compliance matrix is presented in local and global scale to simplify homogenization calculation later on.

$$
\begin{aligned}
\epsilon_{11} &= S_{11}\sigma_{11} + S_{12}\sigma_{22} + S_{13}\sigma_{33} \\
\epsilon_{22} &= S_{12}\sigma_{11} + S_{22}\sigma_{22} + S_{13}\sigma_{33} \\
\epsilon_{33} &= S_{13}\sigma_{11} + S_{13}\sigma_{22} + S_{33}\sigma_{33} \\
\epsilon_{23} &= S_{44}\sigma_{23} \\
\epsilon_{13} &= S_{44}\sigma_{13} \\
\epsilon_{12} &= S_{66}\sigma_{12}
\end{aligned}
\qquad \text{(F.1)}
$$

$$
\begin{aligned}
\epsilon^i_{11} &= S^i_{11}\sigma^i_{11} + S^i_{12}\sigma^i_{22} + S^i_{12}\sigma^i_{33} \\
\epsilon^i_{22} &= S^i_{12}\sigma^i_{11} + S^i_{11}\sigma^i_{22} + S^i_{12}\sigma^i_{33} \\
\epsilon^i_{33} &= S^i_{12}\sigma^i_{11} + S^i_{12}\sigma^i_{22} + S^i_{11}\sigma^i_{33} \\
\epsilon^i_{23} &= S^i_{66}\sigma^i_{23} \\
\epsilon^i_{13} &= S^i_{66}\sigma^i_{13} \\
\epsilon^i_{12} &= S^i_{66}\sigma^i_{12}
\end{aligned}
$$

Because of the layered structure and isotropic layers, loading along $\vec{e}_1$ and $\vec{e}_2$ leads to same stress-strain relations. Hence, loading is considered along $\vec{e}_1$ and $\vec{e}_3$.

F.1 . Loading along $\vec{e}_1$ direction

Loading along $\vec{e}_1$ only with a uniaxial stress σ, this leads to homogeneous deformation:

$$\begin{aligned} \epsilon_{11} &= \epsilon^i_{11} \qquad \sigma_{11} = \frac{1}{\sum_i S_i} \sum_i S_i \sigma^i_{11} \\ \epsilon_{12} &= \epsilon^i_{12} \qquad \sigma_{12} = \frac{1}{\sum_i S_i} \sum_i S_i \sigma^i_{12} \\ \epsilon_{13} &= \epsilon^i_{13} \qquad \sigma_{13} = \frac{1}{\sum_i S_i} \sum_i S_i \sigma^i_{13} \end{aligned} \tag{F.2}$$

Where S_i is the section area of layer i. Considering uniaxial stress along $\vec{e}_1$, this results the local stress tensor to be expressed as:

$$\sigma^i = \begin{bmatrix} \sigma^i_{11} & 0 & 0 \\ 0 & \sigma^i_{22} & 0 \\ 0 & 0 & 0 \end{bmatrix} \tag{F.3}$$

Using the following equations, the general stiffness can be related to the local one:

$$\begin{aligned} \sigma_{11} &= \frac{1}{\sum_i S_i} \sum_i S_i \sigma^i_{11} \\ \sigma_{22} &= \frac{1}{\sum_i S_i} \sum_i S_i \sigma^i_{22} \\ \epsilon_{33} &= \frac{1}{\sum_i e_i} \sum_i e_i \epsilon^i_{33} \end{aligned}$$

$$\begin{aligned} \epsilon_{11} &= S_{11}\sigma_{11} \\ \epsilon_{22} &= S_{12}\sigma_{11} \\ \epsilon_{33} &= S_{13}\sigma_{11} \end{aligned} \tag{F.4}$$

$$\begin{aligned} \epsilon^i_{11} &= S^i_{11}\sigma^i_{11} + S^i_{12}\sigma^i_{22} = \epsilon_{11} \\ \epsilon^i_{22} &= S^i_{12}\sigma^i_{11} + S^i_{11}\sigma^i_{22} = \epsilon_{22} \\ \epsilon^i_{33} &= S^i_{12}\sigma^i_{11} + S^i_{12}\sigma^i_{22} \end{aligned}$$

The local stresses can be related to the global strain using local stress-strain relation in F.4:

$$\sigma^i_{11} = \epsilon_{11}\left[\frac{S^i_{11}}{S^{i2}_{11} - S^{i2}_{12}}\right] - \epsilon_{22}\left[\frac{S^i_{12}}{S^{i2}_{11} - S^{i2}_{12}}\right] \tag{F.5}$$

$$\sigma^i_{22} = \epsilon_{11}\left[\frac{S^i_{12}}{S^{i2}_{12} - S^{i2}_{11}}\right] - \epsilon_{22}\left[\frac{S^i_{11}}{S^{i2}_{12} - S^{i2}_{11}}\right] \tag{F.6}$$

Furthermore, as the stress is uniaxial along $\vec{e}_1$, this results in having the first global stresses from F.4 expressed as:

$$s\sigma_{11} = \epsilon_{11}\sum_i s_i\left[\frac{S^i_{11}}{S^{i2}_{11} - S^{i2}_{12}}\right] - \epsilon_{22}\sum_i s_i\left[\frac{S^i_{12}}{S^{i2}_{11} - S^{i2}_{12}}\right] \tag{F.7}$$

$$0 = \epsilon_{11} \sum_i s_i \left[\frac{S_{12}^i}{S_{12}^{i2} - S_{11}^{i2}} \right] - \epsilon_{22} \sum_i s_i \left[\frac{S_{11}^i}{S_{12}^{i2} - S_{11}^{i2}} \right] \tag{F.8}$$

This gives rise to the following relations:

$$\epsilon_{22} = \epsilon_{11} \frac{\sum_i s_i \left[\frac{S_{12}^i}{S_{12}^{i2} - S_{11}^{i2}} \right]}{\sum_i s_i \left[\frac{S_{11}^i}{S_{12}^{i2} - S_{11}^{i2}} \right]} \tag{F.9}$$

$$\epsilon_{11} = \epsilon_{22} \frac{\sum_i s_i \left[\frac{S_{11}^i}{S_{12}^{i2} - S_{11}^{i2}} \right]}{\sum_i s_i \left[\frac{S_{12}^i}{S_{12}^{i2} - S_{11}^{i2}} \right]} \tag{F.10}$$

Hence, S_{11} constant can be calculated by using F.9 in F.7 and using the global stiffness first relation in F.4.

$$\frac{s}{S_{11}} = \sum_i s_i \left[\frac{S_{11}^i}{S_{11}^{i2} - S_{12}^{i2}} \right] - \sum_i s_i \left[\frac{S_{12}^i}{S_{11}^{i2} - S_{12}^{i2}} \right] \frac{\sum_i s_i \left[\frac{S_{12}^i}{S_{12}^{i2} - S_{11}^{i2}} \right]}{\sum_i s_i \left[\frac{S_{11}^i}{S_{12}^{i2} - S_{11}^{i2}} \right]} \tag{F.11}$$

Similarly, S_{12} constant can be calculated by using F.10 in F.7 and using the global stiffness second relation in F.4.

$$\frac{s}{S_{12}} = \frac{\sum_i s_i \left[\frac{S_{11}^i}{S_{12}^{i2} - S_{11}^{i2}} \right]}{\sum_i s_i \left[\frac{S_{12}^i}{S_{12}^{i2} - S_{11}^{i2}} \right]} \sum_i s_i \left[\frac{S_{11}^i}{S_{11}^{i2} - S_{12}^{i2}} \right] - \sum_i s_i \left[\frac{S_{12}^i}{S_{11}^{i2} - S_{12}^{i2}} \right] \tag{F.12}$$

As for S_{13}, it is calculated using the third relation in F.4, the local expressions of ϵ_{33}^i, σ_{11}^i, σ_{22}^i (F.5), F.6), and the local expressions of ϵ_{11}^i and ϵ_{22}^i from F.4.

$$S_{13}e = S_{11} \sum_i e_i \left(\left[\frac{S_{11}^i S_{12}^i}{S_{11}^{i2} - S_{12}^{i2}} \right] + \left[\frac{S_{12}^{i2}}{S_{12}^{i2} - S_{11}^{i2}} \right] \right) - S_{12} \sum_i e_i \left(\left[\frac{S_{12}^{i2}}{S_{11}^{i2} - S_{12}^{i2}} \right] + \left[\frac{S_{11}^i S_{12}^i}{S_{12}^{i2} - S_{11}^{i2}} \right] \right) \tag{F.13}$$

F.2 . Loading along $\vec{e}_3$ direction

Loading along $\vec{e}_3$ only with a uniaxial σ, this leads to homogeneous stress:

$$\begin{aligned} \sigma_{33} &= \sigma_{33}^i \qquad \epsilon_{33} = \frac{1}{\sum_i e_i} \sum_i e_i \epsilon_{33}^i \\ \sigma_{13} &= \sigma_{13}^i \qquad \epsilon_{13} = \frac{1}{\sum_i e_i} \sum_i e_i \epsilon_{13}^i \\ \sigma_{23} &= \sigma_{23}^i \qquad \epsilon_{23} = \frac{1}{\sum_i e_i} \sum_i e_i \epsilon_{23}^i \end{aligned} \tag{F.14}$$

Where e_i is the thickness area of layer i. Considering uniaxial stress along $\vec{e}_3$, this results the local stress tensor to be expressed as:

$$\sigma^i = \begin{bmatrix} \sigma_{11}^i & 0 & 0 \\ 0 & \sigma_{22}^i & 0 \\ 0 & 0 & \sigma \end{bmatrix} \tag{F.15}$$

Using the following equations, the general stiffness can be related to the local one:

$$\epsilon_{33} = \frac{1}{\sum_i e_i} \sum_i e_i \epsilon_{33}^i$$

$$\begin{aligned} \epsilon_{11} &= S_{13}\sigma_{33} \\ \epsilon_{33} &= S_{33}\sigma_{33} \end{aligned} \tag{F.16}$$

$$\begin{aligned} \epsilon_{11}^i &= S_{11}^i\sigma_{11}^i + S_{12}^i\sigma_{11}^i + S_{12}^i\sigma_{33} = \epsilon_{11} \\ \epsilon_{33}^i &= S_{12}^i\sigma_{11}^i + S_{12}^i\sigma_{11}^i + S_{11}^i\sigma_{33} \end{aligned}$$

The second and fourth equation in F.16 results in:

$$\sigma_{11}^i = \left(\frac{S_{13} - S_{12}^i}{S_{11}^i + S_{12}^i}\right)\sigma_{33} \tag{F.17}$$

In addition, the first and fifth equation lead to:

$$S_{33}\sigma_{33}e = \sum_i e_i(2S_{12}^i\sigma_{11}^i + S_{11}^i\sigma_{33}) \tag{F.18}$$

Hence, to obtain S_{33}, F.17 is used in F.18.

$$S_{33}e = \sum_i e_i(2S_{12}^i\left(\frac{S_{13} - S_{12}^i}{S_{11}^i + S_{12}^i}\right) + S_{11}^i) \tag{F.19}$$

Thus, only S_{44} term remains to be calculated since S_{66} is related to S_{11} and S_{12}.

$$S_{66} = S_{11} - S_{12} \tag{F.20}$$

F.3 . Shear test in the $(\vec{e}_1, \vec{e}_3)$ plane

A global shear stress tensor is considered:

$$\sigma = \begin{bmatrix} 0 & 0 & \sigma_{13} \\ 0 & 0 & 0 \\ \sigma_{13} & 0 & 0 \end{bmatrix} \tag{F.21}$$

This tensor results in the local stress tensor being:

$$\sigma^i = \begin{bmatrix} 0 & 0 & \sigma_{13}^i \\ 0 & 0 & 0 \\ \sigma_{13}^i & 0 & 0 \end{bmatrix} \tag{F.22}$$

The shear stress σ_{13} is applied on the upper surface of normal $\vec{e}_3$ and the side surface of normal $\vec{e}_1$. In the first case, homogeneous stress is applied where as homogeneous deformation is applied for the second case. Considering the homogeneous deformation case, this leads to:

$$\frac{1}{\sum_i s_i} \sum_i s_i \sigma_{13}^i = \sigma_{13}$$

$$\epsilon_{13} = S_{44}\sigma_{13} \tag{F.23}$$

$$\epsilon_{13}^i = S_{44}^i\sigma_{13}^i = \epsilon_{13}$$

Hence, S_{44} can be expressed as:

$$S_{44} = \frac{s}{\sum_i s_i \frac{1}{S_{44}^i}} \tag{F.24}$$

Considering the homogeneous stress case, this gives the following set of equations:

$$\begin{aligned} \frac{1}{\sum_i e_i} \sum_i e_i \epsilon_{13}^i &= \epsilon_{13} \\ \epsilon_{13} &= S_{44} \sigma_{13} \\ \epsilon_{13}^i &= S_{44}^i \sigma_{13} \end{aligned} \tag{F.25}$$

Hence, S_{44} can also be expressed as:

$$S_{44} = \frac{1}{e} \sum_i e_i S_{44}^i \tag{F.26}$$

Thus, to reach an intermediate value of S_{44}:

$$S_{44} = \alpha \frac{s}{\sum_i s_i \frac{1}{S_{44}^i}} + (1 - \alpha) \frac{1}{e} \sum_i e_i S_{44}^i \tag{F.27}$$

Where $\alpha \in [0, 1]$. This allows to check the values from both cases, and in the calculation done for the REBCO tape, 0.5 is chosen as value to consider value of both cases equally. Thus, all mechanical properties of the REBCO tape can be calculated using the analytical homogenization.

G - REBCO Properties Benchmarking using Analytical Homogenization and KEFF Procedure

As REBCO is a layered composite (Fig. 3.1), its mechanical properties can be calculated using analytical homogenization based on classical laminate theory [146] and Cast3m finite element KEFF procedure [147] in the elastic regime. Table G.1 shows the mechanical properties of the layers that are considered isotropic. Hence, REBCO tape is transverse isotropic because of the layered structure.
Local and global stress-strain relations are defined to be to do the analytic homogenization calculation. The calculation is based on the relation between the local and global deformations and stresses. Regarding the local stress-strain relation in the isotropic layers, it can be written using the compliance matrix using the following Voigt representation:

$$\hat{\epsilon}^i = \mathbf{S}^i \cdot \hat{\sigma}^i \qquad \epsilon^i_j = \mathbf{S}^i_{jk} \cdot \sigma^i_k \tag{G.1}$$

As all layers are assumed isotropic, the local compliance tensor (G.2) is made of two coefficients, the young modulus E^i and the poisson ratio ν^i.

$$\mathbf{S}^i = \begin{bmatrix} \frac{1}{E^i} & \frac{-\nu^i}{E^i} & \frac{-\nu^i}{E^i} & 0 & 0 & 0 \\ \frac{-\nu^i}{E^i} & \frac{1}{E^i} & \frac{-\nu^i}{E^i} & 0 & 0 & 0 \\ \frac{-\nu^i}{E^i} & \frac{-\nu^i}{E^i} & \frac{1}{E^i} & 0 & 0 & 0 \\ 0 & 0 & 0 & \frac{1+\nu^i}{E^i} & 0 & 0 \\ 0 & 0 & 0 & 0 & \frac{1+\nu^i}{E^i} & 0 \\ 0 & 0 & 0 & 0 & 0 & \frac{1+\nu^i}{E^i} \end{bmatrix} \tag{G.2}$$

Similarly, the global stress-strain relation can be expressed as:

$$\hat{\epsilon} = \mathbf{S} \cdot \hat{\sigma} \qquad \epsilon_j = \mathbf{S}_{jk} \cdot \sigma_k \tag{G.3}$$

Where the global compliance matrix is expressed as:

$$\mathbf{S} = \begin{bmatrix} S_{11} & S_{12} & S_{13} & 0 & 0 & 0 \\ S_{12} & S_{11} & S_{13} & 0 & 0 & 0 \\ S_{13} & S_{13} & S_{33} & 0 & 0 & 0 \\ 0 & 0 & 0 & S_{44} & 0 & 0 \\ 0 & 0 & 0 & 0 & S_{44} & 0 \\ 0 & 0 & 0 & 0 & 0 & S_{66} \end{bmatrix} \tag{G.4}$$

It can be also expressed using the young modulus and poisson ratio as:

	Young Modulus (GPa)	Poisson Ratio
Hastealloy-C276	167	0.29
Copper	117	0.338
Silver	74	0.395

Table G.1 – RECBO Layers' Mechanical Properties

$$\mathbf{S} = \begin{bmatrix} \frac{1}{E_1} & -\frac{\nu_{12}}{E_1} & -\frac{\nu_{13}}{E_1} & 0 & 0 & 0 \\ -\frac{\nu_{12}}{E_1} & \frac{1}{E_1} & -\frac{\nu_{13}}{E_1} & 0 & 0 & 0 \\ -\frac{\nu_{13}}{E_1} & -\frac{\nu_{13}}{E_1} & \frac{1}{E_3} & 0 & 0 & 0 \\ 0 & 0 & 0 & \frac{1}{2G_{13}} & 0 & 0 \\ 0 & 0 & 0 & 0 & \frac{1}{2G_{13}} & 0 \\ 0 & 0 & 0 & 0 & 0 & \frac{(1+\nu_{12})}{E_1} \end{bmatrix} \tag{G.5}$$

As for the stress and strains, they can be expressed as:

$$\hat{\sigma} = \begin{bmatrix} \sigma_{11} \\ \sigma_{22} \\ \sigma_{33} \\ \sigma_{23} \\ \sigma_{13} \\ \sigma_{12} \end{bmatrix} \quad and \quad \hat{\epsilon} = \begin{bmatrix} \epsilon_{11} \\ \epsilon_{22} \\ \epsilon_{33} \\ \epsilon_{23} \\ \epsilon_{13} \\ \epsilon_{12} \end{bmatrix} \tag{G.6}$$

Because of the layered structure of the REBCO tape, the homogeneous conditions vary depending on the loading conditions and surfaces where forces are applied. To get the parameters, loading across different directions is considered and the equations are solved in Appendix F. After analytical homogenization calculation, the relations between the REBCO tape and the layers' mechanical properties are found.
To further verify the results of analytical homogenization, finite element homogenization is done using Cast3m. The Cast3m procedure KEFF [147] is utilized for the homogenization calculation with the sub-procedure CLPD [148] that defines the stiffness matrix and nodal forces associated with the boundary conditions and the loading in mean strain for the calculation. The homogenization method described by Berger [149] is used in KEFF.
In the finite element homogenization KEFF, the calculation is done on a representative volume element (RVE) assuming that the components of the composite are isotropic and periodic. The assumptions of small displacement and elastic linear behaviour are considered in KEFF. The constitutive law is determined in the RVE through an averaging procedure. In this procedure, the averaged stress and strain over RVE are expressed as:

$$\bar{\sigma}_{ij} = \frac{1}{V} \int_V \sigma_{ij} dV \tag{G.7}$$

$$\bar{\epsilon}_{ij} = \frac{1}{V} \int_V \epsilon_{ij} dV \tag{G.8}$$

where V is the volume of the RVE. The relation between the averaged stress and strain is used to determine the homogenized stiffness matrix. For example, by assuming ϵ_{11} is a non zero constant, first column of stiffness matrix is determined, and the same procedure is applied for determining the remaining columns of stiffness matrix. Then, from the stiffness matrix, the orthotropic properties are determined.
Table G.2 shows that the analytical homogenization results are in agreement with that of KEFF. Furthermore, the hoop modulus and poisson ratio results ν_{thetaz} of homogenization are in accordance with that of tensile testing. However, the radial modulus from diametric compression test is much lower than that of homogenisation because of the winding effect on bulk radial modulus.

	Analytical Homogenization	Cast3m (KEFF)
Radial Modulus (GPa)	147.45	153.23
Hoop Modulus (GPa)	150.4	153.75
Poisson ratio $r\theta$	0.308	0.306
Poisson ratio θz	0.3	0.303
Shear Modulus(GPa) $r\theta$	57.84	57.95

Table G.2 – REBCO Properties

H - Cooling test LN2 SS304 disc / MI CuBe2-SS304

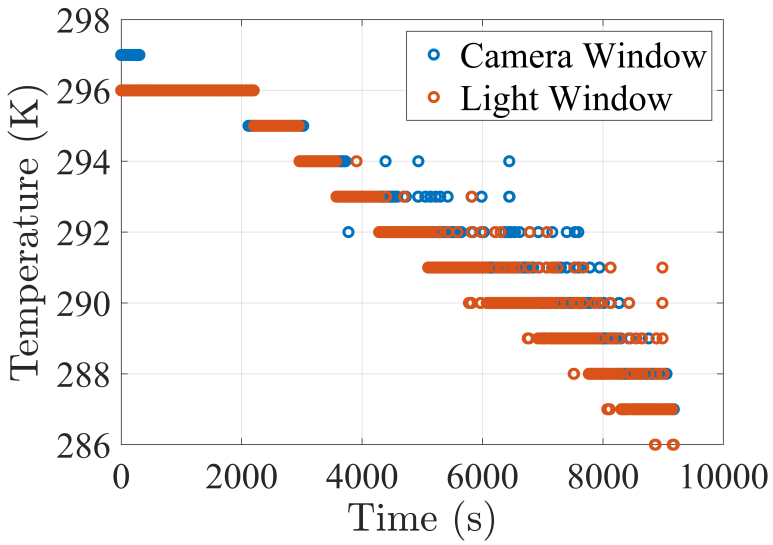

Figure H.1 – Window temperature during cooling test

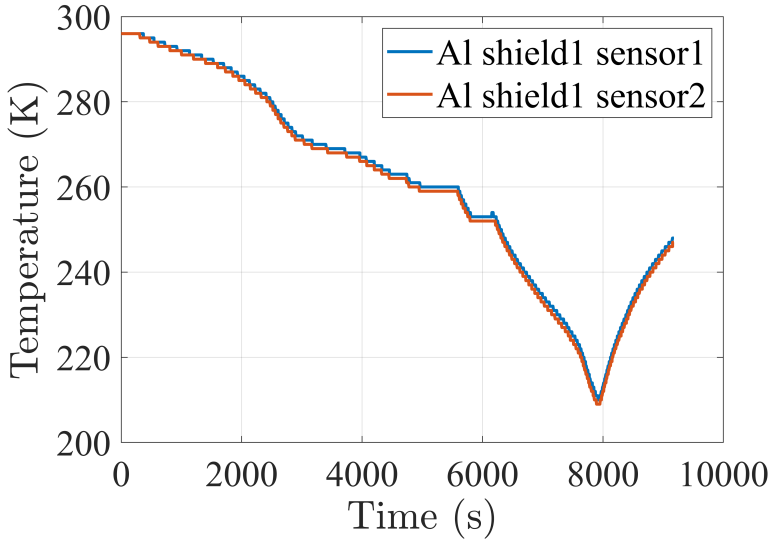

Figure H.2 – Temperature at the first aluminium Heat Shield

With the PT100 being class B category, its uncertainty is 1.3 K at 80 K, and the DAQ module used for measurement was NI 9217 that has an uncertainty of 0.02 K. Thus, the temperature measurement uncertainty for PT100 sensors is calculated using root mean square, which gives a value of 1.3 K.

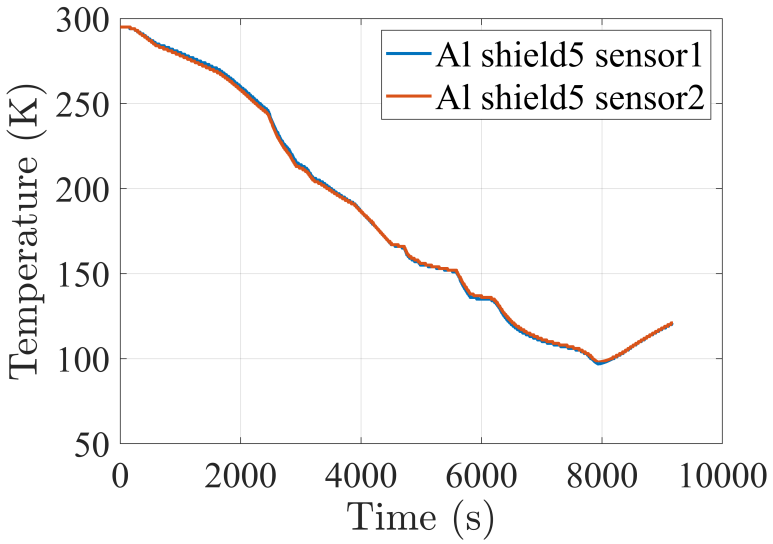

Figure H.3 – Temperature at the fifth aluminium Heat Shield

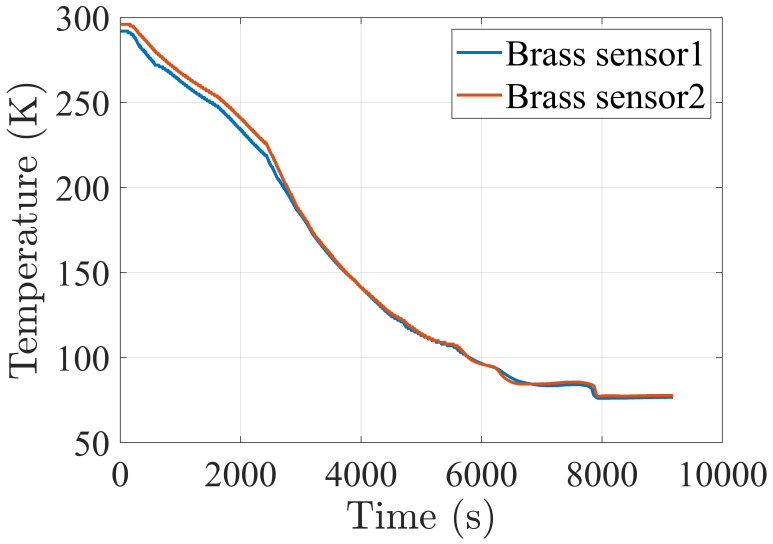

Figure H.4 – Temperature of the brass support

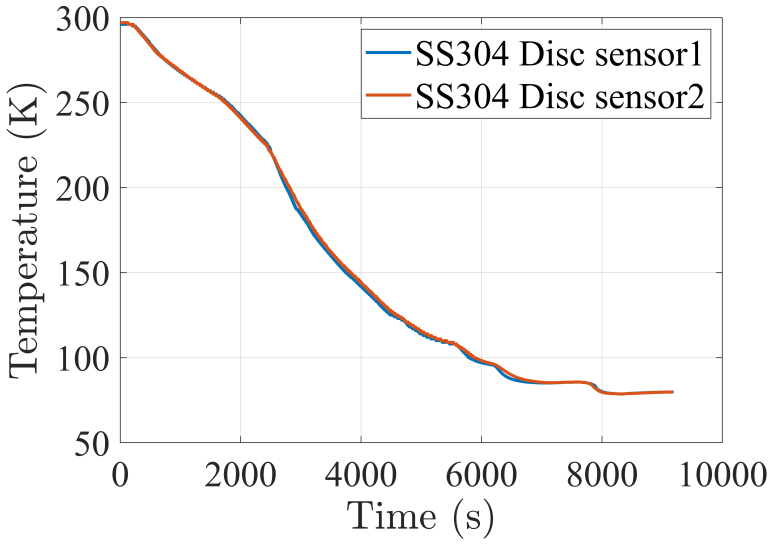

Figure H.5 – Temperature of the stainless steel 304 disc

I - Résume en français: participation aux développements d'un aimant haut-champ 30 T en REBaCuO

I.1 . Bobine HTS à isolation métallique

Le phénomène de supraconductivité (conduction d'un courant électrique avec une résistance négligeable) découvert en 1911, a permis l'amélioration de nombreuses techniques et instruments comme l'imagerie à résonance magnétique (IRM), la résonance magnétique nucléaire (RMN), les accélérateurs de particules, etc... Les alliages niobium-titane, supraconducteurs ductiles, sont adaptés à des applications où le champ peut atteindre 15 T. Cette résistance aux champs élevés a permis la réalisation d'aimants supraconducteurs, au cœur du développement des IRM, de la RMN et des accélérateurs de particules. Les supraconducteurs étaient jusqu'alors limités par leur faible température critique, appelés supraconducteurs à basse température "LTS", où la température critique est de quelques Kelvins, nécessitant un refroidissement à l'hélium liquide (environ 4K). A cette température, le champ magnétique critique est d'environ 28 T pour le supraconducteur niobium-étain.

En 1986, une nouvelle famille de supraconducteurs a été découverte, les supraconducteurs à haute température "HTS", dont la température critique est supérieure à 30 K, atteignant même 92 K dans le supraconducteur YBCO. La température critique de l'YBCO (REBCO) est supérieure au point d'ébullition de l'azote liquide à pression atmosphérique, ce qui ouvre un nouveau champ d'applications pour les supraconducteurs. L'emploi d'azote liquide simplifie considérablement les exigences de refroidissement, l'azote étant moins cher, abondant et présentant une enthalpie de changement d'état élevée. Les premiers supraconducteurs HTS découverts étaient basés sur des matériaux de type perovskite/cuprate, mais d'autres matériaux de la famille des HTS ont été découverts par la suite comme le diborure de magnésium ou les supraconducteurs à base de fer.

Une haute température critique n'est pas le seul point positif des supraconducteurs à haute température. On a également découvert que leur champ magnétique critique est beaucoup plus élevé que les 23,5 T relevés pour le supraconducteur niobium-étain à 4K. Les expériences telles que l'aimant "Nougat", fruit d'un effort conjoint du CEA Saclay et du LNCMI, ont montré qu'il était possible d'atteindre 32,5 T. L'aimant hybride du NHMFL a même atteint 45 T, démontrant la capacité des supraconducteurs à haute température à maintenir la supraconductivité à des champs élevés (l'emploi d'une température cryogénique basse, proche de celle de l'hélium liquide, est cependant nécessaire). Cependant, le phénomène de quench, auquel tout supraconducteur est possiblement sujet, s'est avéré être un problème majeur dans les aimants HTS, contrairement aux aimants LTS.

Le phénomène de quench correspond à une transition soudaine d'un état supraconducteur à un état résistif dans une partie du matériau. Un emballement peut alors apparaître compte tenu des forts courants pouvant amener à la destruction complète de l'électro-aimant . La propagation de la zone transitée (zone de quench) est extrêmement rapide dans les aimants LTS, allant d'un à plusieurs dizaines de mètres par seconde, ce qui rend la détection et la protection efficace (section résistive plus grande permettant de réduire rapidement les densités de courant, alimentation détournée vers une résistance externe). Contrairement aux aimants

LTS, la propagation de la quench dans les aimants HTS est lente, de l'ordre de quelques millimètres à quelques centimètres par seconde, ce qui complique considérablement la détection et la protection contre ce phénomène.

Une configuration d'aimant HTS non isolé (spires conductrices contenant une fine bande de matériau supraconducteur enroulées les unes sur les autres) a été testée et comparée à celle de l'aimant HTS isolé. Il s'est avéré que la configuration sans isolation permet de protéger efficacement l'aimant (il a pu transité plusieurs fois), en permettant au courant de contourner la région transitée et de passer de manière radiale à la spire supraconductrice la plus proche. Malheureusement, la vitesse de montée en courant était significativement détériorée à cause du courant radial généré pendant la rampe en raison de l'inductance mutuelle entre les tours. Ce problème a été résolu en introduisant la configuration d'isolation métallique (MI), où les bandes HTS en REBCO sont co-enroulées avec un fin ruban métallique rigide et à haute limite d'élasticité, cette bande métallique augmente la résistance électrique de contact de manière significative, diminuant ainsi le courant radial pendant la rampe. En outre, il fournit un support mécanique à l'aimant permettant d'atteindre des champs plus élevés.

On a constaté que les rubans REBCO se dégradent si la contrainte mécanique dépasse la limite d'élasticité ou si la déformation axiale dépasse une valeur seuil. La structure de la bande REBCO impose différentes limites mécaniques qui doivent être respectées lors de la conception et du fonctionnement de l'aimant. Ainsi, une étude mécanique des aimants MI HTS REBCO est importante pour assurer leur bon fonctionnement, en particulier pour les aimants à haut champ où les forces de Laplace sont élevées.

L'objectif de cette thèse est de réaliser une étude mécanique poussée des d'électro-aimants MI HTS REBCO aux champs élevés. Le format cylindrique plat et creux est retenu (format galette ou pancake). Différentes formulations analytiques pour évaluer les contraintes et les déplacements pendant les trois chargements mécaniques principaux (bobinage, refroidissement, alimentation électrique) sont d'abord proposées. Ces formulations sont testées et comparées avec les résultats d'une simulation éléments-finis de l'aimant Nougat développée avec le logiciel Cast3m (cette simulation fait office de simulation de référence). Nous cherchons ensuite à caractériser le comportement mécanique du REBCO et d'un acier inoxydable utilisé pour le co-bobinage, grâce à des expériences dédiées dont un essai de compression diamétrale. Nous avons enfin développé un nouveau dispositif expérimental qui permet de mesurer le déplacement plein champ des électroaimants à température cryogénique avec corrélation d'images numériques. Ce dispositif est testé et validé et est utilisé en situation de refroidissement. Les résultats expérimentaux sont comparés aux formulations analytiques et aux résultats numériques.

I.2 . Formulations analytiques des déplacements et des contraintes survenant dans une bobine MI HTS

Les électroaimants MI REBCO sont supposés être des cylindres axisymétriques et sans contraintes de cisaillement (il s'agit en réalité de spirales). Le mandrin en acier inoxydable, le ruban REBCO et le ruban en acier inoxydable (SS) sont des matériaux élasto-plastiques ductiles. Cela signifie que leur comportement est linéaire dans la région élastique en dessous de la limite d'élasticité. Les contraintes dans les rubans sont supposées rester sous leur limite d'élasticité. Ainsi, l'application du principe de superposition est possible pour obtenir les champs de déplacement et de contrainte à la suite des trois opérations.

Le calcul des contraintes et des déplacements est effectué pour chacune des chargements séparément, à savoir l'enroulement, le refroidissement et l'alimentation électrique. Des hypothèses de contrainte plane et de déformation plane généralisée (GPS) ont permis de proposer deux formulations analytiques. En cas de contrainte plane, la contrainte axiale est nulle, tandis que la déformation axiale est fonction du coefficient de Poisson et des contraintes dans le plan. En situation de déformation plane généralisée, une résultante axiale est considérée, somme des densités de forces axiales réparties sur la surface. Cette force peut être nulle ou non-nulle (une composante axiale des forces de Laplace peut éventuellement être considérée). En outre, un contact parfait a été supposé entre toutes les spires, c'est-à-dire que toutes les spires restent en contact les unes avec les autres, et que le déplacement radial et la contrainte radiale sont continus. Les deux formulations sont comparées au calcul par éléments finis Cast3m en situation de contrainte plane.

Les calculs sont effectués en coordonnées cylindriques, à partir des équations d'équilibre générales. En ce qui concerne l'enroulement, il s'agit d'un chargement itératif, où l'enroulement de chaque nouveau tour avec pré-tension constitue un chargement supplémentaire pour les tours déjà enroulés. Ainsi, pour trouver le déplacement et les contraintes finaux, un calcul itératif est effectué tout en respectant la condition de contact parfait. Le même type procédure est utilisée pour le calcul Cast3m, la définition du contact étant cependant moins contraignante puisque les spires peuvent être en contact ou séparées.

En ce qui concerne le refroidissement, on suppose que l'ensemble de l'électroaimant MI est isotherme. La dilatation thermique est implémentée dans la loi de comportement élastique. L'application de l'équation d'équilibre conduit à une nouvelle forme d'équation différentielle sur le déplacement. Par continuité du déplacement à l'interface, les contraintes et les déplacements résultants du refroidissement sont calculés.

En ce qui concerne l'excitation, le champ axial est supposé linéaire au niveau du plan médian de l'électroaimant. Cette hypothèse est valable en raison de ses dimensions. Selon Gray [115], cette hypothèse entraîne une erreur négligeable dans les forces de Laplace radiales. La force de Laplace radiale est finalement implémentée dans l'équation d'équilibre générale comme une densité volumique de force.

Les formulations analytiques et le calcul EF Cast3m ont été utilisées pour le calcul du déplacement et de la contrainte d'un électroaimant MI REBCO de référence composé de 50 tours de REBCO+SS (SS: acier inoxydable) et de 10 tours de SS de sur-bobinage afin d'assurer une pré-tension de 100 MPa. Le refroidissement se fait de la température ambiante à 4 K, et l'alimentation électrique consiste à injecter 270 A sur chaque enroulement REBCO pour respecter la limite de supraconductivité du ruban.

Les résultats des calculs montrent que les formulations analytiques et le calcul EF Cast3m sont en accord pour le calcul des contraintes après bobinage. La contrainte radiale est négative, assurant un contact entre les spires. Lors du refroidissement, la contraction estimée est en accord pour les trois calculs. L'état de contrainte diffère cependant entre l'estimation GPS et le deux autres. L'hypothèse de déformation axiale homogène inhérente à la formulation GPS en est la cause. Comme pour le refroidissement, on observe une différence entre les état de contraintes prédits avec l'hypothèse GPS et les autres calculs pour les simulations de l'effet de l'alimentation électrique. La contrainte radiale totale reste compressive, ce qui prouve l'importance du sur-bobinage puisque la contrainte radiale était positive dans certaines régions pendant le refroidissement et l'alimentation électrique.

Les formulations analytiques et Cast3m sont comparées en prenant en compte les conditions

expérimentales de l'aimant "Nougat" à 30 T de champ central. Les calculs ont été effectués en considérant les conditions de chargement de la bobine centrale de l'aimant (plan médian). Les résultats des calculs analytiques conduisent à l'apparition d'une contrainte radiale positive pour une large portion de l'électroaimant, alors que le calcul EF Cast3m prédit une contrainte radiale nulle dans les mêmes zones. La différence entre les résultats obtenus via Cast3m et les calculs analytiques provient du fait qu'un contact unilatéral a été implémenté dans le code E. Ces résultats indiquent cependant tous que les spires ne sont apparemment plus jointives dans les régions concernées. L'aimant "Nougat" a cependant fonctionné correctement dans les mêmes conditions, sans qu'aucun quench nait pu être détecté. Ce constat nous conduit à devoir réévaluer le comportement mécanique de la bande REBCO et SS puisqu'il conditionne le niveau des contraintes radiales estimées. Il conviendra alors de vérifier si ces modifications de comportement ont un impact sur les prédictions.

I.3 . Caractérisation mécanique d'un ruban REBCO / Acier Inoxydable

Pour caractériser les propriétés mécaniques des rubans, deux essais sont utilisés : un essai de traction et un essai de compression diamétrale. Le premier essai permet d'obtenir le module Young orthoradial, la limite d'élasticité et un premier coefficient de poisson ($\nu_{\theta z}$). Le second essai est couplé à une méthode d'identification intégrée des propriétés via un couplage avec un calcul éléments finis (FEMU) : il permet d'estimer le module de Young radial et un second coefficient de poisson ($\nu_{r\theta}$).

Les deux rubans, REBCO et acier inoxydable, sont des matériaux très fins (quelques micromètres d'épaisseur). Cette faible épaisseur empêche l'utilisation de jauges dont la présence peut modifier les mesures. La corrélation d'images numériques (CIN ou DIC en anglais) est employée pour déterminer les déformations lors des essais de traction. La CIN est une technique de mesure sans contact basée sur la comparaison des niveaux de gris entre l'image déformée et l'image de référence. Les bandes étant très fines, l'application d'un effort axial conduit sans autre précaution à une courbure latérale par effet poisson. Cette courbure peut affecter les résultats de la CIN. Ce problème est corrigé en serrant de manière modérée le ruban entre deux plaques de plexiglass transparentes. Les résultats montrent que la limite d'élasticité et le coefficient de Poisson du REBCO sont conformes aux résultats de la littérature. Les valeurs relevées pour le module de Young de l'acier inoxydable sont en revanche inférieures à celles attendues.

Comme les rubans ne peuvent pas être très difficilement enroulés sur eux-mêmes, on utilise un mandrin pour effectuer les tests de compression diamétrale. Le mandrin est en laiton. Deux enroulements sont alors réalisés en utilisant une pré-tension négligeable : un premier enroulement est réalisé avec uniquement une bande de REBCO, un second avec uniquement une bande d'acier inoxydable (SS). Les premiers essais de compression diamétrale sont effectués sur un mandrin seul (non équipé de bande). La procédure FEMU est appliquée afin de retrouver les propriétés élastiques du laiton. Les valeurs identifiées sont cohérentes. Les propriétés élastiques obtenues sont implémentés dans le calcul FEMU des assemblages "Laiton + REBCO" et "Laiton + SS". La procédure FEMU utilise le champ de déplacement obtenu par DIC et les résultats de chargement expérimental pour ajuster itérativement les paramètres du modèle EF de l'échantillon tout en utilisant les mêmes conditions aux limites que celles de l'expérience. Lorsque le critère de convergence du calcul est satisfait (moyenne quadratique de l'incrément des paramètres), le calcul converge. La procédure appliquée aux deux échantillons, conduit à des modules d'élasticité radiaux beaucoup plus faibles que les valeurs attendues.

Après avoir examiné plusieurs articles concernant le processus de bobinage, il peut être conclu que le processus de bobinage affecte le module radial global. Les raisons sont multiples : les imperfections de planéité des bandes, l'existence d'une rugosité de surface, la présence de poussière et une contrainte d'enroulement trop faible. De plus, on observe aisément que partir des échantillons utilisés pour les tests de compression diamétrale, on remarque que, aussi bien pour l'enroulement REBCO que pour l'enroulement SS, l'épaisseur torale de la zone enroulée est supérieure au produit de l'épaisseur nominale d'une bande et du nombre de tours, démontrant la présence de fines zones creuses. Un calcul d'homogénéisation a été effectué sur une portion angulaire du disque, pouvant être considérée comme une structure planaire multicouches. Le calcul d'homogénéisation a permis de vérifier que l'épaisseur des zones creuses est suffisante pour expliquer les faibles valeurs du module radial moyen des enroulements en REBCO ou en SS.

Comme le ruban REBCO est un matériau stratifié, une homogénéisation analytique et par éléments finis a été effectuée pour vérifier les résultats expérimentaux obtenus. Il a été démontré que les résultats de l'homogénéisation pour le module d'Young orthoradial et le coefficient de Poisson $\nu_{\theta z}$ sont en accord avec les résultats expérimentaux. Ce n'est pas le cas en revanche pour le module Young radial ou le coefficient de Poisson $\nu_{r\theta}$. Les différences observées doivent résulter du processus d'enroulement.

Les propriétés mécaniques caractérisées expérimentalement sont utilisées dans les calculs analytiques de l'électroaimant Nougat. On constate une réduction de la contrainte radiale. Celle-ci reste cependant positive dans la zone discutée préalablement.

I.4 . Mesures de déplacement par corrélation d'images numériques sur un prototype de bobine HTS

Un nouveau dispositif expérimental a été développé pour mesurer le champ de déplacement par CIN pendant le refroidissement (jusqu'à 4K) et l'alimentation électrique d'un électroaimant MI REBCO. Ce dispositif comporte deux fenêtres, l'une pour assurer un éclairage et l'autre pour la prise de vue par caméra (on observe l'échantillon à l'intérieur du cryostat et on fait l'acquisition des images pendant le refroidissement et l'alimentation électrique). Les contraintes de la cryogénie ont été prises en compte lors de la conception de l'installation. L'électroaimant ne peut en particulier pas être immergé dans le bain liquide. Un refroidissement par conduction a été choisi, et le laiton est choisi comme support de l'électroaimant en raison de sa très bonne conductivité thermique. Sa faible résistivité électrique peut en outre de limiter les courants de Foucault pendant la montée en courant lors de la mise sous tension.

Dans un premier temps, un disque en acier inoxydable 304 (SS304) est utilisé dans un test de refroidissement à l'azote liquide pour valider la configuration et l'acquisition des images. Les premiers résultats de CIN permettent de distinguer un mouvement de corps rigide (RBM) non négligeable. Sa suppression par calcul permet d'observer un champ de déplacement conforme à la contraction thermique attendue du disque. Les amplitudes observées sont cependant inférieures à celles déduites d'une approche analytique simple. Cet écart est le résultat de la contraction des tiges de support de l'installation G10, ce qui rapproche l'échantillon de la caméra et conduisant à une dilatation apparente. Cet effet d'agrandissement est retiré des résultats de la CIN pour obtenir le déplacement réel. Après ce post-traitement, les résultats expérimentaux sont en accord avec ceux du calcul analytique. Cette expérience a permis de valider le fonctionnement du montage et de l'acquisition des images.

Un électroaimant MI enroulé avec une pré-tension de 15 N sur un mandrin en laiton et composé de bandes de cuivre au béryllium et d'acier inoxydable 304 (MI CuBe2 / SS304) a ensuite été testé. Nous avons procédé à un essai de refroidissement à l'azote liquide. Comme dans le test précédent, les résultats de la CIN sont post-traités pour éliminer le mouvement du corps rigide et l'effet de grandissement. Les résultats obtenus conduisent à une contraction plus élevée que celle calculée analytiquement en utilisant la formulation en contraintes planes. Cela indique que soit es coefficients de contraction thermique utilisés pour le mandrin en laiton ou en cuivre-béryllium à partir des références ne sont pas corrects, soit que l'effet de grandissement n'a pas été correctement évalué.

I.5 . Conclusion

Dans ce thèse, l'importance de chaque chargement (enroulement, refroidissement et alimentation électrique) pour maintenir toutes les spires en contact dans un électroaimant MI a été soulignée. Le pré-tensionnement du bobinage est un facteur important en raison des contraintes résiduelles de compression qui en résultent. Aussi bien les formulations analytiques et qu'un calcul EF Cast3m appliqués à l'électroaimant Nougat ont montré l'apparition de contraintes radiales de traction dans une région étendue de l'électroaimant, indiquant une perte de contact entre spires, perte de contact non observée expérimentalement.

Ce constat nous a amené à vérifier les valeurs des propriétés mécaniques utilisées pour les rubans REBCO et SS. Les tests effectués ont mis en évidence le rôle essentiel du mode d'enroulement. D'après les essais de compression diamétrale, le module de Young radial des deux matériaux est très inférieur aux valeurs de référence. Ces résultats inattendus s'expliquent par un processus de bobinage imparfait. Plusieurs articles ont montré l'effet de la pré-tension sur le module Young radial à travers différentes formulations. Comme pour l'essai de traction, les deux bandes subissent par exemple une courbure latérale par effet Poisson [133]. Cette courbure modifie le contact entre les spires et réduit le module d'Young radial apparent. En outre, la présence de zones creuses dans l'enroulement est souligné en utilisant par les mesures d'épaisseur. Un calcul d'homogénéisation effectué sur les échantillons "Laiton + REBCO" et "Laiton + SS" confirme qu'il est possible d'expliquer ces faibles modules par cette hypothèse. Les propriétés mécaniques caractérisées expérimentalement sont utilisées pour procéder à une nouvelle estimation des contraintes dans l'électroaimant Nougat. La contrainte radiale est réduite mais reste positive.

Pour suivre l'état mécanique in situ d'un électroaimant MI pendant le refroidissement et l'alimentation électrique, un montage a été développé. Celui-ci permet l'acquisition d'images de la surface de l'électroaimant pendant les essais. Les images sont analysées par CIN pour mesurer les champs de déplacement. Dans un premier temps, le montage et l'acquisition d'images sont validés par un test de refroidissement à l'azote liquide d'un disque en acier inoxydable 304. Le test a montré que deux post-traitements des résultats CIN sont nécessaires pour estimer le déplacement réel : le mouvement du corps rigide et l'effet de grandissement par contraction du montage doivent être supprimés. Malgré ces corrections, des écarts encore inexpliqués ont été observés entre les résultats analytiques et l'expérience lors d'un test de refroidissement d'un électroaimant MI CuBe2 / SS304 à l'azote liquide : il pourrait d'agir de l'emploi d'une valeur erronée du coefficient de contraction thermique du mandrin ou du ruban CuBe2, ou encore d'une erreur dans l'évaluation du grandissement par contraction du montage.

La nouvelle configuration a prouvé qu'une observation complète in-situ du champ de

déplacement des électroaimants MI est possible, ce qui ouvre de nouvelles possibilités pour différents tests. Un essai de refroidissement à l'hélium liquide doit d'abord être réalisé. Il sera suivi d'une alimentation électrique d'un électroaimant seul puis couplé à un second pour assurer une intensité suffisante des forces de Laplace. Il sera alors possible d'observer (ou non) la perte de contact prévue (et redoutée) entre les spires.

Bibliography

[1] Seungyong Hahn et al. “HTS Pancake Coils Without Turn-to-Turn Insulation”. In: 21.3 (June 2011), pp. 1592–1595. DOI: 10.1109/tasc.2010.2093492. URL: https://doi.org/10.1109/tasc.2010.2093492.

[2] Dirk van Delft. “History and significance of the discovery of superconductivity by Kamerlingh Onnes in 1911”. In: *Physica C: Superconductivity* 479 (Sept. 2012), pp. 30–35. DOI: 10.1016/j.physc.2012.02.046. URL: https://doi.org/10.1016/j.physc.2012.02.046.

[3] W.Meissner and R.Ochsenfeld. “Ein neuer Effeckt bei Eintritt der Suprleitfahigkeit”. In: *Naturwissenschaften* 21(44) (1933), pp. 787–788.

[4] H. Kamerlingh Onnes. “The appearance of galvanic resistance in supraconductors which are brought into a magnetic field, at a threshold value of the field”. In: *Commun* 139f (1914).

[5] A. Abrikosov. “On the Magnetic Properties of Superconductors of the Second Group”. In: *Soviet Physics JETP-USSR* 5(6) (1957), pp. 1174–1183.

[6] *Engineering current densities of various superconductors at 4.2K with applied magnetic field*. https://nationalmaglab.org/magnet-development/applied-superconductivity-center/plots. (Visited on 09/15/2020).

[7] *Critical surface of common superconductors*. https://www.lhc-closer.es/taking_a_closer_look_at_lhc/0.superconductivity_in_short. (Visited on 12/15/2021).

[8] Lionel Quettier et al. “Commissioning Completion of the Iseult Whole Body 11.7 T MRI System”. In: *IEEE Transactions on Applied Superconductivity* 30.4 (June 2020), pp. 1–5. DOI: 10.1109/tasc.2020.2983702. URL: https://doi.org/10.1109/tasc.2020.2983702.

[9] J. Voccio et al. “Magic-Angle-Spinning NMR Magnet Development: Field Analysis and Prototypes”. In: *IEEE Transactions on Applied Superconductivity* 23.3 (June 2013), pp. 4300804–4300804. DOI: 10.1109/tasc.2013.2245934. URL: https://doi.org/10.1109/tasc.2013.2245934.

[10] Yuquan Chen et al. “Design, Fabrication, and Test of a 2-T Superconducting Dipole Prototype by Using Tilted Solenoids”. In: *IEEE Transactions on Applied Superconductivity* 29.4 (June 2019), pp. 1–5. DOI: 10.1109/tasc.2018.2867792. URL: https://doi.org/10.1109/tasc.2018.2867792.

[11] Pia Jensen Ray. “Master’s thesis: Structural investigation of La(2-x)Sr(x)CuO(4+y) - Following staging as a function of temperature”. In: (Nov. 2015). DOI: 10.6084/M9.FIGSHARE.2075680.V2. URL: https://figshare.com/articles/thesis/Structural_investigation_of_La_2_x_Sr_x_CuO_4_y_Following_staging_as_a_function_of_temperature/2075680/2.

[12] Md. Atikur Rahman. “A Review on Cuprate Based Superconducting Materials Including Characteristics and Applications”. In: *American Journal of Physics and Applications* 3.2 (2015), p. 39. DOI: 10.11648/j.ajpa.20150302.15. URL: https://doi.org/10.11648/j.ajpa.20150302.15.

[13] D. Turrioni et al. “Study of HTS Wires at High Magnetic Fields”. In: 19.3 (June 2009), pp. 3057–3060. DOI: 10.1109/tasc.2009.2017877. URL: https://doi.org/10.1109/tasc.2009.2017877.

[14] Kiyosumi Tsuchiya et al. “Critical Current Characterization of Commercial REBCO Coated Conductors at 4.2 and 77 K”. In: 27.4 (June 2017), pp. 1–5. DOI: 10.1109/tasc.2016.2625762. URL: https://doi.org/10.1109/tasc.2016.2625762.

[15] J. G. Bednorz and K. A. Muller. “Possible high Tc superconductivity in the BaLaCuO system”. In: *Zeitschrift fur Physik B Condensed Matter* 64.2 (June 1986), pp. 189–193. DOI: 10.1007/bf01303701. URL: https://doi.org/10.1007/bf01303701.

[16] Jun Nagamatsu et al. “Superconductivity at 39 K in magnesium diboride”. In: *Nature* 410.6824 (Mar. 2001), pp. 63–64. DOI: 10.1038/35065039. URL: https://doi.org/10.1038/35065039.

[17] Yoichi Kamihara et al. “Iron-Based Layered Superconductor La O1 xFx FeAs with Tc 26 K”. In: *Journal of the American Chemical Society* 130.11 (Mar. 2008), pp. 3296–3297. DOI: 10.1021/ja800073m. URL: https://doi.org/10.1021/ja800073m.

[18] A. P. Drozdov et al. “Conventional superconductivity at 203 kelvin at high pressures in the sulfur hydride system”. In: *Nature* 525.7567 (Aug. 2015), pp. 73–76. DOI: 10.1038/nature14964. URL: https://doi.org/10.1038/nature14964.

[19] A. P. Drozdov et al. “Superconductivity at 250 K in lanthanum hydride under high pressures”. In: *Nature* 569.7757 (May 2019), pp. 528–531. DOI: 10.1038/s41586-019-1201-8. URL: https://doi.org/10.1038/s41586-019-1201-8.

[20] Hiroshi Maeda et al. “A New High-TcOxide Superconductor without a Rare Earth Element”. In: *Japanese Journal of Applied Physics* 27.Part 2, No. 2 (Feb. 1988), pp. L209–L210. DOI: 10.1143/jjap.27.l209. URL: https://doi.org/10.1143/jjap.27.l209.

[21] J. L. Tallon et al. “High-Tc superconducting phases in the series Bi2.1(Ca,Sr)n lCunO2 4”. In: *Nature* 333.6169 (May 1988), pp. 153–156. DOI: 10.1038/333153a0. URL: https://doi.org/10.1038/333153a0.

[22] A.I. Golovashkin et al. “Low temperature direct measurements of Hc2 in HTSC using megagauss magnetic fields”. In: *Physica C: Superconductivity* 185-189 (Dec. 1991), pp. 1859–1860. DOI: 10.1016/0921-4534(91)91055-9. URL: https://doi.org/10.1016/0921-4534(91)91055-9.

[23] E. Barzi et al. “BSCCO-2212 Wire and Cable Studies”. In: *IEEE Transactions on Applied Superconductivity* 21.3 (June 2011), pp. 2335–2339. DOI: 10.1109/tasc.2011.2106106. URL: https://doi.org/10.1109/tasc.2011.2106106.

[24] J. Tenbrink et al. “Development of technical high-Tc superconductor wires and tapes”. In: *IEEE Transactions on Applied Superconductivity* 3.1 (1993), pp. 1123–1126.

[25] D. C. Larbalestier et al. “Isotropic round-wire multifilament cuprate superconductor for generation of magnetic fields above 30 T”. In: *Nature Materials* 13.4 (Mar. 2014), pp. 375–381. DOI: 10.1038/nmat3887. URL: https://doi.org/10.1038/nmat3887.

[26] M. K. Wu et al. “Superconductivity at 93 K in a new mixed-phase Y-Ba-Cu-O compound system at ambient pressure”. In: *Physical Review Letters* 58.9 (Mar. 1987), pp. 908–910. DOI: 10.1103/physrevlett.58.908. URL: https://doi.org/10.1103/physrevlett.58.908.

[27] Tsuyoshi Sekitani, Yasuhiro H Matsuda, and Noboru Miura. “Measurement of the upper critical field of optimally-doped YBa2Cu3O7 in megagauss magnetic fields”. In: *New Journal of Physics* 9.3 (Mar. 2007), pp. 47–47. DOI: 10.1088/1367-2630/9/3/047. URL: https://doi.org/10.1088/1367-2630/9/3/047.

[28] Kalobaran Maiti et al. “Doping dependence of the chemical potential and surface electronic structure in YBa2Cu3O6 and La(2-x)SrxCuO4 using hard x-ray photoemission spectroscopy”. In: *Physical Review B* 80.16 (Oct. 2009). DOI: 10.1103/physrevb.80.165132. URL: https://doi.org/10.1103/physrevb.80.165132.

[29] J. Bardeen, L. N. Cooper, and J. R. Schrieffer. “Microscopic Theory of Superconductivity”. In: *Physical Review* 106.1 (Apr. 1957), pp. 162–164. DOI: 10.1103/physrev.106.162. URL: https://doi.org/10.1103/physrev.106.162.

[30] G. Balestrino and A. Tebano. “Superconductivity in Cuprate Artificial Structures”. In: *Superconductor Science and Technology* 16.8 (Aug. 2003), R29–R46.

[31] Marlon James Dedicatoria et al. “Electro-mechanical Property Evaluation of REBCO Coated Conductor Tape with Stainless Steel Substrate”. In: *Progress in Superconductivity and Cryogenics* 12 (Jan. 2010).

[32] U. Floegel-Delor et al. “High-Efficient Copper Shunt Deposition Technology on REBCO Tape Surfaces”. In: *IEEE Transactions on Applied Superconductivity* 26.3 (Apr. 2016), pp. 1–5. DOI: 10.1109/tasc.2016.2549859. URL: https://doi.org/10.1109/tasc.2016.2549859.

[33] A Sundaram et al. “2G HTS wires made on 30 micro meter thick Hastelloy substrate”. In: *Superconductor Science and Technology* 29.10 (Sept. 2016), p. 104007. DOI: 10.1088/0953-2048/29/10/104007. URL: https://doi.org/10.1088/0953-2048/29/10/104007.

[34] D. Dimos et al. “Orientation Dependence of Grain-Boundary Critical Currents in YB2Cu3O7 Bicrystals”. In: *Physical Review Letters* 61.2 (July 1988), pp. 219–222. DOI: 10.1103/physrevlett.61.219. URL: https://doi.org/10.1103/physrevlett.61.219.

[35] R Teranishi, T Izumi, and Y Shiohara. “Highlights of coated conductor development in Japan”. In: *Superconductor Science and Technology* 19.3 (Jan. 2006), S4–S12. DOI: 10.1088/0953-2048/19/3/002. URL: https://doi.org/10.1088/0953-2048/19/3/002.

[36] Yijie Li, Linfei Liu, and Xiang Wu. “Fabrication of long REBCO coated conductors by PLD process in China”. In: *Physica C: Superconductivity and its Applications* 518 (Nov. 2015), pp. 51–53. DOI: 10.1016/j.physc.2015.03.020. URL: https://doi.org/10.1016/j.physc.2015.03.020.

[37] Y Zhao et al. “Progress in fabrication of second generation high temperature superconducting tape at Shanghai Superconductor Technology”. In: *Superconductor Science and Technology* 32.4 (Feb. 2019), p. 044004. DOI: 10.1088/1361-6668/aafea5. URL: https://doi.org/10.1088/1361-6668/aafea5.

[38] Yasuhirio Iijima, Kazuomi Kakimoto, and Kaoru Takeda. “Long length ion-beam-assisted deposition template films for Y-123 coated conductors”. In: *Physica C: Superconductivity* 357-360 (Aug. 2001), pp. 952–958. DOI: 10.1016/s0921-4534(01)00450-6. URL: https://doi.org/10.1016/s0921-4534(01)00450-6.

[39] Chao Yao and Yanwei Ma. “Superconducting materials: Challenges and opportunities for large-scale applications”. In: *iScience* 24.6 (2021), p. 102541. ISSN: 2589-0042. DOI: https://doi.org/10.1016/j.isci.2021.102541. URL: https://www.sciencedirect.com/science/article/pii/S2589004221005095.

[40] F. Schmidt et al. “Operation Experience and further Development of a High-Temperature Superconducting Power Cable in the Long Island Power Authority Grid”. In: 36 (2012), pp. 1137–1144. DOI: 10.1016/j.phpro.2012.06.190. URL: https://doi.org/10.1016/j.phpro.2012.06.190.

[41] Song-Ho Sohn et al. “Installation and Power Grid Demonstration of a 22.9 kV, 50 MVA, High Temperature Superconducting Cable for KEPCO”. In: 22.3 (June 2012), pp. 5800804–5800804. DOI: 10.1109/tasc.2011.2180279. URL: https://doi.org/10.1109/tasc.2011.2180279.

[42] M Stemmle. “Ampacity project — Worldwide first superconducting cable and fault current limiter installation in a German city center”. In: *IET Conference Publications* 22 (Jan. 2013), pp. 1–4. DOI: 10.1049/cp.2013.0905.

[43] Mikhail Moyzykh et al. “First Russian 220 kV Superconducting Fault Current Limiter (SFCL) For Application in City Grid”. In: 31.5 (Aug. 2021), pp. 1–7. DOI: 10.1109/tasc.2021.3066324. URL: https://doi.org/10.1109/tasc.2021.3066324.

[44] HyunOk Bae. “Brief review of the field test and application of a superconducting fault current limiter”. In: 19.4 (Dec. 2017), pp. 1–11.

[45] Venkata Suresh Vulusala G and Sreedhar Madichetty. “Application of superconducting magnetic energy storage in electrical power and energy systems: a review”. In: 42.2 (May 2017), pp. 358–368. DOI: 10.1002/er.3773. URL: https://doi.org/10.1002/er.3773.

[46] Poulomi Mukherjee and V.V. Rao. “Design and development of high temperature superconducting magnetic energy storage for power applications - A review”. In: 563 (Aug. 2019), pp. 67–73. DOI: 10.1016/j.physc.2019.05.001. URL: https://doi.org/10.1016/j.physc.2019.05.001.

[47] Weijia Yuan et al. “Design and Test of a Superconducting Magnetic Energy Storage (SMES) Coil”. In: 20.3 (June 2010), pp. 1379–1382. DOI: 10.1109/tasc.2010.2041201. URL: https://doi.org/10.1109/tasc.2010.2041201.

[48] Lucio Rossi and Arnaud et al Badel. “The EuCARD2 Future Magnets Program for Particle Accelerator High-Field Dipoles: Review of Results and Next Steps”. In: *IEEE Transactions on Applied Superconductivity* 28.3 (2018), pp. 1–10. DOI: 10.1109/TASC.2017.2784357.

[49] Xiaorong Wang and Daniel R Dietderich et al. *A 1.2 T canted cos θ dipole magnet using high-temperature superconducting CORC wires*. May 2019. DOI: 10.1088/1361-6668/ab0eba. URL: https://doi.org/10.1088/1361-6668/ab0eba.

[50] Xiaorong Wang and Dmytro Abraimov et al. “Development and performance of a 2.9 Tesla dipole magnet using high-temperature superconducting CORC wires”. In: *Superconductor Science and Technology* 34.1 (Dec. 2020), p. 015012. DOI: 10.1088/1361-6668/abc2a5. URL: https://doi.org/10.1088/1361-6668/abc2a5.

[51] Philippe Fazilleau et al. “38 mm diameter cold bore metal-as-insulation HTS insert reached 32.5 T in a background magnetic field generated by resistive magnet”. In: *Cryogenics* 106 (Mar. 2020), p. 103053. DOI: 10.1016/j.cryogenics.2020.103053. URL: https://doi.org/10.1016/j.cryogenics.2020.103053.

[52] Seungyong Hahn et al. “45.5-tesla direct-current magnetic field generated with a high-temperature superconducting magnet”. In: 570.7762 (June 2019), pp. 496–499. DOI: 10.1038/s41586-019-1293-1. URL: https://doi.org/10.1038/s41586-019-1293-1.

[53] Sangwon Yoon et al. “26 T 35 mm all-GdBa2Cu3O7–xmulti-width no-insulation superconducting magnet”. In: *Superconductor Science and Technology* 29.4 (Mar. 2016), 04LT04. DOI: 10.1088/0953-2048/29/4/04lt04. URL: https://doi.org/10.1088/0953-2048/29/4/04lt04.

[54] *NHMFL32T*. https://nationalmaglab.org/user-facilities/dc-field/instruments-dcfield/dc-field-superconducting-magnets/32-tesla-superconducting-magnet-scm32t. (Visited on 04/15/2022).

[55] *Ascend 1.2 GHz*. https://www.bruker.com/products/mr/nmr/magnets/ascend.html. (Visited on 09/15/2020).

[56] Yuri Lvovsky, Ernst Wolfgang Stautner, and Tao Zhang. “Novel technologies and configurations of superconducting magnets for MRI”. In: *Superconductor Science and Technology* 26.9 (July 2013), p. 093001. DOI: 10.1088/0953-2048/26/9/093001. URL: https://doi.org/10.1088/0953-2048/26/9/093001.

[57] Robert A. Slade, Benjamin J. Parkinson, and Rowan M. Walsh. “Test Results for a 1.5 T MRI System Utilizing a Cryogen-free YBCO Magnet”. In: *IEEE Transactions on Applied Superconductivity* 24.3 (June 2014), pp. 1–5. DOI: 10.1109/tasc.2013.2283660. URL: https://doi.org/10.1109/tasc.2013.2283660.

[58] Takayuki Yachida et al. “Magnetic Field Stability Control of HTS-MRI Magnet by Use of Highly Stabilized Power Supply”. In: *IEEE Transactions on Applied Superconductivity* 27.4 (June 2017), pp. 1–5. DOI: 10.1109/tasc.2017.2655618. URL: https://doi.org/10.1109/tasc.2017.2655618.

[59] Shoichi Yokoyama et al. “Design and Cooling Properties of High Stable Field REBCO Superconducting Magnet for MRI”. In: *IEEE Transactions on Applied Superconductivity* 30.4 (June 2020), pp. 1–4. DOI: 10.1109/tasc.2020.2973936. URL: https://doi.org/10.1109/tasc.2020.2973936.

[60] Ben Parkinson. “Design considerations and experimental results for MRI systems using HTS magnets”. In: *Superconductor Science and Technology* 30.1 (Nov. 2016), p. 014009. DOI: 10.1088/0953-2048/30/1/014009. URL: https://doi.org/10.1088/0953-2048/30/1/014009.

[61] A.P.Martinelli and S.L.Wipf. “Investigation of Cryogenic Stability and Reliability of Operation of Nb_3Sn Coils in Helium Gas Enviornment”. In: *IEEE Proc. Appl. Supercond. Conf. Annapolis,1972* (1973), p. 331.

[62] M.N. Wilson and Y. Iwasa. “Stability of superconductors against localized disturbances of limited magnitude”. In: *Cryogenics* 18.1 (Jan. 1978), pp. 17–25. DOI: 10.1016/0011-2275(78)90132-7. URL: https://doi.org/10.1016/0011-2275(78)90132-7.

[63] Yukikazu Iwasa. *Case Studies in Superconducting Magnets*. Springer US, 2009. DOI: 10.1007/b112047. URL: https://doi.org/10.1007/b112047.

[64] M.N.Wilson. *Superconducting Magnets*. Clarendon Press Oxford, 1983.

[65] A. Ishiyama and H. Asai. “A stability criterion for cryocooler-cooled HTS coils”. In: *IEEE Transactions on Applied Superconductivity* 11.1 (2001), pp. 1832–1835. DOI: 10.1109/77.920204.

[66] Jaakko Paasi et al. “Stability and quench of a HTS magnet with a hot spot”. In: *Superconductor Science and Technology* 13 (2000), pp. 949–954.

[67] Robert J. Corruccini and John J.Gniewek. *Specific Heats and Enthalpies of Technical Solids at Low Temperatures, A Compilation From the Literature*. National Bureau of Standards Monograph 21, 1960.

[68] Taotao Huang et al. “Quench Characteristics of HTS Conductors at Low Temperatures”. In: *IEEE Transactions on Applied Superconductivity* 18.2 (June 2008), pp. 1317–1320. DOI: 10.1109/tasc.2008.920797. URL: https://doi.org/10.1109/tasc.2008.920797.

[69] P. Fazilleau et al. “Analysis and Design of the CMS Magnet Quench Protection”. In: 16.2 (June 2006), pp. 1753–1756. DOI: 10.1109/tasc.2006.873267. URL: https://doi.org/10.1109/tasc.2006.873267.

[70] Carmine Senatore et al. “Progresses and challenges in the development of high-field solenoidal magnets based on RE123 coated conductors”. In: 27.10 (Sept. 2014), p. 103001. DOI: 10.1088/0953-2048/27/10/103001. URL: https://doi.org/10.1088/0953-2048/27/10/103001.

[71] A.V. Polyakov et al. “Small Layer-wound ReBCO Solenoids”. In: 45 (2013), pp. 241–244. DOI: 10.1016/j.phpro.2013.05.012. URL: https://doi.org/10.1016/j.phpro.2013.05.012.

[72] Hyun Chul Jo et al. “Characteristic Comparison for the Various Winding Methods of HTS Magnets”. In: *IEEE Transactions on Applied Superconductivity* 22.3 (June 2012), pp. 4902907–4902907. DOI: 10.1109/tasc.2012.2186549. URL: https://doi.org/10.1109/tasc.2012.2186549.

[73] E Ravaioli et al. “A new quench detection method for HTS magnets: stray-capacitance change monitoring”. In: 95.1 (Dec. 2019), p. 015002. DOI: 10.1088/1402-4896/ab4570. URL: https://doi.org/10.1088/1402-4896/ab4570.

[74] Z. Zhong et al. “Experimental Study of the Normal Zone Propagation Velocity in Double-Layer 2G-HTS Wires by Thermal and Electrical Methods”. In: 25.3 (June 2015), pp. 1–5. DOI: 10.1109/tasc.2014.2366451. URL: https://doi.org/10.1109/tasc.2014.2366451.

[75] E.S. Bobrov, J.E.C. Williams, and Y. Iwasa. “Experimental and theoretical investigation of mechanical disturbances in epoxy-impregnated superconducting coils. 2. Shear-stress-induced epoxy fracture as the principal source of premature quenches and training theoretical analysis”. In: *Cryogenics* 25.6 (June 1985), pp. 307–316. DOI: 10.1016/0011-2275(85)90014-1. URL: https://doi.org/10.1016/0011-2275(85)90014-1.

[76] T. Takematsu et al. “Degradation of the performance of a YBCO-coated conductor double pancake coil due to epoxy impregnation”. In: *Physica C: Superconductivity and its Applications* 470.17-18 (Sept. 2010), pp. 674–677. DOI: 10.1016/j.physc.2010.06.009. URL: https://doi.org/10.1016/j.physc.2010.06.009.

[77] A.V. Dudarev et al. “Superconducting windings with short-circuited turns”. In: 158 (June 1997), pp. 1615–1618.

[78] Y. Wang et al. “Ramping turn-to-turn loss and magnetization loss of a No-Insulation (RE)Ba2Cu3Ox high temperature superconductor pancake coil”. In: 121.11 (Mar. 2017), p. 113903. DOI: 10.1063/1.4978593. URL: https://doi.org/10.1063/1.4978593.

[79] Y Wang, Wan Kan Chan, and Justin Schwartz. “Self-protection mechanisms in no-insulation (RE)Ba2Cu3Oxhigh temperature superconductor pancake coils”. In: 29.4 (Mar. 2016), p. 045007. DOI: 10.1088/0953-2048/29/4/045007. URL: https://doi.org/10.1088/0953-2048/29/4/045007.

[80] Y H Choi et al. “Partial insulation of GdBCO single pancake coils for protection-free HTS power applications”. In: 24.12 (Nov. 2011), p. 125013. DOI: 10.1088/0953-2048/24/12/125013. URL: https://doi.org/10.1088/0953-2048/24/12/125013.

[81] R Gyuráki et al. “Fluorescent thermal imaging of a quench in insulated and non-insulated REBCO-wound pancake coils following a heater pulse at 77 K”. In: *Superconductor Science and Technology* 33.3 (Feb. 2020), p. 035006. DOI: 10.1088/1361-6668/ab6dc0. URL: https://doi.org/10.1088/1361-6668/ab6dc0.

[82] Jung-Bin Song et al. “Construction and Test of a 7 T Metal-as-Insulation HTS Insert Under a 20 T High Background Magnetic Field at 4.2 K”. In: *IEEE Transactions on Applied Superconductivity* 29.5 (Aug. 2019), pp. 1–5. DOI: 10.1109/tasc.2019.2901212. URL: https://doi.org/10.1109/tasc.2019.2901212.

[83] Jung-Bin Song et al. “Over-current quench test and self-protecting behavior of a 7 T/78 mm multi-width no-insulation REBCO magnet at 4.2 K”. In: *Superconductor Science and Technology* 28.11 (Sept. 2015), p. 114001. DOI: 10.1088/0953-2048/28/11/114001. URL: https://doi.org/10.1088/0953-2048/28/11/114001.

[84] Kabindra R Bhattarai et al. “Understanding quench in no-insulation (NI) REBCO magnets through experiments and simulations”. In: *Superconductor Science and Technology* 33.3 (Jan. 2020), p. 035002. DOI: 10.1088/1361-6668/ab6699. URL: https://doi.org/10.1088/1361-6668/ab6699.

[85] Jaemin Kim et al. “Effect of Resistive Metal Cladding of HTS Tape on the Characteristic of No-Insulation Coil”. In: 26.4 (June 2016), pp. 1–6. DOI: 10.1109/tasc.2016.2541687. URL: https://doi.org/10.1109/tasc.2016.2541687.

[86] Kwanglok Kim et al. “Quench behavior of a no-insulation coil wound with stainless steel cladding REBCO tape at 4.2 K”. In: *Superconductor Science and Technology* 30.7 (May 2017), p. 075001. DOI: 10.1088/1361-6668/aa6a8b. URL: https://doi.org/10.1088/1361-6668/aa6a8b.

[87] Thibault Lecrevisse and Yukikazu Iwasa. “A (RE)BCO Pancake Winding With Metal-as-Insulation”. In: 26.3 (Apr. 2016), pp. 1–5. DOI: 10.1109/tasc.2016.2522638. URL: https://doi.org/10.1109/tasc.2016.2522638.

[88] T Lécrevisse et al. “Metal-as-insulation variant of no-insulation HTS winding technique: pancake tests under high background magnetic field and high current at 4.2 K”. In: 31.5 (Apr. 2018), p. 055008. DOI: 10.1088/1361-6668/aab4ec. URL: https://doi.org/10.1088/1361-6668/aab4ec.

[89] Youngjae Kim et al. “Strain in YBCO Double-Pancake Coil With Stainless Steel Overband Under External Magnetic Field”. In: 25.3 (June 2015), pp. 1–4. DOI: 10.1109/tasc.2014.2365738. URL: https://doi.org/10.1109/tasc.2014.2365738.

[90] C Barth, G Mondonico, and C Senatore. “Electro-mechanical properties of REBCO coated conductors from various industrial manufacturers at 77 K, self-field and 4.2 K, 19 T”. In: *Superconductor Science and Technology* 28.4 (Feb. 2015), p. 045011. DOI: 10.1088/0953-2048/28/4/045011. URL: https://doi.org/10.1088/0953-2048/28/4/045011.

[91] Kozo Osamura, Shutaro Machiya, and Damian P Hampshire. “Mechanism for the uniaxial strain dependence of the critical current in practical RE-BCO tapes”. In: *Superconductor Science and Technology* 29.6 (May 2016), p. 065019. DOI: 10.1088/0953-2048/29/6/065019. URL: https://doi.org/10.1088/0953-2048/29/6/065019.

[92] Sang-Soo Oh et al. “Variation of Local Critical Current Due to Mechanical Strain in RCE-REBCO Coated Conductors”. In: *IEEE Transactions on Applied Superconductivity* 24.3 (June 2014), pp. 1–4. DOI: 10.1109/tasc.2013.2281788. URL: https://doi.org/10.1109/tasc.2013.2281788.

[93] Hyung-Seop Shin et al. “Characteristic Strain Response of Ic in SmBCO Coated Conductor Tapes Under Magnetic Field at 77 K”. In: *IEEE Transactions on Applied Superconductivity* 22.3 (June 2012), pp. 6600404–6600404. DOI: 10.1109/tasc.2012.2182978. URL: https://doi.org/10.1109/tasc.2012.2182978.

[94] D C van der Laan et al. “Effect of strain, magnetic field and field angle on the critical current density of Y Ba2Cu3O7-coated conductors”. In: *Superconductor Science and Technology* 23.7 (May 2010), p. 072001. DOI: 10.1088/0953-2048/23/7/072001. URL: https://doi.org/10.1088/0953-2048/23/7/072001.

[95] Kozo Osamura et al. “Internal residual strain and critical current maximum of a surrounded Cu stabilized YBCO coated conductor”. In: *Superconductor Science and Technology* 22.6 (Apr. 2009), p. 065001. DOI: 10.1088/0953-2048/22/6/065001. URL: https://doi.org/10.1088/0953-2048/22/6/065001.

[96] Hyung-Seop Shin and Zhierwinjay Mezona Bautista. “Evaluation of Irreversible Strain/Stress Limits for Ic Degradation in Practical REBCO CC Tapes Under Uniaxial Tension”. In: *IEEE Transactions on Applied Superconductivity* 28.4 (June 2018), pp. 1–5. DOI: 10.1109/tasc.2017.2788078. URL: https://doi.org/10.1109/tasc.2017.2788078.

[97] K Kajita et al. “Degradation of a REBCO conductor due to an axial tensile stress under edgewise bending: a major stress mode of deterioration in a high field REBCO coil’s performance”. In: *Superconductor Science and Technology* 30.7 (May 2017), p. 074002. DOI: 10.1088/1361-6668/aa6c38. URL: https://doi.org/10.1088/1361-6668/aa6c38.

[98] *Superconducting Wire GdBCO*. http://www.i-sunam.com/home/en_product,1,3,1,1,1. (Visited on 07/22/2019).

[99] D C van der Laan and J W Ekin. “Dependence of the critical current of YBa2Cu3O7-δ coated conductors on in-plane bending”. In: *Superconductor Science and Technology* 21.11 (Sept. 2008), p. 115002. DOI: 10.1088/0953-2048/21/11/115002. URL: https://doi.org/10.1088/0953-2048/21/11/115002.

[100] H.S. Shin et al. “Bending strain characteristics of critical current in REBCO CC tapes in different modes”. In: *Physica C: Superconductivity* 469.15-20 (Oct. 2009), pp. 1467–1471. DOI: 10.1016/j.physc.2009.05.067. URL: https://doi.org/10.1016/j.physc.2009.05.067.

[101] Simon Otten et al. “Bending properties of different REBCO coated conductor tapes and Roebel cables at T = 77 K”. In: *Superconductor Science and Technology* 29.12 (Oct. 2016), p. 125003. DOI: 10.1088/0953-2048/29/12/125003. URL: https://doi.org/10.1088/0953-2048/29/12/125003.

[102] J E Huber, D Nowell, and D. A Hills. “On the stress analysis of a wound coil with application to electromagnet manufacture”. In: *The Journal of Strain Analysis for Engineering Design* 42.6 (Aug. 2007), pp. 447–460. DOI: 10.1243/03093247jsa279. URL: https://doi.org/10.1243/03093247jsa279.

[103] H.T. Hahn, E.A. Kempner, and S.S. Lee. “The stress development during filament winding of thick cylinders”. In: *Composites Manufacturing* 4.3 (Sept. 1993), pp. 147–156. DOI: 10.1016/0956-7143(93)90099-t. URL: https://doi.org/10.1016/0956-7143(93)90099-t.

[104] P. M. Lin and J. A. Wickert. “Analysis of Core Buckling Defects in Sheet Metal Coil Processing”. In: *Journal of Manufacturing Science and Engineering* 125.4 (2003), p. 771. DOI: 10.1115/1.1619177. URL: https://doi.org/10.1115/1.1619177.

[105] L.B. Luganski. “Calculation of Mechanical Stresses in Solenoids(A Multilayer Model)”. en. In: *Journal of Applied Physics* 40.12 (Dec. 1995), pp. 1267–1272.

[106] V. Arp. “Stresses in superconducting solenoids”. en. In: *Journal of Applied Physics* 48.5 (May 1977), pp. 2026–2036. ISSN: 0021-8979, 1089-7550. DOI: 10.1063/1.323913. URL: http://aip.scitation.org/doi/10.1063/1.323913 (visited on 04/04/2019).

[107] Lankai Li et al. “Preliminary Mechanical Analysis of a 9.4-T Whole-Body MRI Magnet”. In: *IEEE Transactions on Applied Superconductivity* 25.2 (Apr. 2015), pp. 1–7. DOI: 10.1109/tasc.2015.2396934. URL: https://doi.org/10.1109/tasc.2015.2396934.

[108] H Pan et al. “Static stress analysis of coupling superconducting solenoid coil assembly for Muon Ionization Cooling Experiment”. In: *Nuclear Science and Techniques* 21 (Feb. 2010), pp. 29–34.

[109] S.R. White and Z. Zhang. “The Effect of Mandrel Material on the Processing-Induced Residual Stresses in Thick Filament Wound Composite Cylinders”. In: *Journal of Reinforced Plastics and Composites* 12.6 (June 1993), pp. 698–711. DOI: 10.1177/073168449301200607. URL: https://doi.org/10.1177/073168449301200607.

[110] M. Reza Eslami et al. “Thermal Stresses in Circular Cylinders”. In: *Theory of Elasticity and Thermal Stresses*. Springer Netherlands, 2013, pp. 445–473. DOI: 10.1007/978-94-007-6356-2_18. URL: https://doi.org/10.1007/978-94-007-6356-2_18.

[111] W. Denis Markiewicz et al. “Generalized plane strain analysis of superconducting solenoids”. en. In: *Journal of Applied Physics* 86.12 (Dec. 1999), pp. 7039–7051. ISSN: 0021-8979, 1089-7550. DOI: 10.1063/1.371791. URL: http://aip.scitation.org/doi/10.1063/1.371791 (visited on 04/03/2019).

[112] S. Caspi et al. *Stress-Strain in Shells Under Mechanical Thermal and Magnetic Loads*. en. Lawrence Berkeley Laboratory University of California, Mar. 1998, pp. 1–12.

[113] N. Mitchell and U. Mszanowski. "Stress analysis of structurally graded long solenoid coils". In: *IEEE Transactions on Magnetics* 28.1 (1992), pp. 226–229. DOI: 10.1109/20.119851. URL: https://doi.org/10.1109/20.119851.

[114] James Caldwell. "Electromagnetic forces in high field magnet coils". In: *Applied Mathematical Modelling* 6.3 (June 1982), pp. 157–160. DOI: 10.1016/0307-904x(82)90003-8. URL: https://doi.org/10.1016/0307-904x(82)90003-8.

[115] W. H. Gray and J. K. Ballou. "Electromechanical stress analysis of transversely isotropic solenoids". In: *Journal of Applied Physics* 48.7 (July 1977), pp. 3100–3109. DOI: 10.1063/1.324081. URL: https://doi.org/10.1063/1.324081.

[116] A.W. Cox et al. "Power series stress analysis of solenoid magnets". In: *IEEE Transactions on Magnetics* 32.4 (July 1996), pp. 3012–3015. DOI: 10.1109/20.511510. URL: https://doi.org/10.1109/20.511510.

[117] W.D. Markiewicz et al. "Transverse stress on Nb3Sn conductors in high field NMR magnets". In: *IEEE Transactions on Applied Superconductivity* 3.1 (Mar. 1993), pp. 258–261. DOI: 10.1109/77.233720. URL: https://doi.org/10.1109/77.233720.

[118] Daniel Weisz-Patrault, Alain Ehrlacher, and Nicolas Legrand. "Non-linear simulation of coiling accounting for roughness of contacts and multiplicative elastic-plastic behavior". In: *International Journal of Solids and Structures* 94-95 (Sept. 2016), pp. 1–20. DOI: 10.1016/j.ijsolstr.2016.05.012. URL: https://doi.org/10.1016/j.ijsolstr.2016.05.012.

[119] Edwards W. and Boulton G. "The mystery of coil winding". In: *In: 2001 Iron and Steel Exposition and AISE Annual Convention* (2001), pp. 2001–2017.

[120] B.K. KANDADAI and J.K. GOOD. "Winding virtual rolls". In: *TAPPI Journal* 10.6 (July 2011), pp. 25–31. DOI: 10.32964/tj10.6.25. URL: https://doi.org/10.32964/tj10.6.25.

[121] Y. M. Lee and J. A. Wickert. "Width-Wise Variation of Magnetic Tape Pack Stresses". In: *Journal of Applied Mechanics* 69.3 (May 2002), pp. 358–369. DOI: 10.1115/1.1460911. URL: https://doi.org/10.1115/1.1460911.

[122] Ren Yao. "The wound-on-tension of winders with nip rollers". Oklahoma State University, 2016.

[123] Yu. M. Tarnopol skii, S. T. Peters, and A. I. Beil. "Filament Winding". In: *Handbook of Composites*. Ed. by S. T. Peters. Boston, MA: Springer US, 1998, pp. 456–475. ISBN: 978-1-4615-6389-1. DOI: 10.1007/978-1-4615-6389-1_22. URL: https://doi.org/10.1007/978-1-4615-6389-1_22.

[124] *Cast3m finite element software*. http://www-cast3m.cea.fr/. (Visited on 11/07/2020).

[125] *Stainless steel 316L properties*. https://industeel.arcelormittal.com/wp-content/uploads/2016/01/DS-INOX-UR316Lv2.pdf. (Visited on 11/08/2020).

[126] *Non magnetic stainless steel Durnomag*. https://www.matthey.ch/fileadmin/user_upload/downloads/fichetechnique/FR/Durnomag.pdf. (Visited on 11/08/2020).

[127] Nadezda Bagrets et al. "Thermal properties of 2G coated conductor cable materials". In: *Cryogenics* 61 (May 2014), pp. 8–14. DOI: 10.1016/j.cryogenics.2014.01.015. URL: https://doi.org/10.1016/j.cryogenics.2014.01.015.

[128] Yukikazu Iwasa et al. "A High-Resolution 1.3-GHz/54-mm LTS/HTS NMR Magnet". In: *IEEE Transactions on Applied Superconductivity* 25.3 (June 2015), pp. 1–5. DOI: 10.1109/tasc.2014.2363496. URL: https://doi.org/10.1109/tasc.2014.2363496.

[129] Guy Aubert. *Composantes du champ magnétique créé par un aimant à demi-section axiale rectangulaire et densité de courant azimutale uniforme*. 2020-11-07.

[130] *On Saint Venant's Principle*. https://www.ams.org/journals/bull/1945-51-08/S0002-9904-1945-08394-3/S0002-9904-1945-08394-3.pdf. (Visited on 11/05/2021).

[131] Stephane Avril et al. "Overview of Identification Methods of Mechanical Parameters Based on Full-field Measurements". In: *Experimental Mechanics* 48.4 (July 2008), pp. 381–402. DOI: 10.1007/s11340-008-9148-y. URL: https://doi.org/10.1007/s11340-008-9148-y.

[132] Zvonimir Tomicevc, Francois Hild, and Stephane Roux. "Mechanics-aided digital image correlation". In: *The Journal of Strain Analysis for Engineering Design* 48.5 (June 2013), pp. 330–343. DOI: 10.1177/0309324713482457. URL: https://doi.org/10.1177/0309324713482457.

[133] Keyang Wang et al. "Nonlinear contact behavior of HTS tapes during pancake coiling and CORC cabling". In: 34.7 (May 2021), p. 075003. DOI: 10.1088/1361-6668/abf710. URL: https://doi.org/10.1088/1361-6668/abf710.

[134] *Leclerc H, Neggers J, Mathieu F, Hild F and Roux S 2015 Correli 3.0, IDDN. FR. 001.520008. 000. SP 2015.000.31500 Agence pour la Protection des Programmes Paris (France),*

[135] *Brass CuZn23Al4 Material Mechanical Properties*. http://www.m-lego.com/pdf/BL6-FR.pdf. (Visited on 11/22/2020).

[136] C.C. Clickner et al. "Mechanical properties of pure Ni and Ni-alloy substrate materials for Y–Ba–Cu–O coated superconductors". In: 46.6 (June 2006), pp. 432–438. DOI: 10.1016/j.cryogenics.2006.01.014. URL: https://doi.org/10.1016/j.cryogenics.2006.01.014.

[137] J Sas, K-P Weiss, and A Jung. "The Mechanical and material properties of 316LN austenitic stainless steel for the fusion application in cryogenic temperatures". In: 102 (Dec. 2015), p. 012003. DOI: 10.1088/1757-899x/102/1/012003. URL: https://doi.org/10.1088/1757-899x/102/1/012003.

[138] *Material Properties at Cryogenic Temperature NIST*. https://trc.nist.gov/cryogenics/materials/materialproperties.htm. (Visited on 06/28/2021).

[139] F. Mathieu et al. "Estimation of Elastoplastic Parameters via Weighted FEMU and Integrated DIC". In: *Experimental Mechanics* 55.1 (May 2014), pp. 105–119. DOI: 10.1007/s11340-014-9888-9. URL: https://doi.org/10.1007/s11340-014-9888-9.

[140] P. Kaboré et al. "Modelling Radial Compressive Modulus in Wound Rolls". In: *Measurement and Control* 40.7 (Sept. 2007), pp. 207–210. DOI: 10.1177/002029400704000702. URL: https://doi.org/10.1177/002029400704000702.

[141] THEVA. In: *THEVA Pro-Line HTS tapes* (Nov. 2021). URL: https://www.theva.com/products/#pro-line (visited on 11/01/2021).

[142] *Boron Nitride Application*. https://www.bn.saint-gobain.com/. (Visited on 07/22/2021).

[143] J. Pelegrin, W. O. S. Bailey, and D. A. Crump. "Application of DIC to Extract Full Field Thermo-Mechanical Data From an HTS Coil". In: *IEEE Transactions on Applied Superconductivity* 28.4 (June 2018), pp. 1–5. DOI: 10.1109/tasc.2018.2807376. URL: https://doi.org/10.1109/tasc.2018.2807376.

[144] Rory Bigger et al. *A Good Practices Guide for Digital Image Correlation*. Tech. rep. Oct. 2018. DOI: 10.32720/idics/gpg.ed1. URL: https://doi.org/10.32720/idics/gpg.ed1.

[145] A.S. Chernyatin, Yu.G. Matvienko, and P. Lopez-Crespo. "Mathematical and numerical correction of the DIC displacements for determination of stress field along crack front". In: *Procedia Structural Integrity* 2 (2016), pp. 2650–2658. DOI: 10.1016/j.prostr.2016.06.331. URL: https://doi.org/10.1016/j.prostr.2016.06.331.

[146] Caterina Casavola et al. "Orthotropic mechanical properties of fused deposition modelling parts described by classical laminate theory". In: 90 (Jan. 2016), pp. 453–458. DOI: 10.1016/j.matdes.2015.11.009. URL: https://doi.org/10.1016/j.matdes.2015.11.009.

[147] Keff Procedure. In: *Cast3M* (Nov. 2020). URL: http://www-cast3m.cea.fr/index.php?page=procedures&procedure=%40keff (visited on 11/22/2020).

[148] CLPD. In: *Procédure Cast3M* (Nov. 2020). URL: http://www-cast3m.cea.fr/index.php?page=procedures&procedure=%40clpd (visited on 11/22/2020).

[149] H. Berger et al. "Numerical and Analytical Approaches for Calculating the Effective Thermo-Mechanical Properties of Three-Phase Composites". In: 30.8 (July 2007), pp. 801–817. DOI: 10.1080/01495730701415665. URL: https://doi.org/10.1080/01495730701415665.